

FIRE TEST ON AN ADMINISTRATIVE BUILDING IN MOKRSKO



Czech Technical University in Prague

Fire Test on an Administrative Building in Mokrsko

Summary of the Results from the Fire Experiment

fire.fsv.cvut.cz/firetest_mokrsko

Wald F., Kallerová P., Chlouba P., Sokol Z., Strejček M.,
Pospíšil J., Štroner M., Křemen T., Smítka V.

ISBN 978-80-01-04571-8

Printing house Česká technika, Czech Technical University in Prague
Prague, May 2010

250 copies, 152 pages, 38 tables, 161 figures

LIST OF CONTENTS

| | |
|--|-----|
| Introduction | 5 |
| 1 Experimental structure | 7 |
| 2 Loading | 13 |
| 2.1 Mechanical load | 13 |
| 2.2 Fire load | 15 |
| 3 Gas temperatures | 17 |
| 4 Temperatures of structures | 25 |
| 4.1 Structural elements | 25 |
| 4.2 Connections | 33 |
| 4.3 External column | 38 |
| 4.4 Composite slab | 41 |
| 4.5 Wall temperatures | 43 |
| 4.6 Plaster wall temperatures | 50 |
| 5 Deformations | 53 |
| 5.1 Deflectometers | 53 |
| 5.2 Trigonometric measurement | 58 |
| 5.3 Laser scanning | 79 |
| 6 Relative stresses | 99 |
| 7 Weather conditions, flux density of heat | 103 |
| 8 Summary | 107 |
| References | 113 |
| Annexes | |
| A Location of load and measurements | 115 |
| B Tables of measured values | 129 |

INTRODUCTION

The main objective of the fire test in Mokrsko was to study the overall behaviour of the structure, which may not be observed on separate tests on individual elements. Six wall structures with mineral wool were tested and three types of flooring systems. The results of the fire test can be applied in advanced building technologies and fire design methods to increase fire resistance and economy. The test was focused on improving the description of the element and its connection behaviour. The results provide increasing reliability of structure design exposed to fire with advanced fire modelling in the fire compartment, transfer and development of heat into the structure and the behaviour of the structure exposed to high temperatures. Gas and element temperature as well as overall and relative deformations, gas pressure, humidity, radiation of the compartment to the structural element and the external steel column, plus transport of moisture through the walls and climatic conditions during the test were all measured during the fire. The performance was documented by photographs, video and thermo image records.

The fire experiment was conducted in Mokrsko district, Příbram in Central Bohemia, Czech Republic, which is located 50 km south of Prague, under the supervision of the staff of Department of Steel and Timber Structures, Czech Technical University in Prague 18 September 2008. The new building was prepared at CTU in the Prague Educational Centre, Joseph Gallery. The experiment followed seven large fire tests in the Cardington Laboratory on a steel frame conducted between 1998 and 2003, see [1] and [2]. During the experiment, knowledge learned during the Ostrava fire test was also applied; see [3] and [4] as well.

The structure was designed at ambient temperature by the partner companies in the Consortium, which was established to perform the test, see [5]. The fire design of the structure was prepared at the Czech Technical University in Prague, the University of Sheffield and the Slovak Technical University in Bratislava, based on European standards; see [6] and [7]. The steel-to-concrete composite slab increases the fire resistance of the ceiling even with some unprotected secondary beams. The expected deformation of the slab 9 x 12 m simulated by the VULCAN programme was over 700 mm in 60 min. The behaviour of slender castellated beams and beams with a corrugated web were simulated including the concrete slab and the connection behaviour at an elevated temperature. The design drawings were prepared by EXCON a.s. Prague in cooperation with the parties involved in the structural parts delivery. The construction of the experimental building is documented in Fig. 1.1. Figs. 1.2 to 1.9 show the erection of the structure from March 2008 to September 2008.

The preparation, execution and evaluation of the experiment was in addition supported by the Research Centre of the Ministry of Education, Youth and Sports CIDEAS No. 1M0579, Research Plan Sustainable Construction No. 6840770005 and grants Component Methods of Joints Exposed to Elevated Temperature GACR No. 103-07-1142 and Fire Improved Joints No. OC 190.

The fire test was conducted by the Czech Technical University in Prague in cooperation with the Institute of Applied Mechanics of the Academy of Sciences of the Czech Republic, Pavus a.s., The University of Sheffield, The Slovak University of Technology in Bratislava, the General Directorate of Fire Prevention, The Fire and Rescue Service of the Czech Republic The Ministry of Interior, The Professional Chamber of Fire Prevention, The Technical Institute of Fire Prevention, and Faculty of Safety Engineering of The Technical University in Ostrava. The erection and demolition of the experimental building was carried out by ArcelorMittal Long Carbon R&D Centre, EXCON a.s., Rockwool a.s., Promat s.r.o.,

HAIRONVILLE VIKAM s.r.o., Metrostav a.s., TBG Metrostav s.r.o., DYWIDAG PREFA a.s., Kovové profily s.r.o., Kingspan a.s., SGB a Hünnebeck CZ s.r.o., Skála a Vít s.r.o. et al. Public Relations support was provided by Donath-Burson-Marsteller. The journal Konstrukce helped as a media partner.

The authors contributed to the chapters of this publication as follows: Petra Kallerová editor and chapters 2 to 5.1 and 7, Annexes A and B, Tomáš Křemen chapters 5.2 and 5.3, Jiří Chlouba chapters 4 and 5.1, Jiří Pospíšil chapters 5.2 and 5.3, Zdeněk Sokol chapter 4.2, Michal Strejček chapter 6., Václav Smítka chapters 5.2 and 5.3., Martin Štroner chapters 5.2 and 5.3, František Wald editor and chapters 1 to 5.1 and 6 to 8. The publication was kindly reviewed by Magdaléna Chladná and Aleš Dudáček.

Further materials about the fire test may be found on these web pages, see [8] and [9].

In Prague June 2010
František Wald

1 EXPERIMENTAL STRUCTURE

The experimental structure represented one floor of an administrative building 12 x 18 m, with a height of 4 m, see Fig. 1.1. The orientation of the wall with a window opening was 21° to the Southeast.

The composite slab above the cellular Angelina beams was designed with a span 9 to 12 m and the overhead beams with corrugated webs with a span 9 to 6 m. The composite slab consisted of a simple trapezoidal CF60 sheet 0.75 mm thick and the height of the rib was 60 mm. The height of the slab was 60 mm; the total thickness of the ceiling structure was 120 mm. A smooth mesh \varnothing 5 mm 100/100 mm was used in the concrete with the strength of 500 MPa and 20mm coverage. The concrete used for the composite slab was classified as concrete C30/37. During the concreting, three specimens of the same concrete were used. The specimen was a cube with the edge length of 150 mm. The average values of the density were 2230 kg/m³ and the compressive cube strength was 34 MPa. After the fire test, three specimens of the composite structure above the secondary Angelina beams were cut. The specimens were taken from the places where the concrete in pressure hadn't failed in the cylinders with a diameter of 150 mm. The average values of the density were 2340 kg/m³ and compressive cylindrical strength was 32.5 MPa.

Prefabricated hollow core Spiroll (S1-S5) panels 320 mm high with hollow core openings form a span of 9 m. The panels were supported by a concrete wall and the primary hollow beam from a welded double IPE 400 section.

The height of the castellated beams with the sinusoid Angelina (AS1-AS7), openings designed by ArcelorMittal, was 395 mm. They were made from an IPE 270 profile and from steel S235. The beams with corrugated webs (CS1-CS4), designed by Kovové profily s.r.o., were WTB 500, the thickness of the web was 2.5 mm, the flanges dimensions were 220 x 15 mm. Steel S320 was used.

The edge beams were from sections IPE 400 steel S235. The fire protected columns were prepared from HEB 180 sections.

Two cladding walls were composed from linear trays, mineral wool in the middle and external corrugated sheets. In two 6 m spans a system with an internal grid and horizontal sheeting and a system with vertical sheeting without the internal grid were compared. Two other walls were made of sandwich panels 150 mm thick filled with mineral wool.

The horizontal stiffness of the frame was constructed with concrete walls 250 mm thick made of concrete C30/37 and two cross braces of L 80 x 80 x 8.

The beam to beam and beam to column connections were designed as header plate connections, 10 mm with four bolts M20 class 8.8. The improved fire resistance was achieved by placing two upper bolts into the concrete slab.

Fire protection of columns, primary and edge beams as well as bracings was designed for resistance R60 by board protection of 2 x 15 mm of Promatect H.

Two window openings were in the front wall, the diameter of each was 2.34 x 4.00 mm, and height above the floor was 800 mm. The openings were without glass. The door with fire protection was situated in the back part of the fire compartment and its width was 800 mm. This door was in the wall of the fire compartment due to the initiation burning of the fire load. During the entire fire test it was closed.

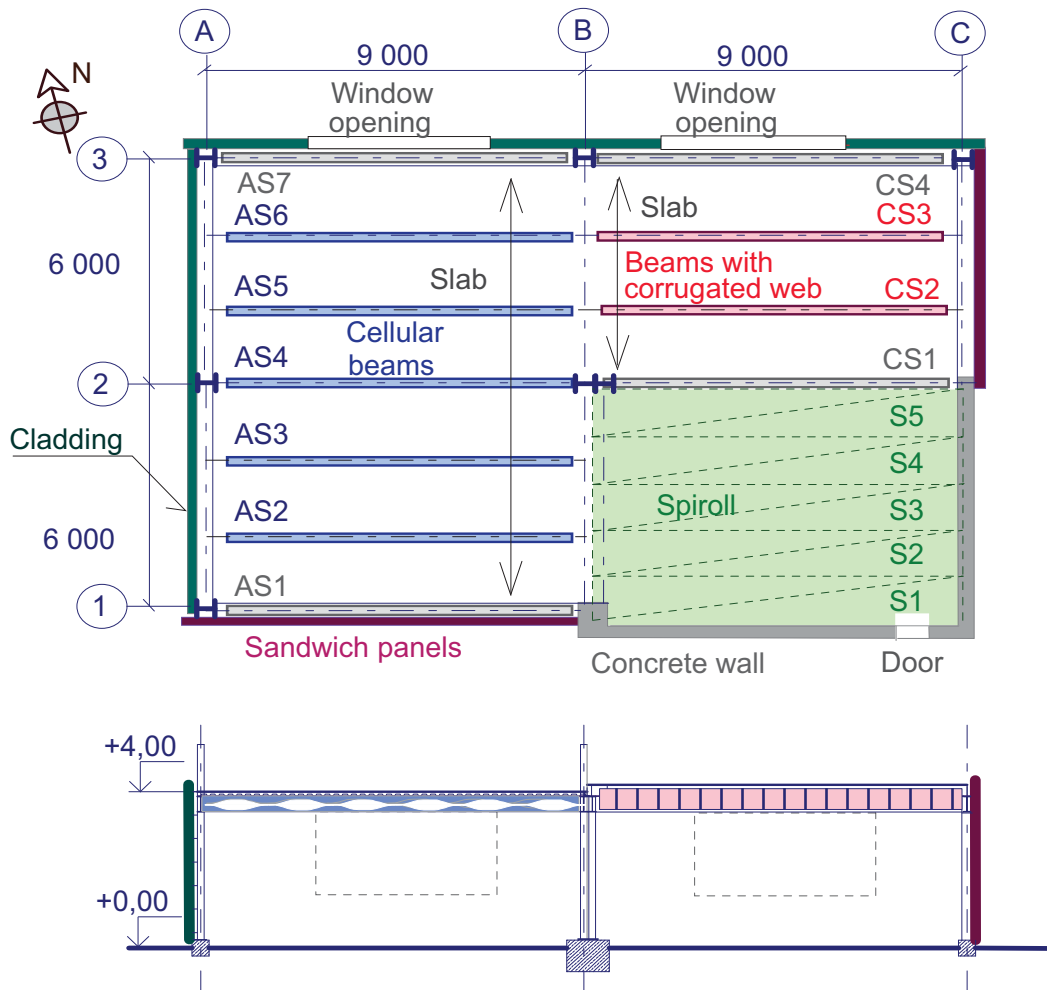


Fig. 1.1 - Fire compartment with description of the major floor and wall structures

In Figs. 1.2 to 1.9 the structure of the ground floor of the administrative building is shown. Here is a list of the figures: erection of the steel structure in Fig. 1.2, horizontal stiffness of the frame in Figs. 1.2 and 1.8, connections of the secondary beams to the primary beams or to the columns in Figs. 1.4 and 1.5, and 1.7, the composite slab before concreting in Fig. 1.6, the composite slab with cellular beams in Fig. 1.3 and views of the fire compartment in Figs. 1.8 and 1.9.



Fig. 1.2 - Erection of the steel structure



Fig. 1.3 - Composite slab with castellated beams



Fig. 1.4 - Connections to the secondary beam



Fig. 1.5 - Connections to the edge beam and internal column



Fig. 1.6 - Connection of the reinforcing mesh on the secondary beam



Fig. 1.7 - Connections to the secondary beam



Fig. 1.8 - The west part of the fire compartment before the test



Fig. 1.9 - The east part of the fire compartment before the test

2 LOADING

2.1 Mechanical load

The mechanical load was situated above the testing composite slab and pre-stressed panels. This load was designed to comply with a regular administrative building, in which the variable action varies from 2.5 to 3.5 kN/m². The dead load of the tested structure reached 2.6 kN/m². During the fire situation, the mechanical load did not reach maximal values. The variable load during the fire experiment was 3.0 kN/m² and it was simulated by plastic bags filled with road-metal. The weight of each bag varied from 793 kg to 1087 kg. The bags on the composite slab were organized into six rows, between steel beams and they were placed on wooden pallets to ensure uniform distribution of the mechanical load on the ceiling structure. On the pre-stressed panels, the bags with mechanical load were placed without pallettes. The distribution of the bags with their weights can be seen in Fig. 2.1 to 2.3. The average weight of each bag was 900 kg. The applied load represented the characteristic value of the variable action at an elevated temperature of 3.0 kN/m² and the characteristic value of flooring and partitions 1.0 kN/m².

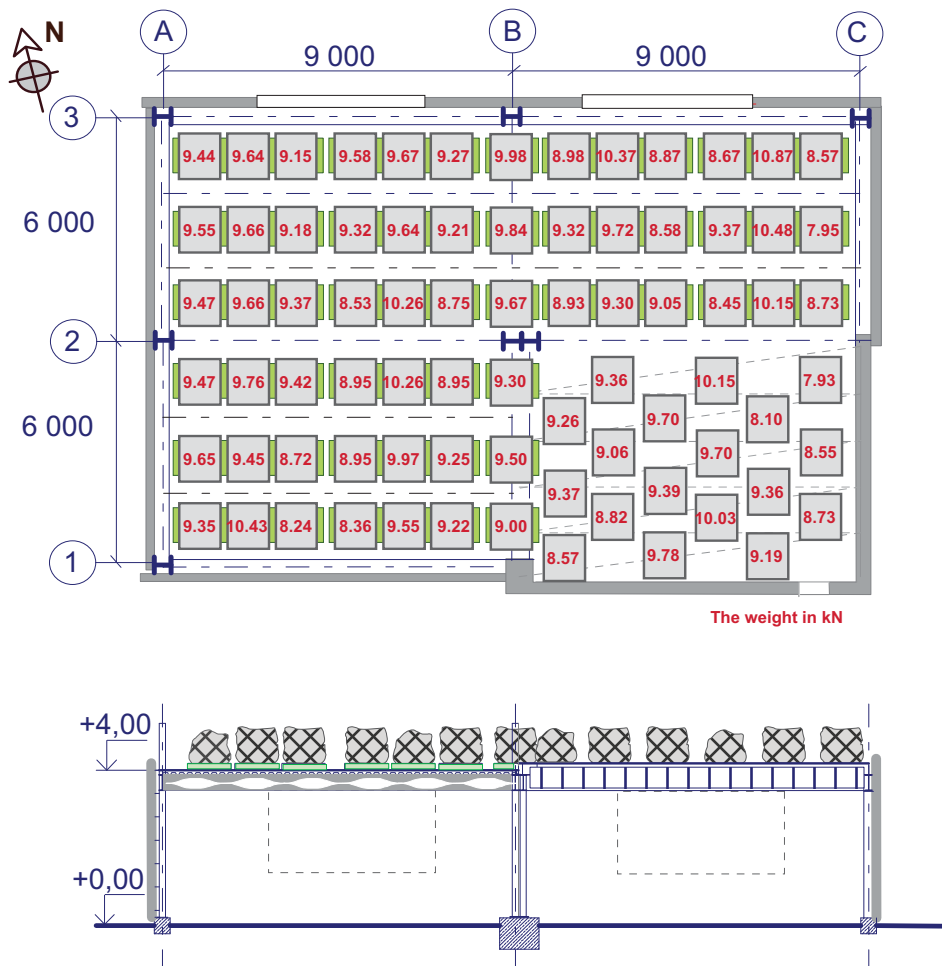


Fig. 2.1 - Mechanical load on the floor with bags with road metal, the weight in kN



Fig. 2.2 - Position of the mechanical load on the floor



Fig. 2.3 - Mechanical load on the floor in bags on wooden pallets

2.2 Fire load

The fire load was created by unwrought wooden cribs 50×50 mm of length 1 m of softwood. The total volume of ligneous mass used in the fire compartment was 15 m³. On the ground area of the compartment 50 wooden piles were placed, see Figs. 2.4 to 2.5. Each pile consisted of 12 rows with 10 cribs, a total of 120 cribs; that means 35.5 kg/m² of timber and it simulated a fire load of 620 MJ/m². The design of the fire load of the administrative building is calculated as 420 MJ/m². In the third layer of cribs four piles were joined together by thin-walled channels filled by mineral wool and penetrated by paraffin. Due to it, simultaneous ignition of the piles was achieved. The fire test was started by the whistle of the leader of this test and it was at the moment when the gas temperature in the compartment reached 50 °C. Two openings of 2.54 m and total length 8.00 m with a parapet of 800 mm ventilated the compartment. To allow a smooth development of fire no glass was installed.

Moisture and the heat of combustion were measured. The cribs were dried to moisture to 12%. The heat of combustion of the timber cribs was measured at the Institute of Chemical Technology, Prague (ICT) and at the Technical Institute of Fire Protection (TUPO), where the calorimeter IKA C-200 was calculated manually as well as in isoperibolic mode. The average value of the heat of combustion of all measurements is 18.6 MJ.kg⁻¹. The results are summarised in Tab. 2.1 and Tab. 2.2.

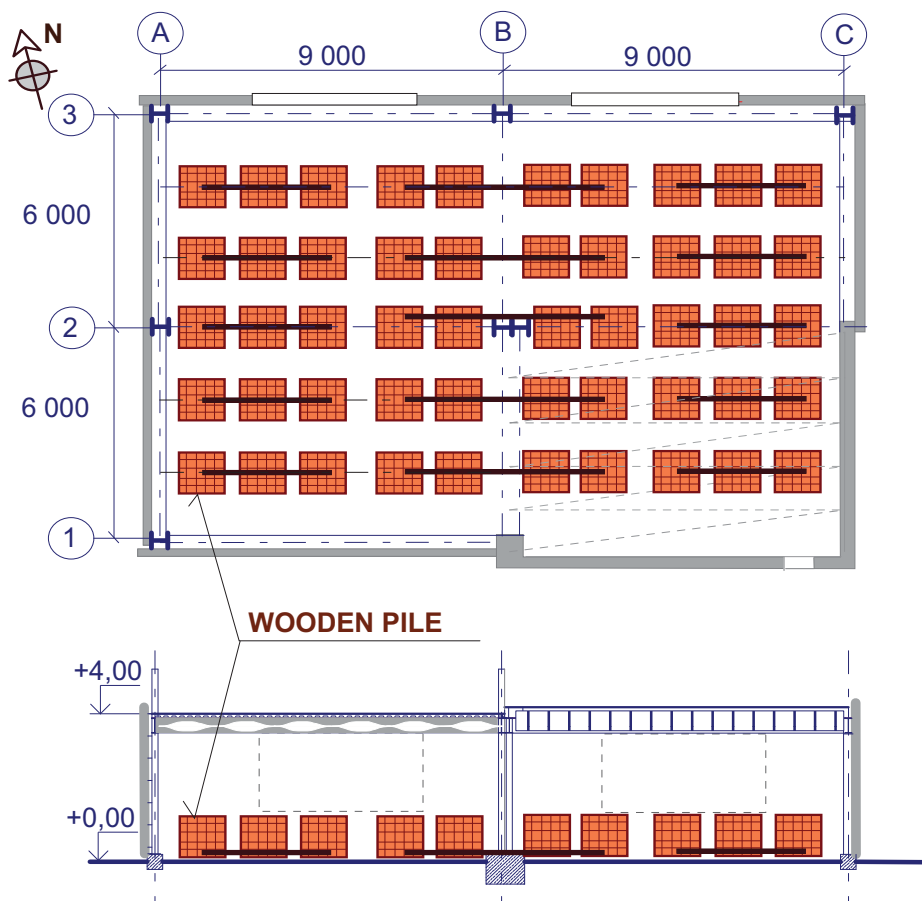


Fig. 2.4 - Position of timber piles on the floor of the fire compartment



Fig. 2.5 - Location of the fire load

Tab. 2.1 Heat of combustion of the timber cribs from ICT

| Institute of Chemical Technology (ICT) | Heat of combustion | Net calorific value | Humidity | Ash |
|--|------------------------|------------------------|-------------|-------------|
| | [MJ.kg ⁻¹] | [MJ.kg ⁻¹] | [% hm.] | [% hm.] |
| ICT 1 | 18.68 | 17.30 | 7.51 | 0.48 |
| ICT 2 | 18.76 | 17.37 | 7.44 | 0.27 |
| ICT 3 | 18.79 | 17.40 | 7.41 | 0.22 |
| ICT 4 | 19.10 | 17.71 | 7.77 | 0.26 |
| ICT 5 | 18.94 | 17.56 | 7.47 | 0.24 |
| ICT 6 | 18.74 | 17.35 | 7.77 | 0.19 |
| ICT 7 | 18.64 | 17.24 | 7.99 | 0.19 |
| ICT 8 | 18.83 | 17.45 | 7.35 | 0.21 |
| ICT 9 | 18.71 | 17.32 | 7.76 | 0.20 |
| ICT 10 | 18.79 | 17.40 | 7.75 | 0.13 |
| Average (1-10) | 18.80 | 17.40 | 7.60 | 0.20 |

Tab. 2.2 Heat of combustion of timber cribs from TUPO

| Technical Institute of Fire Protection (TUPO) | Heat of combustion | | Heat of combustion | | Heat of combustion |
|---|------------------------|---------|------------------------|------------------------|------------------------|
| | [MJ.kg ⁻¹] | | [MJ.kg ⁻¹] | | [MJ.kg ⁻¹] |
| TUPO 1 | 18.329 | TUPO 6 | 18.487 | TUPO 11 | 18.455 |
| TUPO 2 | 18.786 | TUPO 7 | 18.001 | TUPO 12 | 18.349 |
| TUPO 3 | 18.289 | TUPO 8 | 18.424 | TUPO 13 | 18.831 |
| TUPO 4 | 18.566 | TUPO 9 | 18.341 | TUPO 14 | 18.360 |
| TUPO 5 | 18.733 | TUPO 10 | 18.373 | TUPO 15 | 18.544 |
| Average (1-10) | | | 18.433 | Average (11-15) | 18.501 |

3 GAS TEMPERATURES

The gas temperature in the fire compartment was measured by 12 jacketed thermocouples with diameters of 3 mm, which were located 0.5 m below the ceiling at the level of the beams lower flanges (TG01, TG04-TG10, TG24-TG27). The temperature profile along the compartment height was measured by 5 thermocouples between the window openings (TG20-TG21, TG23), and in the back of the fire compartment below the prefabricated hollow core Spiroll (TG02-TG04), panels see Figs. 3.1 to 3.6. Six thermocouples were placed in the two openings (TG11-TG13, TG28-TG30), Figs. 3.7 to 3.8. The location of the thermocouples is shown in Annex A, the tables of the measured values for each thermocouple which measured the gas temperature is shown in Annex B.

Generally the highest gas temperatures were reached in the front of the fire compartment at the beginning of the fire and in the back of the fire compartment during the full developed fire. Different temperature development was perceptible for the east and west part of the fire compartment as well. It was due to different enclosure walls and due also to a light wind. The cladding from the mineral wool with external trapezoidal sheets and sandwich panels were under a composite slab with Angelina castellated beams (west part) and the concrete walls of the 1st floor ceiling were made from pre-stressed panels and a composite slab with beams with corrugated webs (east part). The direction of the wind during the fire test changed from North-West to South-West, see Chapter 7.

The comparison of the prediction of the gas temperature by nominal and parametric fire curve to the measured average temperatures from the two parts and from the whole fire compartment is shown in Fig. 3.3. The shapes of these curves are similar and comparable. In the west part of the fire compartment the gauged gas temperatures were 510°C at the 15. min, 780°C at the 30. min, 940°C at the 45min. and 60. min, Fig. 3.1. In the east part of the fire compartment the temperature reached 510°C at the 15 min., 850°C at the 30 min, and 800°C at the 45 min, see Fig. 3.2. The measured gas temperature in the window openings were presented in Figs. 3.7 and 3.8.

In Figs. 3.9 to 3.12 are photographs of the entire experimental structure with the view of the mail wall with window openings. In these pictures, flames can be seen flowing from the openings.

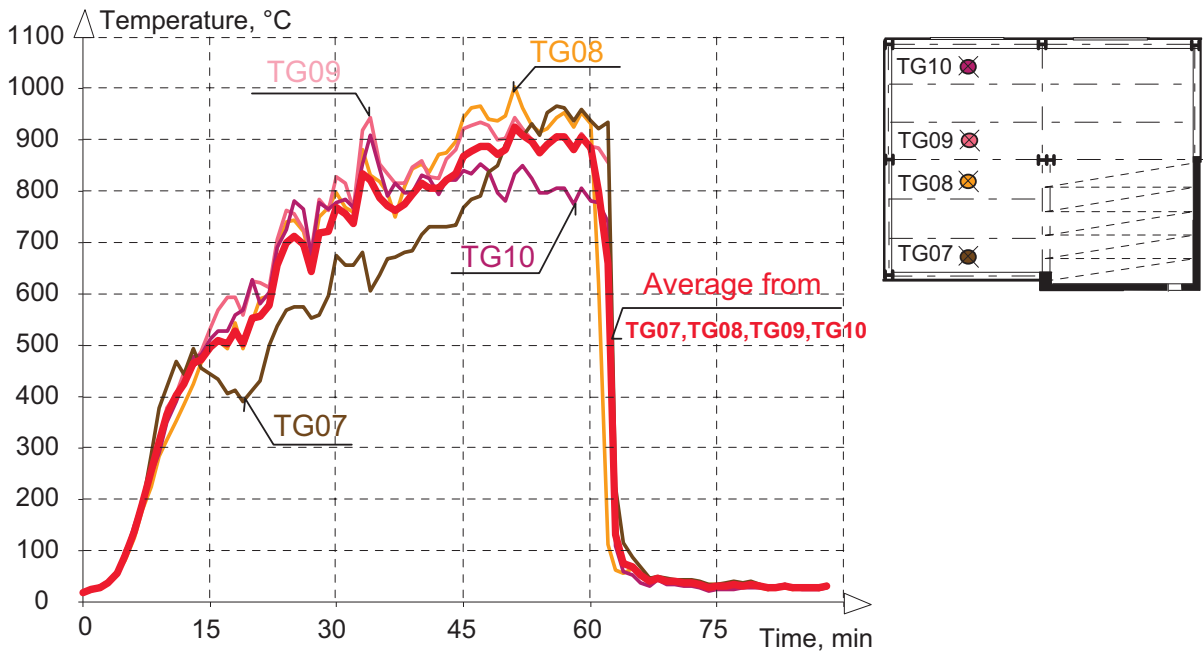


Fig. 3.1 - Measured gas temperature under the composite slab with Angelina castellated beams at the level of its lower flanges

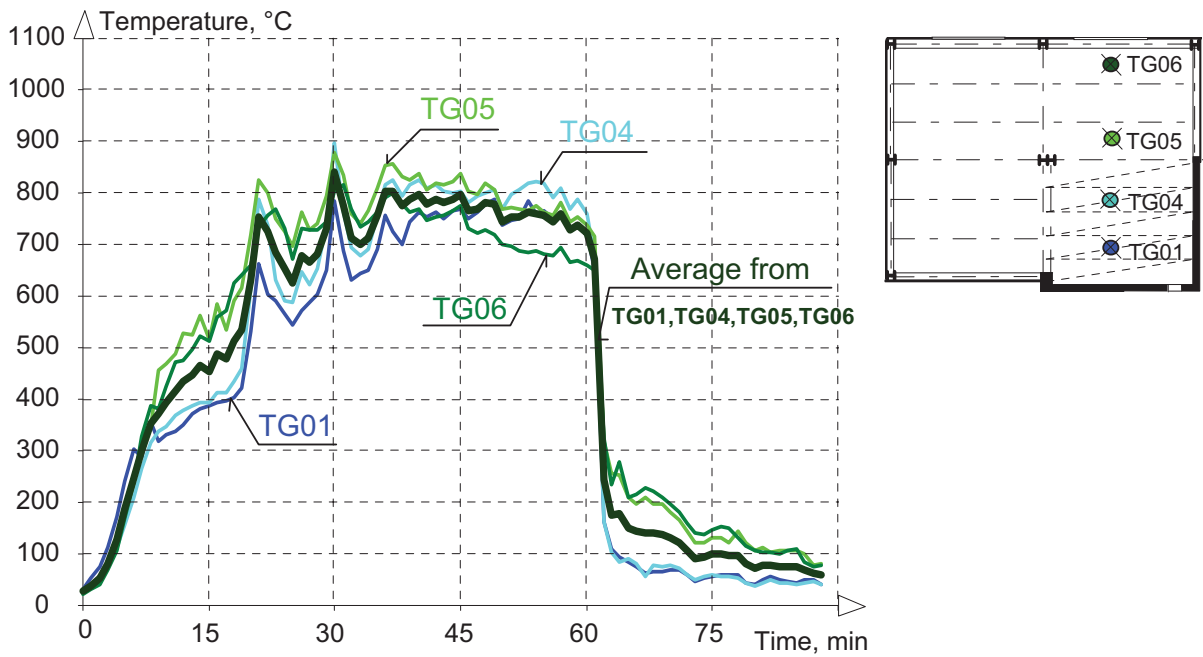


Fig. 3.2 - Measured gas temperature under the composite slab with beams with corrugated web and the hollow core slab at the level of its lower flanges

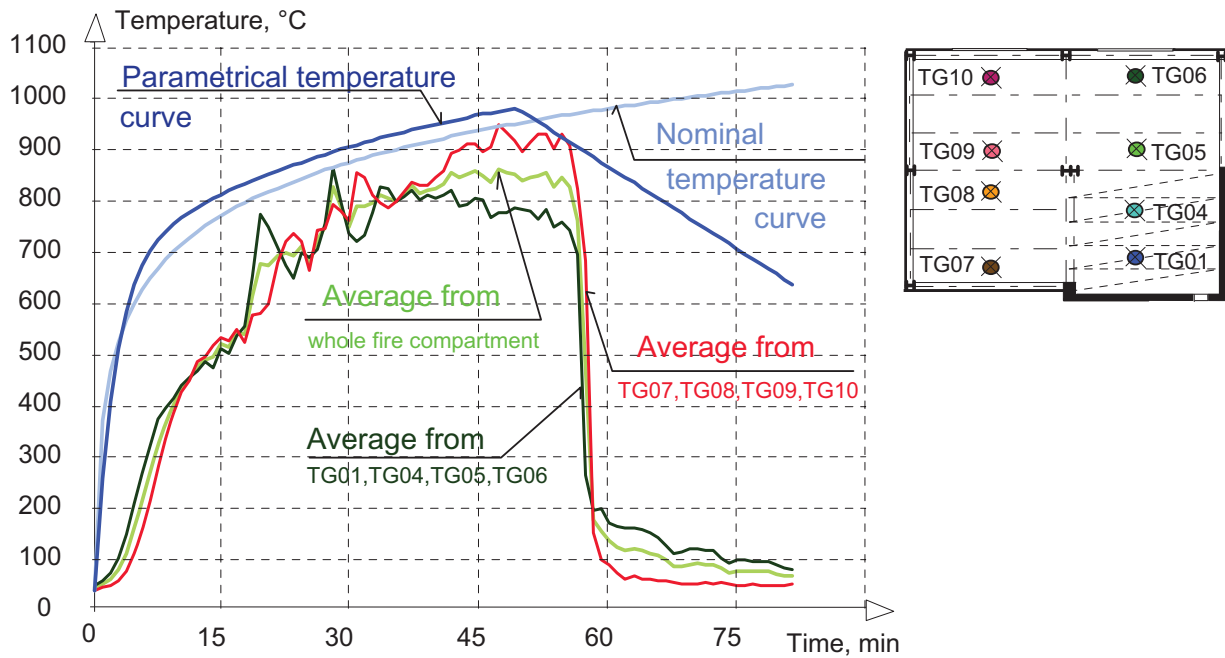


Fig. 3.3 - Comparison of predictions of the gas temperature by nominal and parametric fire curve to the measured average temperatures from part and whole fire compartment; thermocouples 500 mm under the ceiling

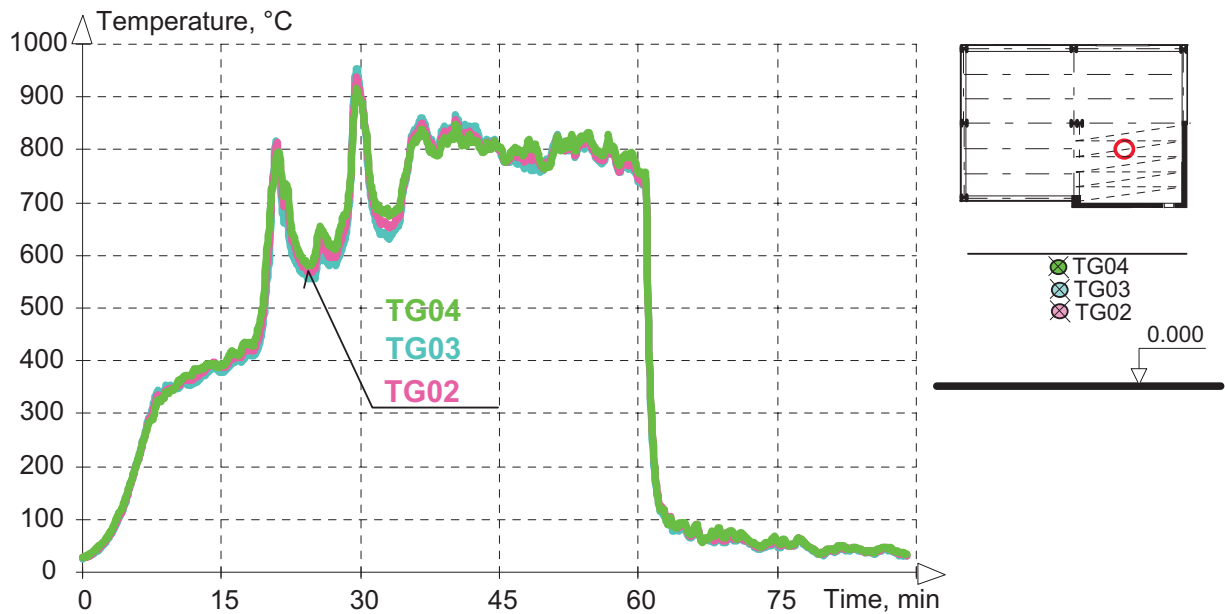


Fig. 3.4 - Gas temperature measured along the fire compartment height, TG02 1100 mm, TG03 800 mm and TG02 500 mm placed under the ceiling

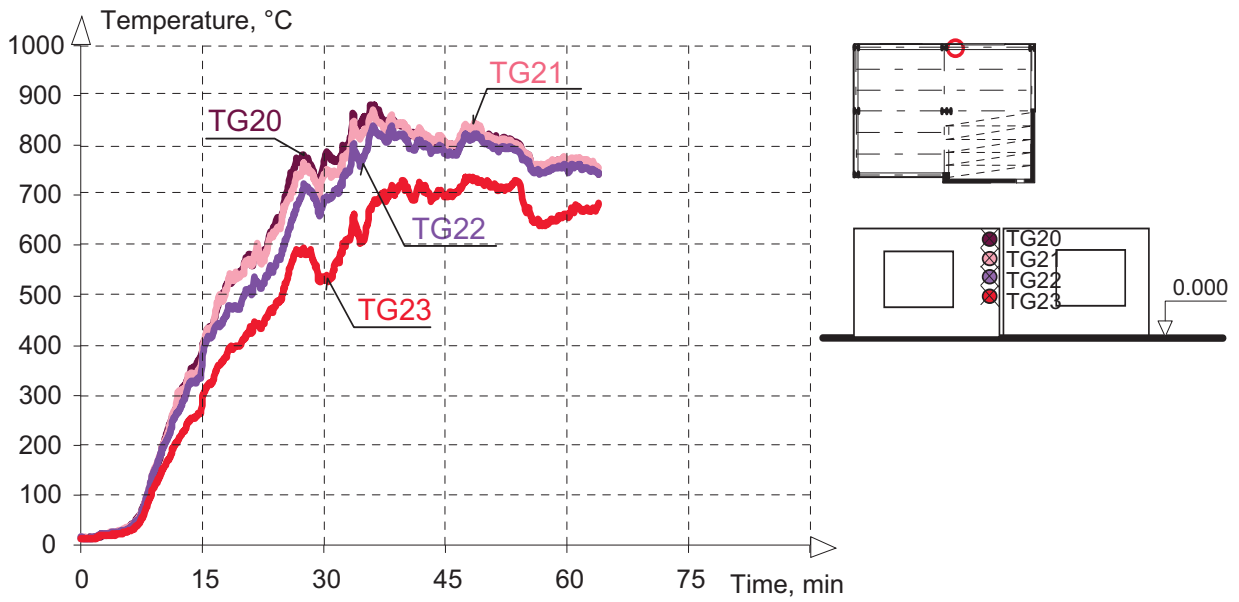


Fig. 3.5 - Gas temperature measured along the fire compartment height close to the window; TG20 on the ceiling surface, TG21 300 mm, TG22 500 mm, TG23 1800 placed under ceiling; location 220 mm from the secondary beam CS4 and 270 mm from the wall with opening

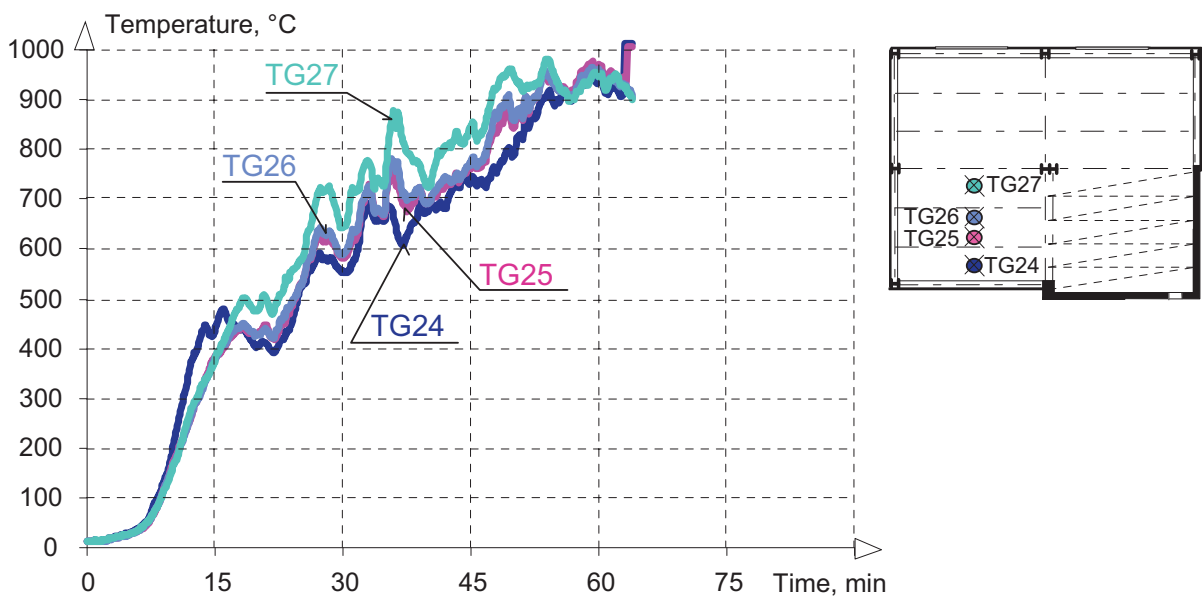


Fig. 3.6 - Gas temperature measured under the slab with cellular beams in its lower flange, 500 mm under the ceiling; height at different depth at the end of the fire compartment; TG24 1000 mm, TG25 2650 mm, TG26 3350 mm and TG27 5000 mm at the distance of the back wall

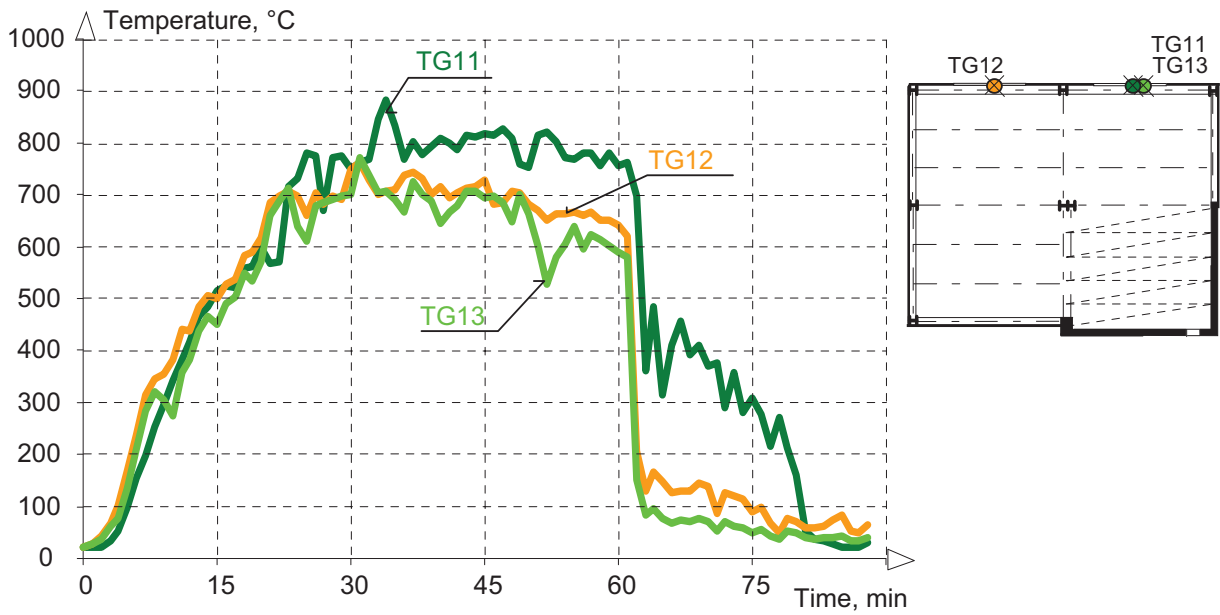


Fig. 3.7 - Measured gas temperature in the window openings; TG11 750 mm, TG12 250 mm, TG13 250 mm from the top of the window

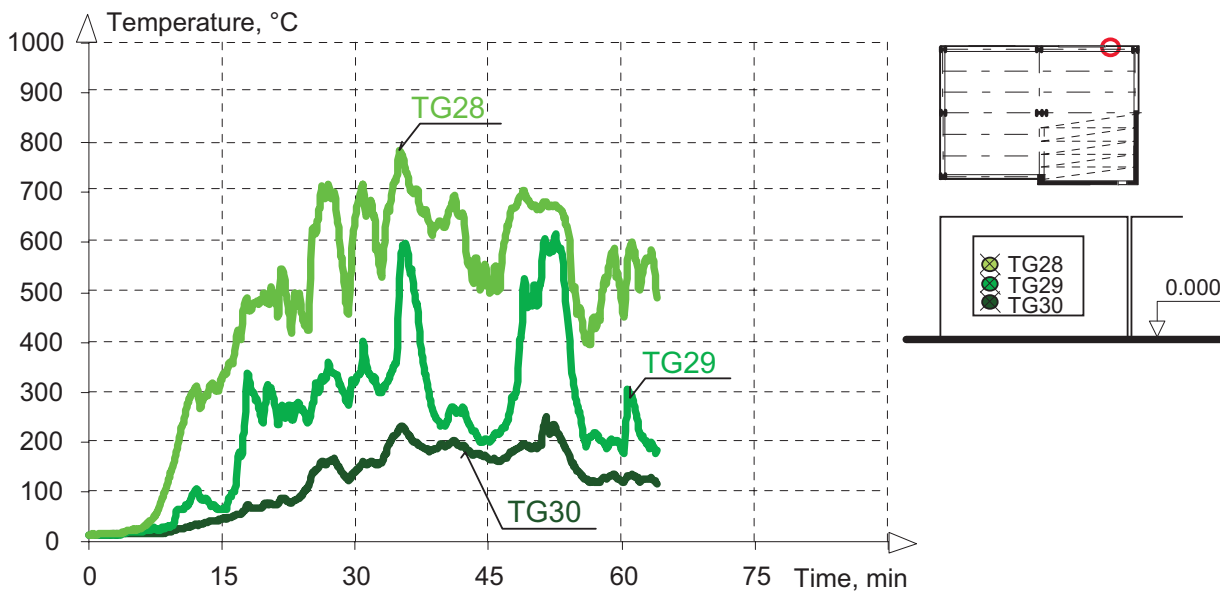


Fig. 3.8 - Gas temperature measured about window height 500 mm from the east edge of the window opening; TG28 from the bottom edge of the window opening 2000 mm, TG29 1200 mm and TG30 respectively 400 mm



Fig. 3.9 - The view of the experimental structure; flames at the 35. min of the fire test



Fig. 3.10 - The view at the experimental structure; flames in the east opening at the 36. min of the fire test



Fig. 3.11 - The view of the experimental structure; flames in the west opening at the 50. min of the fire test



Fig. 3.12 - Flames in the west opening at the 52. min of the fire test

4 TEMPERATURES OF STRUCTURES

Temperatures on the steel secondary beams and in their connections to the primary beams or to the column, on the internal column in the middle of the plan of the fire compartment, on the cladding or concrete walls, over the thickness of the composite slab on the external column in front of the window opening were all were gauged. 8 thermocouples were designed in the composite slab, as well as on beams (15), in bolted connections (46), in the hollow core panels (2), in concrete walls (10), in the external cladding (24), in the fire protected internal column (7) and on the external column (24). This chapter is divided into parts which are aimed at specific members of the experimental structure. The temperature measurements were performed by jacketed thermocouples with a diameter of 2 mm or board thermocouples.

The detailed location of the thermocouples with respect to individual structural members is shown in Annex A. The tables of the measured values for each thermocouple which measured gas temperature are summarised in Annex B.

4.1 Structural elements

Nine thermocouples were located at the midspan of the Angelina beams and six thermocouples in the middle of the beams with corrugated web to measure the temperature in the steel member. In Figs. 4.1 to 4.5 are the results from measurements on the lower and upper flanges and in the middle of the web of the cellular Angelina beam AS2, AS4, AS5 and AS6. The photos of the middle parts of the Angelina beams are shown in Figs. 4.6 and 4.7.

The course of the temperature along the cross-section of the beam with corrugated web CS2 was measured, see Fig. 4.8. The temperatures measured on the lower flange in the middle of beams CS2 and CS3 are in Figs 4.9 and 4.10. Deformed beams with corrugated webs at the 47. min of the fire test is shown in Fig. 4.12. Fig. 4.13 shows the visualisation of the temperatures measured by a thermo-image camera on the beams with corrugated webs at the 15. min of the fire test and Fig. 4.14 at the 63. min of the fire test.

Seven jacketed thermocouples were located along the high edge of the internal column in the centre of the fire compartment, see Fig. 4.15. The column (B2) was fire protected and it was constructed from a double HEB 160 cross-section.

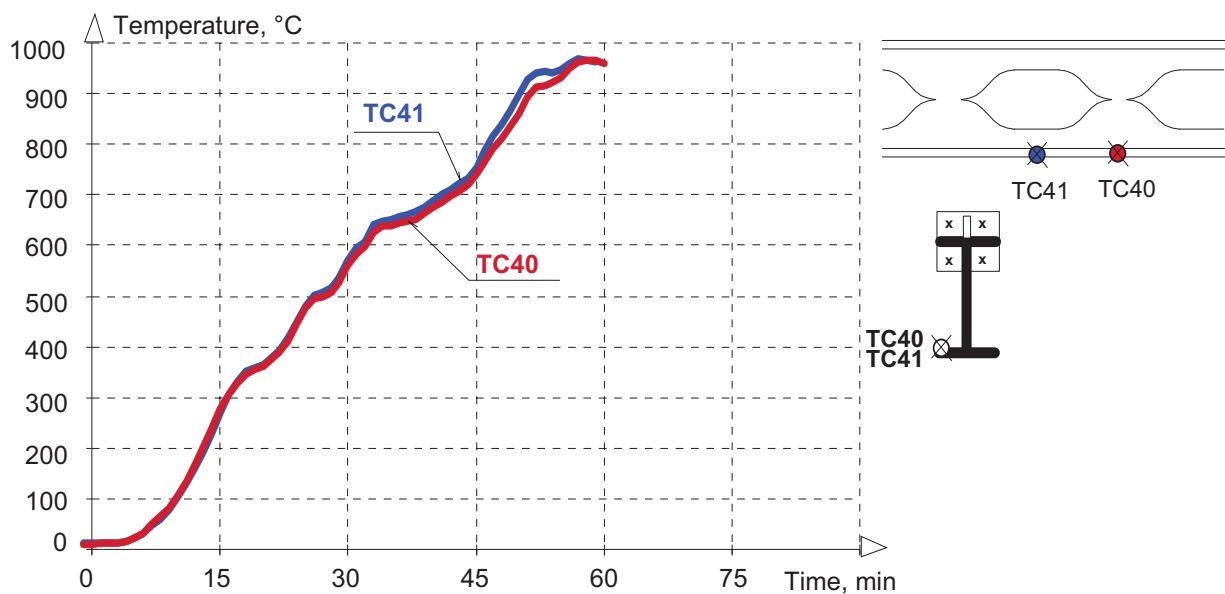


Fig. 4.1 - Temperatures measured at the midspan on the lower flange of the Angelina beam AS2

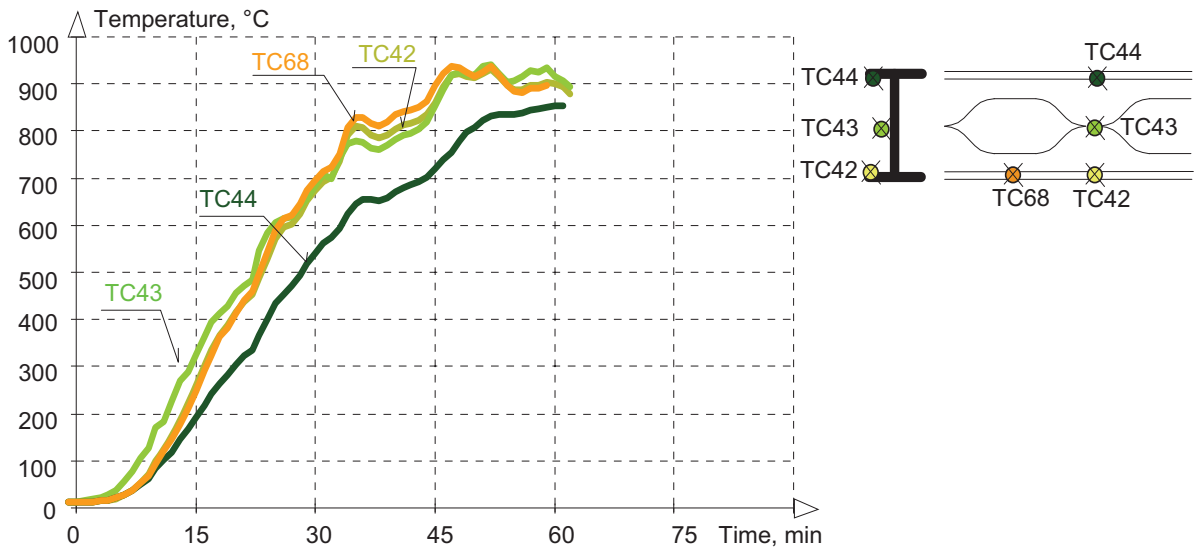


Fig. 4.2 - Temperatures measured at the midspan of the cellular Angelina beam AS4



Fig. 4.3 - Temperatures measured at the midspan of the cellular Angelina beam AS5

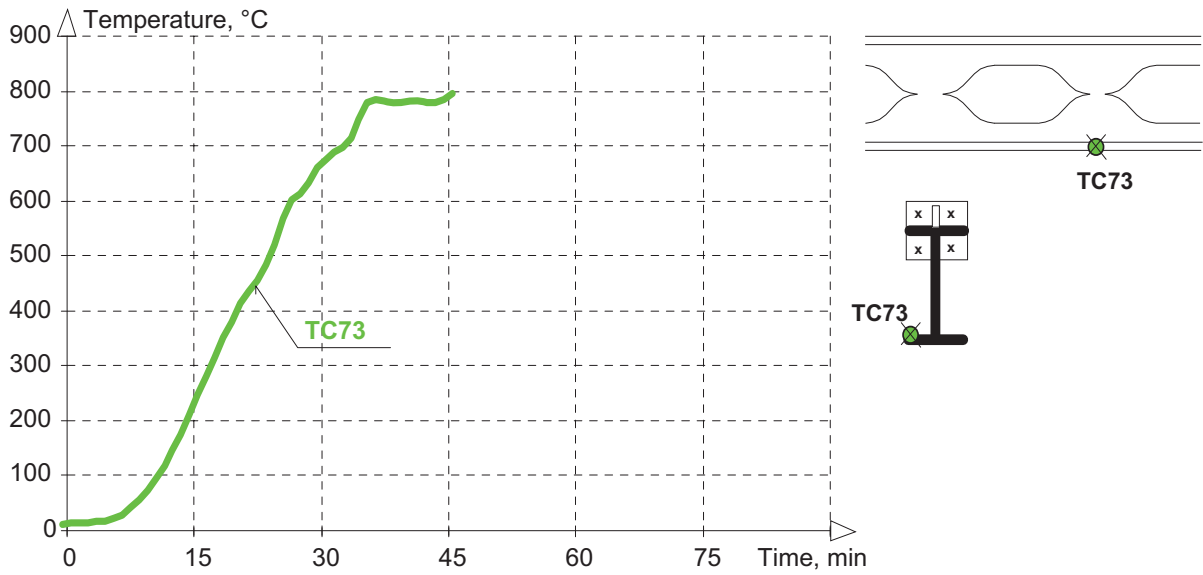


Fig. 4.4 - Temperatures measured at the midspan of the lower flange of the Angelina beam AS6

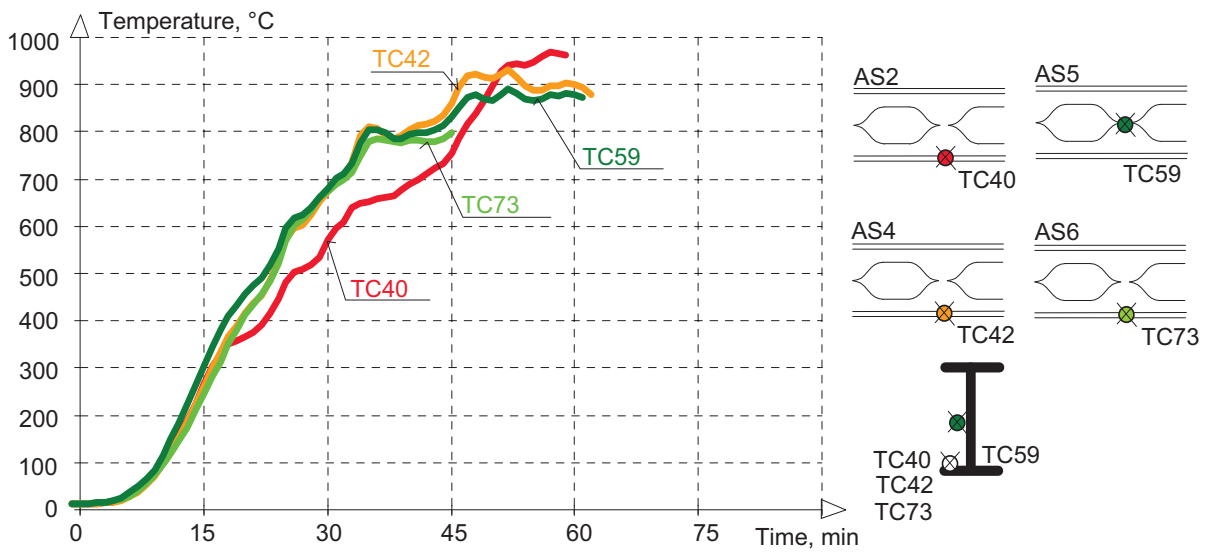


Fig. 4.5 - Temperatures measured at the midspan of castellated Angelina beams AS2, AS4, AS5 and AS6



Fig. 4.6 - Thermocouples located at the midspan of the cellular beams and at their connections



Fig. 4.7 - Thermocouples located at the midspan and along the height of the Angelina beam AS4

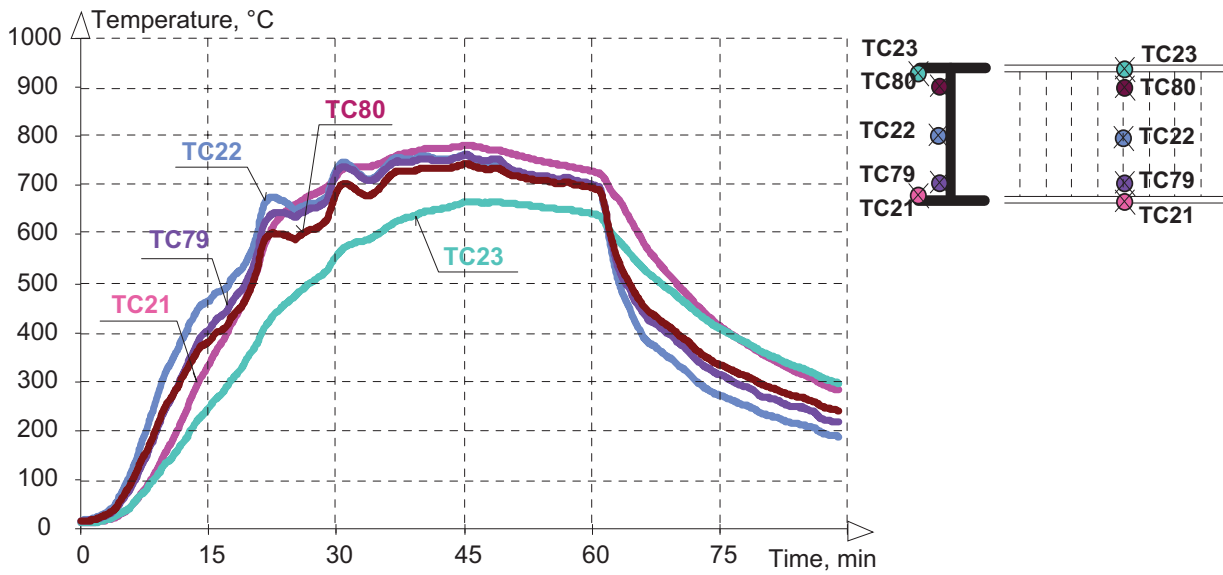


Fig. 4.8 - Temperatures measured at the midspan of the beam with corrugated web CS2

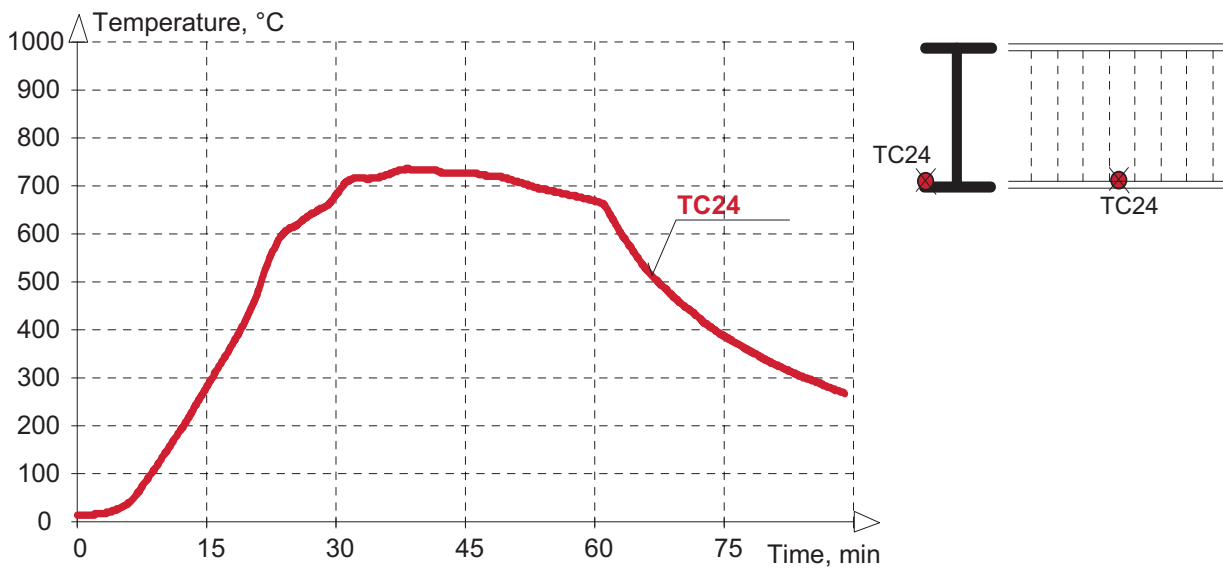


Fig. 4.9 - Temperatures measured at the midspan on the lower flange of the beam with corrugated web CS3

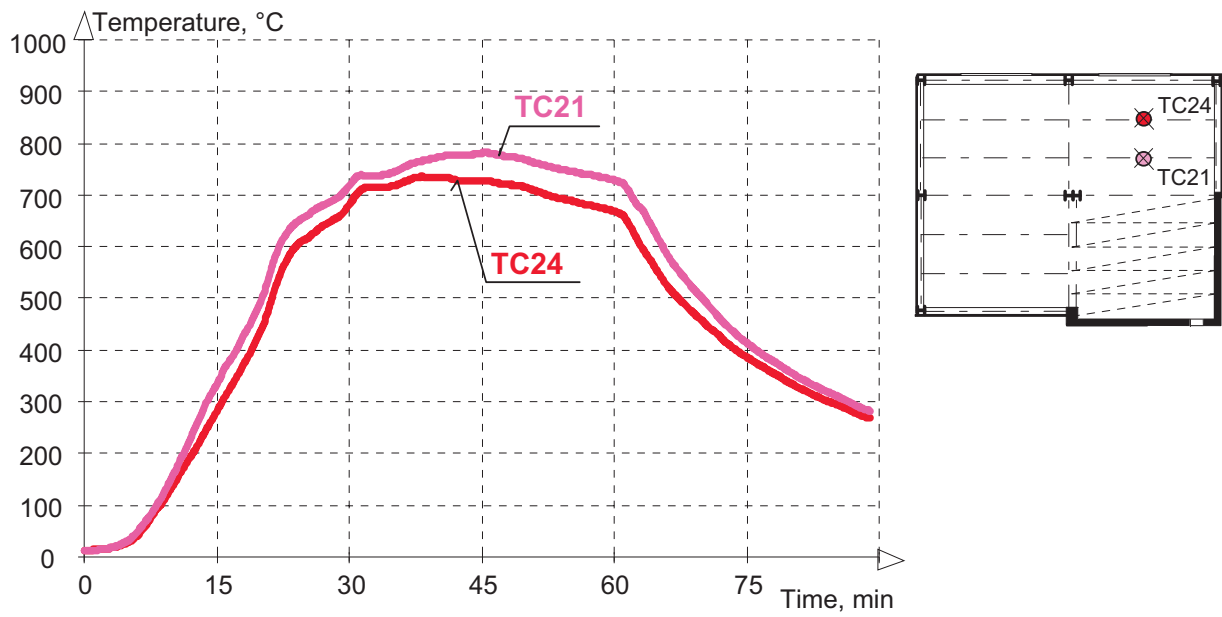


Fig. 4.10 - Temperatures measured at the midspan on the lower flanges of beams with corrugated webs CS2 and CS3

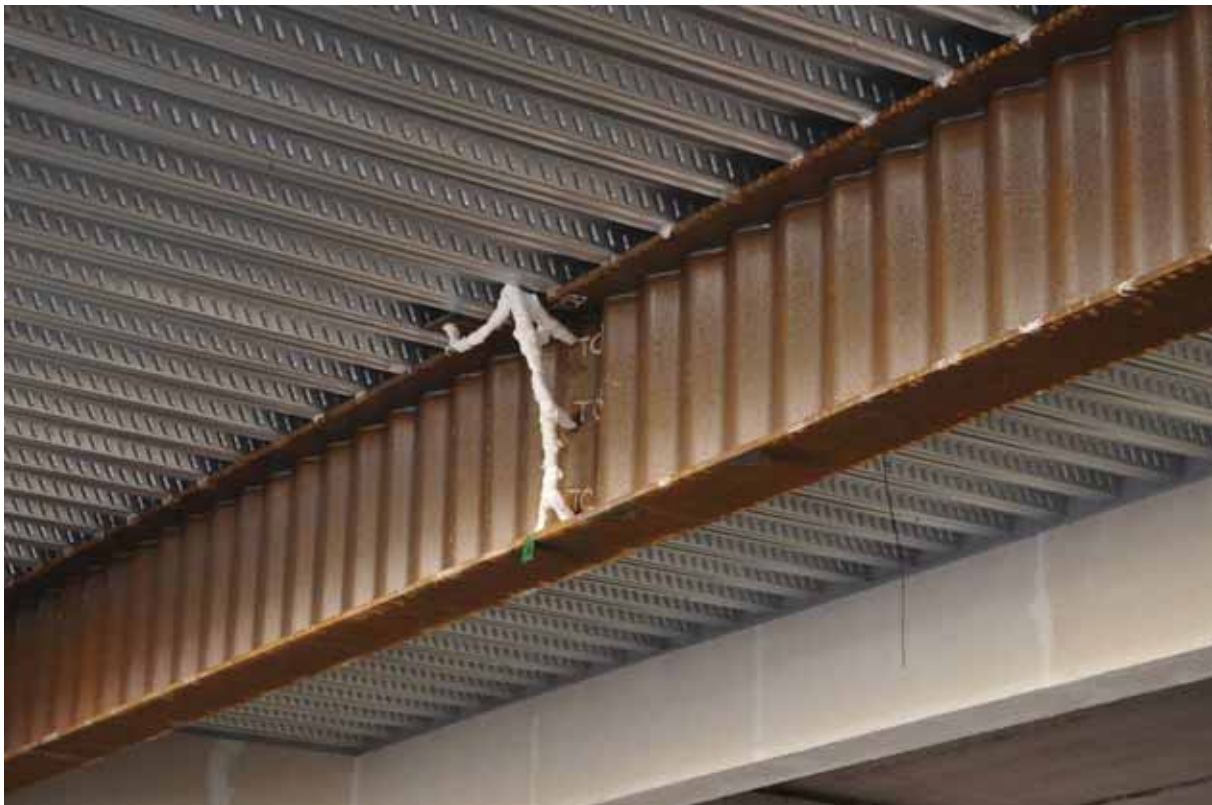


Fig. 4.11 - Thermocouples located at the midspan of the beam with corrugated web CS2



Fig. 4.12 - The deformed beams with corrugated webs at the 47. min of the fire test

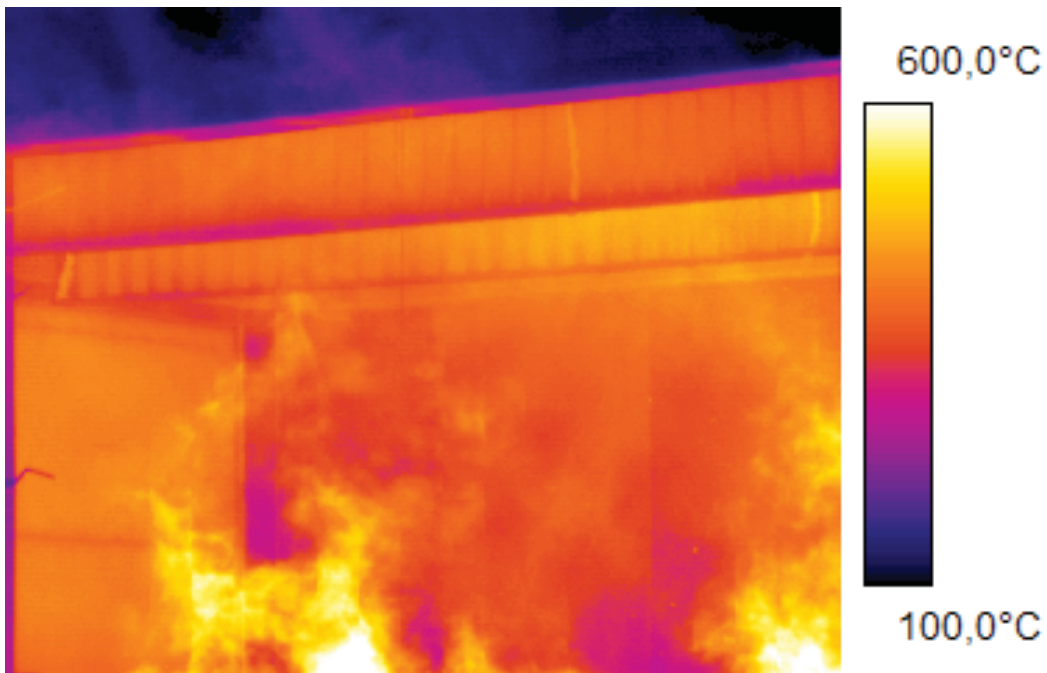


Fig. 4.13 - The visualisation of the temperatures measured by the thermo-image camera on beams with corrugated web at the 13. min of the fire test

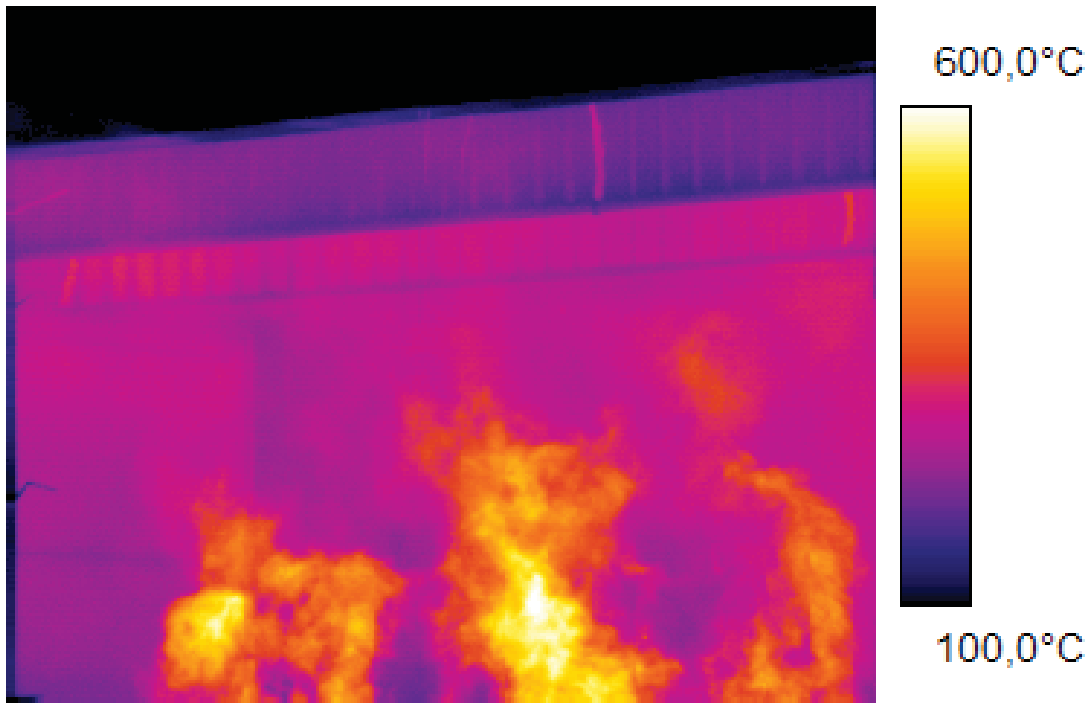


Fig. 4.14 - The visualisation of the temperatures measured by the thermo-image camera on beams with corrugated web at the 9. min of the fire test

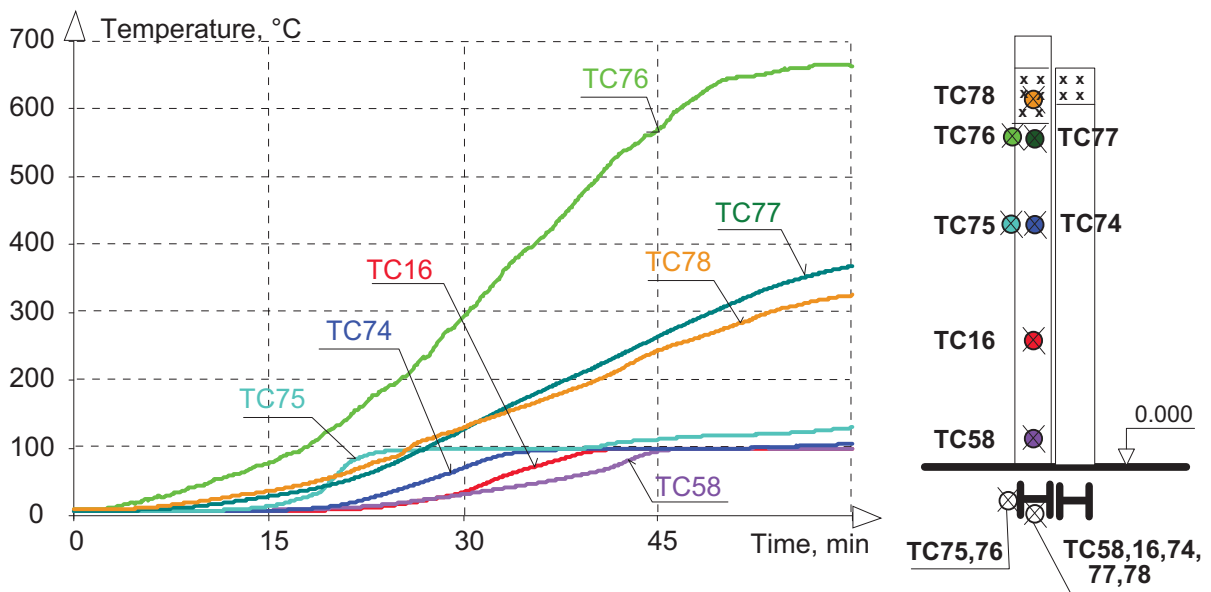


Fig. 4.15 - Steel temperature measured on the central fire protected column of a double HEB 160 section

4.2 Connections

During the fire test temperature measurements on the header plate connections which were partially encased in the concrete slab were measured; two Angelina beams (AS4, AS5) and one beam with corrugated web (CS2).

At connection B the temperatures of the lower flange, in the first third of the cross-section height of the Angelina beam and the lower bolt on the header plate were observed. Seven measurement points were performed in connection A. The temperatures of the upper and lower bolts, of the header plate near the bolts of the upper and lower flanges and in the first and second thirds of the Angelina web were all measured.

On the side with connection B of the beam with the corrugated web the temperature of the lower bolt and the temperature of the lower flange were measured. On the second side of the same beam the temperatures of the upper and lower bolts, the temperatures of the header plate near the bolts were monitored. The temperatures along the height of the web in three levels from the end of this beam were recorded as well.

The course of the temperatures and the location of the thermocouples in the connections are shown in Figs. 4.17 and 4.18 for Angelina beam AS5, in Figs. 4.19 and 4.20 for cellular Angelina beam AS4 and in figs. 4.23 and 4.24 for the beam with corrugated web CS2. The photos of the connections before the fire test are in Figs. 4.16 and 4.22. The visualisation of the temperatures measured by the thermo-image camera at the 39. min of the fire test near the connection is in Fig. 4.21.

The highest temperatures for the header plate near the upper bolt, which was encased in the concrete slab, were at the 60. min approximately 240°C, 190°C and 220°C for beams AS5, AS4 and CS2 respectively. The highest temperatures for all three beams were between 400°C and 500°C for the header plate near the lower bolt. Temperatures 750°C, 750°C and 820°C were measured for the lower flange near the connections of the beams AS5, AS4 and CS2 respectively.



Fig. 4.16 - Location of thermocouples at connections A and B on Angelina beam AS5

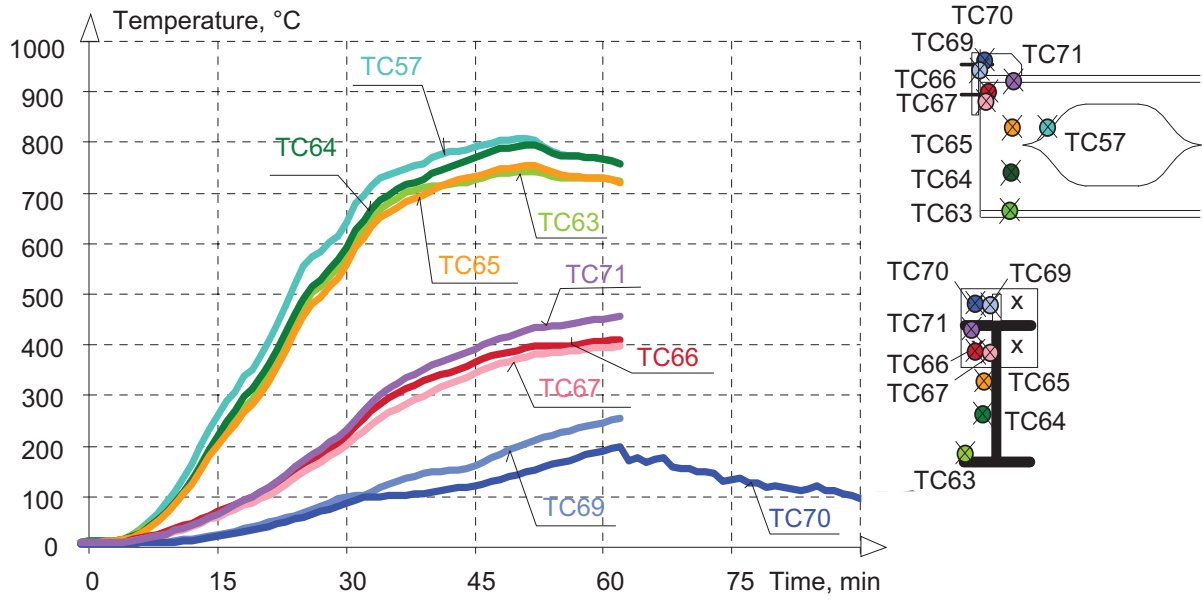


Fig. 4.17 - Measured temperatures at connection A on cellular Angelina beam AS5

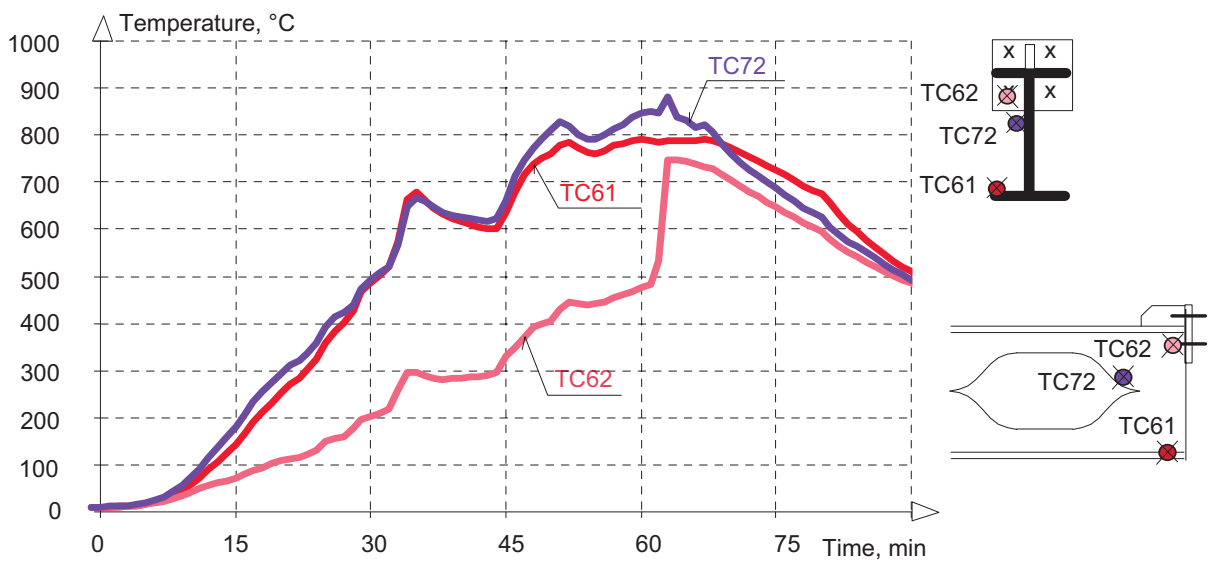


Fig. 4.18 - Measured temperatures at connection B on cellular Angelina beam AS5

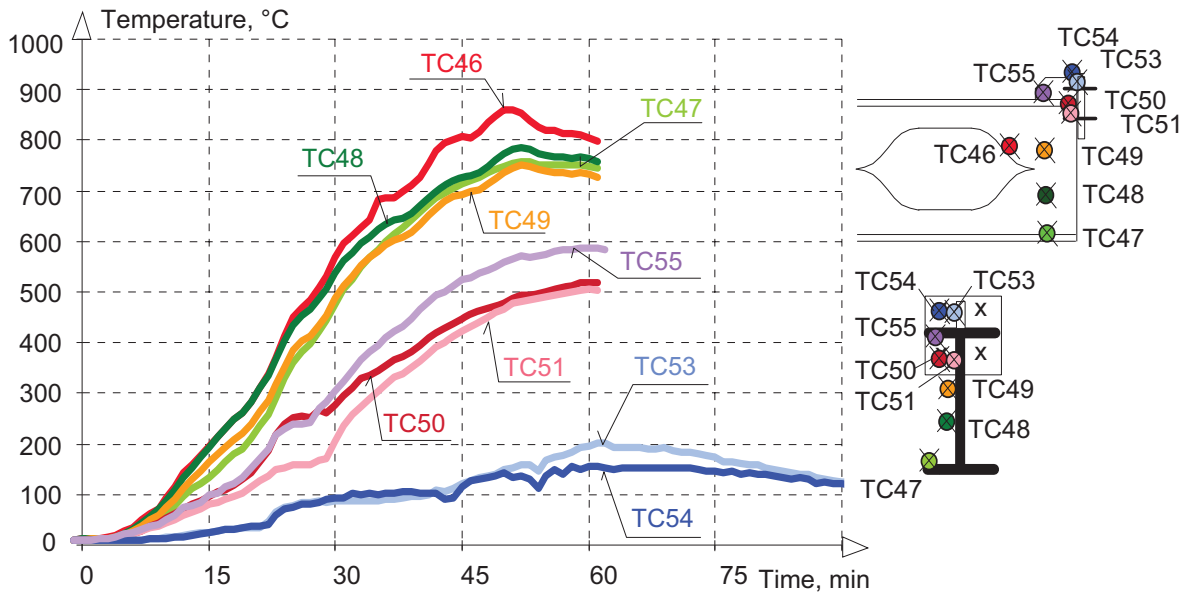


Fig. 4.19 - Measured temperatures at connection A on cellular Angelina beam AS4

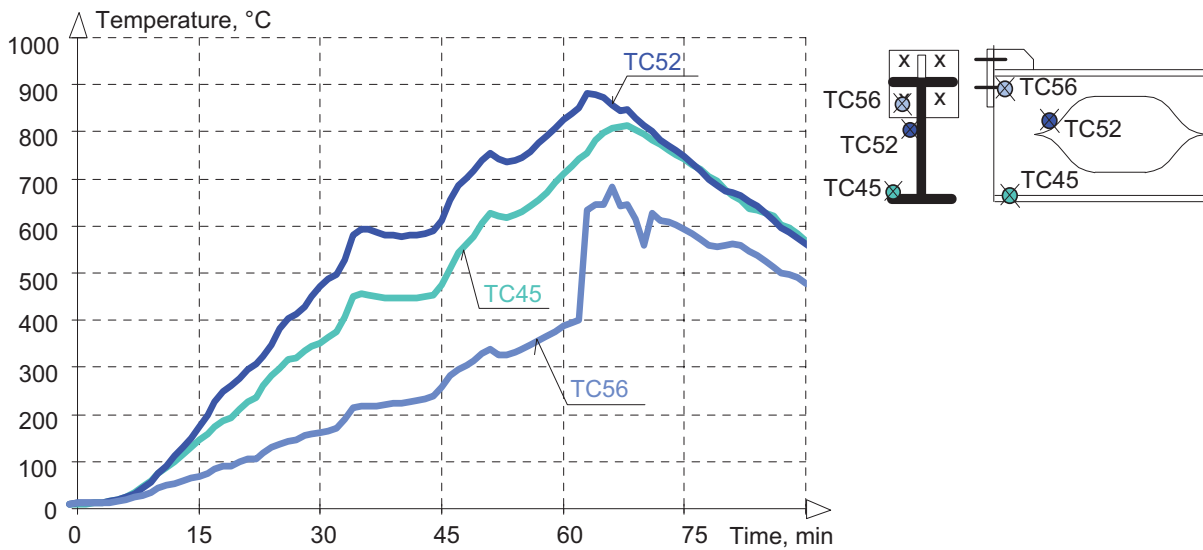


Fig. 4.20 - Measured temperatures at connection B on cellular Angelina beam AS4

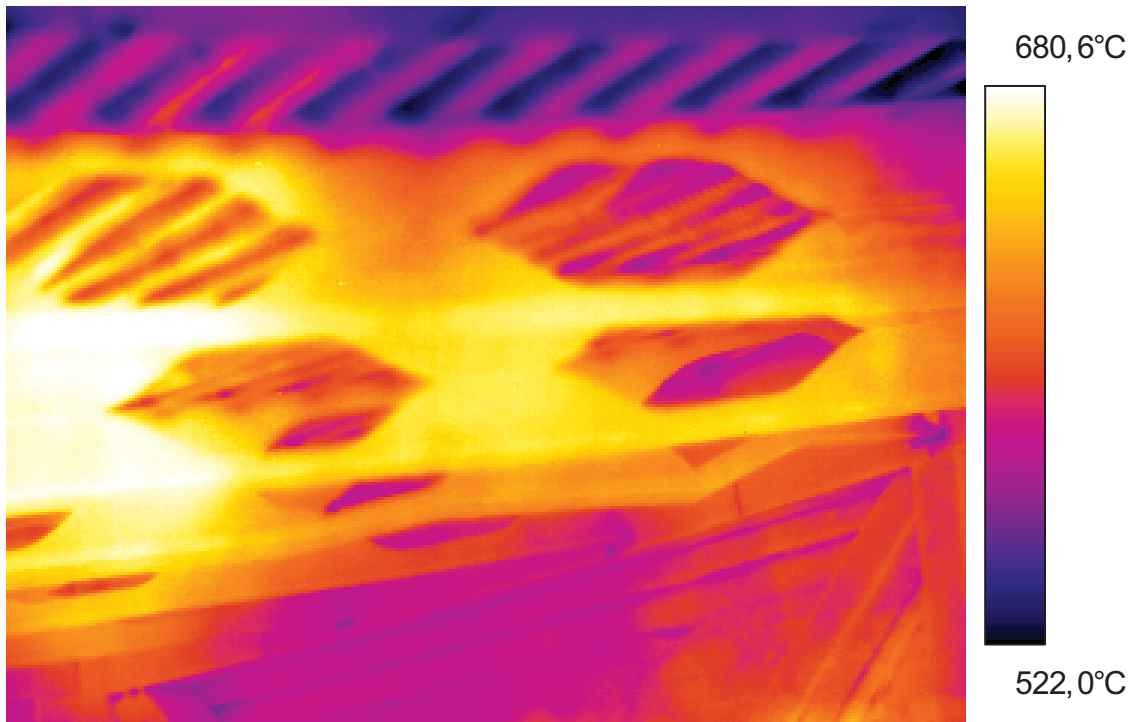


Fig. 4.21 - The visualisation of the temperatures measured by the thermo-image camera at the 39. min of the fire test

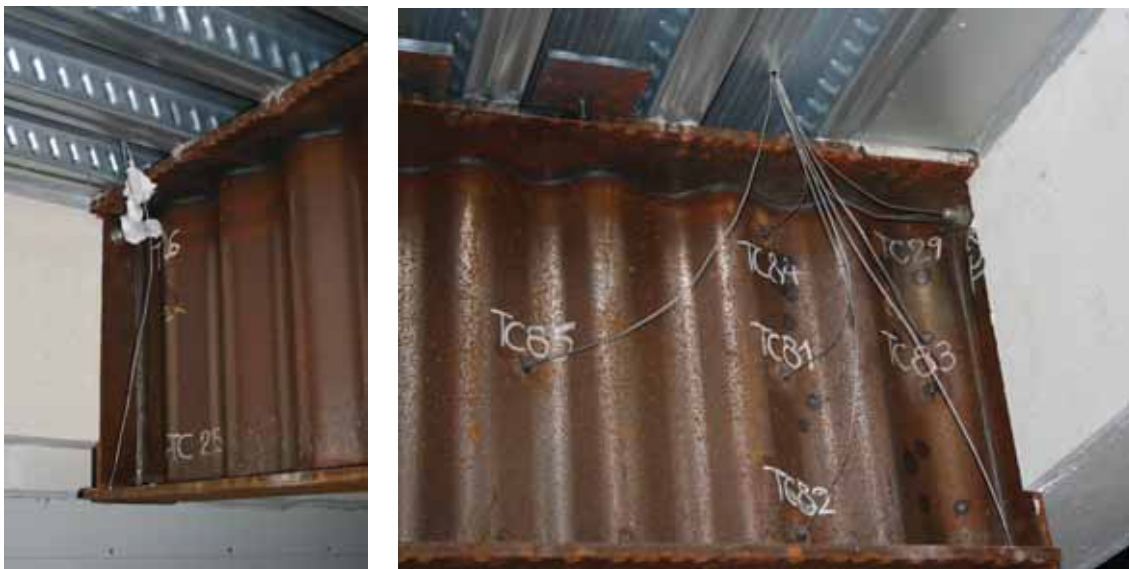


Fig. 4.22 - Location of thermocouples at connection A and B on the beam with corrugated web CS2

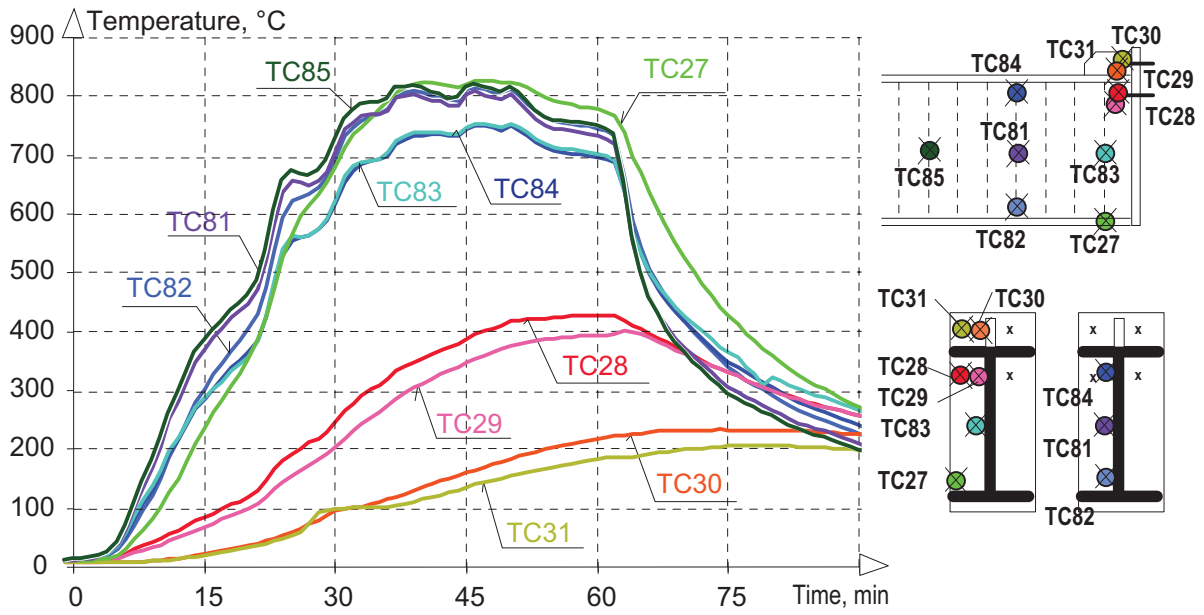


Fig. 4.23 - Measured temperatures at connection A on the beam with corrugated web CS2

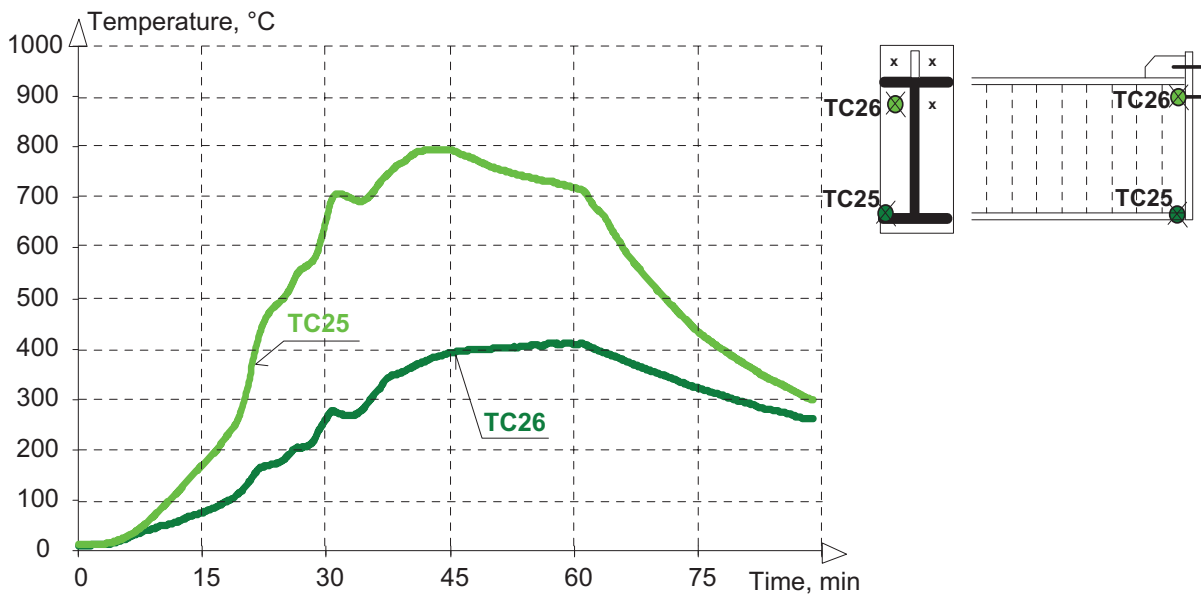


Fig. 4.24 - Measured temperatures at connection B on the beam with corrugated web CS2

4.3 External Column

The column, which was situated 1 m in front of the east window opening at 950 mm axially of the left edge, 1050 mm axially of the middle of the opening respectively, simulated the external steel structure.

Temperatures of the steel external column were measured on both flanges of the cross-section in eight levels along the height of the column; in total 16 thermocouples were used. Thermocouples to monitor gas temperatures were placed in the same eight height levels of the column. The distance between flanges which were closer to the window opening and the gas thermocouple was 100 mm in the axis plane in the direction to the opening.

The measured gas temperatures values are presented in Figs. 4.25 and 4.26, the temperatures of the external column are shown in Figs. 4.27 and 4.28. In Fig. 4.29 the location of the column and the thermocouples themselves can be seen as well. Based on the height levels, temperatures of the column were from 220 to 400°C and gas temperatures from 100 to 650°C at the 45. min.

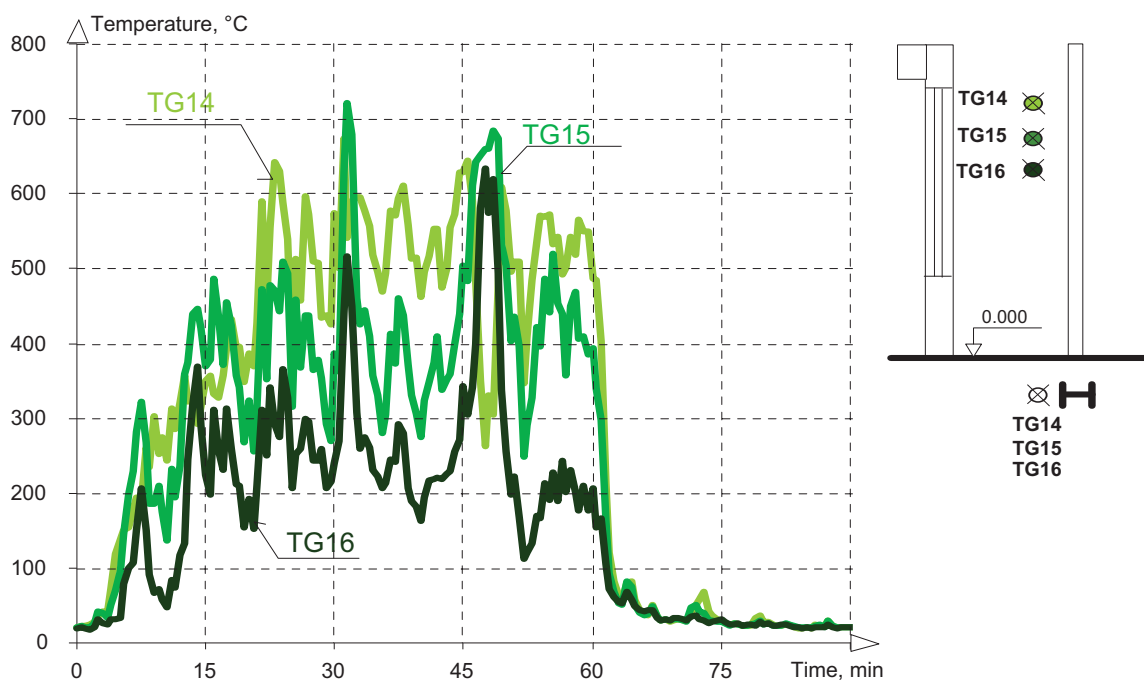


Fig. 4.25 - Gas temperature in front of the upper part of the external column

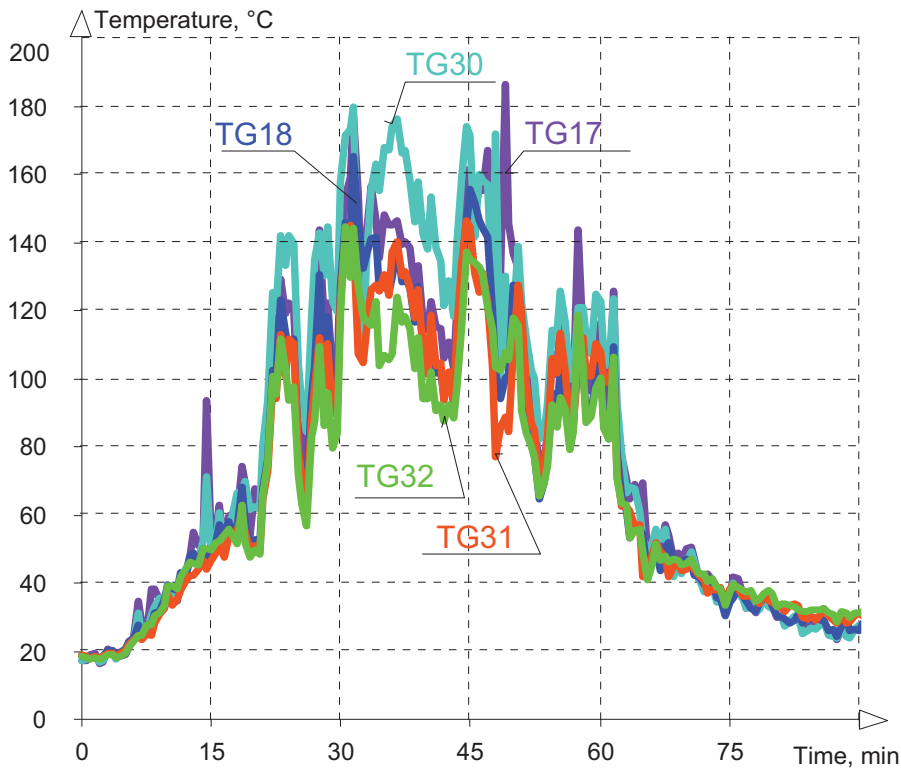


Fig. 4.26 - Gas temperature in front of the lower part of the external column

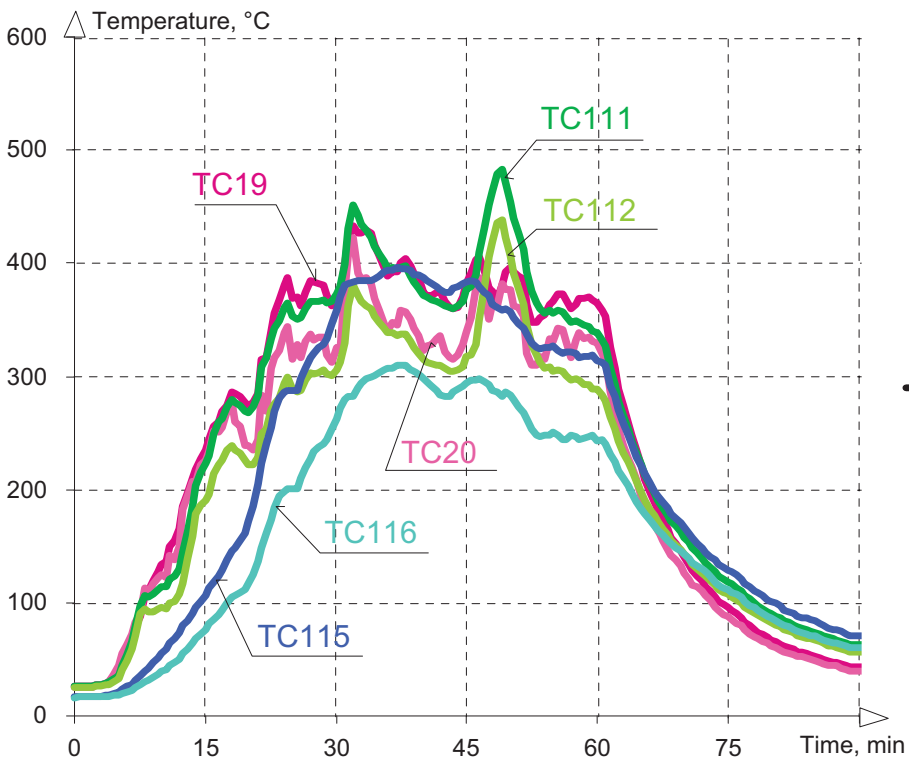


Fig. 4.27 - Temperatures of the upper part of the external column

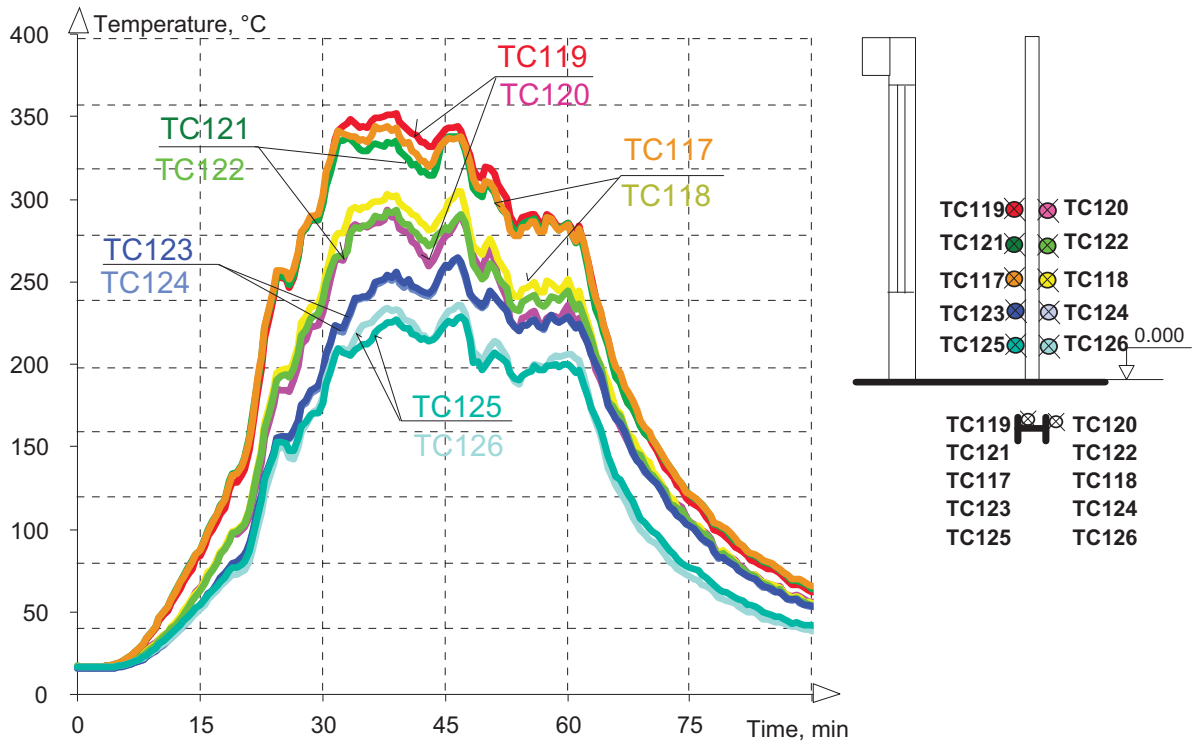


Fig. 4.28 - Temperatures of the lower part of the external column



Fig. 4.29 - The thermocouples on the column before and during the fire test

4.4 Composite slab

The composite slab was created from C30/37 concrete and a simple trapezoidal sheet of Cofraplus CF60 0.75 mm thick. The thickness of the composite slab was 60 mm and in the rib it was 120 mm.

Eight thermocouples were located in the slab at different height levels, four in the rib and four over the thickness of the slab, see Figs. 4.30 and 4.31. Due to the height deformation of the slab; thermocouples were measured only approximately 45 min from the beginning of the fire. Developments of two temperature measurements in the prefabricated hollow core panels were documented in Fig. 4.32. In Fig. 4.33, a photo of a cut of the composite slab after the fire experiment is presented.

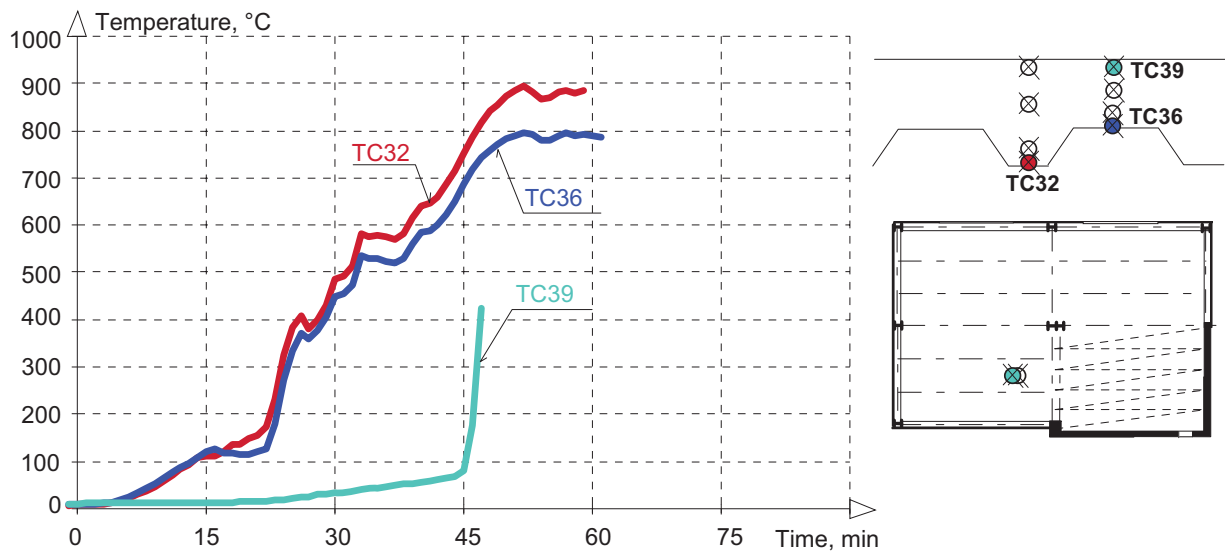


Fig. 4.30 - Temperatures measured on the composite slab with castellated beams

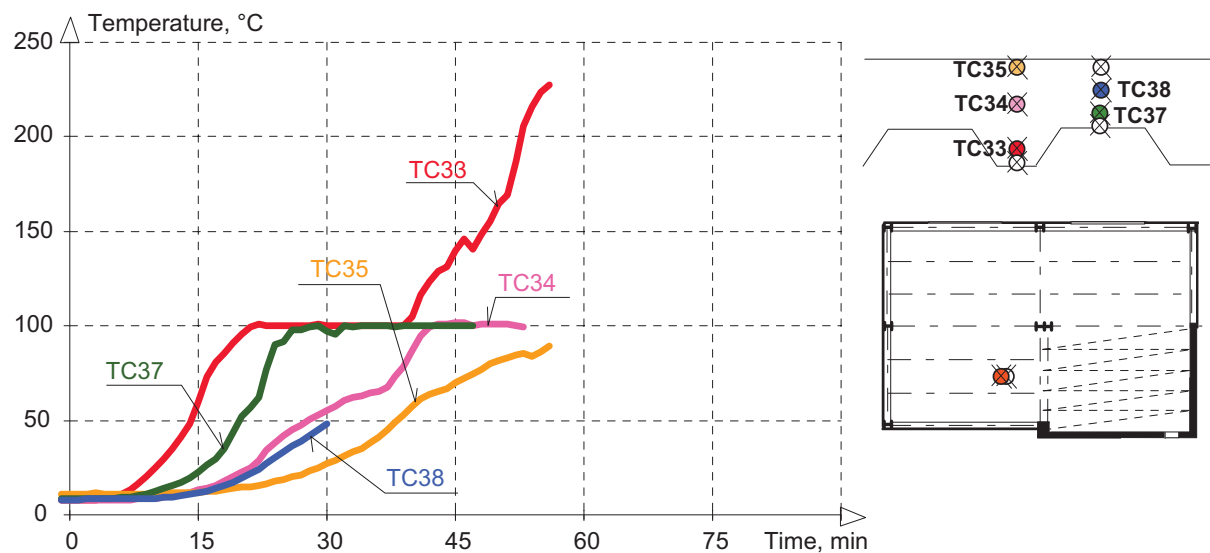


Fig. 4.31 - Temperatures measured on the composite slab with castellated beams

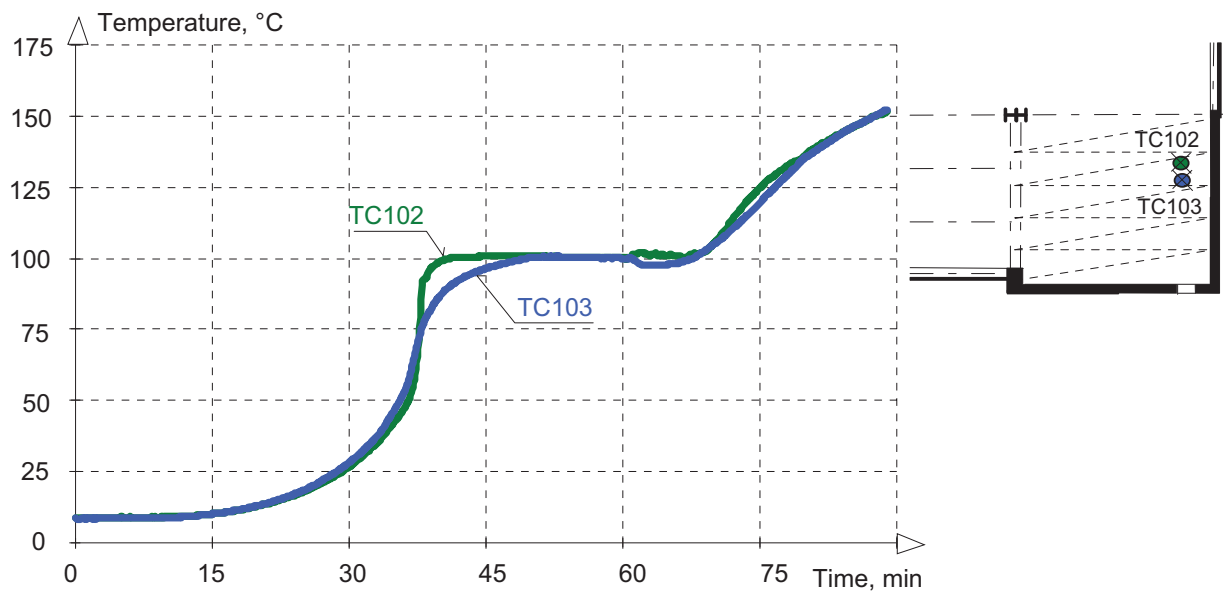


Fig. 4.32 - Temperatures measured in the hollow core slab, 265 mm from the top surface of the panels 320 mm thick, 10 mm above the reinforcement



Fig. 4.33 - The cross-section of the composite slab after the fire experiment

4.5 Wall temperatures

The temperatures of the composed claddings, sandwich panels and concrete wall were gauged. In Fig. 4.36 the placement of the thermocouple to the thin external sheet of cladding is provided. Four temperatures of two walls from the sandwich panel were monitored; see Figs. 4.34 to 4.35 and 4.37 to 4.38. The thermocouples were located to the external and internal sheet of sandwich panel. The Rockwool Company conducted its own measurements of the composed cladding with mineral wool; the temperature-time relationship is shown of Fig. 4.39.

The highest temperature of the internal surface of the sandwich panel was 950 °C at the 31. min of fire test and the temperature on the external surface was 37 °C at the 62. min. The maximum temperature measured 100 mm from the internal surface for the composed cladding with mineral wool reached 1055 °C at the 35. min. The integrity of the walls until the damage of the ceiling was recorded by thermo-image cameras, see Fig. 4.40.

Temperature developments in the concrete wall are shown in Figs. 4.42 to 4.44. Thermocouples in Fig. 4.42 were inserted into a drilled hole in the concrete wall before the fire experiment at three depth levels (20, 40, 60 mm) and then the space in the hole was filled with mineral wool. Jacketed thermocouples were used. In Figs. 4.43 and 4.44 the results from the measurements of the Department of Material Engineering and Chemistry are available. They used thermocouples in the form of trees. Each tree was concreted to a special concrete block which was separately inserted and then before the fire test it was built into the prearranged hole in the structure of the concrete wall. One tree monitored six temperatures in at different thicknesses of the concrete wall (0, 10, 20, 30, 40, 50 and 70 mm) at the same place. A tree in tube form for thermocouple TC127, see Fig. 4.43, and a tree in cube form for thermocouples TC128, see Fig. 4.44, were used. Thermocouple TC128 measured until the 32. min.

Water transport from the concrete of the wall started at the 25. min of the fire and it is documented in Figs. 4.45 and 4.46. The view of the fire protected door by the thermo-image camera is in Fig. 4.41. Spalling and blasting of the concrete on the wall started to be visible at the 25. min of the fire. Fig. 4.47 shows the development at the 45. min of the fire and in Fig. 4.48 the loss of the covering layer of the concrete wall and the top of the concrete column is visible.

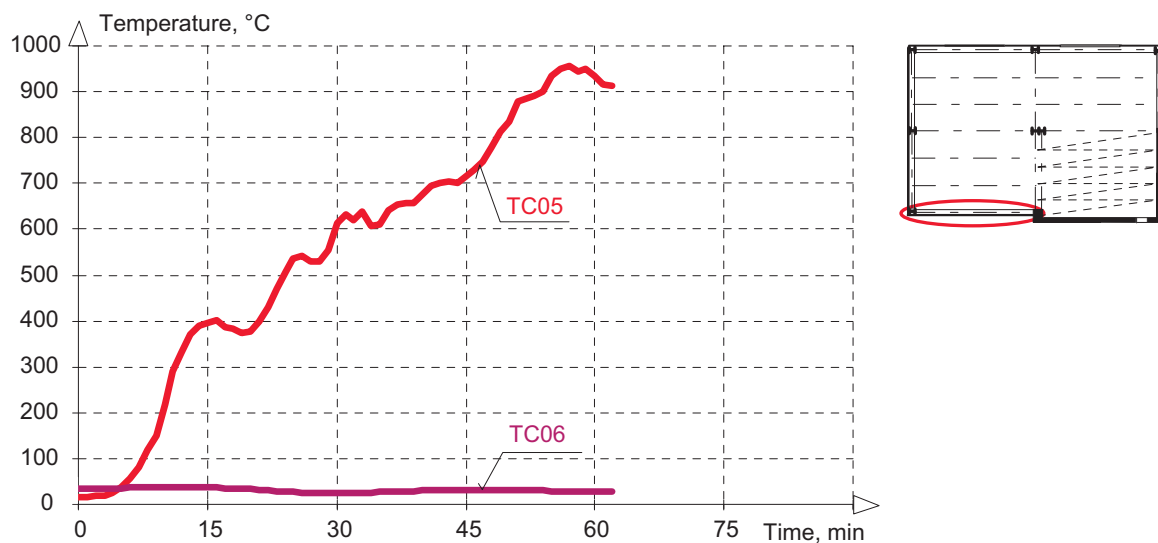


Fig. 4.34 - Temperatures measured in the middle of the external and internal sheet of the sandwich panel, wall AB1



Fig. 4.35 - Temperatures measured in the middle of the external sheet of the sandwich panel, wall AB1

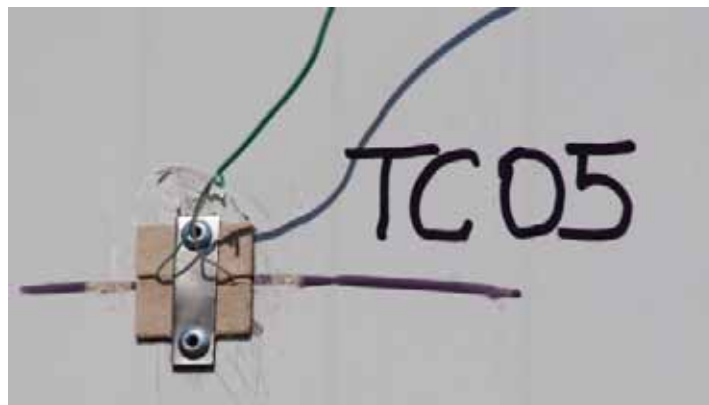


Fig. 4.36 - Placing of the thermocouples to of the thin external and internal sheets

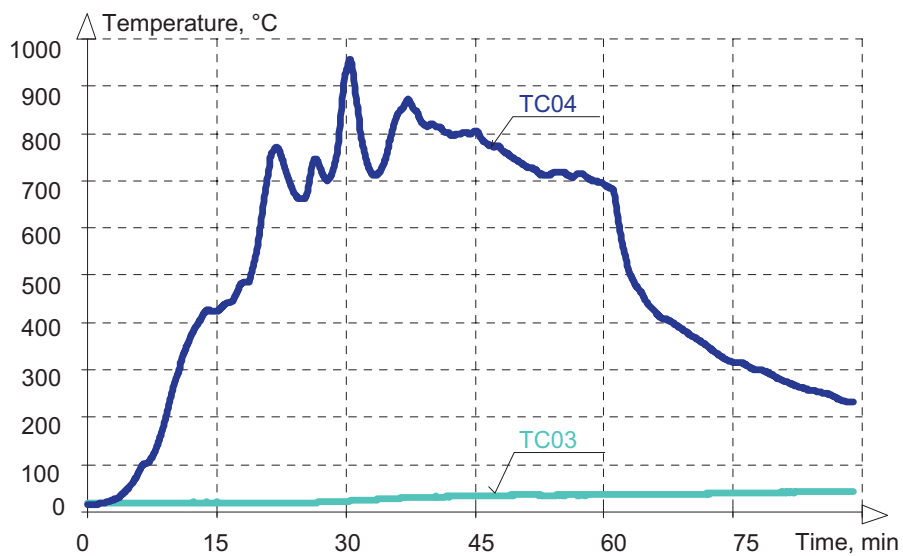


Fig. 4.37 - Temperatures measured in the middle of the external and internal sheet of the sandwich panel, C23

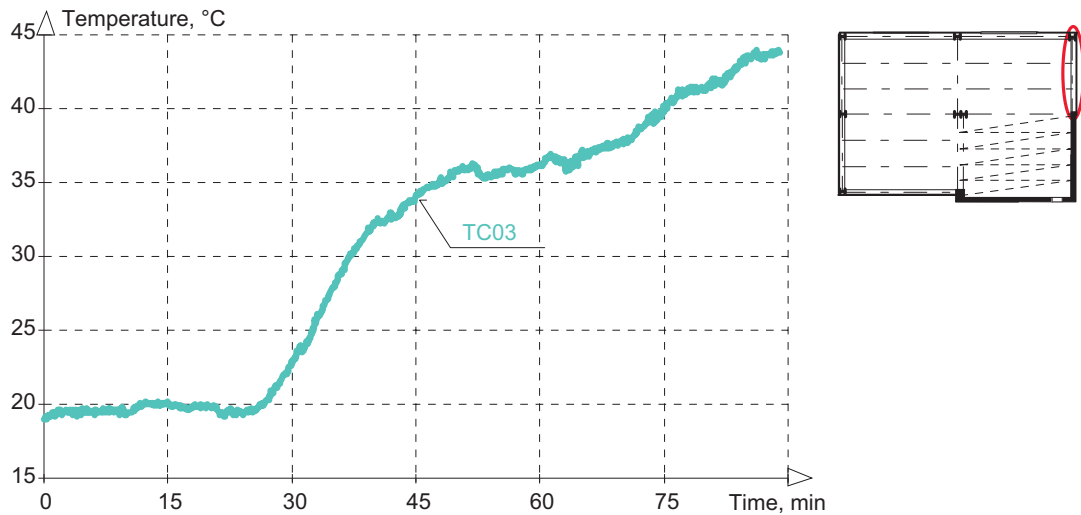


Fig. 4.38 - Temperatures measured in the middle of the external sheet of the sandwich panel, C23

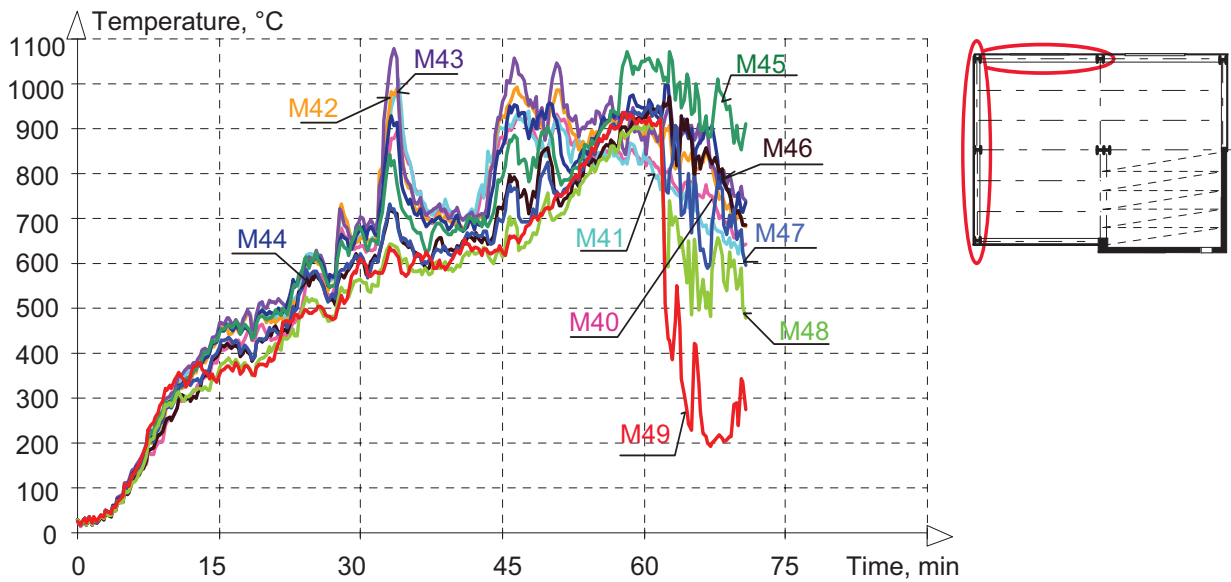


Fig. 4.39 Temperatures measured 100 mm from the internal surface of the mid-height on the internal sheet of the composed cladding with mineral wool

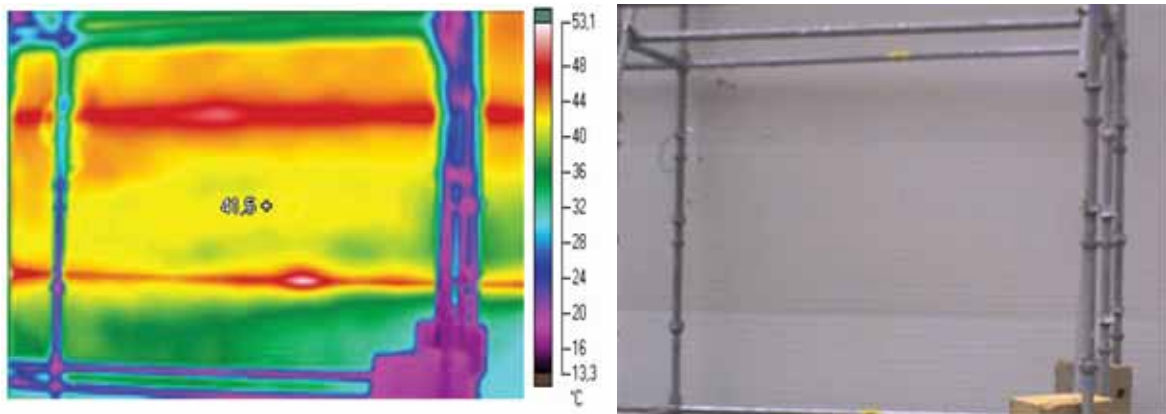


Fig. 4.40 - The visualisation of the temperatures measured by the thermo-image camera

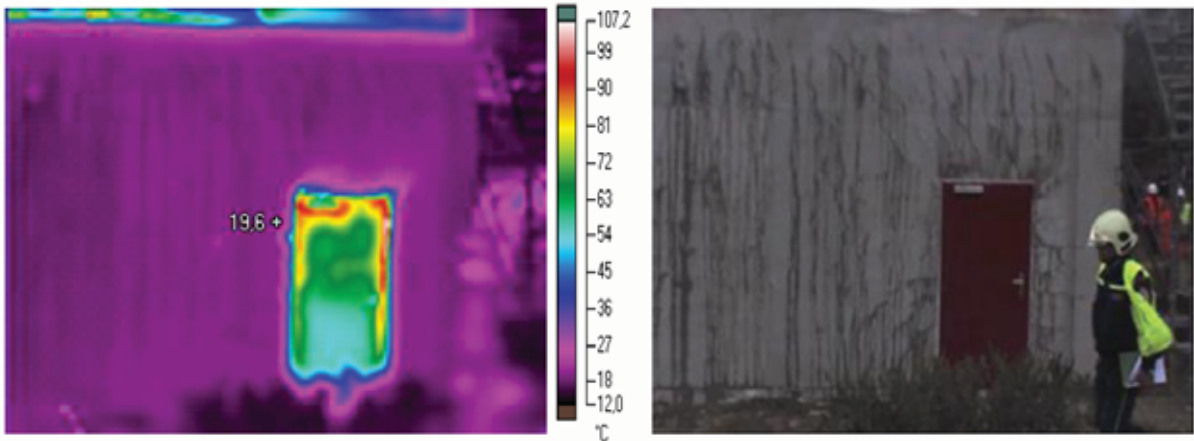


Fig. 4.41 - The visualisation of the temperatures measured by the thermo-image camera

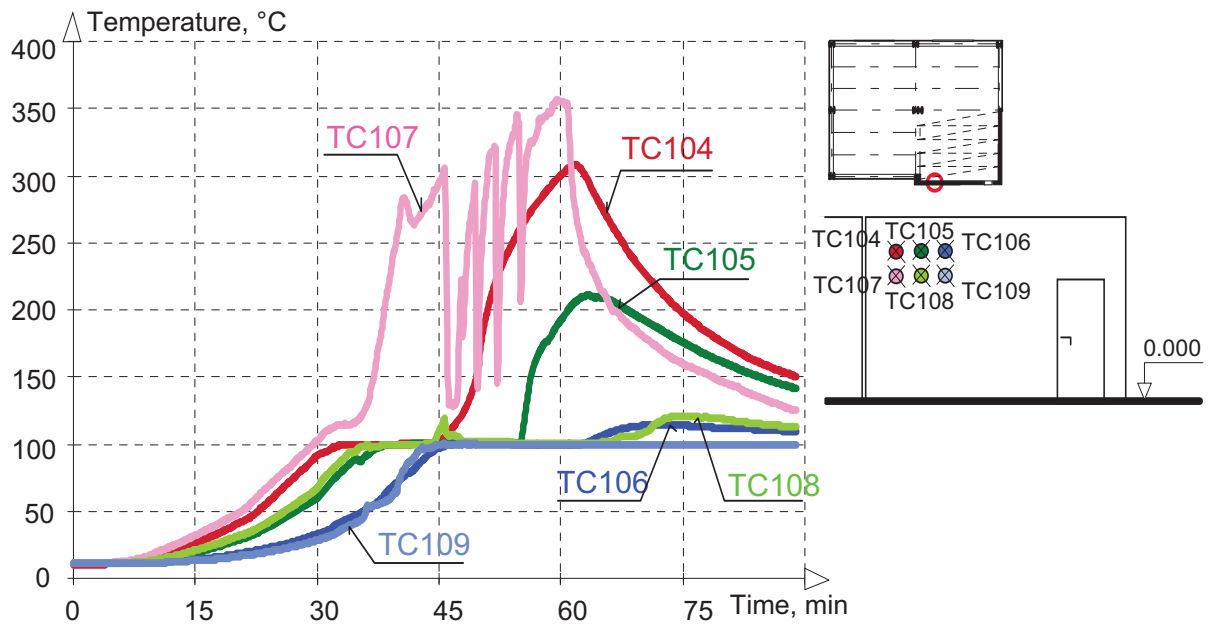


Fig. 4.42 - Temperatures measured in the concrete wall: TC104, TC105 and TC106 550 mm from top edge of the wall; TC107, TC108 and TC109 850 mm; TC104 and TC107 2800 mm from the west vertical edge and 20 mm from the internal surface; TC105, TC108 from 2850 mm and 40 mm; TC106, TC109 2900 mm and 60 mm

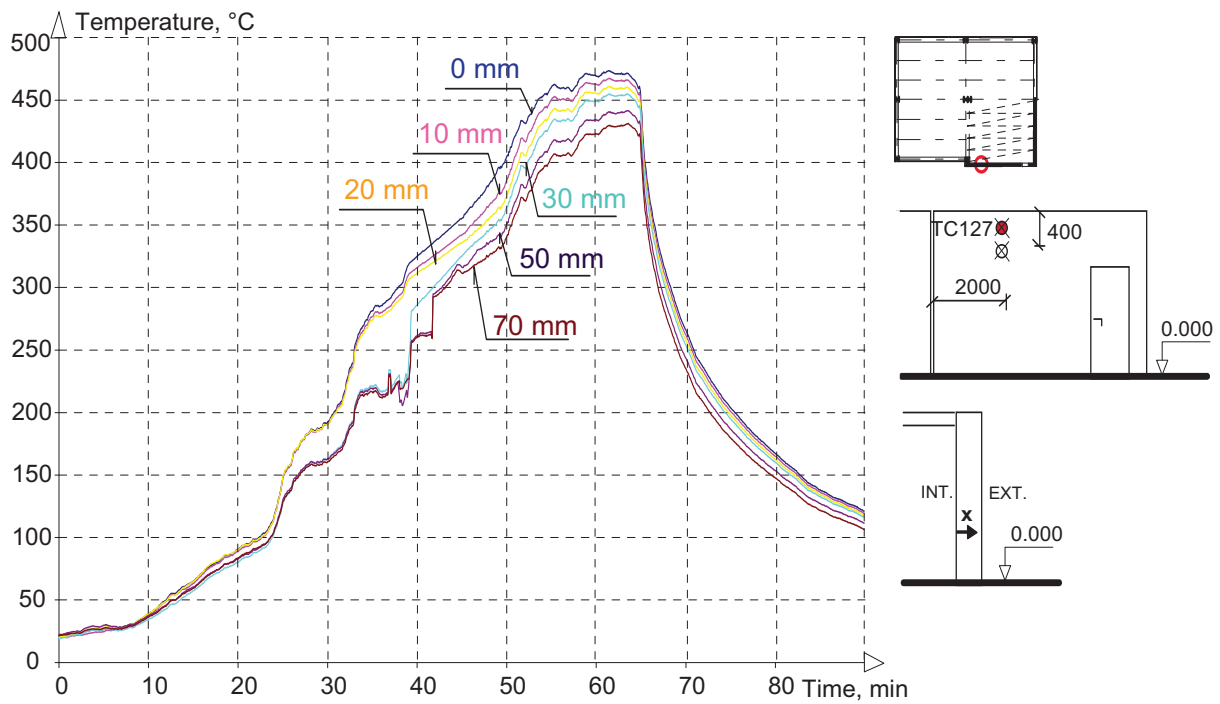


Fig. 4.43 - Temperature distribution along the thickness of concrete wall BC1 for thermocouple TC127; the measurements were performed from the internal surface to the external side of the wall

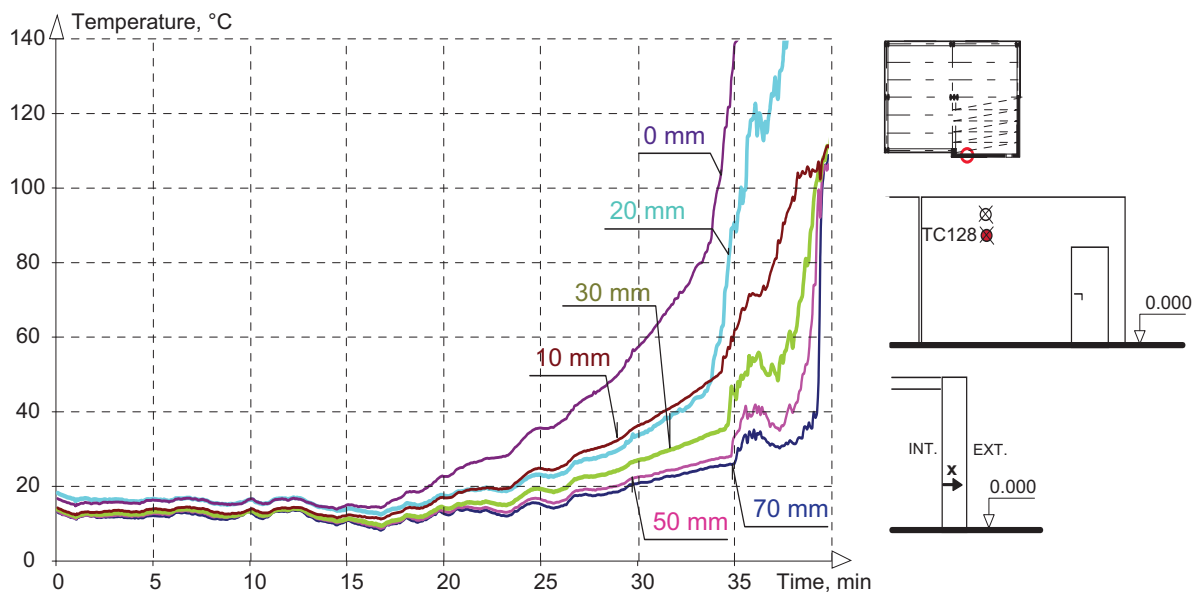


Fig. 4.44 - Temperature distribution along the thickness of concrete wall BC1 for thermocouple TC128; the measurements were performed from the internal surface to the external side of the wall



Fig. 4.45 - Transport of water to the external face of the concrete wall at the 30. min of the fire



Fig. 4.46 - Water transport from the concrete on the wall at the 25. min of the fire



Fig. 4.47 - Spalling of the concrete on the wall at the 45. min of the fire



Fig. 4.48 - Loss of concrete in the wall and at the top of the column

4.6 Plaster wall temperatures

The plaster wall was situated in front of the concrete wall under hollow core panel S4 in the fire compartment, see Fig. 4.52. The temperatures in six places at different depths over the the thickness of plaster wall by tree thermocouples were measured. At three places precise measurements were conducted. In Figs. 4.49 to 4.5,1 the temperature distribution along the thickness of plaster wall is shown.

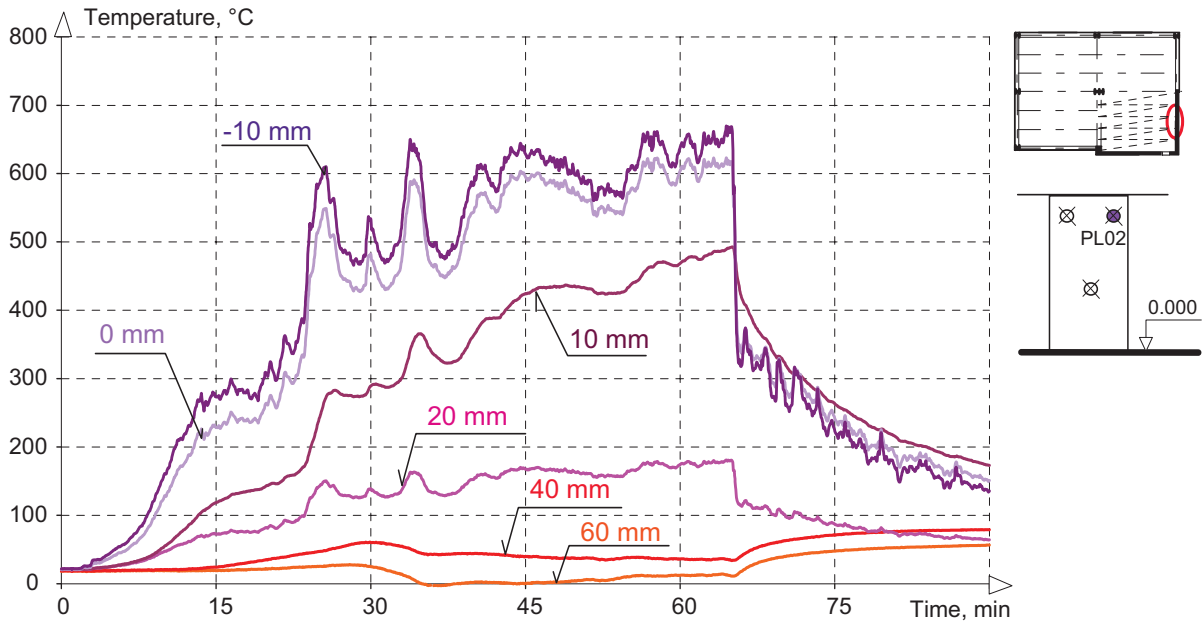


Fig. 4.49 - Temperatures of the plaster wall at the place PL02 for different depth levels from the internal surface: -10 mm, 0 mm, 10 mm, 20 mm, 40 mm and 60 mm

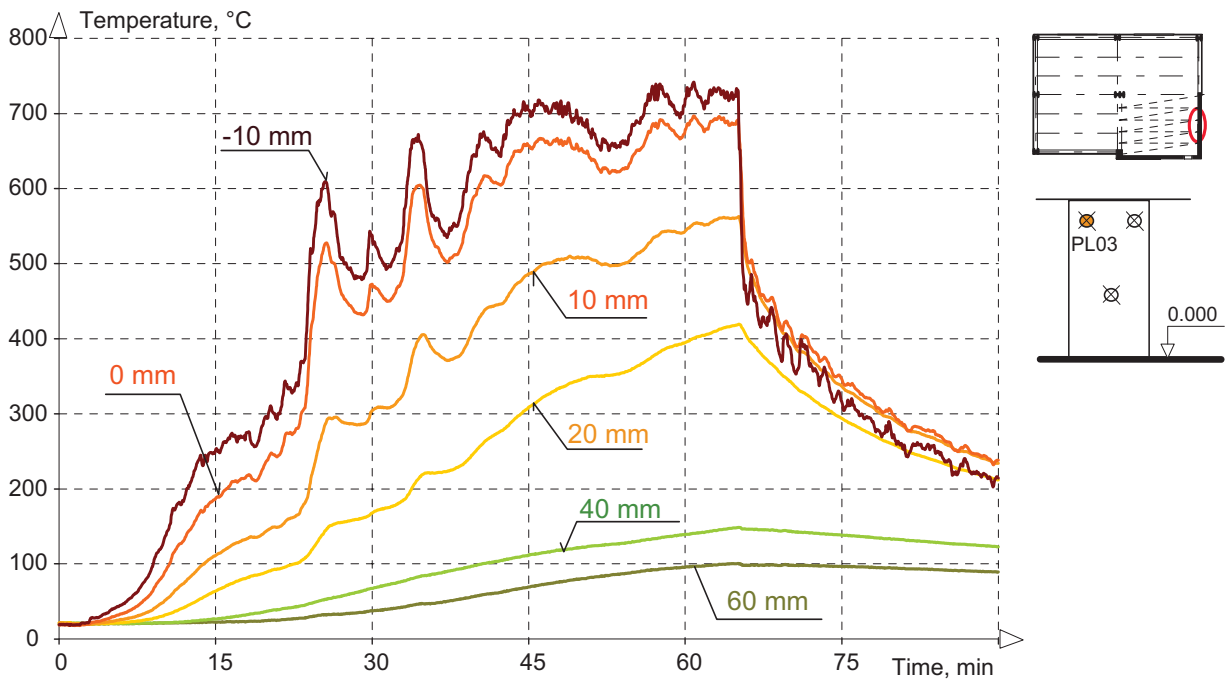


Fig. 4.50 - Temperatures of the plaster wall at the place PL03 for different depth levels from the internal surface: -10 mm, 0 mm, 10 mm, 20 mm, 40 mm and 60 mm

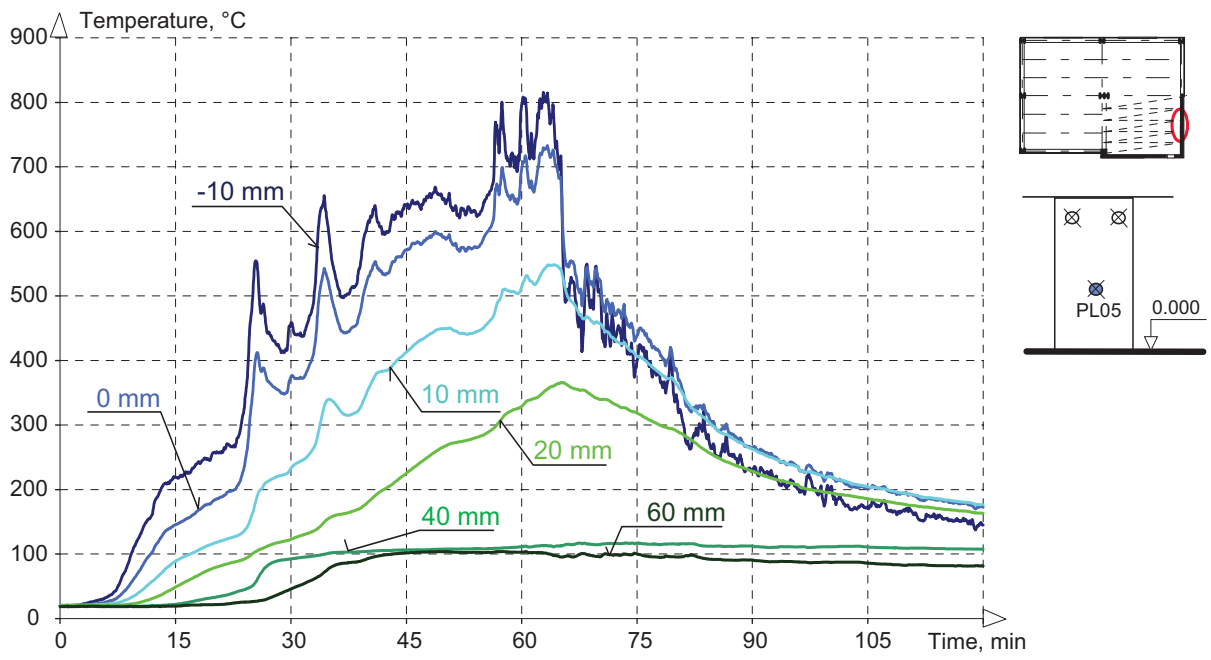


Fig. 4.51 - Temperatures of the plaster wall at the place PL05 for different depth levels from the internal surface: -10 mm, 0 mm, 10 mm, 20 mm, 40 mm and 60 mm



Fig. 5.52 - The view of the plaster wall in front of the concrete wall under hollow core panels in the fire compartment before the fire test

5 DEFORMATIONS

The horizontal and vertical deflection on the experimental structure was gauged by deflectometers. Trigonometric measurements and laser scanning were performed by the Department of Special Geodesy. The trigonometric measurements of vertical deformation were carried out by eight sticks with two self navigating targets fixed on the floor surface. Laser scanning was used for scanning the entire interior of the structure before and after the fire experiment.

5.1 Deflectometers

Scaffolds around the experimental building were erected (scaffold SGB CZ) for the horizontal deflection measurements. On the west and east sides of the building, linear system scaffolds were installed. Load bearing towers were placed between the windows and in the back of the compartment, which supported the two truss girders across the building at a span of 14 m. Vertical deformations were measured from the twin timber formwork beams, which were fixed on linear scaffolds and on bridged truss girders 1.5 m above the building floor, see Fig. 5.4.

Eight measurements of the vertical deformations were performed. The deflection of the composite slab above the midspan of Angelina beams AS2, AS3, AS4 and AS5, above the midspan of beams with corrugated web CS2 and CS3 and at the midspan of the prestressed panel S3 and S4 were monitored. The course of the deflection is shown in Figs. 5.1 and 5.2. The lower flanges at the midspan of the unprotected castellated beam reached about 450 °C at the 23. min with a deformation of 135 mm. At the 33 min. of the fire the temperature was about 800 °C and the deflection 368 mm. At the 58 min. the rapid increase of vertical deflection of the composite slab started above the Angelina beams. The damage to the slab occurred at the 62 min. of the test in the cooling phase of the fire with the measured temperature of the lower flange beam at the mid span a bit lower then 900 °C. The beams with corrugated web reached the maximal deflection of 256 mm at 780 °C. At the 20. min of the fire, the temperature was 450 °C and at the 32. min. it was 715 °C. The maximal deflection for the slab above the beams with corrugated webs was 250 mm and for the hollow core panels it was 100 mm.

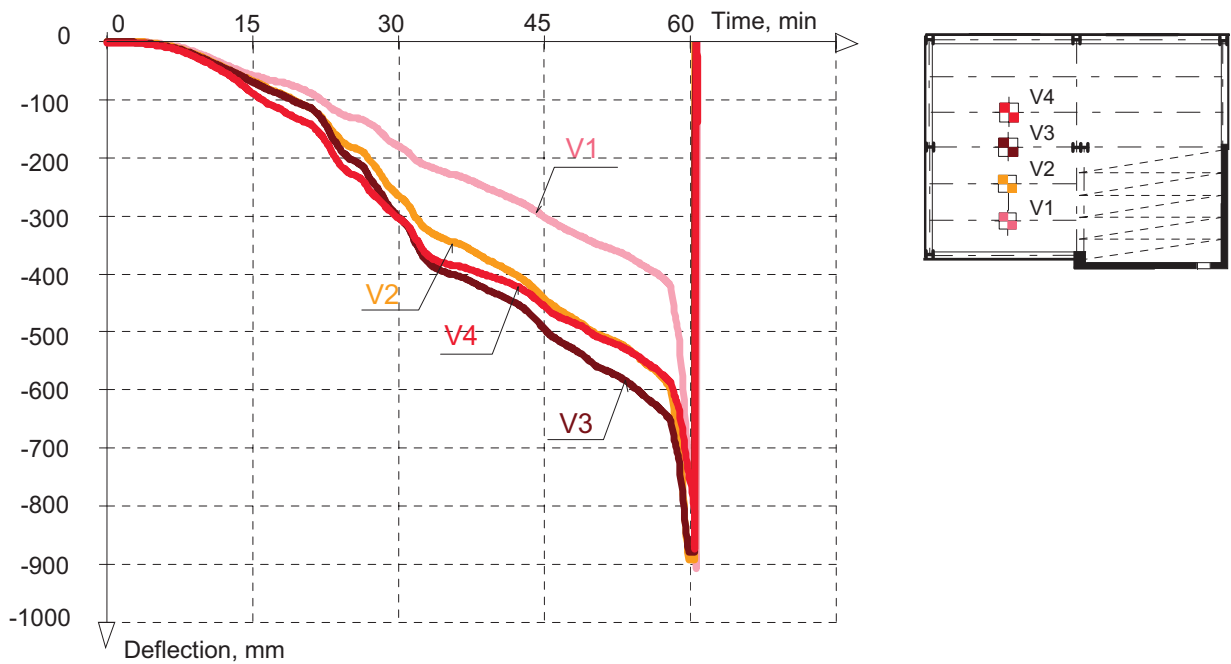


Fig. 5.1 - Deflections of the composite slab above the castellated beams

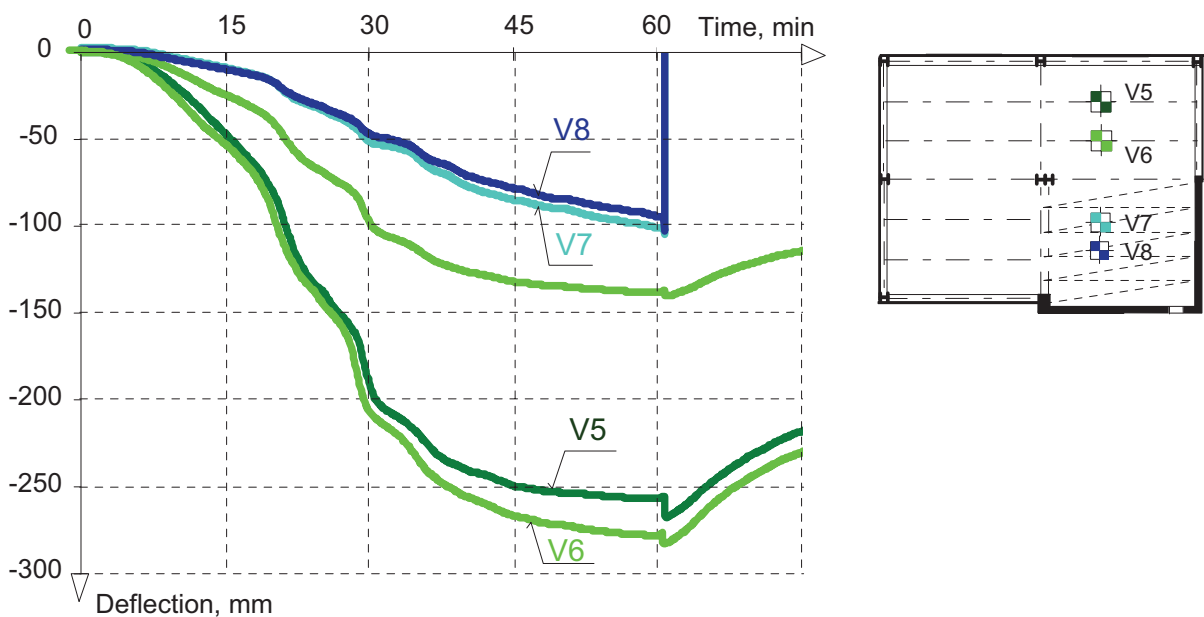


Fig. 5.2 - Deflections of hollow core panels and the composite slab above the beams with corrugated webs

Three horizontal deformations on the composite slab above the cellular Angelina beams and two horizontal deformations on the composite slab above the beams with corrugated webs were measured. In Fig. 5.3, the location of the measurements; three deflectometers at a span 9 m, one for a span of 6m and one for a span of 12 m are displayed. The horizontal deformation of the slab was measured only until the 30 min, of the fire due to large vertical deformations.

Figs. 5.5 to 5.7 show the deformed cellular Angelina beams and beams with corrugated webs at different times during the fire experiment.

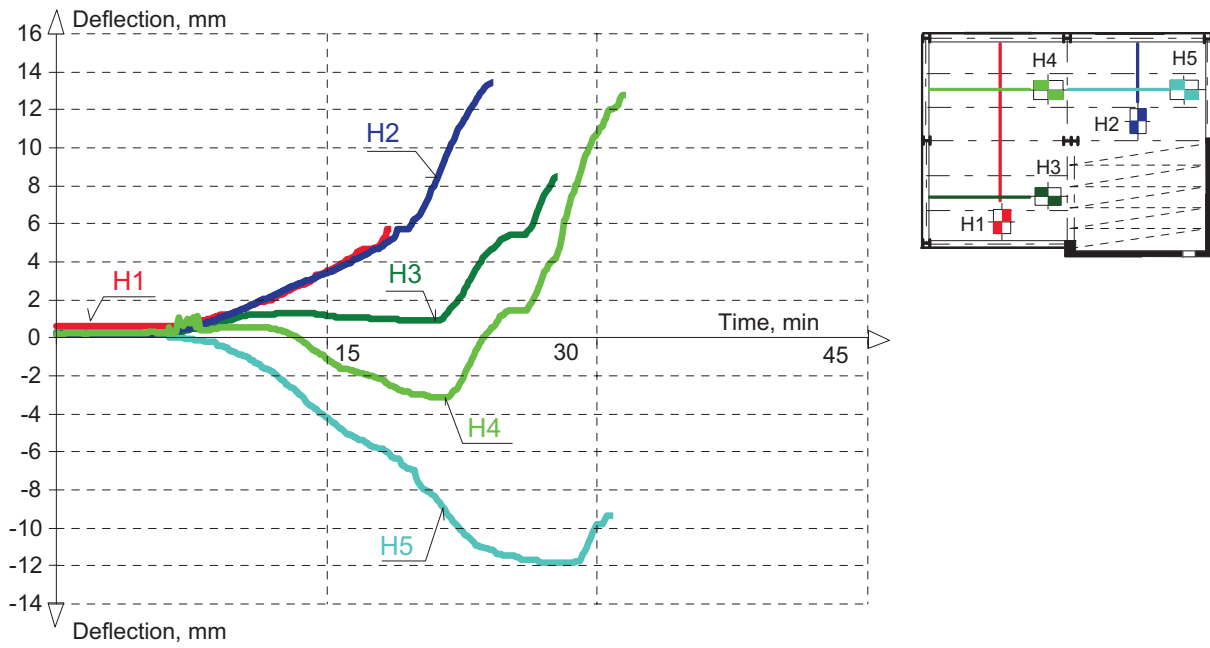


Fig. 5.3 - Horizontal deformation of the slabs



Fig. 5.4 - Independent scaffolding for deflection measurement



Fig. 5.5 - The deformed beams with corrugated web at the 25. min of the fire test



Fig. 5.6 - Deformation of castellated beams behind the deflected beams with corrugated web at the 37. min of the fire



Fig. 5.7 - Deformed Angelina beam at the 48 min. of the fire test

5.2 Trigonometric Measurement

The choice of a measurement method in the given case was not very complicated. With respect to possible very high temperatures on the object it was not possible to use levelling, because it is not possible to firmly stabilize levelling rods in a vertical position with regard to the deformation of the object. Other methods are not also suitable or executable as well and therefore we chose the trigonometric method. Considering the fact that speed for this almost dynamic measurement is important, we chose automatic measurement including targeting.

5.2.1 Measurement Configuration

Location of the standpoint, measured points on the object and their numbering is schematically illustrated in Fig. 5.8. Distance standpoints S – points 1 to 4 was approximately 28 m, standpoint S – points 5 and 6 approximately 36 m. The measured zenith angles were within limits 95 gon to 100 gon. Fig. 5.8 shows the observed points illustrated in the context of the construction and its load.

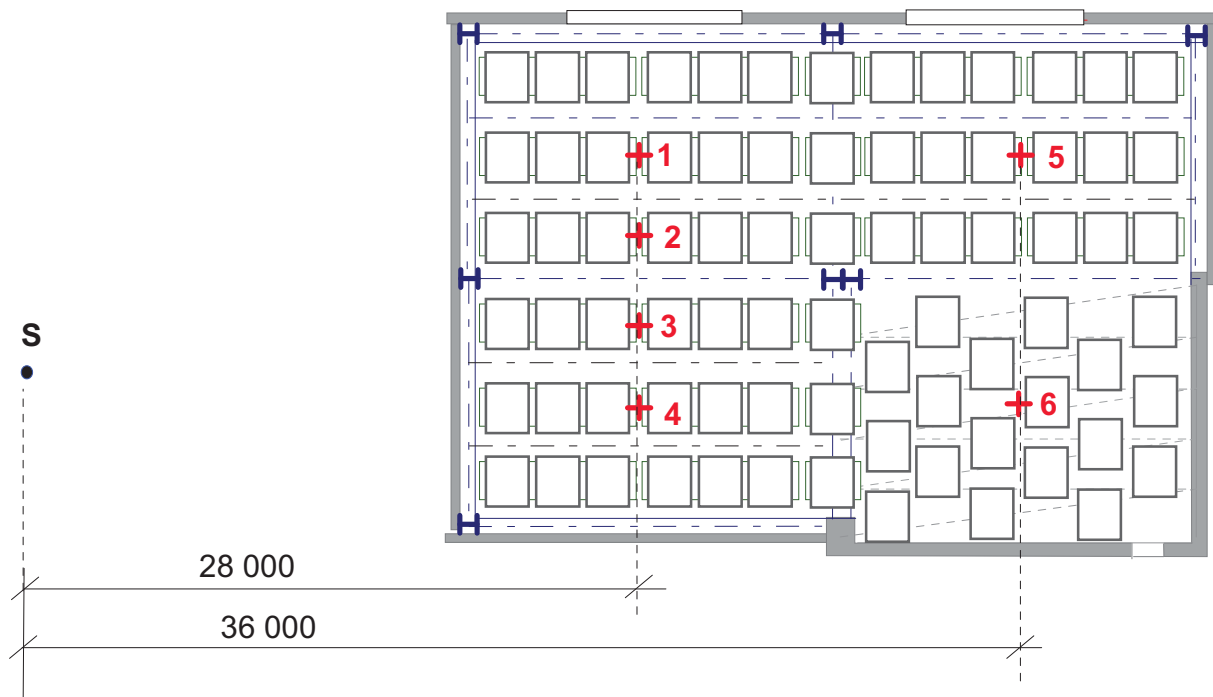


Fig. 5.8 - Scheme of measurement configuration

5.2.2 Stabilization of the Standpoint and Signalization of Observed Points

The standpoint was stabilized with metal tubes embedded in the concrete, 300 mm deep. The instrument was put on a tripod with tips set into the stated tubes, overshadowed by a square tent with metal construction with a ground plan of 3.3 m x 3.3 m, see Fig. 5.9.

The observed points were stabilized by iron framing squares 3 m long with two welded plates - size 50 mm x 50 mm, to which reflecting foil (40 mm x 40 mm, a Leica Company product) was applied. A signalized point is given by the intersection of the rod sign with the surface of the construction. The distance of the targets for the nearer points was 500 mm (points 1 - 4), for more distant points 750 mm (points 5 - 6). Different distances were necessary with respect to the fact that automatic targeting of the Trimble S6 instrument (described in more detail below) does not work correctly, if there is more than one target in the field of view in size approximately 1 gon x 1 gon. The target rod is schematically illustrated in Fig. 5.10.

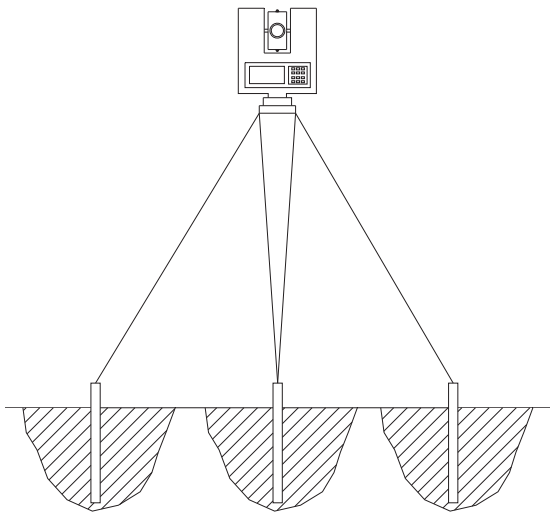


Fig. 5.9 - Stabilization of the standpoint



Fig. 5.10 - Schematic illustration of target signalization

Framing squares were welded onto two strips on an iron plate organized into a cross screwed to the roof of the object in the observed points preferably in a vertical position, turned in the direction to the standpoint. This strange and complicated method was chosen because the object was covered to 1.4 m with load in the form of sacks with sand and then on the object with independent constructions bearing was other measuring sensors. With respect to supposed failures at most 500 mm a suitable reserve was necessary. It is also not possible to guarantee unchanging tilt of the target rod during measurement time, and therefore it was necessary to set up the rod with two targets, which (as will be shown below) enabled the calculation of the height of a point.

Stabilization tilt is possible when using this method, but its success depends on its rotation or deformation (i.e. deflection).

5.2.3 Used Apparatus Outfit

The Trimble S6 High Precision instrument was chosen for the measurement from the available instruments of the Department of Special Geodesy at the Faculty of Civil Engineering of CTU in Prague. In total, it has the highest accuracy of length measurements and sufficient accuracy of direction and zenith angle measurements. The instrument provides automatic targeting and a program for repeated measurements of a set of directions, zenith angles and lengths for fast automatic measurement. This total station integrates in itself many innovations in direction of basic measurement principles and in construction. The instrument was used in combination with a distance meter with a standard deviation of $1 \text{ mm} + 1 \text{ ppm} \cdot D$ and a standard deviation of direction and zenith angle measurement in two positions 0.3 mgon .

The following listing of technologies with a description is a sufficient argument why the instrument is considered unique. MagDrive™ is servo technology using a magnetic pillow, which enables faster movement of the alidade and reduces mechanical instrument abrasion. MultiTrack™ is search technology and monitoring a current prism with its unique identification by means of additional infrared transmitter located under the prism. SurePoint™ is a system that retains line of sight in the position where it was set with clamping screws, that means during movement (i.e. vibration) the instrument sets itself in the position of the alidade and the telescope. Other interesting qualities we can state e.g. removable control unit with colour touch screen, Windows CE operating system, processor 400MHz, RAM 64MB, internal memory 256MB, Bluetooth, using the same software of the control unit for different types of measurement and also for servo focusing, and a prism-less distance meter with passive reflection for measuring long distances. Further information can be found e.g. in [10], [11].

The only problem of the stated instrument is the method of evaluating pictures during automatic targeting, because when there is more than one target in the sensor field processing reflection of signal, automatic targeting fails. The size of the field of view, when the problem arises, was experimentally examined in size approximately $1.0 \text{ gon} \times 0.8 \text{ gon}$. The size of the targets on the rods was originally supposed to be deflections of 0.5 m , but with respect to this problem it was however necessary to increase it to 0.75 m at more distant targets.

5.2.4 Calculation Procedure

Targets were placed in the axis of the stabilization rod, distance marks was further marked D , distance from the upper aiming mark to the lower edge of the rod was further marked L . Parameters are illustrated in Fig. 5.11.

During the calculation process various versions of the calculation appeared with respect to various influences. If it was possible to carry out exact determination of distance of targets D before measurement, it was possible to execute calculations according to paragraph 5.2.5, if it was not the case or if D is variable, it was necessary to calculate according to paragraph 5.2.7.

In both versions it was necessary to measure in each epoch on both targets slope lengths s_1, s_2 , zenith angles z_1, z_2 .

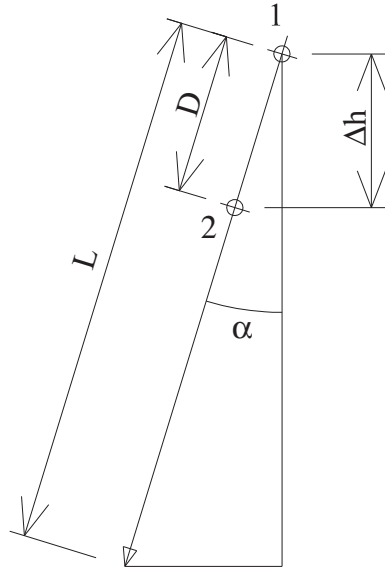


Fig. 5.11 – Parameters characterizing target rods

5.2.5 Calculation with Constant D

Measurement and calculation method was suitable, if it was not possible to measure horizontal directions on targets (e.g. for classical optical measurement with regard to time reasons) and it was possible to determine distance D very accurately.

Height difference of the aiming marks h_1 (h_2) from the instrument trunnion axis was calculated according to formulae:

$$h_1 = s_1 \cdot \cos(z_1) \quad (1)$$

$$h_2 = s_2 \cdot \cos(z_2) \quad (2)$$

Distance D was known from calibration measurements (i.e. with scales used in machine engineering or geodetically according to paragraphs 5.2.7). Then it was possible to derive a simple relation for the height of the rod footer

$$H = h_1 - \cos(\alpha) \cdot L = h_1 - \frac{\Delta h}{D} \cdot L \quad (3)$$

where

$$\Delta h = H_1 - H_2 \quad (4)$$

The resulting formula

$$h = s_1 \cdot \cos(z_1) - \frac{s_1 \cdot \cos(z_1) - s_2 \cdot \cos(z_2)}{D} \cdot L \quad (5)$$

This calculation is one of many versions, it is however extremely useful in cases when sights are almost horizontal ($z \approx 100$ gon), because of length error, which is a usually a restrictive factor of accuracy, and is of very little of use.

Height shift ΔH between two epochs determine which is actually the target of the measurement, is then calculated as a difference of heights in both epochs

$$\Delta H_{i,j} = h_j - h_i \quad (6)$$

5.2.6 Determination of Parameter D by Trigonometric Method

If it is not possible to carry out calibration measurements in advance or if automatic targeting is used, which does not measure on a geometric centre of the foil marked with a cross from the point of intensity of the signal returning from the reflecting foil, it is possible to determine parameter D by trigonometric measurement, i.e. by measurement on both aiming marks of oblique lengths s_1, s_2 , zenith angles z_1, z_2 , horizontal directions φ_1, φ_2 .

Parameter D is the distance of aiming marks on the target rod, which lies in the general plane. Derivation of the formula for its calculation comes from the following formulae for calculation of coordinates of targets, where $i = 1, 2$.

$$x_i = s_i \cdot \sin(z_i) \cdot \cos(\varphi_i) \quad (7)$$

$$y_i = s_i \cdot \sin(z_i) \cdot \sin(\varphi_i) \quad (8)$$

$$h_i = s_i \cdot \cos(z_i) \quad (9)$$

D is then calculated

$$D = \sqrt{(x_1 - x_2)^2 + (y_1 - y_2)^2 + (h_1 - h_2)^2} \quad (10)$$

The resulting formula can be acquired by insertion and by a few simple adjustments

$$D = \sqrt{s_1^2 + s_2^2 - 2 \cdot s_1 \cdot s_2 \cdot \left(\frac{\sin(z_1) \cdot \sin(z_2) \cdot \cos(\varphi_1 - \varphi_2) + \cos(z_1) \cdot \cos(z_2)}{\cos(z_1) \cdot \cos(z_2)} \right)} \quad (11)$$

Well known formulae are used with advantage during derivation

$$\sin^2(\alpha) + \cos^2(\alpha) = 1 \quad (12)$$

$$\cos(\alpha \pm \beta) = \cos(\alpha) \cdot \cos(\beta) \mp \sin(\alpha) \cdot \sin(\beta) \quad (13)$$

Parameter D can be then determined in this way repeatedly. It is possible to determine the most probable value with higher accuracy by means of arithmetic mean.

5.2.7 Calculation with unknown or variable D

The calculation is identical as in paragraph 5.2.5 with one difference – formula (11) is used instead of parameter D .

5.2.8 Measuring Procedure

Horizontal directions, zenith angles and oblique lengths were measured on aiming points in each epoch. With respect to the fact that it is a measurement of changes in approximately stable configuration, systematic errors from measurement in one position are not of use and therefore it was measured only in one position of the telescope in order to accelerate measurement. The second reason is the dynamic character of the measured changes, which means that for the consistency of the results it is necessary to measure an epoch as quickly as possible. Therefore the aiming points were measured as well on one rod immediately one after another and fully automatic targeting and measurement was used. Measurement of one epoch took less than 2 min. 15 epochs were measured in total, out of which 9 epochs were measured before ignition; other epochs could not be measured because of thick and non-transparent smoke.

5.2.9 Accuracy Analyses before Measurement

From the stated configuration it is possible to calculate expected determination accuracies of the functions of the measured quantities by means of the law of standard deviation propagation, [12]. Different versions dependent on ambient conditions discussed in the previous paragraph may arise during calculation. Accuracy description does not comprise systematic influence of refraction (nonlinear course of light beam through atmosphere).

Determination Accuracy of Distance of Targets from Calibration Measurements

According to the law of standard deviation propagation, standard deviation σ of function σ of independent quantities x_1, x_2, x_n is determined from the knowledge of their standard deviations in the following way:

$$f = f(x_1, x_2, \dots, x_n) \quad (14)$$

$$\sigma_f^2 = \left(\frac{\partial f}{\partial x_1} \cdot \sigma_{x_1}\right)^2 + \left(\frac{\partial f}{\partial x_2} \cdot \sigma_{x_2}\right)^2 + \dots + \left(\frac{\partial f}{\partial x_n} \cdot \sigma_{x_n}\right)^2 \quad (15)$$

Parameter D is the function according to formula (11):

$$D = D(s_1, s_2, z_1, z_2, \varphi_1, \varphi_2) \quad (16)$$

The formula for the calculation of standard deviation is formulated in the following way: (Note: Direction and angle standard deviations have to be inserted in radians.)

$$\sigma_D^2 = \left(\begin{aligned} &\left(\frac{\partial D}{\partial s_1} \cdot \sigma_{s_1}\right)^2 + \left(\frac{\partial D}{\partial s_2} \cdot \sigma_{s_2}\right)^2 + \left(\frac{\partial D}{\partial z_1} \cdot \sigma_{z_1}\right)^2 + \\ &+ \left(\frac{\partial D}{\partial z_2} \cdot \sigma_{z_2}\right)^2 + \left(\frac{\partial D}{\partial \varphi_1} \cdot \sigma_{\varphi_1}\right)^2 + \left(\frac{\partial D}{\partial \varphi_2} \cdot \sigma_{\varphi_2}\right)^2 \end{aligned} \right) \quad (17)$$

Derivations are:

$$\frac{\partial D}{\partial s_1} = \frac{1}{D} \cdot \left(s_1 - s_2 \cdot \left(\begin{aligned} &\sin(z_1) \cdot \sin(z_2) \cdot \cos(\varphi_1 - \varphi_2) + \\ &+ \cos(z_1) \cdot \cos(z_2) \end{aligned} \right) \right) \quad (18)$$

$$\frac{\partial D}{\partial s_2} = \frac{1}{D} \cdot \left(s_2 - s_1 \cdot \left(\begin{aligned} &\sin(z_1) \cdot \sin(z_2) \cdot \cos(\varphi_1 - \varphi_2) + \\ &+ \cos(z_1) \cdot \cos(z_2) \end{aligned} \right) \right) \quad (19)$$

$$\frac{\partial D}{\partial z_1} = \frac{1}{D} \cdot \left(-s_1 \cdot s_2 \cdot \left(\begin{aligned} &\cos(z_1) \cdot \sin(z_2) \cdot \cos(\varphi_1 - \varphi_2) - \\ &- \sin(z_1) \cdot \cos(z_2) \end{aligned} \right) \right) \quad (20)$$

$$\frac{\partial D}{\partial z_2} = \frac{1}{D} \cdot \left(-s_1 \cdot s_2 \cdot \left(\begin{aligned} &\sin(z_1) \cdot \cos(z_2) \cdot \cos(\varphi_1 - \varphi_2) - \\ &- \cos(z_1) \cdot \sin(z_2) \end{aligned} \right) \right) \quad (21)$$

$$\frac{\partial D}{\partial \varphi_1} = \frac{1}{D} \cdot \left(s_1 \cdot s_2 \cdot \left(\sin(z_1) \cdot \sin(z_2) \cdot \sin(\varphi_1 - \varphi_2) \right) \right) \quad (22)$$

$$\frac{\partial D}{\partial \varphi_2} = \frac{1}{D} \cdot \left(-s_1 \cdot s_2 \cdot \left(\sin(z_1) \cdot \sin(z_2) \cdot \sin(\varphi_1 - \varphi_2) \right) \right) \quad (23)$$

After the use of the approximate configuration of closer points, where the measured values are approximately $s_1 = s_2 = 28$ m, $z_1 = 95.00$ gon, $z_2 = 96.14$ gon (D is approximately 0.5 m) and the standard deviations of the measured values are $\sigma_s = 1$ mm, $\sigma_z = \sigma_\varphi = 1.5$ mgon is the standard deviation of D is $\sigma_D = 0,9$ mm. For more distant points, where $s_1 = s_2 = 35$ m; $z_1 = 95.00$ gon, $z_2 = 96.36$ gon gon (D is approximately 0.75 m) the standard deviation of the determination of D parameter is $\sigma_D = 1.2$ mm. The average value from nine stages in total

would have a standard deviation of 0.3 mm for closer targets, or 0.4 mm for more distant targets.

Accuracy of Determination of Height Shift with Constant D

So as to determine the accuracy of the vertical shift we arrived from formula (6), which we derive required accuracy by means of procedure mentioned in paragraph 5.2.5 by means of the law of standard deviation propagation:

$$\Delta H_{i,j} = H_j - H_i = \left(\left(s_{1j} \cdot \cos(z_{1j}) - \frac{s_{1j} \cdot \cos(z_{1j}) - s_{2j} \cdot \cos(z_{2j})}{D} \cdot L \right) - \left(s_{1i} \cdot \cos(z_{1i}) - \frac{s_{1i} \cdot \cos(z_{1i}) - s_{2i} \cdot \cos(z_{2i})}{D} \cdot L \right) \right) \quad (24)$$

$$\sigma_{\Delta H_{i,j}} = \sqrt{\left(\left(\frac{\partial \Delta H_{i,j}}{\partial s_{1j}} \cdot \sigma_{s_{1j}} \right)^2 + \left(\frac{\partial \Delta H_{i,j}}{\partial s_{1i}} \cdot \sigma_{s_{1i}} \right)^2 + \left(\frac{\partial \Delta H_{i,j}}{\partial s_{2j}} \cdot \sigma_{s_{2j}} \right)^2 + \left(\frac{\partial \Delta H_{i,j}}{\partial s_{2i}} \cdot \sigma_{s_{2i}} \right)^2 + \left(\frac{\partial \Delta H_{i,j}}{\partial z_{1j}} \cdot \sigma_{z_{1j}} \right)^2 + \left(\frac{\partial \Delta H_{i,j}}{\partial z_{1i}} \cdot \sigma_{z_{1i}} \right)^2 + \left(\frac{\partial \Delta H_{i,j}}{\partial z_{2j}} \cdot \sigma_{z_{2j}} \right)^2 + \left(\frac{\partial \Delta H_{i,j}}{\partial z_{2i}} \cdot \sigma_{z_{2i}} \right)^2 + \left(\frac{\partial \Delta H_{i,j}}{\partial D} \cdot \sigma_D \right)^2 + \left(\frac{\partial \Delta H_{i,j}}{\partial L} \cdot \sigma_L \right)^2 \right)} \quad (25)$$

where

$$\frac{\partial \Delta H_{i,j}}{\partial s_{1j}} = \cos(z_{1j}) - \frac{\cos(z_{1j})}{D} \cdot L \quad (26)$$

$$\frac{\partial \Delta H_{i,j}}{\partial s_{1i}} = - \left(\cos(z_{1i}) - \frac{\cos(z_{1i})}{D} \cdot L \right) \quad (27)$$

$$\frac{\partial \Delta H_{i,j}}{\partial s_{2j}} = \frac{\cos(z_{2j})}{D} \cdot L, \quad (28)$$

$$\frac{\partial \Delta H_{i,j}}{\partial s_{2i}} = - \left(\frac{\cos(z_{2i})}{D} \cdot L \right), \quad (29)$$

$$\frac{\partial \Delta H_{i,j}}{\partial z_{1j}} = - \sin(s_{1j}) \cdot \sin(z_{1j}) + \frac{s_{1j} \cdot \sin(z_{1j})}{D} \quad (30)$$

$$\frac{\partial \Delta H_{i,j}}{\partial z_{1i}} = \sin(s_{1i}) \cdot \sin(z_{1i}) - \frac{s_{1i} \cdot \sin(z_{1i})}{D} \quad (31)$$

$$\frac{\partial \Delta H_{i,j}}{\partial z_{2j}} = - \sin(s_{2j}) \cdot \sin(z_{2j}) + \frac{s_{2j} \cdot \sin(z_{2j})}{D} \quad (32)$$

$$\frac{\partial \Delta H_{i,j}}{\partial z_{2i}} = \sin(s_{2i}) \cdot \sin(z_{2i}) - \frac{s_{2i} \cdot \sin(z_{2i})}{D} \quad (33)$$

$$\frac{\partial \Delta H_{i,j}}{\partial D} = \frac{L}{D^2} \cdot \left(\left(s_{1j} \cdot \cos(z_{1j}) - s_{2j} \cdot \cos(z_{2j}) \right) - \left(s_{1i} \cdot \cos(z_{1i}) - s_{2i} \cdot \cos(z_{2i}) \right) \right) \quad (34)$$

$$\frac{\partial \Delta H_{i,j}}{\partial L} = \frac{1}{D} \cdot \left(\left(-s_{1j} \cdot \cos(z_{1j}) + s_{2j} \cdot \cos(z_{2j}) \right) - \left(-s_{1i} \cdot \cos(z_{1i}) + s_{2i} \cdot \cos(z_{2i}) \right) \right) \quad (35)$$

For accuracy analysis it is possible to suppose identical standard deviations of length and angle measurement in the individual stages and also similar measurement configurations and thus to simplify the formula:

$$\sigma_{\Delta H_{i,j}} = \sqrt{2 \cdot \left(\frac{\partial \Delta H_{i,j}}{\partial s_1} \cdot \sigma_{s_1}\right)^2 + 2 \cdot \left(\frac{\partial \Delta H_{i,j}}{\partial s_2} \cdot \sigma_{s_2}\right)^2 + 2 \cdot \left(\frac{\partial \Delta H_{i,j}}{\partial z_1} \cdot \sigma_{z_1}\right)^2 + 2 \cdot \left(\frac{\partial \Delta H_{i,j}}{\partial z_2} \cdot \sigma_{z_2}\right)^2 + \left(\frac{\partial \Delta H_{i,j}}{\partial D} \cdot \sigma_D\right)^2 + \left(\frac{\partial \Delta H_{i,j}}{\partial L} \cdot \sigma_L\right)^2} \quad (36)$$

The resulting standard deviation is then dependent on the size of the height shifts, if they were very small, the influence of determination accuracy D and L would be insignificant.

Standard deviation of determination of maximum expected height shift $\Delta H_{\max} = 0.5$ m according to accuracy analysis:

- a) on rods 1 – 4: 7.3 mm,
- b) on rods 5 – 6: 5.8 mm.

Standard deviations of angle measurement 1.5 mgon in respect to possible movement or vibration of targets (owing to wind) and determination accuracy of parameter D $\sigma_D = 0.5$ mm were used for accuracy analysis.

Accuracy of Determination of Height Shifts with Unknown D

This calculation comes from formula (24), where distance D is replaced by the function expressed by formula (11). The function for the calculation is:

$$\Delta H_{i,j} = H_j - H_i = f \left(\begin{matrix} s_{1i}, s_{1j}, s_{2i}, s_{2j}, z_{1i}, z_{1j}, z_{2i}, z_{2j}, \\ \varphi_{1i}, \varphi_{1j}, \varphi_{2i}, \varphi_{2j}, L \end{matrix} \right) \quad (37)$$

Standard deviation of the height shift $\Delta H_{i,j}$:

$$\sigma_{\Delta H_{i,j}} = \sqrt{\begin{matrix} \left(\frac{\partial \Delta H_{i,j}}{\partial s_{1j}} \cdot \sigma_{s_{1j}}\right)^2 + \left(\frac{\partial \Delta H_{i,j}}{\partial s_{1i}} \cdot \sigma_{s_{1i}}\right)^2 + \left(\frac{\partial \Delta H_{i,j}}{\partial s_{2j}} \cdot \sigma_{s_{2j}}\right)^2 + \\ + \left(\frac{\partial \Delta H_{i,j}}{\partial s_{2i}} \cdot \sigma_{s_{2i}}\right)^2 + \left(\frac{\partial \Delta H_{i,j}}{\partial z_{1j}} \cdot \sigma_{z_{1j}}\right)^2 + \left(\frac{\partial \Delta H_{i,j}}{\partial z_{1i}} \cdot \sigma_{z_{1i}}\right)^2 + \\ + \left(\frac{\partial \Delta H_{i,j}}{\partial z_{2j}} \cdot \sigma_{z_{2j}}\right)^2 + \left(\frac{\partial \Delta H_{i,j}}{\partial z_{2i}} \cdot \sigma_{z_{2i}}\right)^2 + \left(\frac{\partial \Delta H_{i,j}}{\partial \varphi_{1j}} \cdot \sigma_{\varphi_{1j}}\right)^2 + \\ + \left(\frac{\partial \Delta H_{i,j}}{\partial \varphi_{1i}} \cdot \sigma_{\varphi_{1i}}\right)^2 + \left(\frac{\partial \Delta H_{i,j}}{\partial \varphi_{2j}} \cdot \sigma_{\varphi_{2j}}\right)^2 + \left(\frac{\partial \Delta H_{i,j}}{\partial \varphi_{2i}} \cdot \sigma_{\varphi_{2i}}\right)^2 + \\ + \left(\frac{\partial \Delta H_{i,j}}{\partial L} \cdot \sigma_L\right)^2 \end{matrix}} \quad (38)$$

Standard deviations of length measurement can be taken for the same (σ_s), as well as standard deviations of the zenith angle and horizontal direction (σ_z , σ_φ) measurements. The formula can be simplified in this way:

$$\sigma_{\Delta H_{i,j}} = \sqrt{\left(\left(\frac{\partial \Delta H_{i,j}}{\partial s_{1j}} \right)^2 + \left(\frac{\partial \Delta H_{i,j}}{\partial s_{1i}} \right)^2 + \left(\frac{\partial \Delta H_{i,j}}{\partial s_{2j}} \right)^2 + \left(\frac{\partial \Delta H_{i,j}}{\partial s_{2i}} \right)^2 \right) \cdot \sigma_s^2 + \left(\left(\frac{\partial \Delta H_{i,j}}{\partial z_{1j}} \right)^2 + \left(\frac{\partial \Delta H_{i,j}}{\partial z_{1i}} \right)^2 + \left(\frac{\partial \Delta H_{i,j}}{\partial z_{2j}} \right)^2 + \left(\frac{\partial \Delta H_{i,j}}{\partial z_{2i}} \right)^2 \right) \cdot \sigma_z^2 + \left(\left(\frac{\partial \Delta H_{i,j}}{\partial \varphi_{1j}} \right)^2 + \left(\frac{\partial \Delta H_{i,j}}{\partial \varphi_{1i}} \right)^2 + \left(\frac{\partial \Delta H_{i,j}}{\partial \varphi_{2j}} \right)^2 + \left(\frac{\partial \Delta H_{i,j}}{\partial \varphi_{2i}} \right)^2 \right) \cdot \sigma_\varphi^2 + \left(\frac{\partial \Delta H_{i,j}}{\partial L} \right)^2 \cdot \sigma_L^2} \quad (39)$$

The individual terms do not have to be stated, they can be acquired by simple differentiation and or we can eventually calculate the derivations numerically. Standard deviation is determined from this analysis in explored cases, i.e. for points in distance 28 m and 35 m, lower than 1 mm (measurement accuracy is the same as in the previous analysis, i.e. standard deviation of the horizontal direction and zenith angle measurement $\sigma_z = \sigma_\varphi = 1.5$ mgon, standard deviations of the determined height shift are 0.8 mm for 35 m, 0.6 mm for 28 m, starting the zenith angle on the upper target 95 gon, maximum shift 0.5 m).

Numerical Model of the trajectory of Beam of Rays through Optical Environment

The nonlinear course of the trajectory of a beam of rays of electromagnetic radiation is one of the basic influences restricting accuracy during optical measurements. Fermat's principle [14] is valid for the spread of electromagnetic radiation in the given environment.

$$\delta \int_A^C n(x, y, z) dl = 0 \quad (40)$$

where n is the refraction index of a trajectory of ray between points A and C. A rule precedes the spread of rays between points A, C on a trajectory that the first variance of the optical trajectory is equal to zero. It would be necessary to know the refraction index of the air in the environment around the trajectory of the ray for a set of real trajectories. The refraction index of the air can be determined on the basis of temperature, pressure, air humidity and eventually CO₂ content, which is not technically possible with sufficient accuracy and density in a real environment, because too many incalculable influences are involved for example wind gust, which measuring sensors monitor with considerable delay. Therefore we chose not to try to directly model the immediate influences on measurement, but to model the worst situation that can arise and thus to determine the maximum possible influence on the measurement with a statement that the accuracy of the results comprise of other errors and also systematic errors.

An original numerical method of the calculation of the trajectory of a ray through the atmosphere from a point of height was developed for the calculation of influence. This method is based on Snell's law [14], which describes the process on the interface of two different optical environments.

$$n_1 \cdot \sin(\alpha) = n_2 \cdot \sin(\beta) \quad (41)$$

where n_1, n_2 are indices of refraction and α, β are angles of incidence (from perpendicular), according to Fig. 5.12.

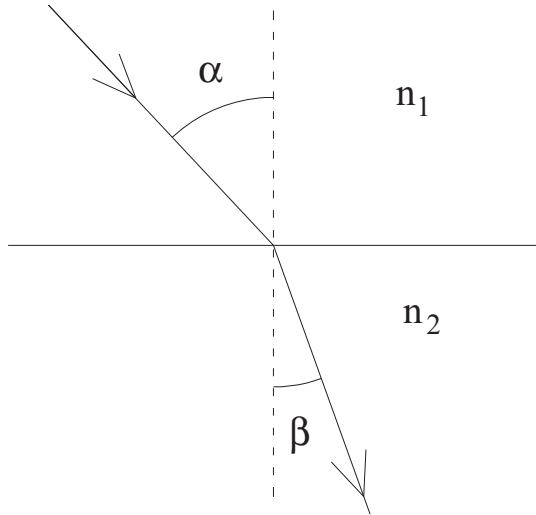


Fig. 5.12 – Snell's law

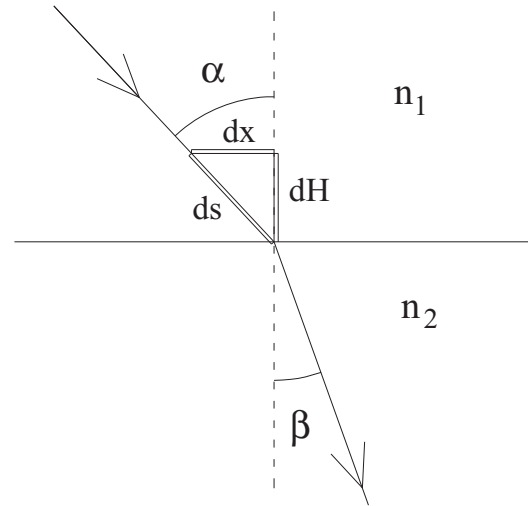


Fig. 5.13 – Snell's law in differential form

The atmosphere can be divided into differential layers and the layers for individual interfaces with different refractive index n and calculate trajectory of a beam of rays can be taken through the atmosphere one single differential step after another. With respect to this fact, it is necessary to modify Snell's law into differential form:

$$n_1 \cdot \frac{dx_1}{ds_1} = n_2 \cdot \frac{dx_2}{ds_2} \quad (42)$$

The situation is schematically illustrated in Fig. 5.13; dH is the differential change of height, dx the differential horizontal shift and ds the differential trajectory element.

The relationship of differential elements also results from Fig. 5.13

$$ds^2 = dx^2 + dH^2 \quad (43)$$

The refractive index of air can be according to [15] determined for example by means of the Barrell – Sears' formula with a correction from the influence of temperature and pressure determined by Kohlrausch.

$$N(\lambda) = 287,604 + \frac{1,6288}{\lambda^2} + \frac{0,0136}{\lambda^4} \quad (44)$$

$$n(\lambda, t, p, h) = 1 + \left(\frac{N(\lambda)}{1 + \frac{t}{273,15}} \cdot \frac{p}{101325} - \frac{5,5 \cdot 10^{-2}}{1 + \frac{t}{273,15}} \cdot \frac{h}{133,322} \right) \cdot 10^{-6} \quad (45)$$

where

- λ wave length of electromagnetic radiation in μm ,
- t air temperature in $^\circ\text{C}$,
- p air pressure in Pa,
- h partial pressure of water vapours in Pa.

The biggest influence of the refraction index is temperature, from which extreme values are expected during the experiment; air pressure and humidity can be taken for normal for purposes of the simulation.

For purposes of calculation, it is further necessary to modify Snell's law in a differential form into a form suitable for the calculation of direction of a ray spread behind the interface on the basis of knowledge of the refraction index in front of and behind the interface (n_1, n_2) and the direction of the ray spread in front of the interface dx_1/ds_1 .

$$\frac{dx_2}{ds_2} = \frac{dx_1}{ds_1} \cdot \frac{n_1}{n_2} \quad (46)$$

The following presumptions were chosen for numerical simulation:

1. Air temperature t changes linearly with height H . (The worst possible model, because the temperature will probably fall with height more rapidly than linearly.)
2. Temperature of the construction surface according to preliminary calculations is supposed to be at the most 120 °C.
3. Air temperature 4 metres above the construction will be the same as in the environment, i.e. approximately $t_0 = 15$ °C.
4. Distribution of temperatures on the trajectory from the instrument above the border of the construction will be taken for homogenous, i.e. the spread of rays will be taken for linear.
5. The horizontal distance through the non-homogenous environment to the most distant point is 13,5 m (it implies from size of the object and layout of points).
6. The height of the target is 3 m above the construction, zenith angle of the ray at entry into the non-homogenous environment is $z_0 = 95$ gon and the height above the object is 2m.
7. The wave length of radiation source for automatic targeting of the instrument is 870 nm, wave length for optical observations with a meter is 555 nm.

The situation is illustrated in Fig. 5.14.

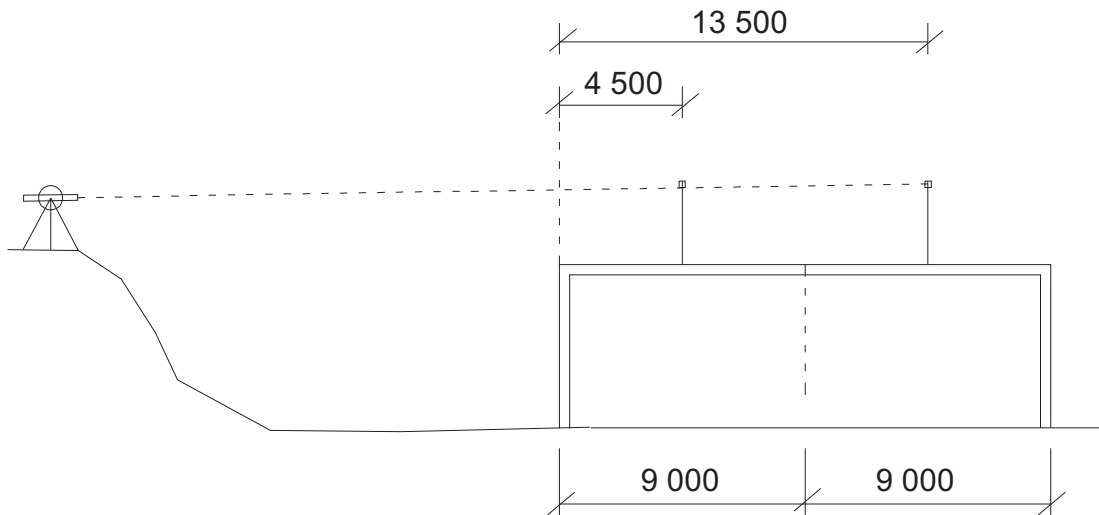


Fig. 5.14 – Supposed situation of measurement

The form of the function for the calculation of temperature:

$$t(H) = a + b \cdot H \quad (47)$$

Calculation step Δx is chosen for the calculation and it will be calculated in the first step:

$$\frac{dx_0}{ds_0} = \sin(z_0) \quad (48)$$

We can then calculate in the relevant number of steps so as to reach the total distance of 13.5m.

$$n_1 = n\left(\lambda, t\left(H - \frac{dH}{2}\right), p, h\right) \quad (49)$$

$$n_2 = n\left(\lambda, t\left(H + \frac{dH}{2}\right), p, h\right) \quad (50)$$

$$\frac{dx_2}{ds_2} = \frac{dx_1}{ds_1} \cdot \frac{n_1}{n_2} \quad (51)$$

$$X_i = X_{i-1} + \Delta x \quad (52)$$

$$dH_i = \sqrt{\left(\Delta x \cdot \frac{ds_i}{dx_i}\right)^2 - \Delta x^2} \quad (53)$$

$$H_i = H_{i-1} + dH_i \quad (54)$$

For chosen steps $\Delta x = 0.1\text{m}; 0.01\text{ m}; 0.001\text{ m}$ the results differed at most by 0.01 mm. The height of the point for the stated values differs in comparison with the linear propagation of the rays by 1.74 mm for automatic targeting (wave length 870 nm) and by 1.76 mm for targeting with a meter (wave length 555 nm). The influence of the refraction shows very little especially with respect to the short transit length through the non-homogenous environment; the temperature gradient is very high. Error during transit through an identical environment at a distance of 30 m was 9.25 mm; or 9.35 mm, at 100 m it was 161.22 mm, or 163.05 mm.

Beside this model, which seems to be very intuitive, we can use a differential equation of wave front transit through a non-homogenous environment for the calculation (the model will be further called DRPV), which is stated and derived e.g. in [16] and used in [17] :

$$\frac{d^2 r}{dt^2} = n(r) \cdot \nabla n(r) = f(r) \quad (55)$$

where

$$r = \begin{pmatrix} x \\ y \\ z \end{pmatrix}, n(r) = n(x, y, z), \nabla n(r) = \begin{pmatrix} dn(r)/dx \\ dn(r)/dy \\ dn(r)/dz \end{pmatrix} \quad (56)$$

r is the radius vector of a trajectory point, n is the refraction index expressed by the model (as in the previous case), ∇ is Hamilton operator and dt the trajectory element. So as to clarify significance derivations it is suitable to introduce indication:

$$u = \frac{dr}{dt}, \frac{du}{dt} = \frac{d^2 r}{dt^2} \quad (57)$$

U is here the direction of the wave front movement (tangent line to movement curve) and du/dt is the differential change of this direction. Initial conditions are position (coordinate) and the initial direction of the wave front propagation, or beam of rays. The second-rate differential equation determined in this way can be solved numerically; the simplest way is Euler's method. When using a computer we can choose a sufficiently small step for the

solution. The equation will be transformed to two differential first-rate equations, which are solved simultaneously in the steps with chosen size Δt . The form of the equations is:

$$\frac{du}{dt} = f(r) \quad (58)$$

$$\frac{dr}{dt} = u \quad (59)$$

Initial conditions:

$$u = u_0 \quad (60)$$

$$r = r_0 \quad (61)$$

Calculation:

$$dr_{i+1} = u_i \cdot \Delta t \quad (62)$$

$$r_{i+1} = r_i + dr_{i+1} \quad (63)$$

$$du_{i+1} = f(r_{i+1}) \cdot \Delta t \quad (64)$$

$$u_{i+1} = u_i + du_{i+1} \quad (65)$$

This calculation gives practically the same results as the previous calculations. The results of the two stated models are compared in different situations on different distances in the table stated below, together with a simplified model of Prof. Böhm according to [18].

$$\Delta H = 4,65 \cdot 10^{-7} \cdot s^2 \cdot \sin(z) \cdot \left(0,034 + \frac{dT}{dH}\right) \quad (66)$$

ΔH is the “apparent” shift of the target in the vertical direction, z is the zenith angle, dT/dH is the temperature gradient. The same values as in the previous calculation were used for non stated quantities.

The stated models can be simply evaluated in the following way: the model of Prof. Böhm is usable with sufficient accuracy on shorter distances and for small temperature gradients (as it is usual for current geodetic measurements). The other two models give practically the same results and they can be taken for exact in this respect. The only problem here is in case of propagation of the beam in a direction parallel to the temperature layers of the Snell model.

The result of the numerical modelling of the worst probable situation is a reasoned presumption that the influence of the vertical component of the refraction does not damage the measurement results with a greater systematic error of more than 2 mm.

Tab.5.1 A comparison of the results of various models (deviations from straight-line propagation, determined for normal pressure and humidity, distance 13.5 m) in mm

| dT/dH [°C/m] | 26.25 | 20.00 | 15.00 | 10.00 | 5.00 | 2.00 | 1.00 |
|--------------|-------|-------|-------|-------|------|------|------|
| Böhm | 2.2 | 1.7 | 1.3 | 0.8 | 0.4 | 0.2 | 0.1 |
| Snell | 1.8 | 1.4 | 1.1 | 0.8 | 0.4 | 0.2 | 0.1 |
| DRPV | 1.8 | 1.4 | 1.1 | 0.8 | 0.4 | 0.2 | 0.1 |

The results of the numeric simulation of the influence of temperature division on the transit of a beam of rays through a non-homogenous atmosphere are stated in the following two tables.

Tab. 5.2 The comparison of the results of various models (deviations from straight-line propagation in mm, determined for normal pressure and humidity, temperature gradient 1°C/m) on distance D in mm

| D [m] | 13.5 | 20.0 | 50.0 | 100.0 | 500.0 | 1000.0 | 2000.0 |
|-------|------|------|------|-------|-------|--------|--------|
| Böhm | 0.1 | 0.2 | 1.1 | 4.5 | 112.1 | 448.2 | 1792.8 |
| Snell | 0.1 | 0.2 | 1.2 | 4.9 | 131.6 | 587.8 | 3135.3 |
| DRPV | 0.1 | 0.2 | 1.2 | 4.9 | 131.7 | 588.1 | 3137.8 |

Tab. 5.3 Simulation of the influence of the distribution of temperatures on the zenith angle measurement (divergences in mm from straight-line, determined for normal pressure and humidity and $z = 95$ gon)

| dT/dH [°C/m] | 26.25 | 20.00 | 15.00 | 10.00 | 5.00 | 2.00 | 1.00 |
|-----------------|-------|-------|-------|-------|------|------|------|
| Distance [m] | | | | | | | |
| 10,0 | 1.0 | 0.8 | 0.6 | 0.4 | 0.2 | 0.1 | 0.05 |
| 13,5 | 1.8 | 1.4 | 1.1 | 0.8 | 0.4 | 0.2 | 0.10 |
| 20,0 | 4.0 | 3.3 | 2.5 | 1.8 | 0.9 | 0.4 | 0.20 |
| 30,0 | 9.4 | 7.5 | 5.8 | 4.0 | 2.1 | 0.9 | 0.44 |
| 50,0 | 28.8 | 22.4 | 17.1 | 11.6 | 6.0 | 2.4 | 1.22 |
| 100,0 | 163.1 | 113.4 | 80.5 | 51.4 | 24.9 | 9.8 | 4.89 |

5.2.10 Measuring Procedure and Calculations

The measurement was started with the timing advance at 12:25 for the verification of technology and measuring speed. The first two epochs were measured with maximum possible speed, the other epochs after five minutes. Ignition was carried out at 13:03, then the measurement went without problems up to the fifteenth stage (13:30), in the course of which white non-transparent smoke with a consistency of thick vapour started to spread from the construction, which made it impossible to measure rod 5 and all further measurements. Smoke was dispersed by sporadic gusts of wind only for short moments, which did not suffice even for the measurement of two targets of one rod. Individual measurement times are stated in Tab 5.4. Soon after 14:00, the maximum temperature of the wall construction surface (89 °C) was reached and shortly after that it $\frac{3}{4}$ of the construction collapsed.

With respect to significant changes of the optical environment through which the aiming curve passed; significant variations of parameter D during the measurement occurred. In terms of the difference of heights these changes are not essential with respect to the required accuracy (as it results from numerical modelling stated in paragraph 0), but owing to their influence it would lead to inconsistent processing of the measurement and the determined tilts of the rods would not be correct. For these reasons we used a variation of the calculation with unknown parameter D . Values D calculated in individual measuring stages are stated in Tab 5.4.

Tab. 5.4 Parameter D in the individual epochs

| Epoch | Time / [H:min] | D [m] | | | | | |
|-------|-------------------|---------|--------|--------|--------|--------|--------|
| | | 1. | 2. | 3. | 4. | 5. | 6. |
| 1. | 12:25 | 0.5039 | 0.5021 | 0.5050 | 0.5026 | 0.7494 | 0.7477 |
| 2. | 12:27 | 0.5035 | 0.5024 | 0.5046 | 0.5016 | 0.7481 | 0.7479 |
| 3. | 12:30 | 0.5037 | 0.5021 | 0.5048 | 0.5022 | 0.7488 | 0.7478 |
| 4. | 12:35 | 0.5037 | 0.5022 | 0.5049 | 0.5017 | 0.7487 | 0.7479 |
| 5. | 12:40 | 0.5044 | 0.5020 | 0.5044 | 0.5017 | 0.7492 | 0.7475 |
| 6. | 12:45 | 0.5043 | 0.5017 | 0.5046 | 0.5018 | 0.7494 | 0.7473 |
| 7. | 12:50 | 0.5033 | 0.5015 | 0.5045 | 0.5012 | 0.7502 | 0.7478 |
| 8. | 12:55 | 0.5035 | 0.5020 | 0.5046 | 0.5015 | 0.7497 | 0.7476 |
| 9. | 13:00 | 0.5036 | 0.5021 | 0.5045 | 0.5009 | 0.7494 | 0.7478 |
| 10. | 13:05 | 0.5041 | 0.5029 | 0.5059 | 0.5027 | 0.7495 | 0.7482 |
| 11. | 13:10 | 0.5083 | 0.5048 | 0.5064 | 0.5041 | 0.7494 | 0.7481 |
| 12. | 13:15 | 0.5057 | 0.5032 | 0.5062 | 0.5027 | 0.7499 | 0.7477 |
| 13. | 13:20 | 0.5090 | 0.5086 | 0.5102 | 0.5046 | 0.7506 | 0.7478 |
| 14. | 13:25 | 0.5074 | 0.5049 | 0.5107 | 0.5072 | 0.7519 | 0.7488 |
| 15. | 13:30 | 0.5092 | 0.5074 | 0.5077 | 0.5027 | 0.6928 | 0.7573 |

5.2.11 Accuracy Analyses after Measurement

The first 9 stages were measured for testing technology on the spot, but also for determining inner accuracy. The following tables summarize the standard deviations calculated from the repetition on the current terms of measurement, without the influence of temperature changes caused by fire.

Tab. 5.5 contains the standard deviations of measured directions, zenith angles and oblique lengths. Each rod is equipped with two targets, standard deviations are determined for each target. Sampling the standard deviations characterizing all accomplished measurements of the given quantity are stated in the last line. The results of the accuracy analysis confirm suitably chosen standard deviations used during a priori accuracy analysis.

The change of height of the individual points ΔH was repeatedly determined. Sampling the standard deviations for the individual rods are stated in Tab 5.6, the result also complies with a priori accuracy analysis. Mean sampling the standard deviation for nine repetitions ought to be 1.5 times more than the standard deviation from a priori analysis.

Tab. 5.5 Standard deviations of the measured values

| Rod | point | s_z [mgon] | s_ϕ [mgon] | s_s [m] |
|------|-------|--------------|-----------------|-----------|
| 1 | 1 | 1.30 | 0.94 | 0.5 |
| | 2 | 0.99 | 1.10 | 0.7 |
| 2 | 3 | 0.86 | 1.24 | 0.4 |
| | 4 | 1.37 | 1.55 | 0.7 |
| 3 | 5 | 1.52 | 1.90 | 0.5 |
| | 6 | 1.70 | 1.13 | 0.3 |
| 4 | 7 | 1.53 | 0.73 | 0.2 |
| | 8 | 1.65 | 1.00 | 0.2 |
| 5 | 9 | 1.18 | 1.12 | 0.2 |
| | 10 | 0.83 | 1.07 | 0.3 |
| 6 | 11 | 0.66 | 1.42 | 0.6 |
| | 12 | 0.85 | 0.83 | 0.6 |
| Mean | | 1.25 | 1.21 | 0.5 |

Tab. 5.6 Sampling the standard deviations of determination of height shifts

| Rod | $s_{\Delta H}$ / mm |
|------|---------------------|
| 1 | 0.57 |
| 2 | 0.38 |
| 3 | 0.60 |
| 4 | 0.62 |
| 5 | 0.68 |
| 6 | 0.34 |
| Mean | 0.55 |

The mean sampling of the standard deviation describes a non-homogenous file of measurements on variously distant points; it provides a total image of accuracy. After the accuracy analysis it is possible to state on the whole that the results of the measurement analysis comply with a priori accuracy analysis.

5.2.12 Measurement results and their evaluation

Determined height shifts are stated in Tab. 5.7. They are graphically illustrated in Fig. 5.15.

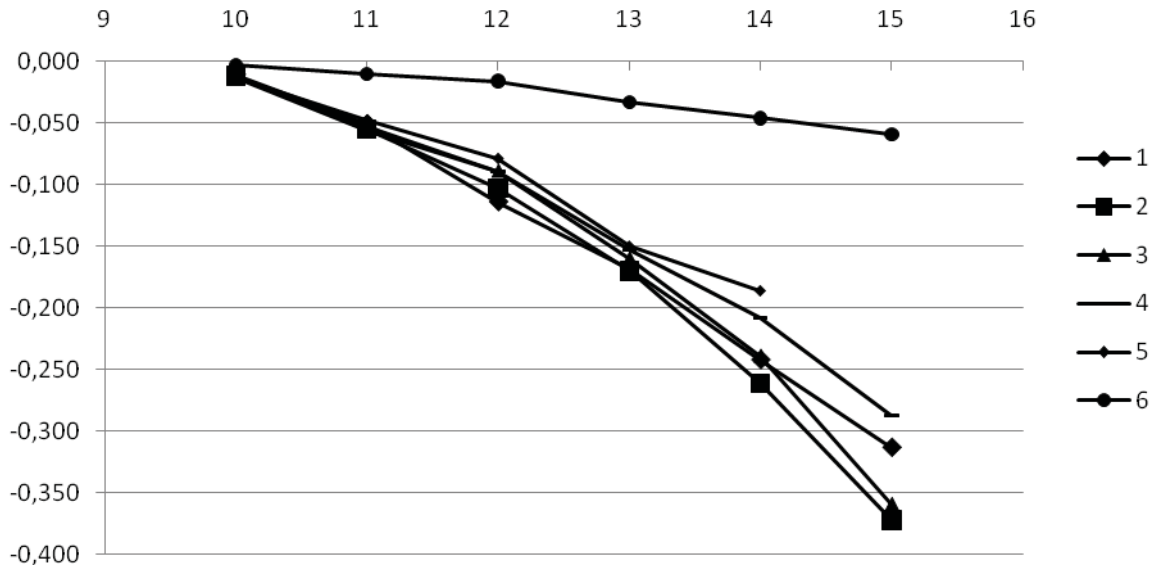


Fig. 5.15 - Graph of vertical shifts

Tab. 5.7 Height shifts on observed points

| Epoch | Time [H:min] | ΔH [m] | | | | | |
|-------|-----------------|----------------|--------|--------|--------|--------|--------|
| | | 1. | 2. | 3. | 4. | 5. | 6. |
| 1. | 12:25 | 0.000 | 0.000 | 0.000 | 0.000 | 0.000 | 0.000 |
| 2. | 12:27 | -0.002 | -0.000 | -0.001 | -0.001 | -0.001 | 0.001 |
| 3. | 12:30 | -0.001 | -0.000 | -0.000 | 0.000 | 0.000 | 0.000 |
| 4. | 12:35 | -0.000 | -0.000 | -0.000 | -0.000 | -0.000 | 0.000 |
| 5. | 12:40 | 0.000 | -0.000 | -0.000 | 0.000 | 0.001 | 0.001 |
| 6. | 12:45 | -0.000 | -0.000 | 0.000 | 0.001 | 0.001 | 0.001 |
| 7. | 12:50 | -0.001 | 0.001 | 0.001 | 0.001 | 0.001 | 0.001 |
| 8. | 12:55 | -0.000 | 0.000 | 0.001 | -0.000 | 0.001 | 0.000 |
| 9. | 13:00 | -0.001 | -0.001 | -0.001 | -0.001 | -0.000 | 0.000 |
| 10. | 13:05 | -0.011 | -0.012 | -0.012 | -0.013 | -0.013 | -0.003 |
| 11. | 13:10 | -0.051 | -0.055 | -0.053 | -0.056 | -0.048 | -0.010 |
| 12. | 13:15 | -0.114 | -0.103 | -0.089 | -0.089 | -0.079 | -0.016 |
| 13. | 13:20 | -0.168 | -0.170 | -0.160 | -0.153 | -0.150 | -0.033 |
| 14. | 13:25 | -0.242 | -0.261 | -0.239 | -0.208 | -0.186 | -0.046 |
| 15. | 13:30 | -0.313 | -0.372 | -0.359 | -0.287 | - | -0.059 |

Sign “-“ in Tab. 5.7 means that the measurements weren't performed with respect to poor visibility.

The further stated graphs are more illustrative; they show the declines of points in the front (Fig. 5.8, points 1 - 4) and back profile (Fig. 5.98, points 5 - 6). The graphs obviously show an almost linear course of decline in time.

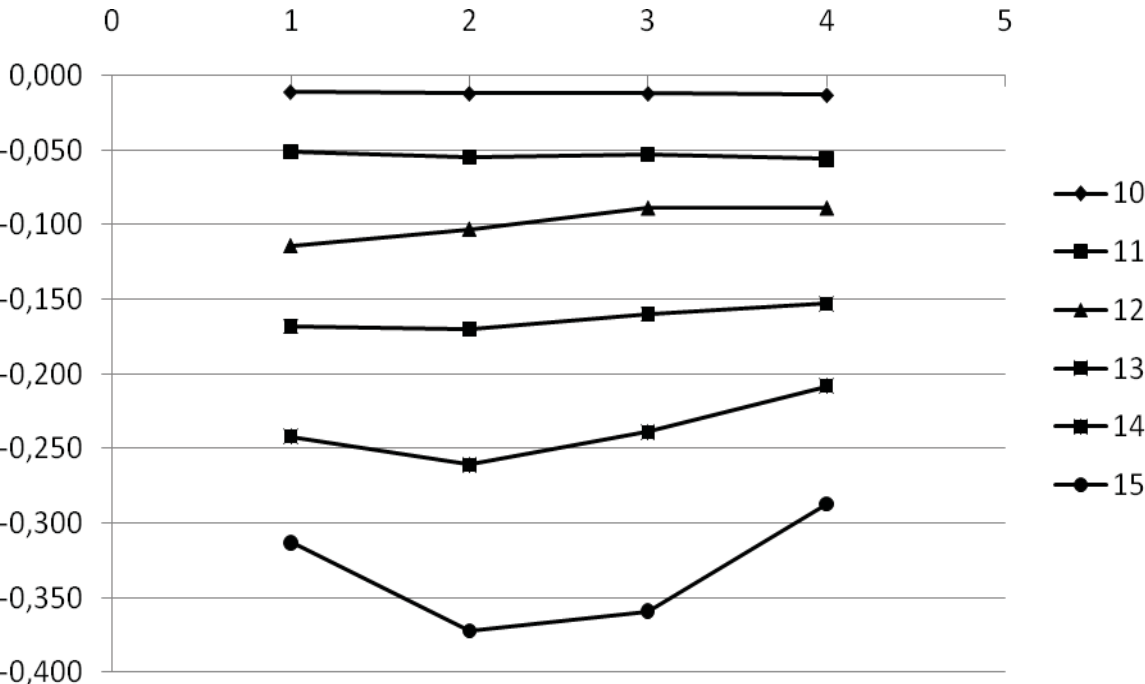


Fig. 5.16 - Graph of movement of points 1 – 4 in epochs 10 to 15

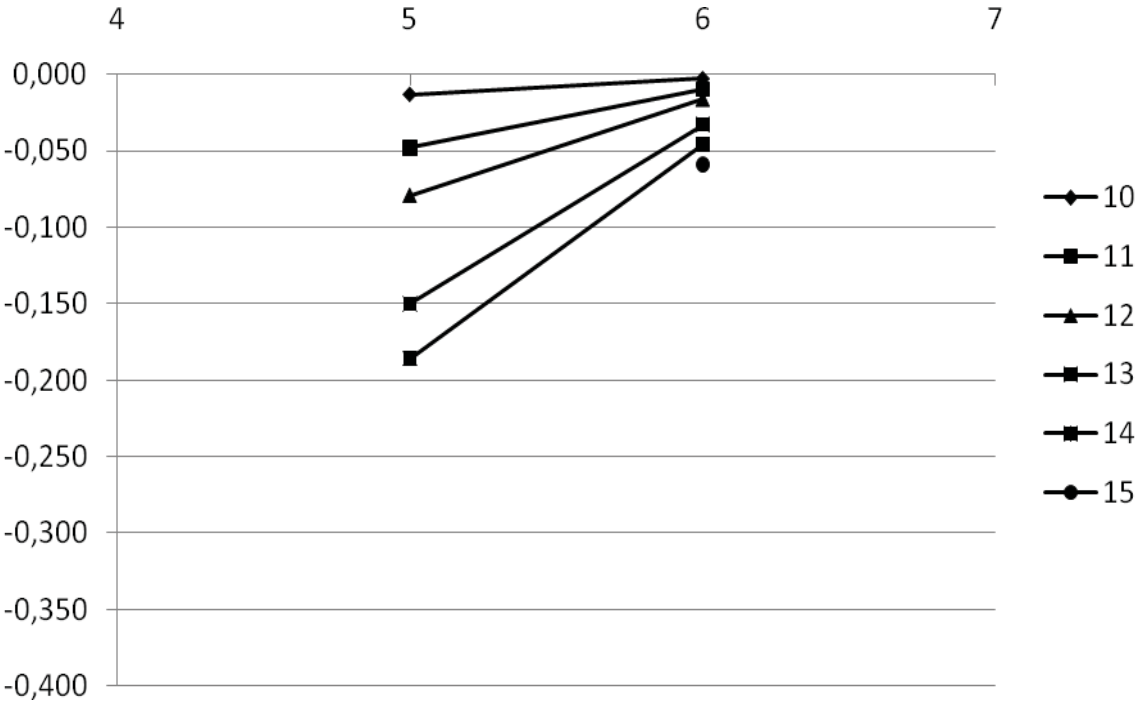


Fig. 5.17 - Graph of movement of points 5 – 6 in epochs 10 to 15

5.2.13 Conclusion of Trigonometric Measurement

For a period when it was possible to carry out optical measurement, i.e. 30 min after the ignition of the fire, the measurements worked according to plan and from the accuracy analysis carried out after the measurements; it implies that it corresponds to a priori analyses and accuracy derived in them. A great unknown quantity is the influence of refraction, which is as a variable and exactly incalculable influence and limiting factor, its maximum influence on short distance in this case was estimated by means of numeric modelling less than 2 mm. The results of the analysis after the measurements describe a situation practically without this influence, because of changes in temperature and therefore a rapid increase of the temperature gradient only after ignition.

The usability of the measuring and evaluation procedure was proved beside this limitation resulting in vertical shifts which can be monitored with high accuracy.

5.3 Laser scanning

The laser scanning method was used in two of the three stages of the geodetic works carried out in connection with the fire test in Mokrsko. In the first stage the whole interior of the object was scanned approximately 14 days before fire, when all the construction work of the object had been finished, but other elements necessary for the execution of the fire test had not been installed. The second stage was the measurement of the construction after the fire test. This scanning took place approximately one week after the fire, when the construction cooled down and when there was minimum danger of its collapse.

5.3.1 3D laser scanning principle

The basic principle of activity of the scanner is the base polar method, see Fig. 5.18. It is necessary to know the length of the d radius vector (measured length) and lengths ζ , ω to determine the coordinates of point P . Angles are gained for example from positions of the mirrors that deflect the laser beam and the length is gained for example with a scanner impulse distance meter in a synchronized way with the position of the mirrors, see [19].

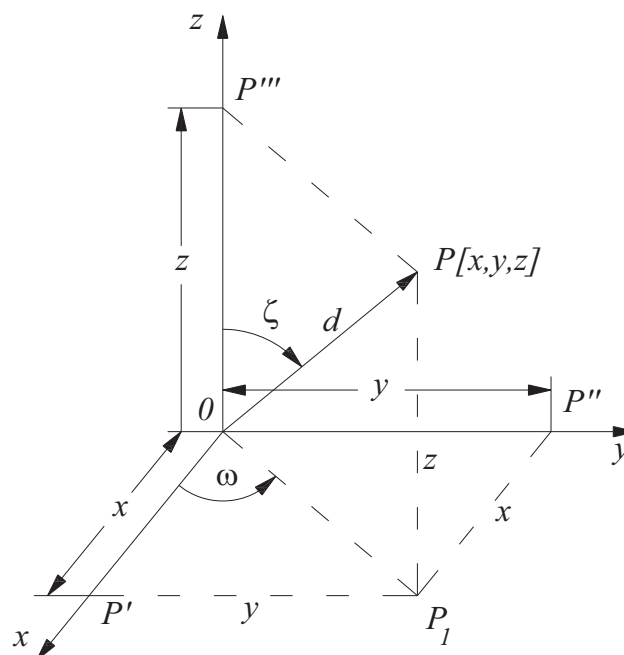


Fig. 5.18 - Schematic illustration of the space polar method

Electronic distance meters used in the scanning systems are divided according to the measuring principle in impulse electronic distance meters and phase distance meters.

An impulse distance meter is based on transit time measurement, which an electromagnetic impulse needs so that double the measured length can go through. A distance meter transmitter sends out an impulse that starts an electronic time measurement. An impulse reflects from the reflection system and falls on the distance meter receiver, by which it terminates the time measurement. It is possible to determine double of the measured distance from a known speed of impulse propagation through the atmosphere. As the speed of propagation of electromagnetic waves is approximately $3 \cdot 10^8 \text{ m.s}^{-1}$, transit time is low, for example the transit time for length 30 m is $0.2 \mu\text{s}$ ($2 \cdot 10^{-7} \text{ s}$), that is why high requirements are imposed on accuracy of transit time measurements.

A phase distance meter is based on phase difference measurement, which arises between a sent and received signal. A phase distance meter sends out modulated waves with a certain phase φ_v and reflected waves with phase φ_o come back from the object. Then the measured length is determined from the phase difference. It results from the principle that the wave has to be longer than the measured distance, because otherwise it is not possible to determine the number of complete waves. This reduces the range on the length of the modulated wave for scanners using phase distance meters.

Instrument measurement errors are length measurement errors, measurement errors of zenith and horizontal angles, random components of which are described by standard deviations. Beside standard errors, the scanner is influenced by several systematic errors, the origin of which is directly dependent on the scanner's principle. Several analogical eccentricities to axis theodolite errors can be classed among these errors. Other systematic errors are systematic errors of length measurement and systematic errors of angle measurement, influence of synchronization of length and angle measurement has also a systematic character with variable size. These influences can be suppressed by calibrating the system and cannot be suppressed by the measuring procedure. Axis errors can have relatively great influence, there is however no scanner enabling removal of these errors by measuring in two positions.

Considering the fact that the prevailing part of laser scanning systems uses the space polar method to determine the location of a point, it is suitable to state here that error analysis of the determination of coordinates and location of a point. The equation for calculating coordinates x, y, z :

$$x = d \cdot \cos(\omega) \cdot \sin(\zeta) \quad (67)$$

$$y = d \cdot \sin(\omega) \cdot \sin(\zeta) \quad (68)$$

$$z = d \cdot \cos(\zeta) \quad (69)$$

with measured variables d (slant distance), ω (horizontal angle), ζ (zenith angle). The situation is illustrated in Fig. 5.18. The derived equations are valid for the system of coordinated defined by the scanner, which can be generally recorded and placed in space. If levelling of the instrument is carried out, it is only the shift and rotation of the system around z-axis.

The relations for real errors ε , according to [20], are stated below, real angle errors and standard deviations of angles are stated in arc measure (radians).

$$\varepsilon_x = \cos(\omega) \cdot \sin(\zeta) \cdot \varepsilon_d - d \cdot \sin(\omega) \cdot \sin(\zeta) \cdot \varepsilon_\omega + d \cdot \cos(\omega) \cdot \cos(\zeta) \cdot \varepsilon_\zeta \quad (70)$$

$$\varepsilon_y = \sin(\omega) \cdot \sin(\zeta) \cdot \varepsilon_d + d \cdot \cos(\omega) \cdot \sin(\zeta) \cdot \varepsilon_\omega + d \cdot \sin(\omega) \cdot \cos(\zeta) \cdot \varepsilon_\zeta \quad (71)$$

$$\varepsilon_z = \cos(\zeta) \cdot \varepsilon_d - d \cdot \sin(\zeta) \cdot \varepsilon_\zeta \quad (72)$$

If the standard deviations of the measured quantities σ_d , σ_ω , σ_ζ , are known, formulae for the calculation of the standard deviations of the coordinates of a point determined in this way calculated according to [12] can be derived according to the law of standard deviation propagation.

$$\sigma_x^2 = \left(\begin{array}{l} \cos^2(\omega) \cdot \sin^2(\zeta) \cdot \sigma_d^2 + d^2 \cdot \sin^2(\omega) \cdot \sin^2(\zeta) \cdot \sigma_\omega^2 + \\ + d^2 \cdot \cos^2(\omega) \cdot \cos^2(\zeta) \cdot \sigma_\zeta^2 \end{array} \right) \quad (73)$$

$$\sigma_y^2 = \left(\begin{array}{l} \sin^2(\omega) \cdot \sin^2(\zeta) \cdot \sigma_d^2 + d^2 \cdot \cos^2(\omega) \cdot \sin^2(\zeta) \cdot \sigma_\omega^2 + \\ + d^2 \cdot \sin^2(\omega) \cdot \cos^2(\zeta) \cdot \sigma_\zeta^2 \end{array} \right) \quad (74)$$

$$\sigma_z^2 = \cos^2(\zeta) \cdot \sigma_d^2 + d^2 \cdot \sin^2(\zeta) \cdot \sigma_\zeta^2 \quad (75)$$

The stated equations describe the influence of random errors of the measured quantities on the standard deviations of the determined coordinates.

So as to be able to determine the standard deviation in the position of point σ_P , i.e. characteristic describing size of distance of the measured point from its correct position, it is necessary to determine the equation for the real error of location of point ε_P .

$$\varepsilon_P = \sqrt{\varepsilon_x^2 + \varepsilon_y^2 + \varepsilon_z^2} \quad (76)$$

Then it is possible to derive the following equation using the law of standard deviation propagation:

$$\sigma_P^2 = \sigma_d^2 + d^2 \cdot \sin^2 \zeta \cdot \sigma_\omega^2 + d^2 \cdot \sigma_\zeta^2 \quad (77)$$

Mixed terms of real errors (covariances) were not neglected when deriving the equation; the formula will be simplified into the stated form by trivial arrangements.

5.3.2 Measurement

The first stage of the geodetic measurement, the zero stage, of the experimental object in Mokrsko took place on 5. 9. 2008. In the course of this measurement the interior of the building was completely scanned. The strongest emphasis was placed on the measurement of the ceiling and the wall constructions. The interior space was measured from four standpoints, the location of which is illustrated in the following scheme, see Fig. 5.19. Total measuring time was approximately 8 hours.

The standpoints were chosen near walls and corners of the objects so that it is possible to scan as much of the interior as possible from each standpoint using a spherical sector defining

scanning range with the smallest possible horizontal angle range, which contributed to a significant acceleration of measurement.

The second measurement of the examined object was carried out on 25. 9. 2008 (the first stage). This was scanning of the still standing constructions – approximately ½ of the wall constructions and ¼ of the ceiling constructions. The scanned territory in the figure is drawn in grey. The measurement was carried out from three standpoints and it took approximately 6 hours, see Fig. 5.20.

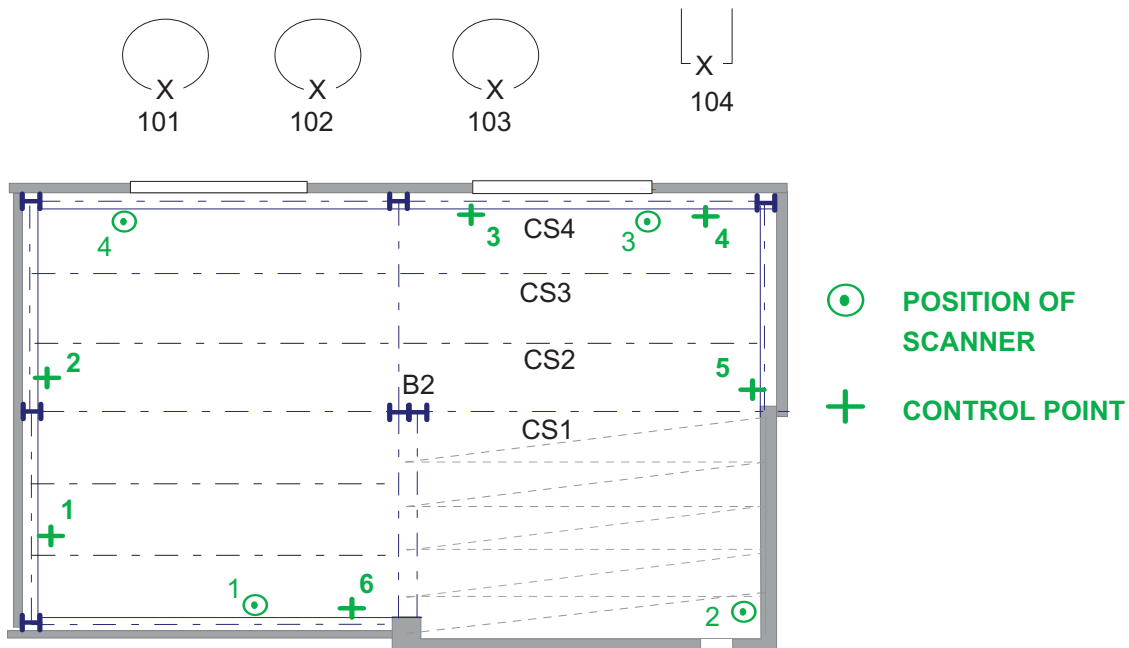


Fig. 5.19 - Position of scanner and control points scheme in zero stage

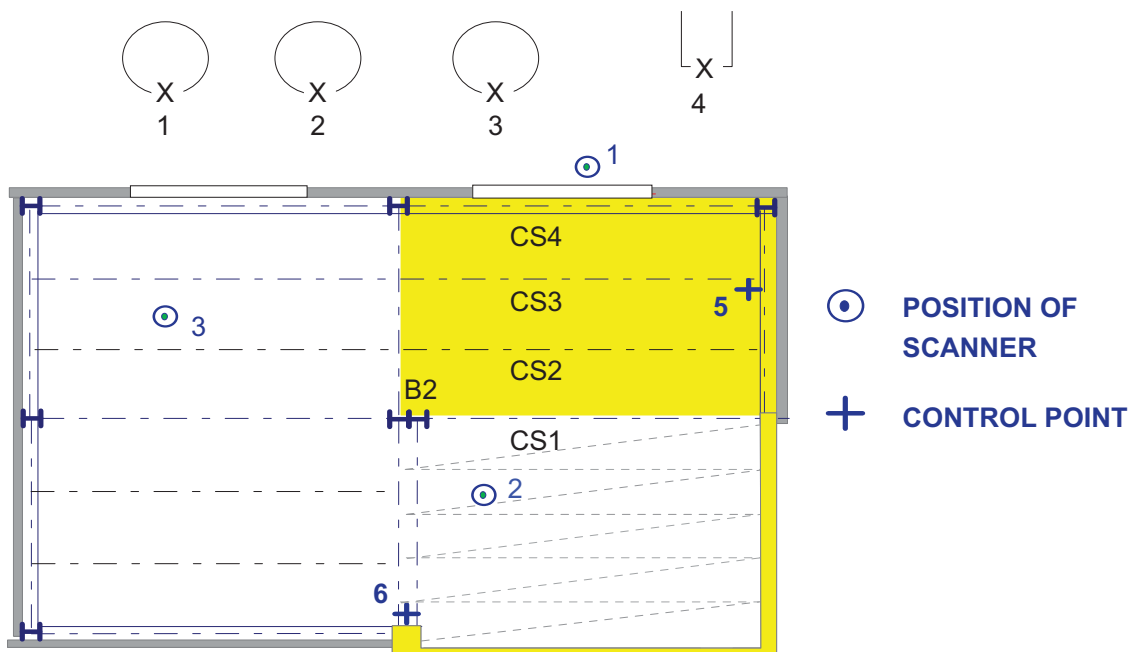


Fig. 5.20 - Scheme of placing the standpoints and the control points in first stage

Demands on placing the standpoints in the first stage were similar as in the zero stage, but their selection was significantly influenced by a large amount of rubble situated in the space of the object after the damage to the construction.

An important criterion for selecting the standpoints in both stages was the highest possible number of control points that were possible to measure from individual standpoints. The control points were signalized by means of plane HDS targets inside and outside the observed construction. Control points inside the object were stabilized temporarily, whereas control points outside the object were stabilized permanently. Inside and outside control points were used to create the whole cloud within one stage. Total clouds from the zero and the first stage were placed into one system of coordinates by means of outside control points.

5.3.3 Measurement on the standpoint

The scanning process on each standpoint can be divided into two parts:

- Scanning the scene, on the basis of the set parameters – scanning density, range of the scanned field of view
- Scanning control points, special scanning regimes with high scanning density, in the surroundings of the control point marked in the service software in the gained point cloud, the result is finding the centre of the control target

The operating period of the individual scanning parts was variable. It was influenced by the size of the measured territory and by the scanning density. The operating period was approximately 60 minutes for the mostly used scanning setting; one quarter of sphere. The second part of the scanning in the standpoint – measuring the control points – took approximately 30 min, but even this information is only approximate and it changed in dependence on a number of control points and on the speed of the localization of these points in the cloud. In some cases it was necessary to carry out some additional measurements of the nearest surroundings of the control point, so that it is possible to localize the target correctly, which caused an extension of the measuring period again.

5.3.4 Instrumentation

The HDS 3000 laser scanning system is an instrument produced by Leica Geosystems, see [21]. It is a scanning system based on the principle of the space polar method, see [22].

The scanner field of view is 360° in the horizontal direction and 270° the vertical direction. The measurement range is 134 m for reflectance 18%. The stated measuring accuracy values are 6 mm in the single point position, 4 mm in length measuring accuracy and angle accuracy in both directions is 60 micro-radians. These values are guaranteed by the manufacturer until 50 m. A pulse laser with which the scanner is equipped sends out radiation of green colour and is placed into safety class 3R according to IEC 60825-1. The size of the laser track for a distance of 50 m is smaller than 6 mm. The HDS 3000 is placed during measurement onto a strengthened geodetic tripod with a standard Leica tribrach. The scanning speed is up to 4000 points per second. The maximum number of points gained from one scan is 100 million. A digital camera is built in the scanner. Cyclone software is used for operating the scanner and processing the measured data.

5.3.5 Measurement processing

The first step of processing of the measured data was connecting (registration) the clouds from the individual standpoints and placing them into the selected system of coordinates. The

resulting system of coordinates was defined by the coordinates of the outside control points in the system of coordinates of the first standpoint of the zero stage. Registration was carried out for each stage separately in the Cyclone system. Tab. 5.8 shows details of the registrations in the individual stages.

Tab. 5.8 Information about registration

| | |
|--|--|
| Registration of measurements before fire | 4 standpoints 9 control points Average error: 0.9 mm |
| Registration of measurements after fire | 3 standpoints 6 control points Average error: 0.8 mm |

Checking the transformation accuracy of both stages was carried out by a comparison of an intersection of two planes, which arose by fitting point clouds measured on the concrete wall at the zero stage with a corresponding intersection in the first stage. The upper section of the intersections was compared for reasons of damage during fire. The difference in the position of the upper point of the intersections is 16 mm. The size of this difference is caused by damage during the fire (flaking of the walls reaches size up to 20 mm in the observed corner) and by error in transformation. The accuracy of the accomplished transformation was therefore taken for sufficient.

In the second step it was necessary to clean the resulting cloud from each stage from points that were not desirable for our needs, Fig. 5.21 and Fig. 5.22. The cleaned cloud was further segmented into parts from which we consequently separated the individual construction components for to determine their deformation after the fire. These components were the ceiling beams, the construction of the side walls and the central column. Evaluation of the deformation of processes and procedures of these construction components will be described in the following part.

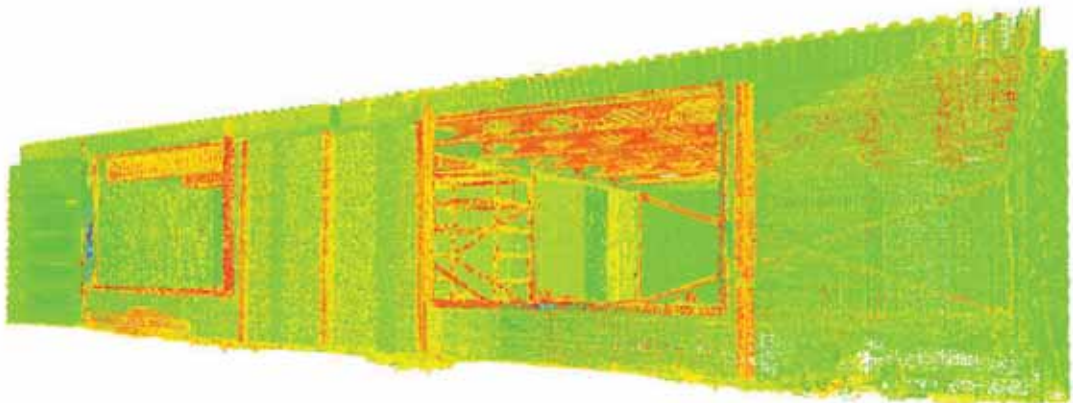


Fig. 5.21 - Final point cloud from the zero stage and its comparison with photo

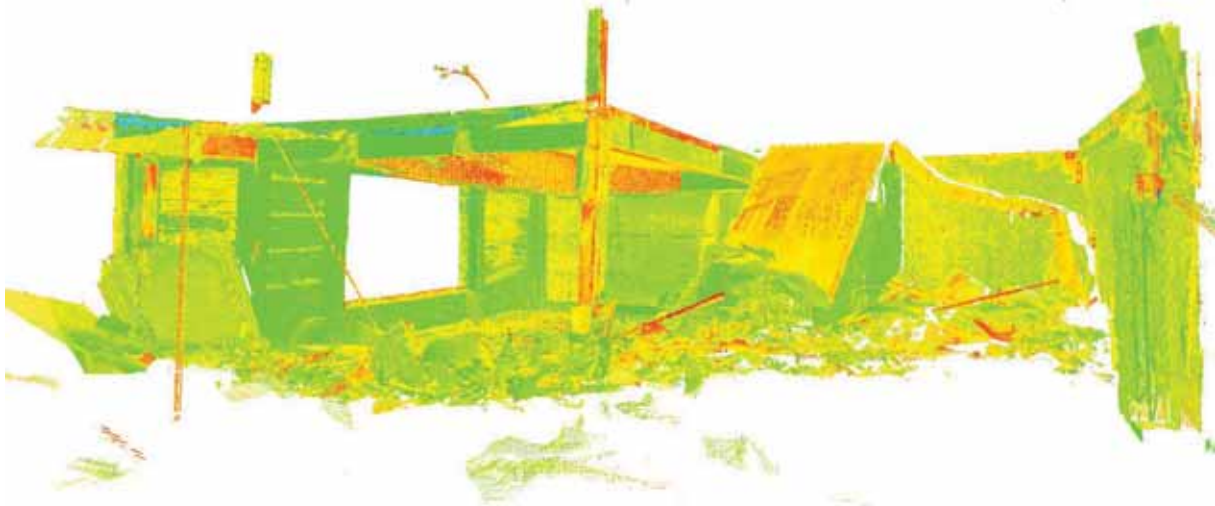


Fig. 5.22 - Final point cloud from the first stage and its comparison with photo

5.3.6 Processing and evaluation of the ceiling beams

We evaluated three ceiling beams, two beams with corrugated web CS2, CS3 and one beam from profile IPE, CS1, see Fig. 5.19. When evaluating beams we used the method of cross cuts [23]. The first step of this process was the insertion of the cleaned beams from both stages into one model, see Fig. 5.23. In this model we created a new system of coordinates that was related to one of the beams in the zero stage (to the beam with corrugated web CS2 calculated from the window). An X-axis was inserted into the longitudinal axis, a Y-axis was inserted upright to the X axis into the horizontal plane and a Z-axis was inserted into the vertical. Consequently we created cross sections upright to the horizontal axis with a step of 100 mm, by which we gained profiles of all the beams in both measuring stages, see Fig. 5.24. From these profiles we consequently subtracted the coordinates of the corner points of the individual beams. We determined the height and cross shifts (buckling) of the beams between the stages from the differences in the position of these points. These values were placed into

graphs in Fig. 5.25 to Fig. 5.35. The description of the beam corners in the individual graphs is taken from the view of an observer standing with his back towards the wall and having the window holes at his right hand.

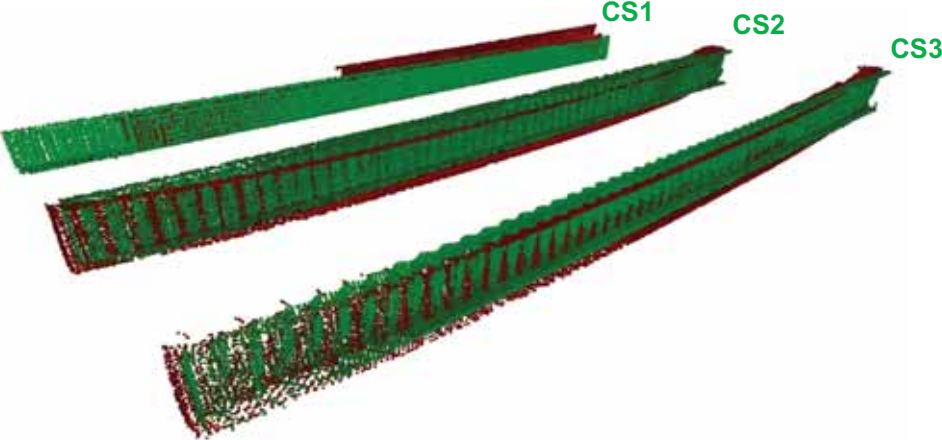


Fig. 5.23 - Connection of the beams from the zero and the first stage into one model



Fig. 5.24 - Cross section through all beams

Stationing of the individual beams is illustrated in the X axis in the graphs. This stationing grows in the positive direction of the X-axis. The zero value of the stationing corresponds to the beam edge adjoining to the enclosure wall. Cross or vertical shifts in the individual stationing are illustrated in axis Y.

A relatively strong dispersion between the individual values of the shifts appeared in some graphs. That is why the calculated values in all the graphs showing cross shifts were interlaid with a regression polynomial second degree curve. These curves were inserted into the graphs, so that the trend of the individual buckling was more apparent. Similar curves were also inserted into the graphs of vertical the shifts for beam CS1. These dispersions were caused by a selection of width of cross sections in the Cyclone software (50 mm) and by scanning density, when the position of the subtracted end points did not always have to be identical to the real beam edge.

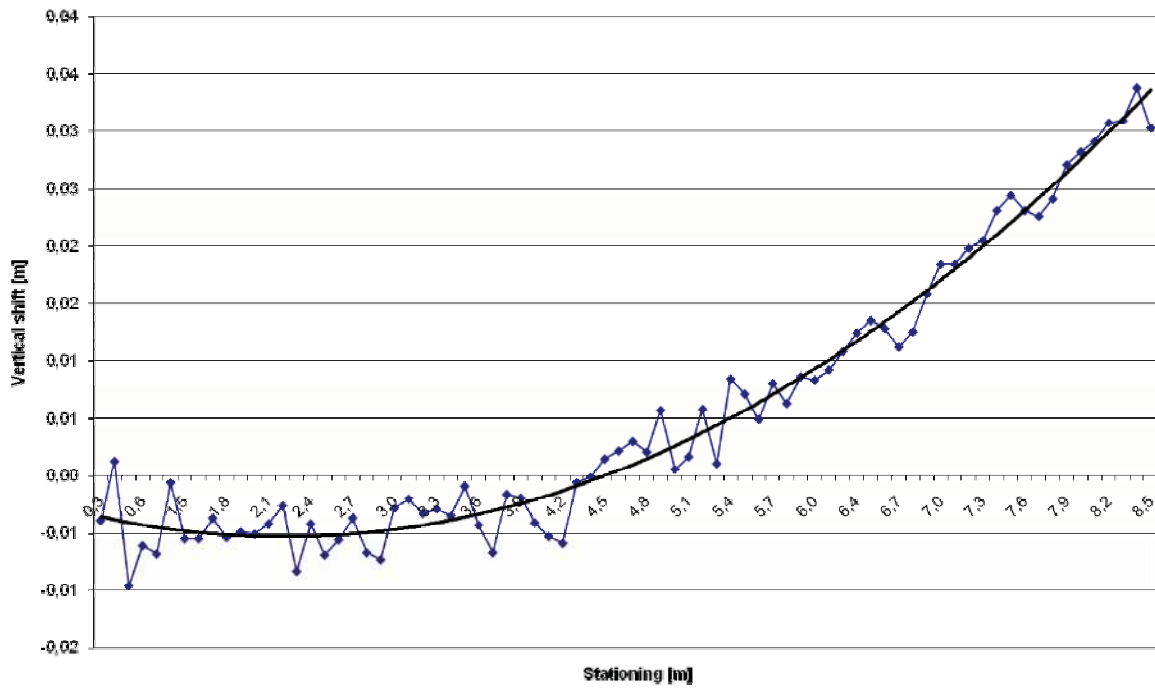


Fig. 5.25 - Vertical shifts of beam CS1 - left lower corner

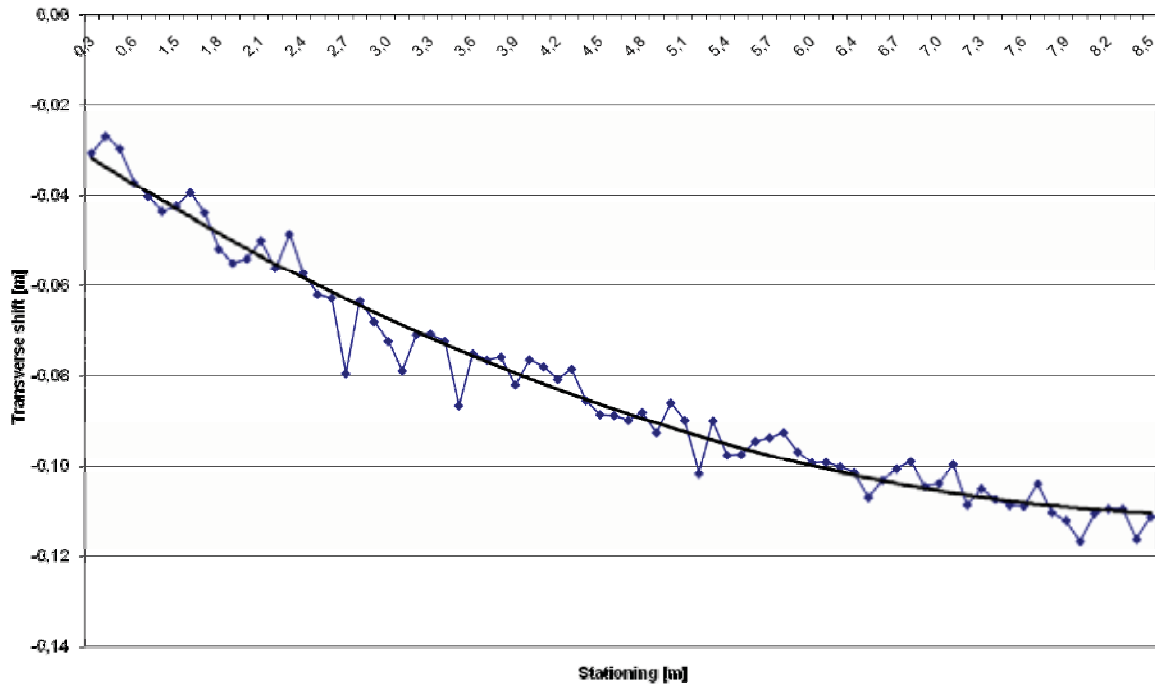


Fig. 5.26 - Transverse shifts of beam CS1 - left lower corner

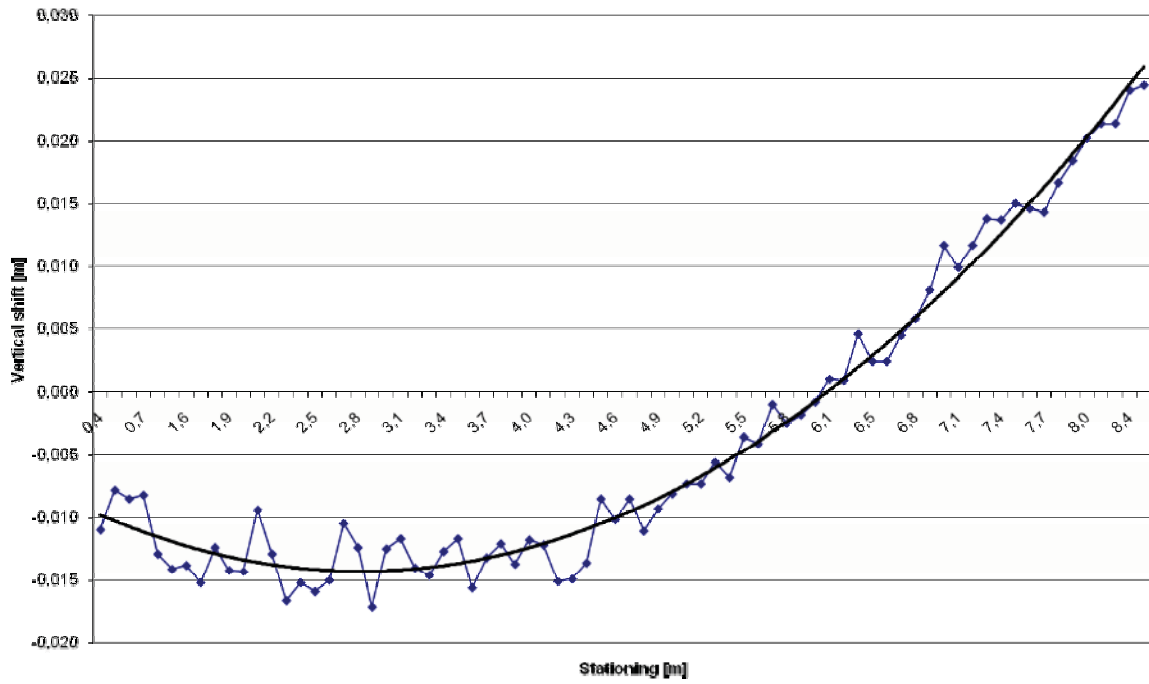


Fig. 5.27 - Vertical shifts of beam CS1 - right lower corner

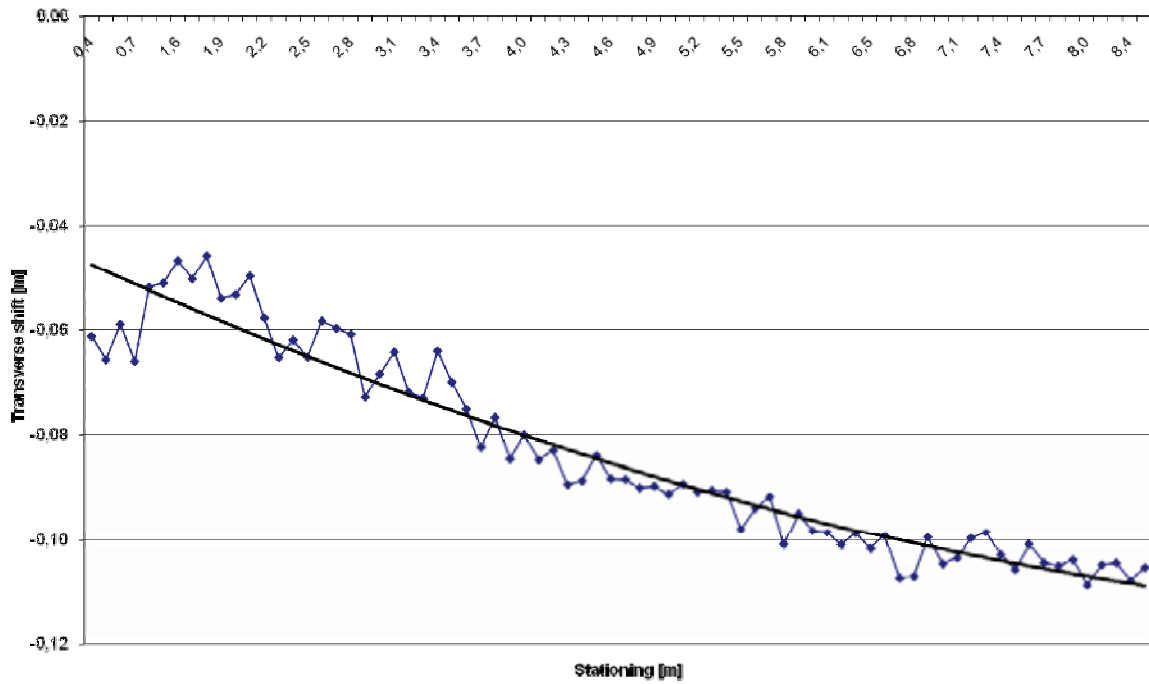


Fig. 5.28 - Transverse shifts of beam CS1 - right lower corner

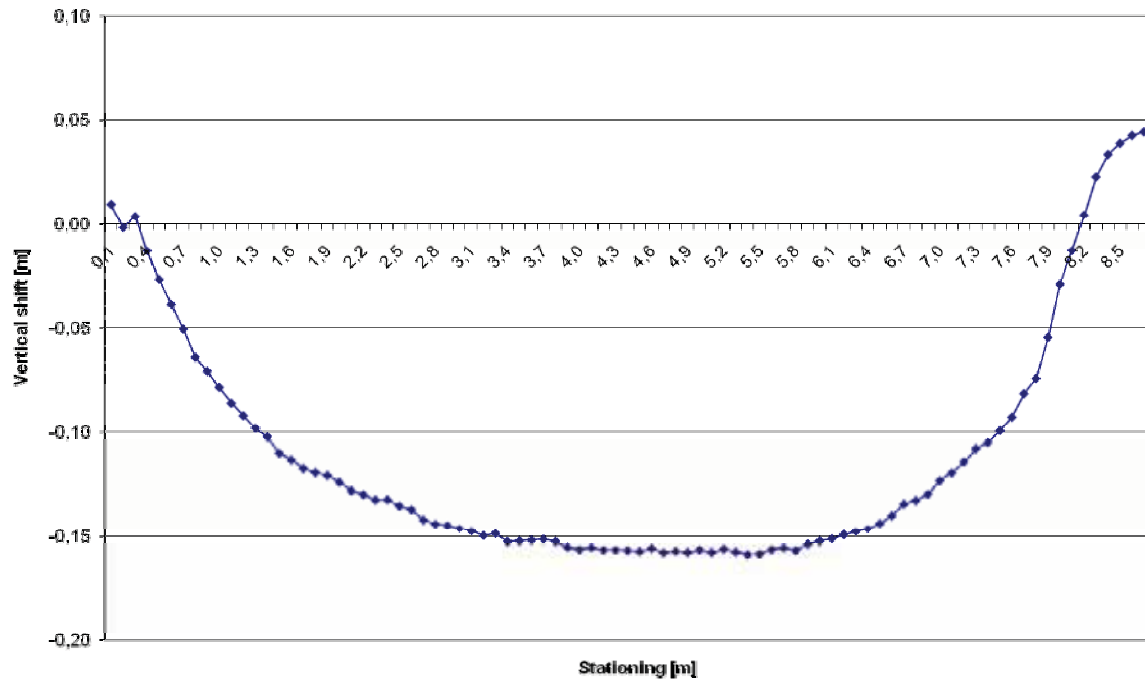


Fig. 5.29 - Vertical shifts of beam with corrugated web CS2 - left lower corner

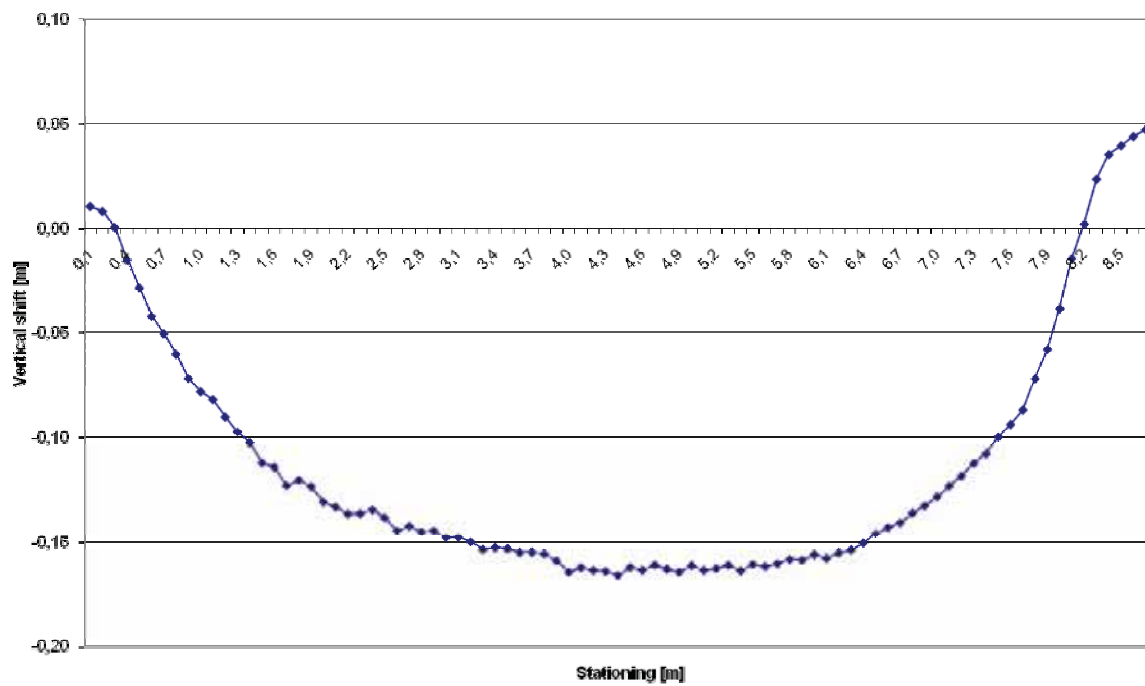


Fig. 5.30 - Vertical shifts of beam with corrugated web CS2 - right lower corner

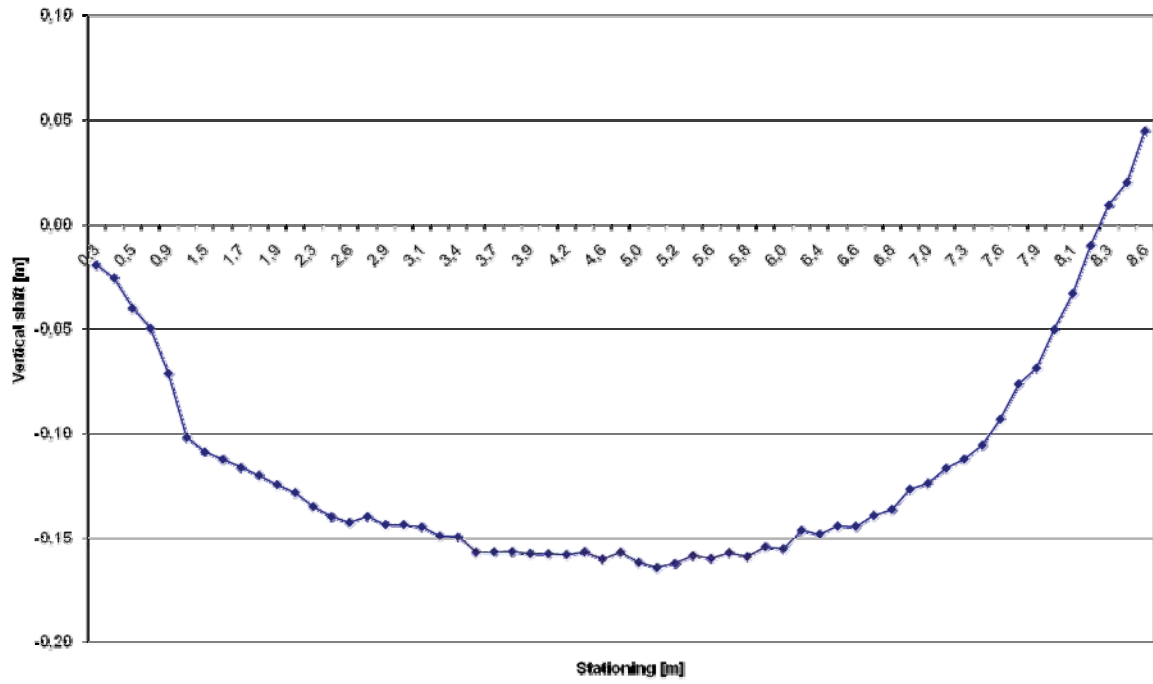


Fig. 5.31 - Vertical shifts of beam with corrugated web CS2 - left upper corner

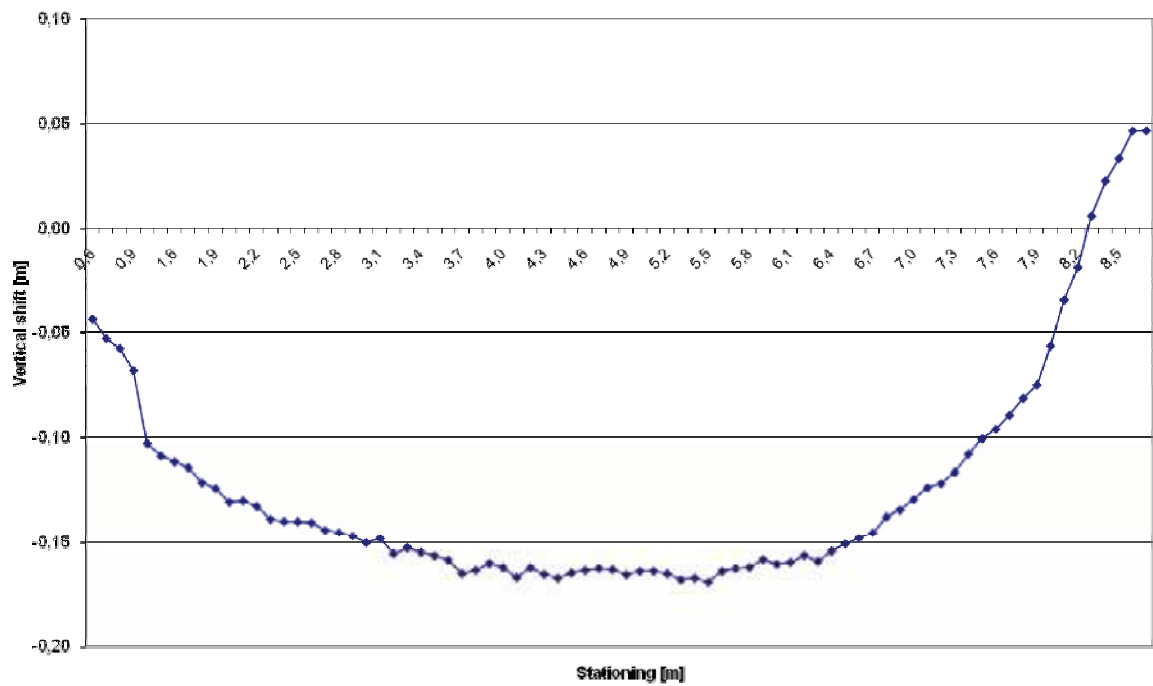


Fig. 5.32 - Vertical shifts of beam with corrugated web CS2 - right upper corner

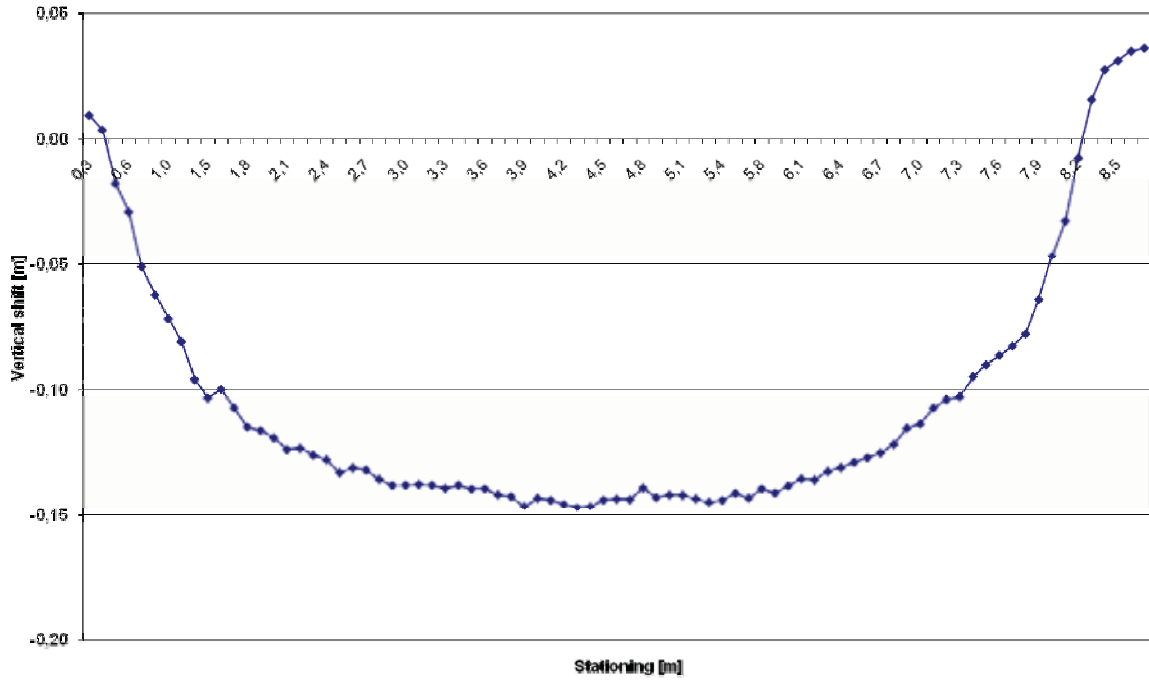


Fig. 5.33 - Vertical shifts of beam with corrugated web CS3 - left lower corner

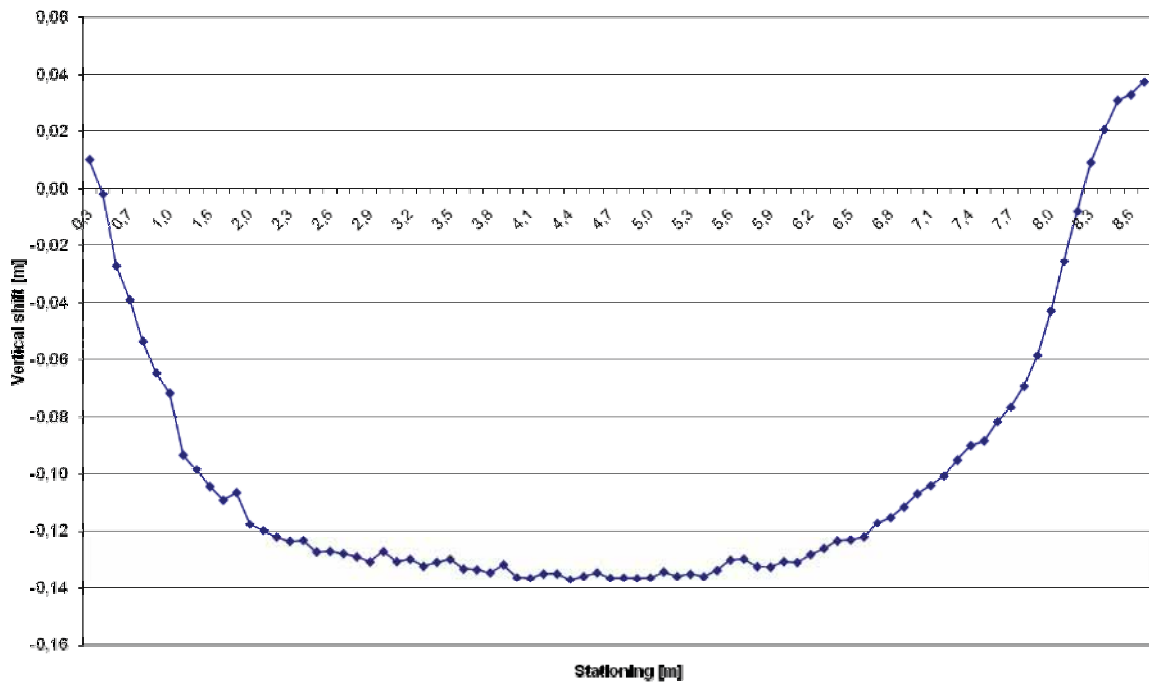


Fig. 5.34 - Vertical shifts of beam with corrugated web CS3 - right lower corner

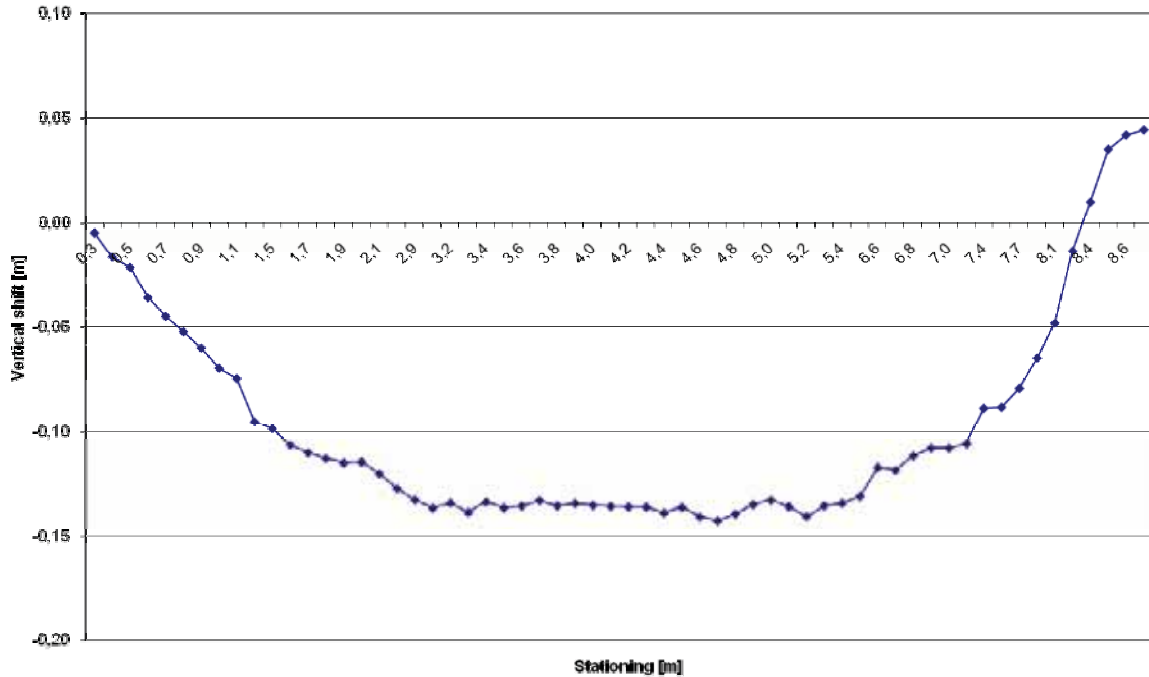


Fig. 5.35 - Vertical shifts of beam with corrugated web CS3 - right upper corner

5.3.7 Processing and evaluating the wall construction

The deformation of the wall construction was determined in a comparison with the beams by another method. This method consists in the creation of a difference model characterizing the divergences in the wall construction between zero and the first stage. The measured data from the individual stages were entered into the calculation in the form of triangular nets (concretely TIN nets) that were created in the first processing step. Then we created a reference plane that is approximately parallel to the observed walls. In our case, the reference plane was inserted into the wall plane at the zero stage. Perpendicular distances to the reference plane were determined to the individual triangular nets in discrete points in regular spacing of 20 mm. The differences of the perpendicular distances of the nets were calculated. The calculated values of the differences were assigned as height coordinates (taken from the reference plane) to discrete points. A triangular net was created from the points calculated in this way in the final version of the processing. This triangular net represented the difference wall recreation model between the stages. The difference models of the individual walls are illustrated in Fig. 5.36 to Fig. 5.38. The differences are expressed by means of hypsometric scale.

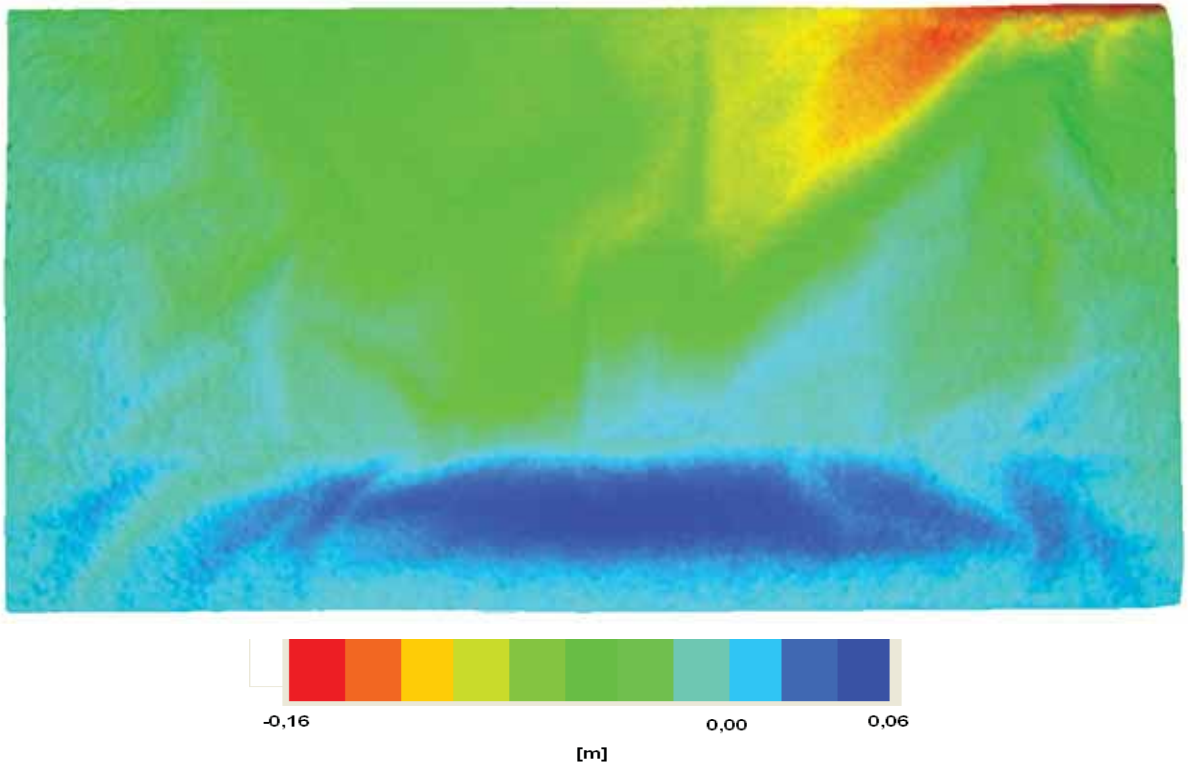


Fig. 5.36 - Difference model of the wall created by sandwich panels

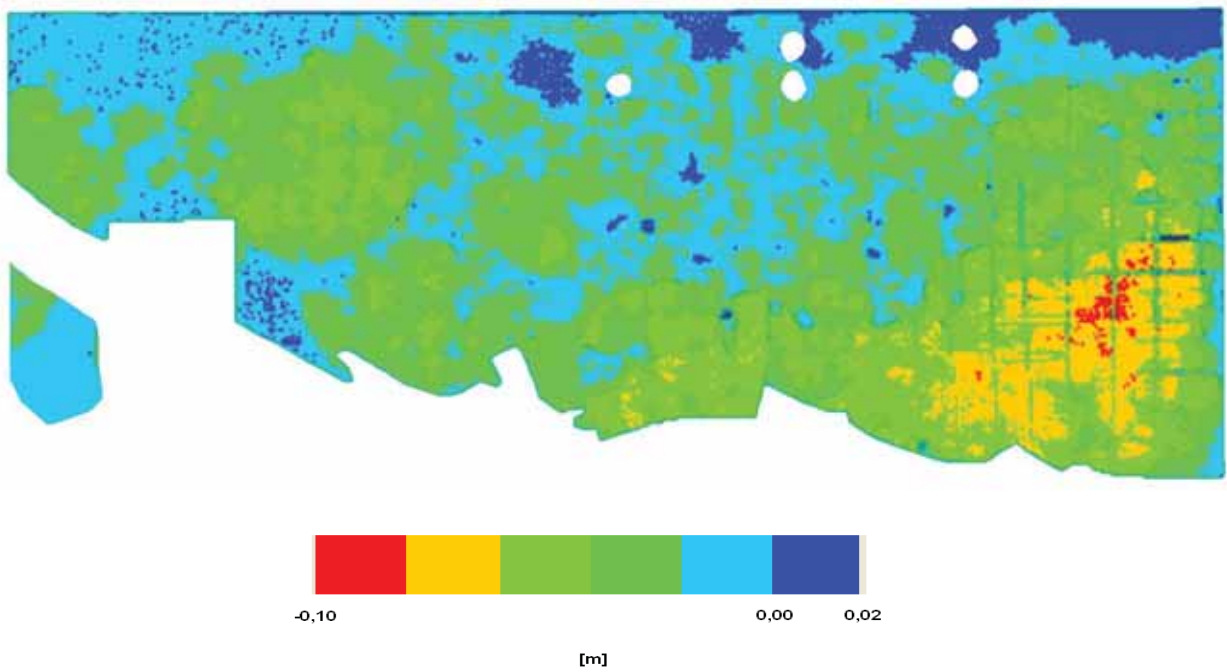


Fig. 5.37 - Difference model of a monolithic concrete wall

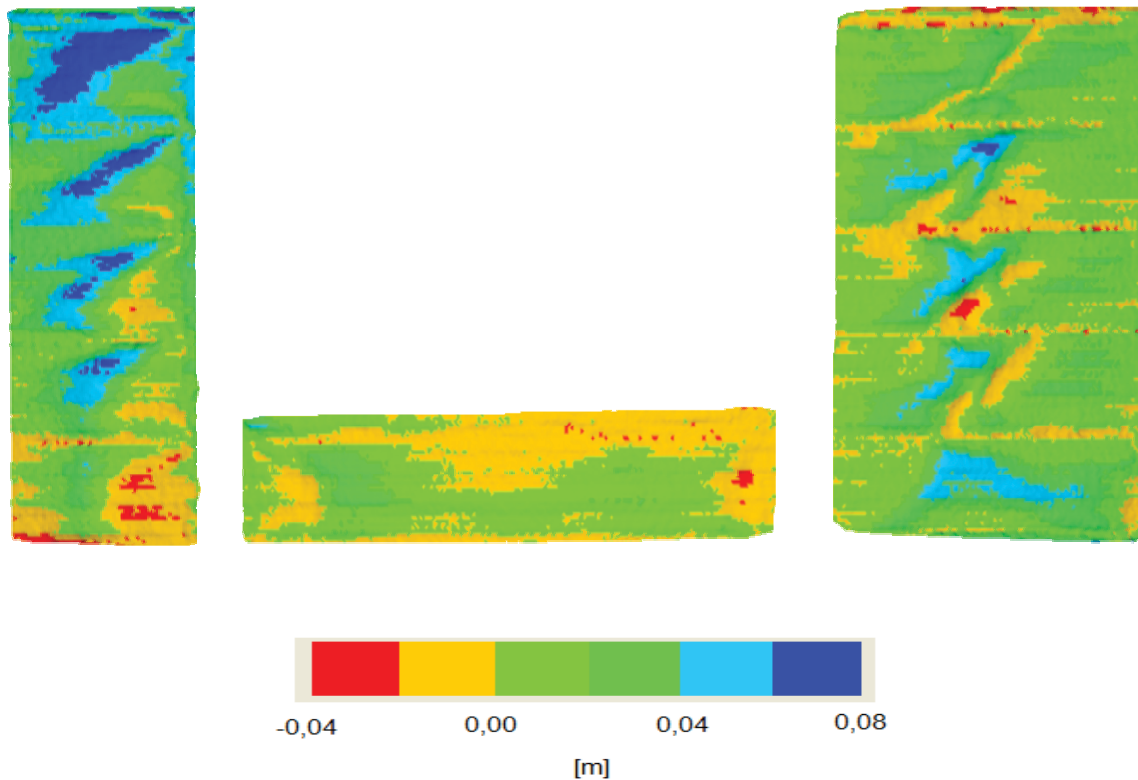


Fig. 5.38 - Difference model of the walls around the window

5.3.8 Processing and evaluating the HEB 280 central column

The evaluation of the HEB 280 central was carried out in a similar way as the evaluation of the ceiling beams. The coordinates of the corner points of the central column were subtracted by means of the cross sections in both stages. A system of coordinates was selected so that the Z-axis was inserted into a vertical edge of the central column, the X-axis was inserted into the edge of the column base parallel to window plane and the Y-axis was inserted into the edge of the column base upright to the window plane. The beginning of the coordinate system was inserted into the left lower column corner from the view of an observer standing with his back to the wall with the window holes. Shifts in the direction of the X and Y-axes were consequently calculated from the subtracted coordinates. The values of the calculated shifts were consequently put into graphs in Fig. 5.40 to Fig. 5.47 in dependence on column stationing. Description of beam corners in the graphs is considered with respect to the same observer as the system of the coordinates. The calculated values in all graphs were interlaid with a regression polynomic second grade curve, so that the trend of individual buckling is more apparent.

In Fig. 5.39 buckling of the HEB 280 column is clearly visible in the direction from the wall with the window holes. The column in the picture measured at the zero stage is illustrated in black and the column measured in the first stage is illustrated in white.

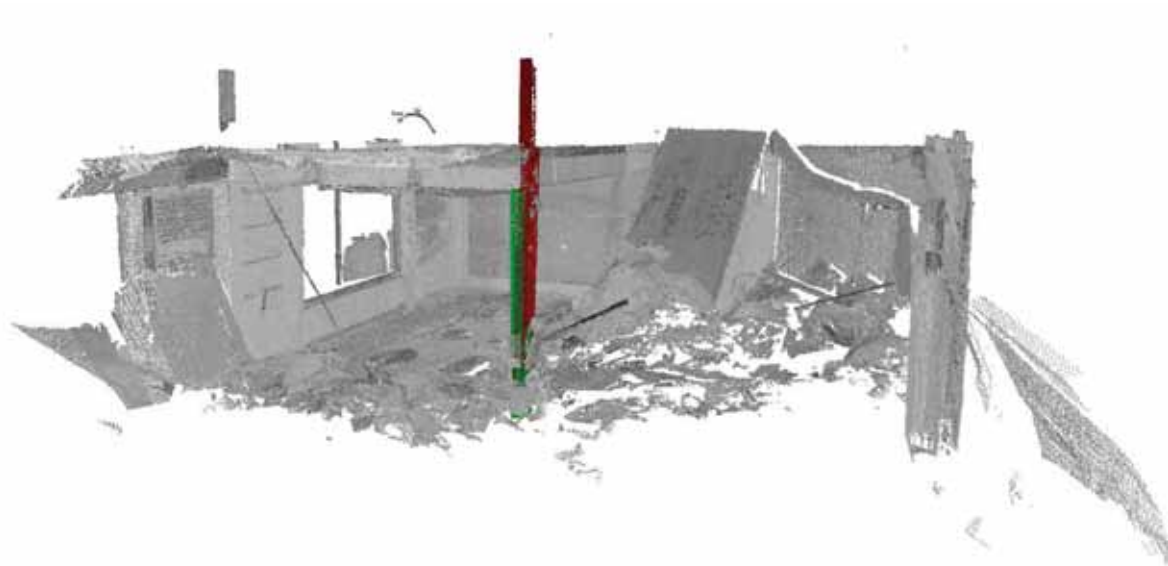


Fig. 5.39 - Connection of the column from the zero and first stage into one

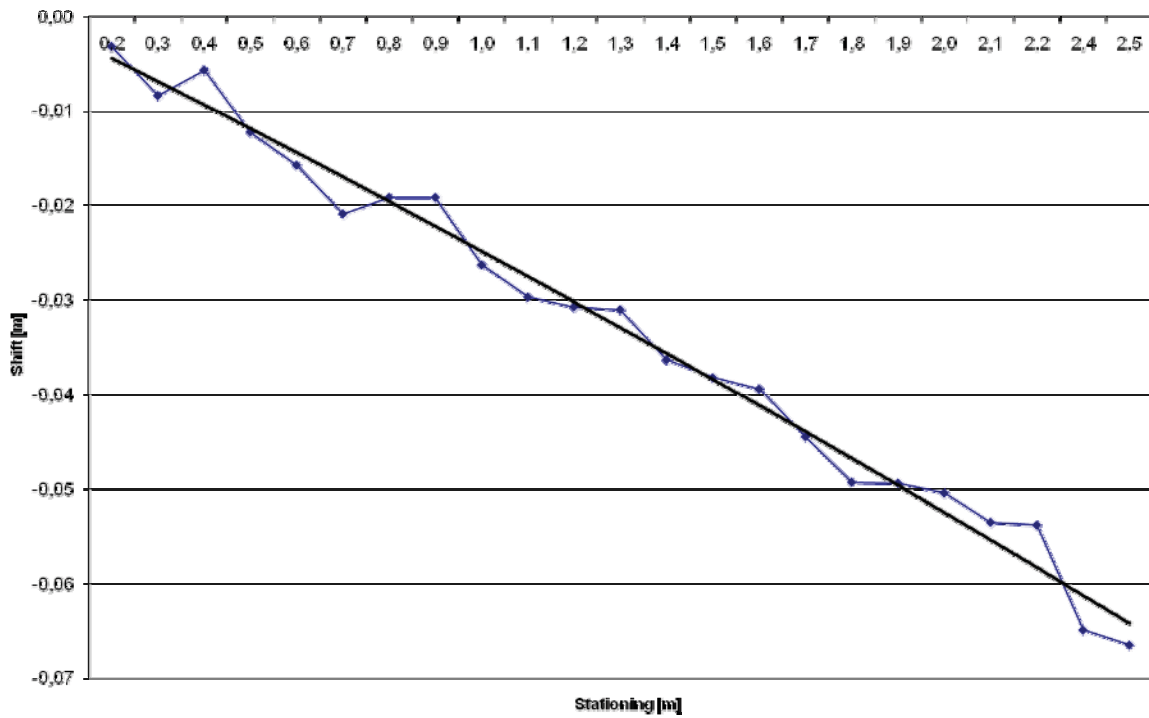


Fig. 5.40 - Shifts in the direction of the X axis of HEB 280 column B2 - left upper corner

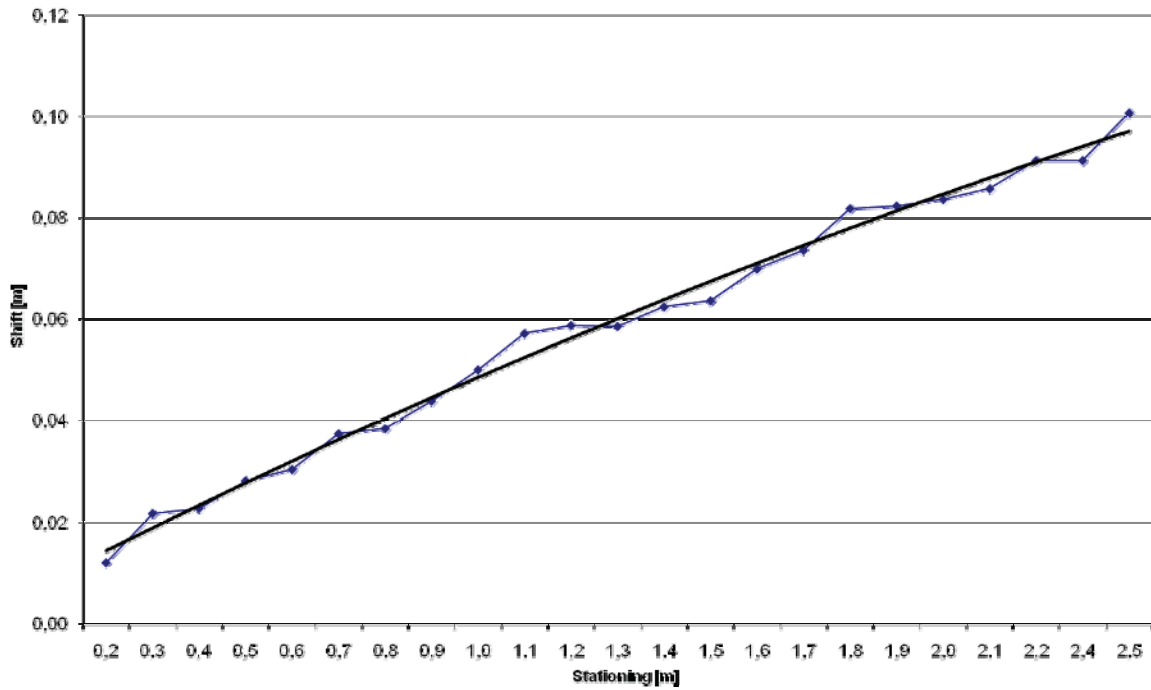


Fig. 5.41 - Shifts in the direction of the Y axis of HEB 280 column B2 - left upper corner

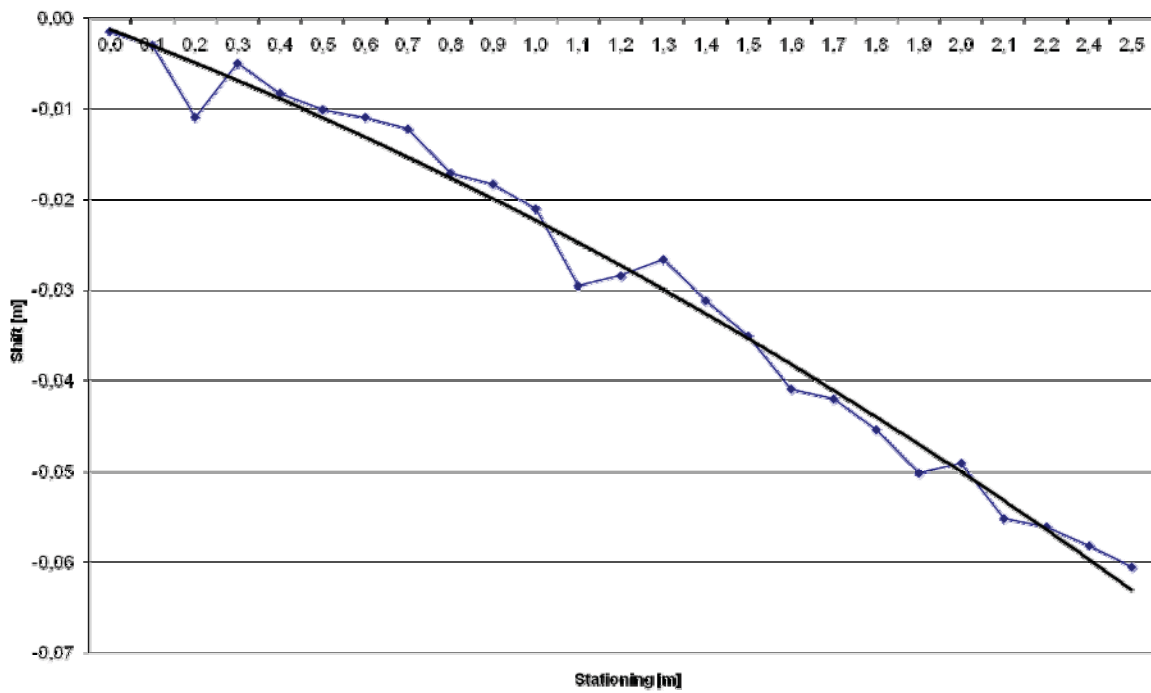


Fig. 5.42 - Shifts in the direction of the X axis of internal column B2 - left lower corner

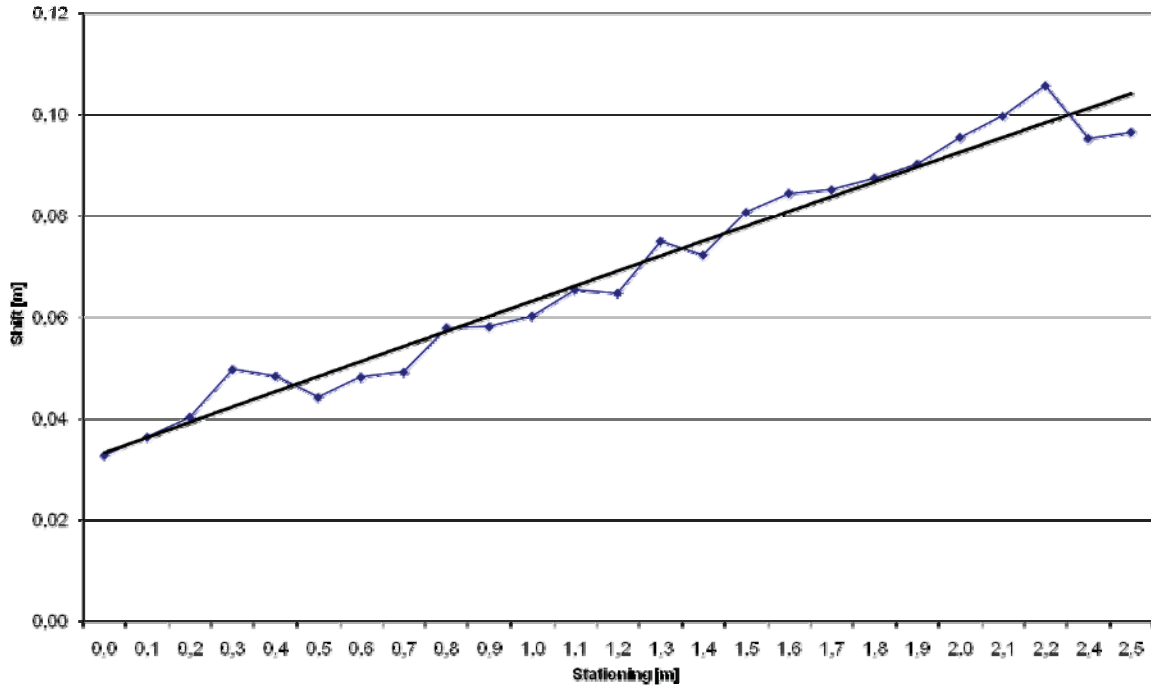


Fig. 5.43 - Shifts in the direction of the Y axis of internal column B2 - left lower corner

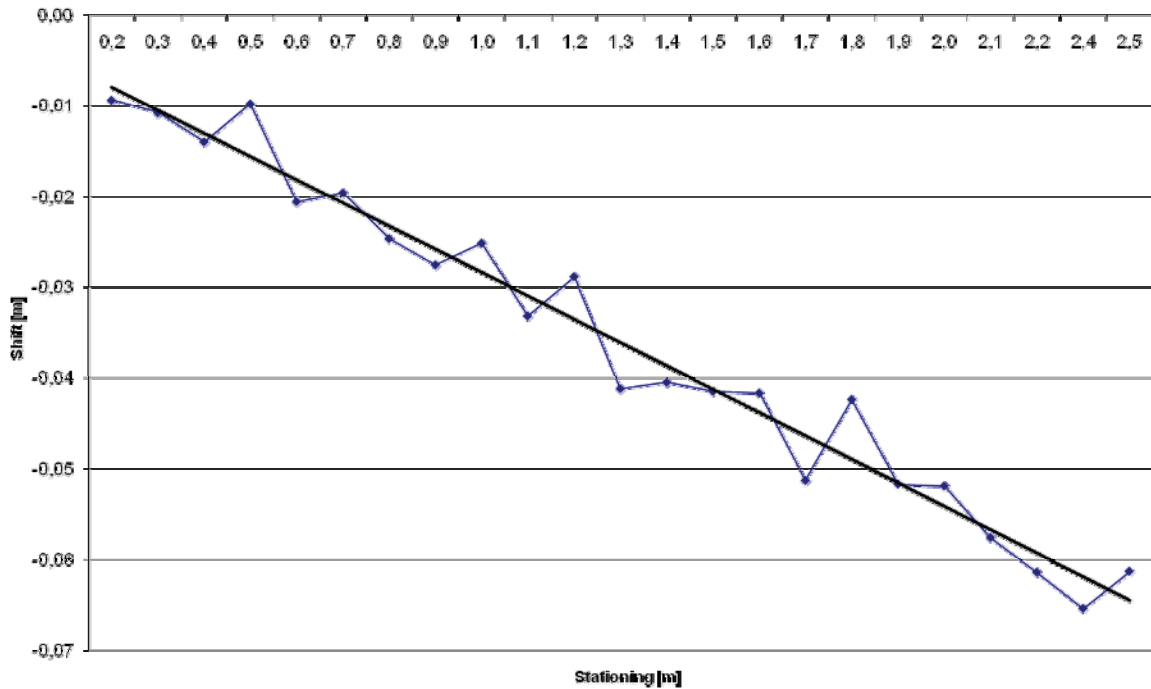


Fig. 5.44 - Shifts in the direction of the X axis of internal column B2 - right upper corner

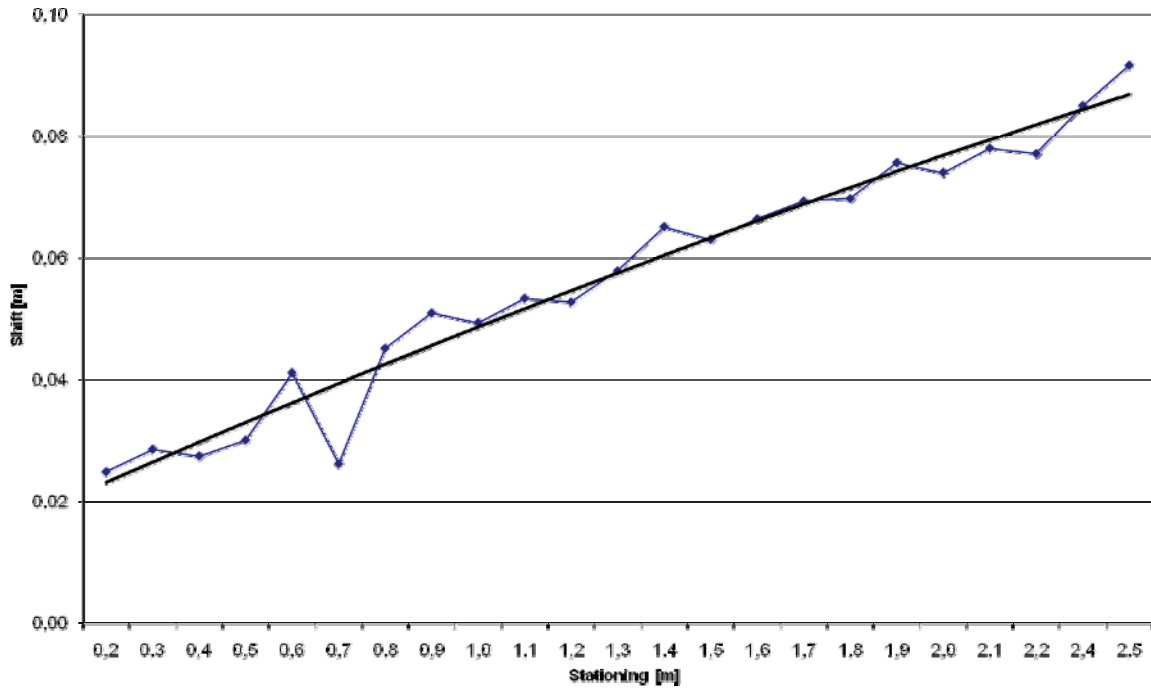


Fig. 5.45 - Shifts in the direction of the Y axis of internal column B2 - right upper corner

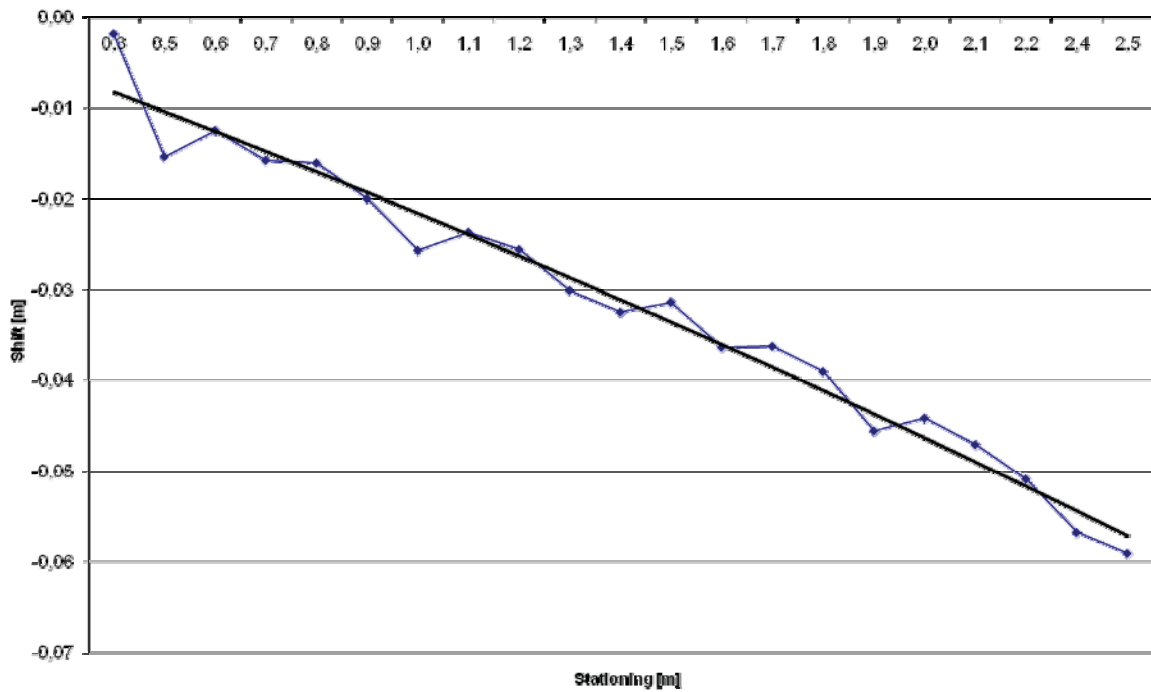


Fig. 5.46 - Shifts in the direction of the X axis of internal column B2 - right lower corner

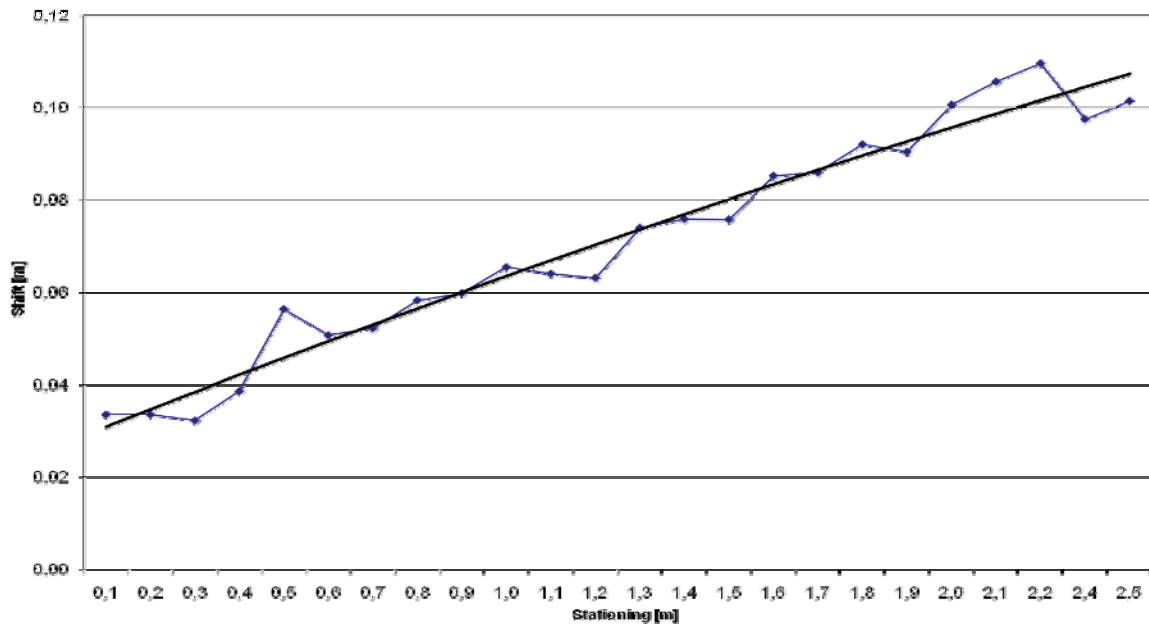


Fig. 5.47 - Shifts in the direction of the Y axis of internal column B2 - right lower corner

5.3.9 Summary of laser scanning

We evaluated the deformation of the experimental building object after the fire test by means of terrestrial laser scanning. We measured two beams with corrugated web CS2, CS3 and the beam from profile IPE 400 CS4, an internal column B2 from profile HEB 280, wall construction from monolithic concrete, wall construction created by sandwich panels and wall construction created by the linear trays, mineral wool and external corrugated sheets.

When evaluating the beams we noted vertical shifts and cross shifts (buckling). As for the beams with corrugated web, we determined a maximum vertical shift of 160 mm and maximum cross buckling of 110 mm. As for the IPE 400 beam, maximum vertical shift was 15 mm and maximum buckling was 110 mm. Vertical shift of this beam is about 10 times smaller than for beams with the corrugated webs. This could be caused by its covering of mineral wool and with plasterboard, which protected it from the fire. Cross buckling of the beams was caused by the deformation of the central column, which arose owing to the fire and owing to the partial collapse of the construction. The individual constructions at the end of all beams (in the middle of the object) were lifted above the position in which they were before the fire test (approximately 40 mm). This phenomenon can be put down to the fact that the zero stage was measured with loading placed on the ceiling of the object (sacks of gravel), whereas the first stage was measured only after the loading had been removed. Difference models characterizing deformation of all the wall constructions after the fire test were created for all types of the wall constructions. Heavy concrete spalling (up to 100 mm) is apparently visible in the hypsometric plan of the monolithic concrete wall. This concrete spalling arose during the fire in consequence of the transformation of water present in the wall construction into water vapour. When observing the wall created by sandwich panels it is apparent that it bulged inwards into the object (up to 60 mm) in the lower part of the object, whereas in the space near the ceiling (in place with the highest temperature) it bulged outwards from the object (up to 160 mm). The difference model of the wall created by the bearing cassettes shows the deformation of all the bearing cassettes in a similar way. It always bulged through the cover trapezoidal sheet in the middle of the cassette construction (up to 80 mm).

6 RELATIVE STRESSES

The relative deformation of the steel beam web was measured by seven ceramic strain gauges for high temperatures. The beams with corrugated web and castellated beams were installed close to connections with strain gauges for high temperatures to assume the shear stress across their webs during the fire test. The application of the free-filament high-temperature strain gauges, which are sandwiched between two thin ceramics cement layers, allow for measurements up 1150 °C. The accuracy of the measurement is 3 % until the 5000 μm .

Two strain gauges were applied in the middle third of the web height of the castellated beam, see Figs. 6.1 and 6.2. Three strain gauges were located near both flanges and in the mid-point of the corrugated web height. They were installed to monitor the shear stress of the web of the beam, see Fig. 6.1 and 6.3. In Fig. 6.4, the web of the beam with corrugated web after the fire test is visible with strain gauges and thermocouples. The measured strain and calculated stresses are summarised for castellated beam AS4 and for the beam with corrugated web CS2 in Tab. 6.1.

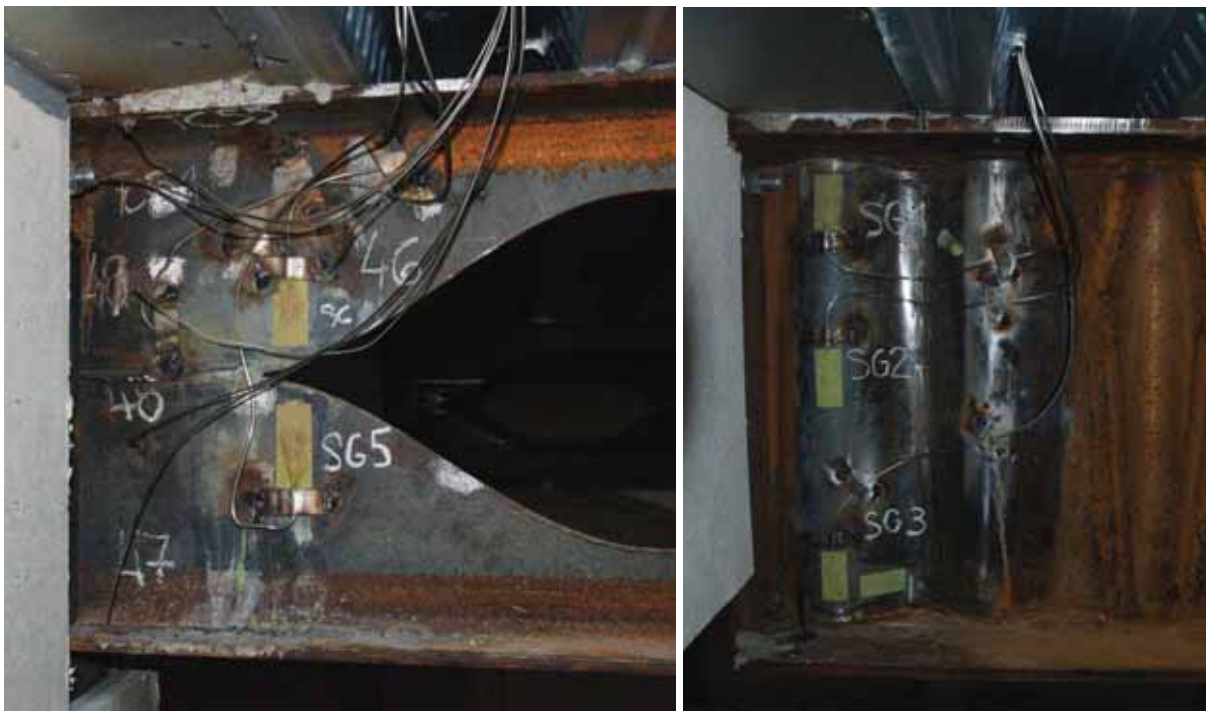


Fig. 6.1 - Strain gauges on the web of castellated beam AS4 and on the beam with corrugated web CS2

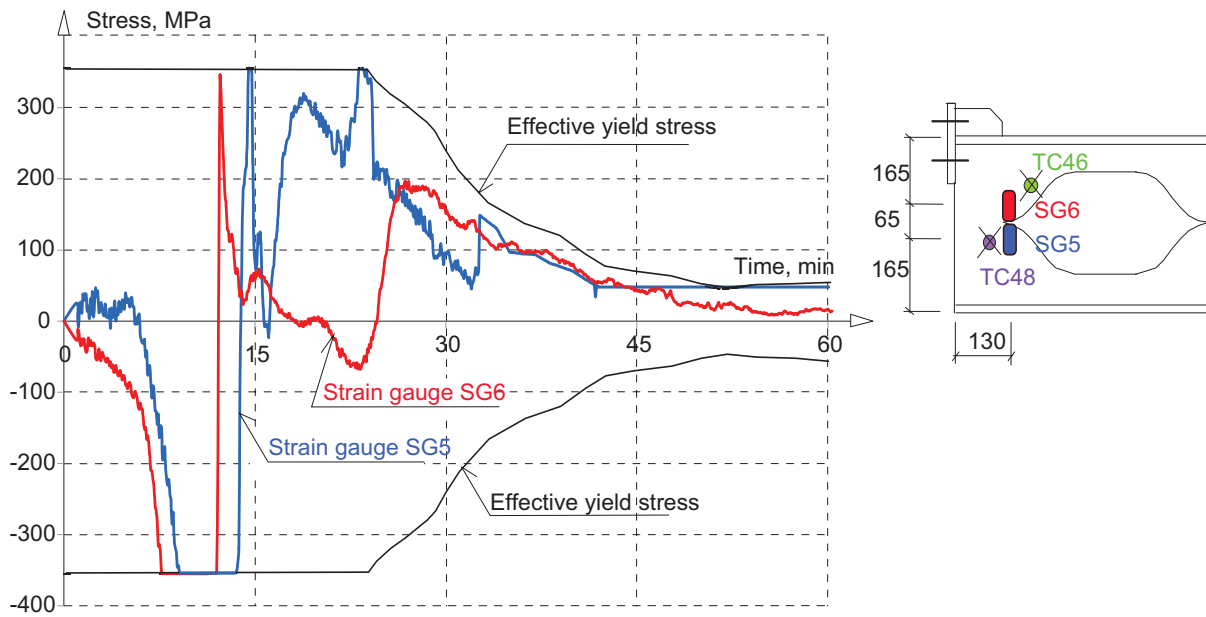


Fig. 6.2 - Measured stresses on the web of the castellated beam AS4

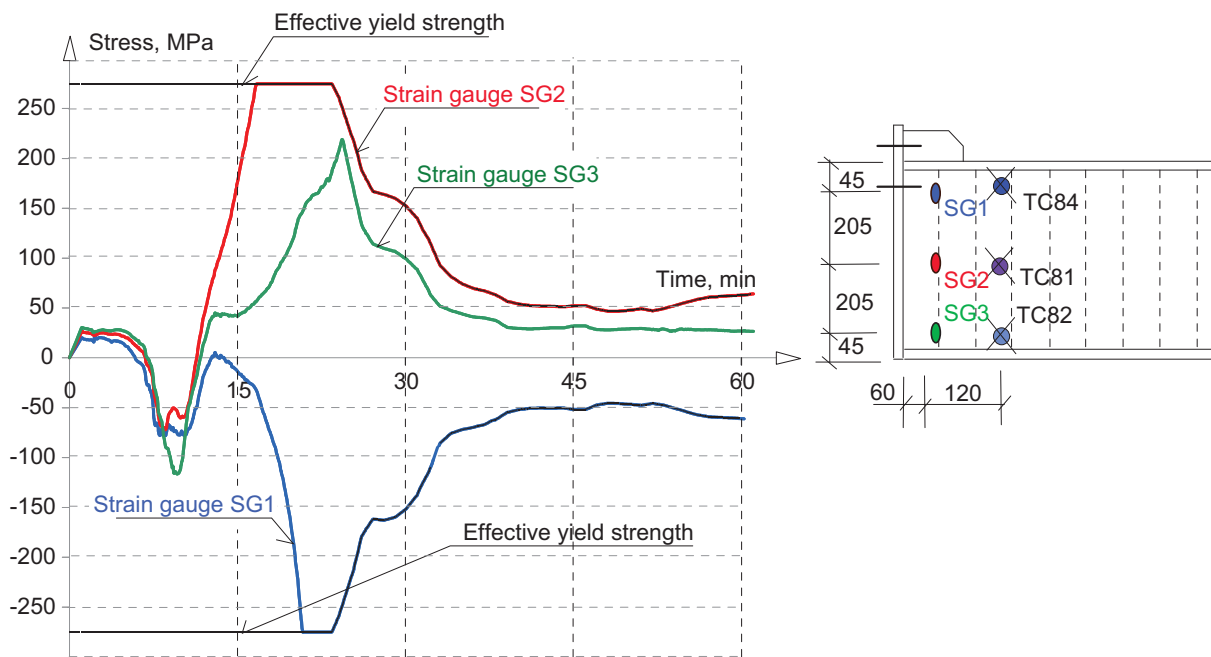


Fig. 6.3 - Measured stresses in the beam with corrugated web CS2

Tab. 6.1 Evaluations of the stresses on the web of castellated beam AS4 an on the corrugated web of beam CS2

| Time [min] | SG1 | | SG2 | | SG3 | | SG5 | | SG6 | |
|---------------|---------------------------------------|-----------------|---------------------------------------|-----------------|---------------------------------------|-----------------|---------------------------------------|-----------------|---------------------------------------|-----------------|
| | Strain $\mu\epsilon \cdot 10^{-3}$ | Stress [MPa] |
| 0 | 0.000 | 0 | 0.000 | 0 | 0.000 | 0 | 0.000 | 0 | 0.000 | 0 |
| 5 | -0.017 | -4 | 0.049 | 10 | 0.082 | 17 | -0.090 | -19 | -0.550 | -115 |
| 10 | -0.289 | -58 | -0.090 | -18 | -0.145 | -30 | -4.687 | -355 | -9.045 | -355 |
| 15 | -0.145 | -25 | 1.364 | 238 | 0.292 | 50 | -0.045 | -8 | 0.276 | 51 |
| 20 | -1.972 | -275 | 3.878 | 275 | 1.029 | 154 | 1.602 | 266 | -0.099 | -16 |
| 25 | -7.615 | -179 | 9.427 | 188 | 3.223 | 134 | 1.310 | 173 | 1.244 | 169 |
| 30 | -12.043 | -137 | 6.902 | 140 | 2.582 | 88 | 1.061 | 72 | 1.546 | 137 |
| 35 | -8.978 | -70 | 5.827 | 70 | 2.206 | 41 | 32.000 | 95 | 1.863 | 98 |
| 40 | -6.011 | -51 | 5.483 | 53 | 1.738 | 29 | 32.000 | 58 | 1.995 | 64 |
| 45 | -5.572 | -52 | 5.570 | 53 | 1.730 | 32 | - | - | 1.741 | 43 |
| 50 | -5.167 | -48 | 5.629 | 49 | 1.619 | 29 | - | - | 0.807 | 16 |
| 55 | -5.599 | -57 | 5.198 | 59 | 1.287 | 28 | - | - | 0.416 | 9 |
| 60 | -6.101 | -62 | 5.081 | 64 | 1.141 | 26 | - | - | 0.688 | 15 |



Fig. 6.4 - The web of the beam with corrugated web after the fire test with visible strain gauges and thermocouples

7 WEATHER CONDITIONS, FLUX DENSITY OF HEAT

On the west linear scaffold, a meteorological station was installed to record external temperatures, humidity of the external air, wind speed and wind direction. The measurement point was located 2 m above the ground and was conducted by the Technical University of Ostrava.

In Fig. 7.1 and Fig. 7.2 the description of the temperature course of the external air and humidity of the external air respectively is provided. The monitored maximal and average wind speed is shown in Fig. 7.3. During the fire experiment the direction of the wind shifted from northwest to southwest. This influenced the development of gas and flames in the fire compartment. Components of the wind speed in north-south and east-west directions are derived in Fig. 7.4.

Temperatures and pressures of the concrete walls for two different distances along the thickness of the wall are given in Fig. 7.5.

The Technical Institute of Fire Protection carried out measurements in the east window during the fire test. Flux density of heat was measured under the slab with cellular beams in the level of the lower flanges of the cellular beams at the back of the fire compartment, see Fig. 7.6. Measured concentrations of O_2 and CO_2 are shown in Fig. 7.7, the concentration of CO in Fig. 7.8 and concentration of NO , NO_2 and SO_2 in Fig. 7.9.

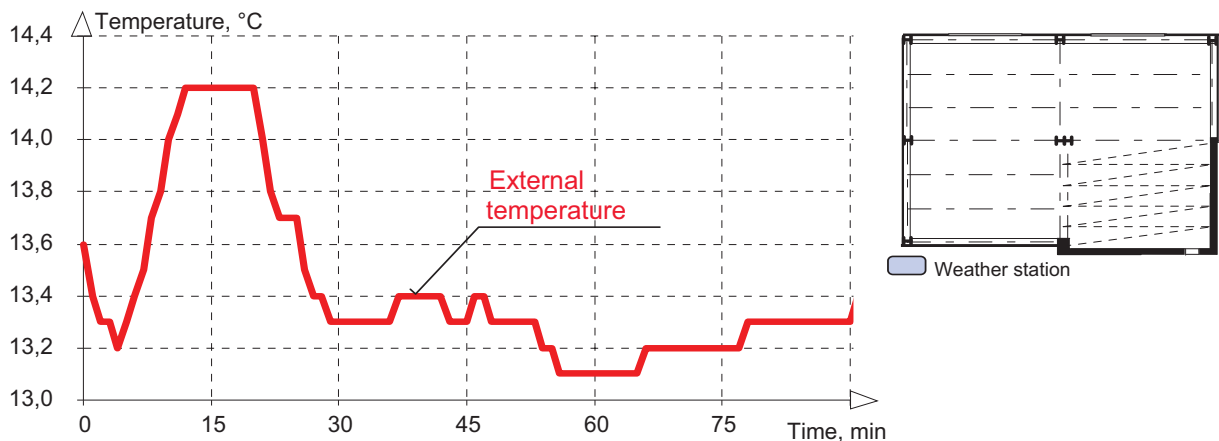


Fig. 7.1 - Temperature of the external air in the weather station

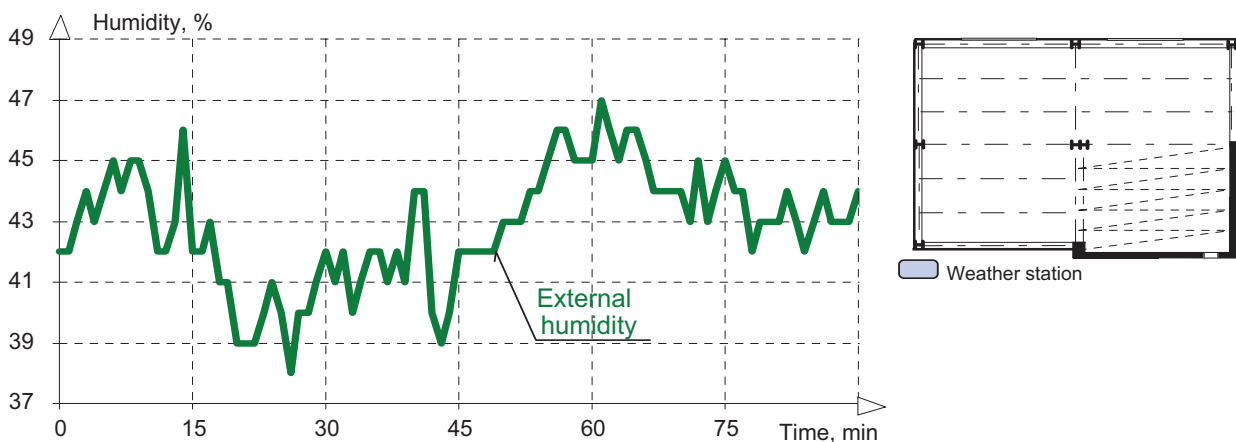


Fig. 7.2 - Humidity of the external air in the weather station

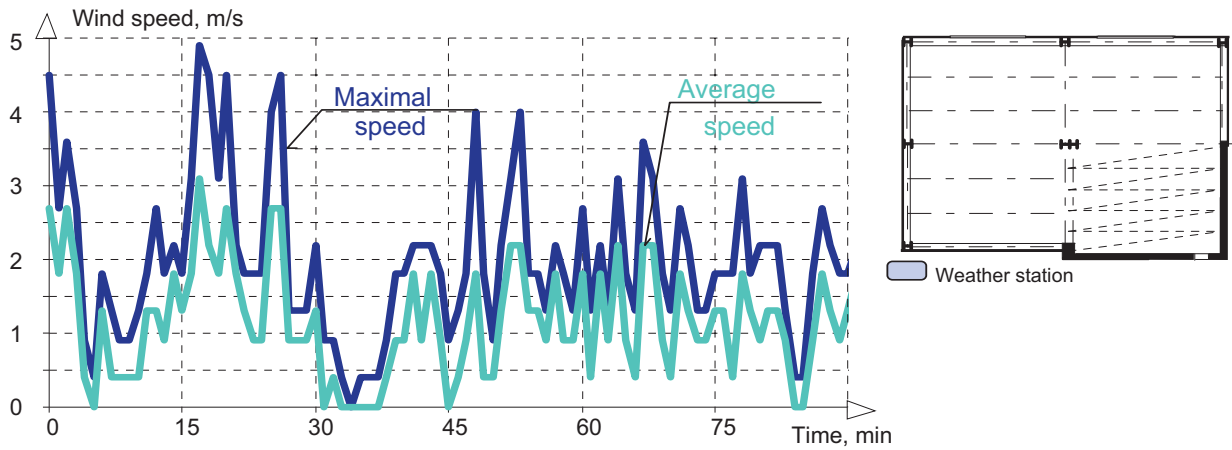


Fig. 7.3 - Measured average and maximal wind speed

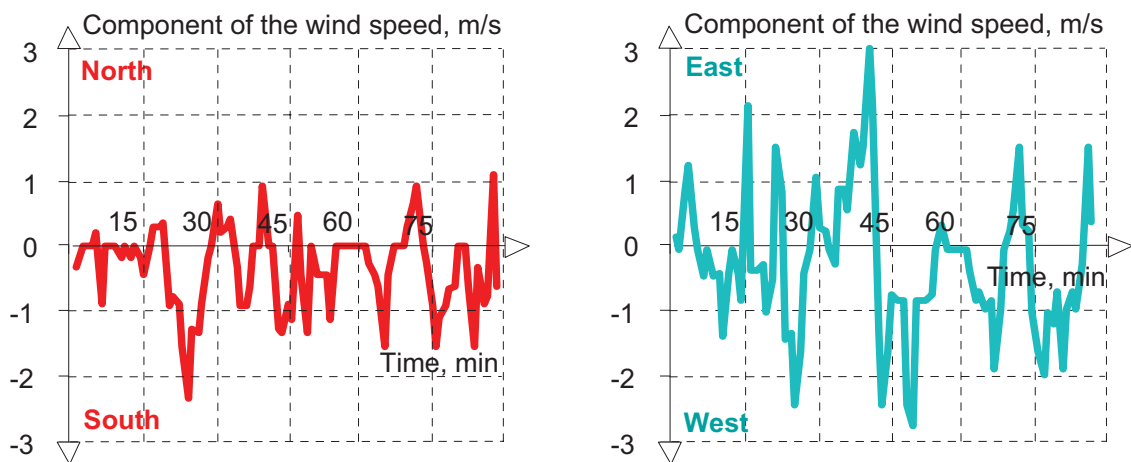


Fig. 7.4 - Components of wind speed in a north-south direction and an east-west direction

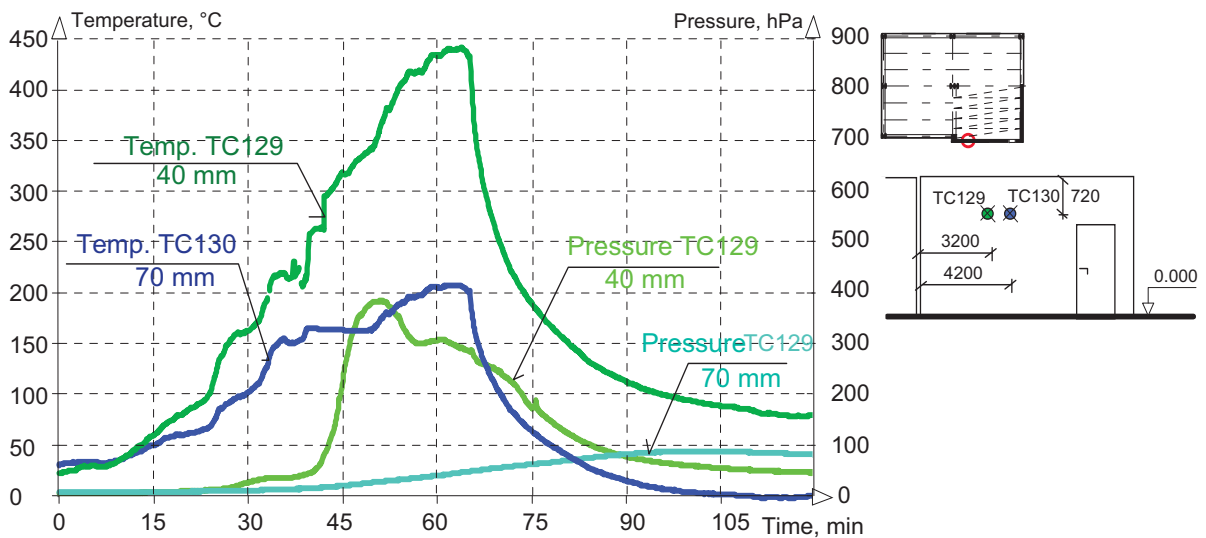


Fig. 7.5 - Temperatures and pressures of concrete walls for two different places at the distance 40 mm and 70 mm from the internal surface

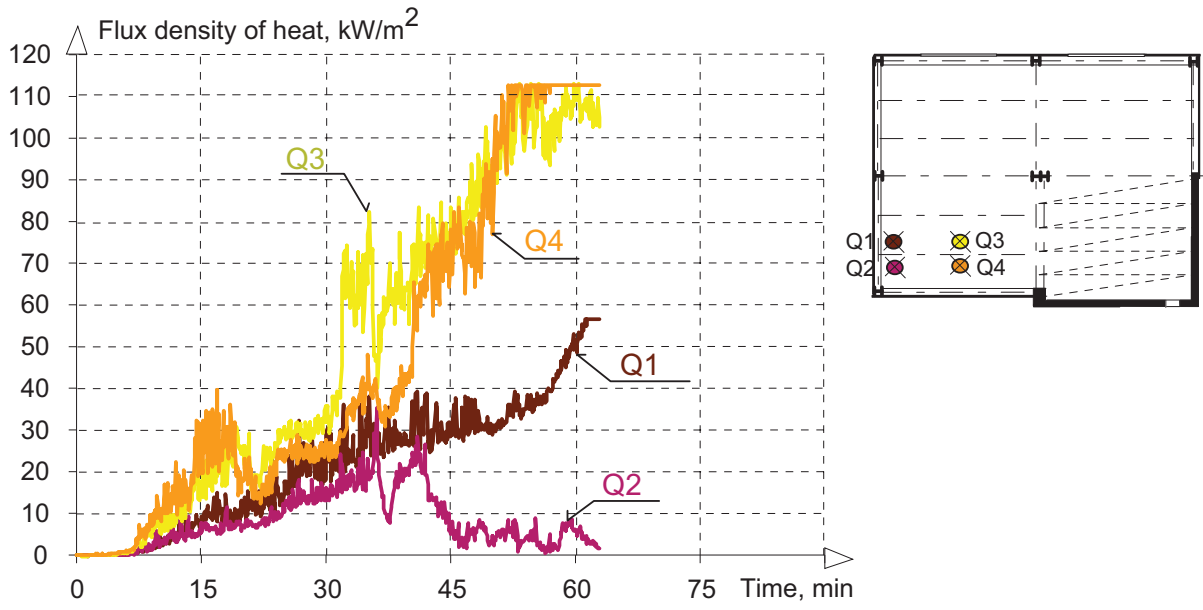


Fig. 7.6 - Flux density of heat measured under the slab with cellular beams at the level of the lower flanges of the cellular beams at the back of the fire compartment

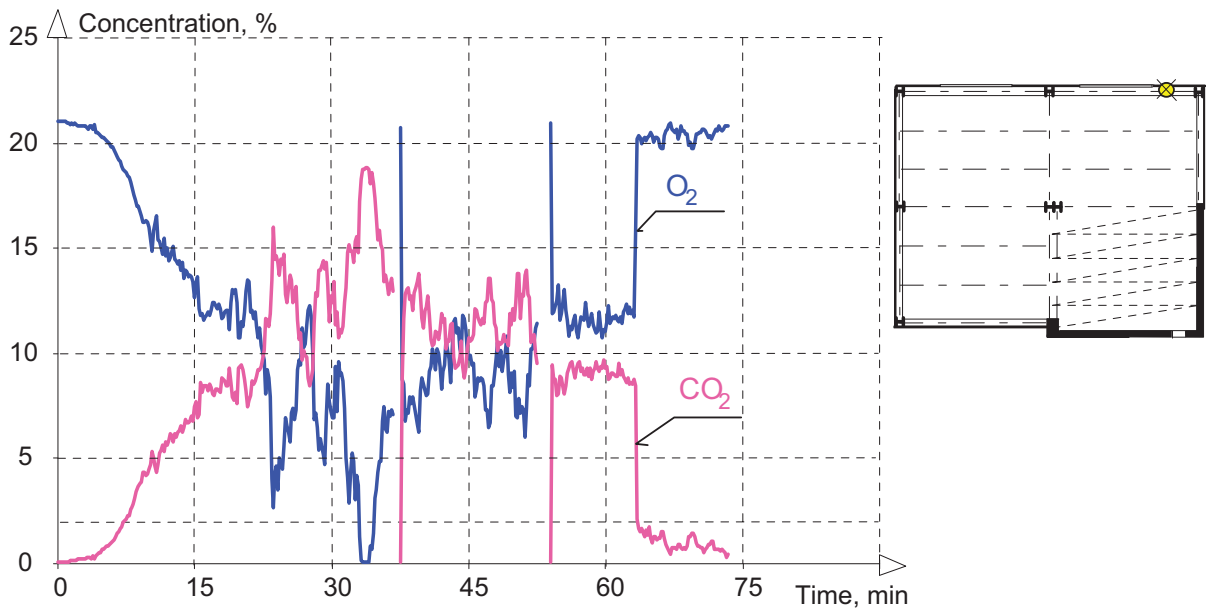


Fig. 7.7 - Concentration of O₂ and CO₂ in the east window during the fire test

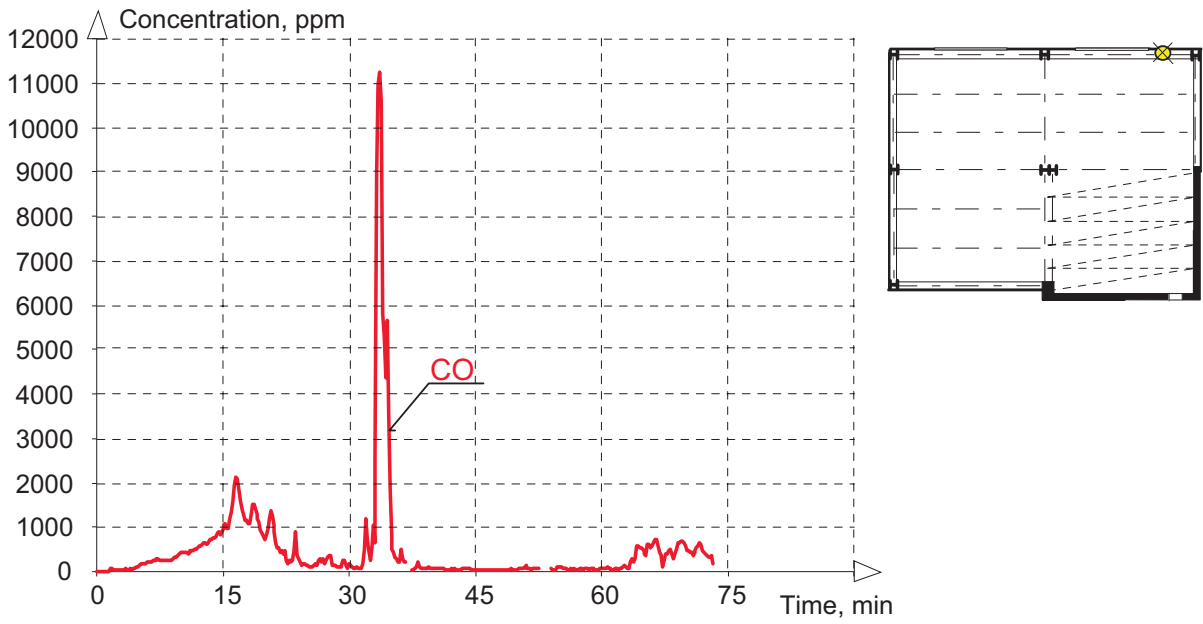


Fig. 7.8 - Concentration of CO in the east window during the fire test

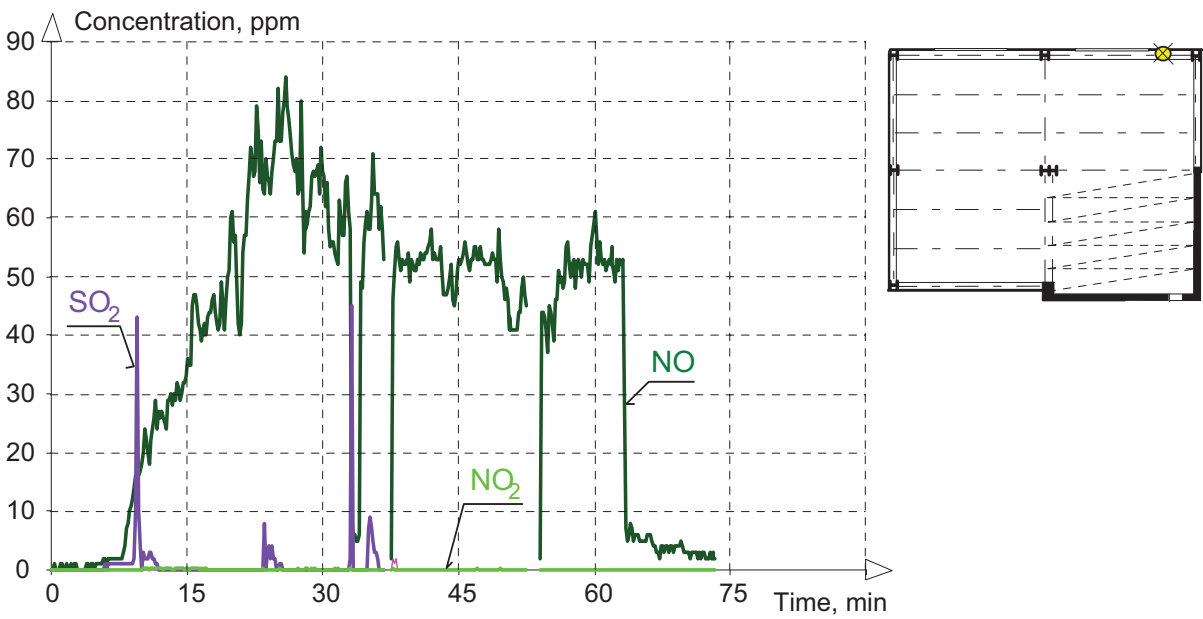


Fig. 7.9 - Concentration of NO, NO₂ and SO₂ in the east window during the fire test

8 SUMMARY

The damage to the ceiling started in the southwest corner. The slab lost resistance in compression at the 62. min of the experiment, see Figs. 7.1 to 7.6. The edge beam buckled on its developed free length, see Figs. 7.7 to 7.8. Due to the spalling of the top of the concrete column the anchors lost tensile resistance. The bolted connection of the primary box girder was exposed to torsion, which led to a loss of shear resistance of the bolts.

The fire test showed the differences between the behaviour of the element and of the structure exposed to high temperatures during fire. The collapse of the composite slab was reached. Fire resistance R60 of applied structural elements and cladding was approved.



Fig. 8.1 - North view of the structure after the fire test



Fig. 8.2 - The top view of the slab under the castellated beams after the fire test



Fig. 8.3 - Panoramic top view of the slab under the castellated beams after cleaning of the mechanical load



Fig. 8.4 - The panoramic top view of the slab under the castellated beams with visualised major cracks



Fig. 8.5 - The corner of the composite slab, where the initial damage began



Fig. 8.6 - Edge of the slab affected by the crushing of the concrete



Fig. 8.7 - The edge beam in the corner of the slab after buckling



Fig. 8.8 - The edge beam in the corner of the slab after buckling



Fig. 8.9 - The rest of the Angelina beam to the central column connection after the break of the composite slab



Fig. 8.10 - The cellular Angelina beam to the central primary beam connection on the primary beam after its collapse

REFERENCES

- [1] Bailey C.G., Lennon T., Moore D.B., The Behaviour of Full-scale Steel Framed Buildings Subjected to Compartment Fires, *Struct. Eng.*, Vol. 77(8), p. 15–21, 1999.
- [2] Wald F., Simões da Silva L., Moore D.B., Lennon T., Chladná M., Santiago A., Beneš M. and Borges L., Experimental Behaviour of a Steel Structure under Natural Fire”, *Fire Safety Journal* 2006, Volume 41, Issue 7, p. 509-522.
- [3] Kallerová P., Wald F., Ostrava Fire Test, Czech Technical University, Prague, CIDEAS report No. 3-2-2-4/2, www.cideas.cz.
- [4] Chlouba J., Wald F., Sokol Z., Temperature of Connections during Fire on a Steel Framed Building, *International Journal of Steel Structures* 2009, Volume 9, Issue 1, p. 47-55.
- [5] Kallerová P., Wald F., Fire Test on Experimental Structure in Mokrsko, in *Czech: Požární zkouška na experimentálním objektu v Mokrsku*, CTU in Prague, August 2008, ISBN 978-80-01-04146-8.
- [6] EN 1991-1-2: 2002. Eurocode 1: Basis of Design and Actions on Structures - Part 2-2: Actions on Structures - Actions on Structures Exposed to Fire, CEN, Brussels.
- [7] EN 1993-1-2: 2005. Eurocode 3: Design of Steel Structures - Part 1-2: General Rules - Structural Fire Design, CEN, Brussels.
- [8] The Mokrsko fire test web page: fire.fsv.cvut.cz/firetest_mokrsko
- [10] Pospíšil J., Štroner M., Moderní geodetické technologie a přístroje pro měření délek a úhlů, *Stavební obzor*, 2005, 14/9, p. 279-286, ISSN 1210-4027.
- [11] www.trimble.com, 25.9.2008.
- [12] Böhm J., Radouch V., Hampacher M., *Teorie chyb a vyrovnávací počet*, geodetický a kartografický podnik Praha, 2. ed., 1990, ISBN80-7011-056-2.
- [13] www.scilab.org, 23.3.2008.
- [14] Horák Z., Krupka F., Šindelář V., *Technická fyzika*, Státní nakladatelství technické literatury, Praha 1961, 3. ed.
- [15] Štroner M., *Metody výpočtu indexu lomu vzduchu, Jemná mechanika a optika*, 2000, roč. 45, č. 7-8, p. 224-228, ISSN 0447-6441.
- [16] Kravcov Ju., Orlov Ju., *Geometričeskaja optika neodnorodnyh sred*, Nauka, Moskva, 1980, 304 p.
- [17] Mikš A., Pospíšil J., *Počítačová simulace vlivu atmosféry na geodetická měření*, *Stavební obzor*, 1998, 7/7, p. 220 – 225, ISSN 1210-4027.
- [18] Hauf M. a kol., *Geodézie - technický průvodce*, SNTL - nakladatelství technické literatury, Prague 1982, 544s.
- [19] Kašpar M., Pospíšil J., Štroner M., Křemen T., Tejkal M., *Laserové skenovací systémy ve stavebnictví*, 1. ed., Vega, 2003, 112 p., ISBN 80-900860-3-9.
- [20] Štroner, M., Pospíšil, J., *Terestrické skenovací systémy*, 1. ed, Praha: Česká technika - nakladatelství ČVUT, 2008, 187 p., ISBN 978-80-01-04141-3.
- [21] Kašpar M., Pospíšil J., Štroner, M., Křemen T., Tejkal M., *Laser Scanning in Civil Engineering and Land Surveying*, Vega, 2004, 103 p., ISBN 80-900860-7-1.

- [22] Pospíšil J., Štroner M., Moderní geodetické technologie a přístroje pro laserové skenování, *Stavební obzor*, 2005, 14/8, p. 249-253, ISSN 1210-4027.
- [23] Křemen T., Koska B., Pospíšil J., Kyrinovič P., Haličková J., Kopáček A., Checking of Crane Rails by Terrestrial Laser Scanning Technology, Measuring the Changes, 13th FIG Symposium on Deformation Measurement and Analysis, Lisbon, 2008.

ANNEX A.
LOCATION OF LOAD AND MEASUREMENTS



LIST OF FIGURES

Fig. A.1 - Mechanical load 118

Fig. A.2 - Fire load 119

Fig. A.3 - Location of thermocouples for gas temperatures and radiometers 120

Fig. A.4 - Location of gas thermocouples 121

Fig. A.5 - Location of thermocouples for structural temperature 122

Fig. A.6 - Location of measurements on Angelina beams AS2 and AS4 123

Fig. A.7 - Location of measurements on Angelina beams AS5 and AS6 124

Fig. A.8 - Location of measurements on beams with corrugated web CS2 and CS3 125

Fig. A.9 - Location of measurements on the internal column, composite slab, concrete and
plaster walls 126

Fig. A.10 - Location of measurements on the external column 127

Fig. A.11 - Location of measurements for vertical and horizontal deflection 128

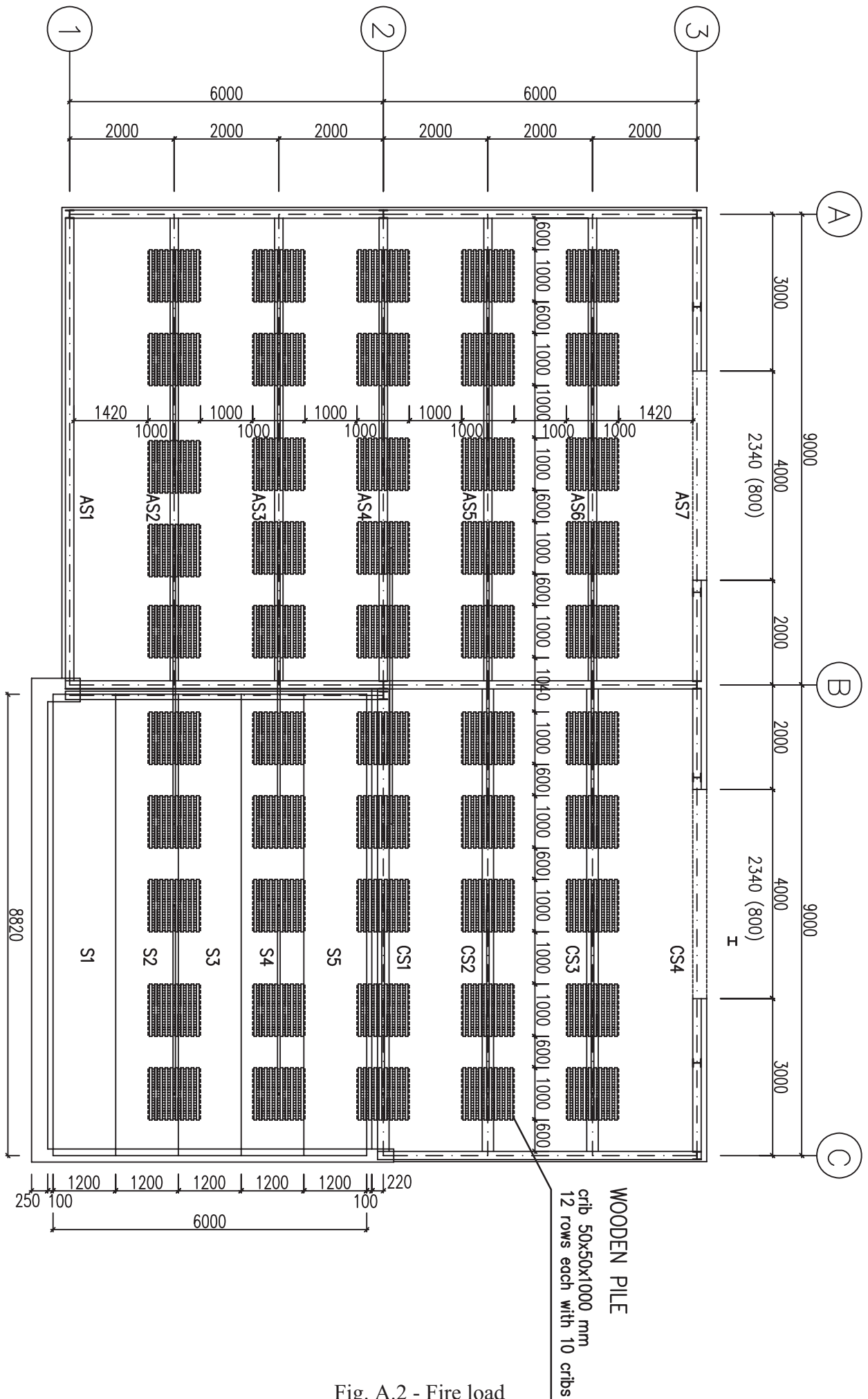


Fig. A.2 - Fire load

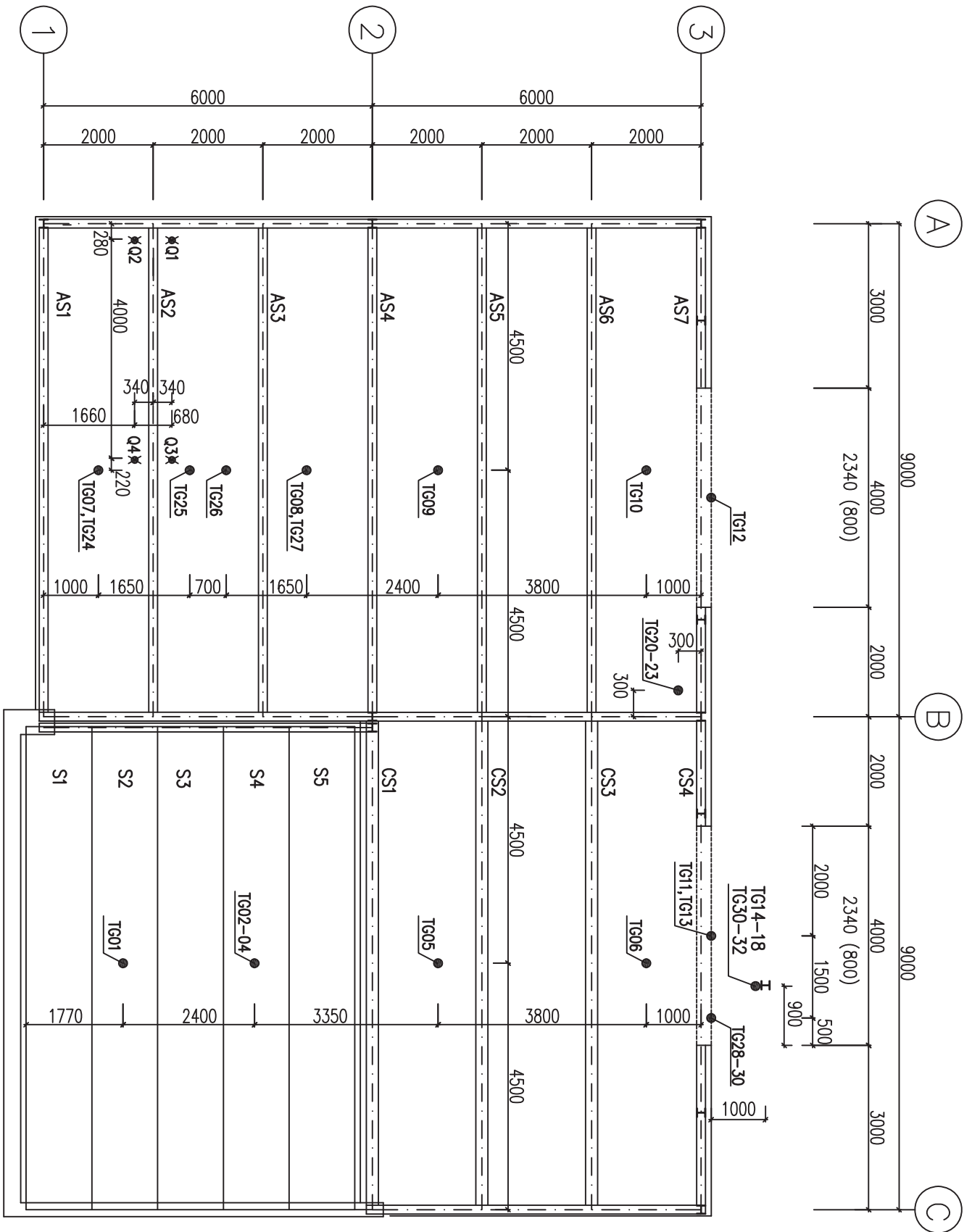


Fig. A.3 - Location of thermocouples for gas temperatures and radiometers

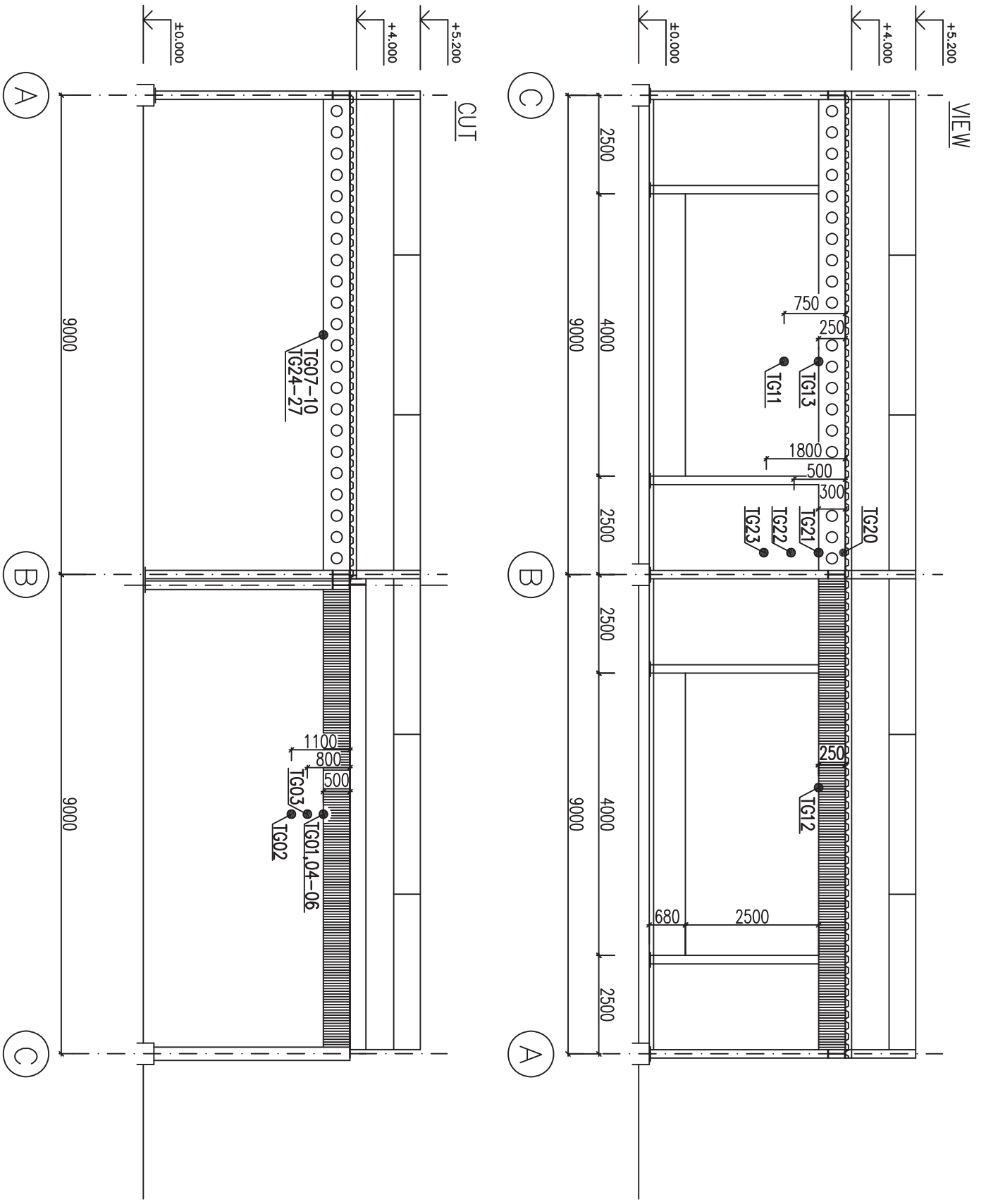


Fig. A.4 - Location of gas thermocouples

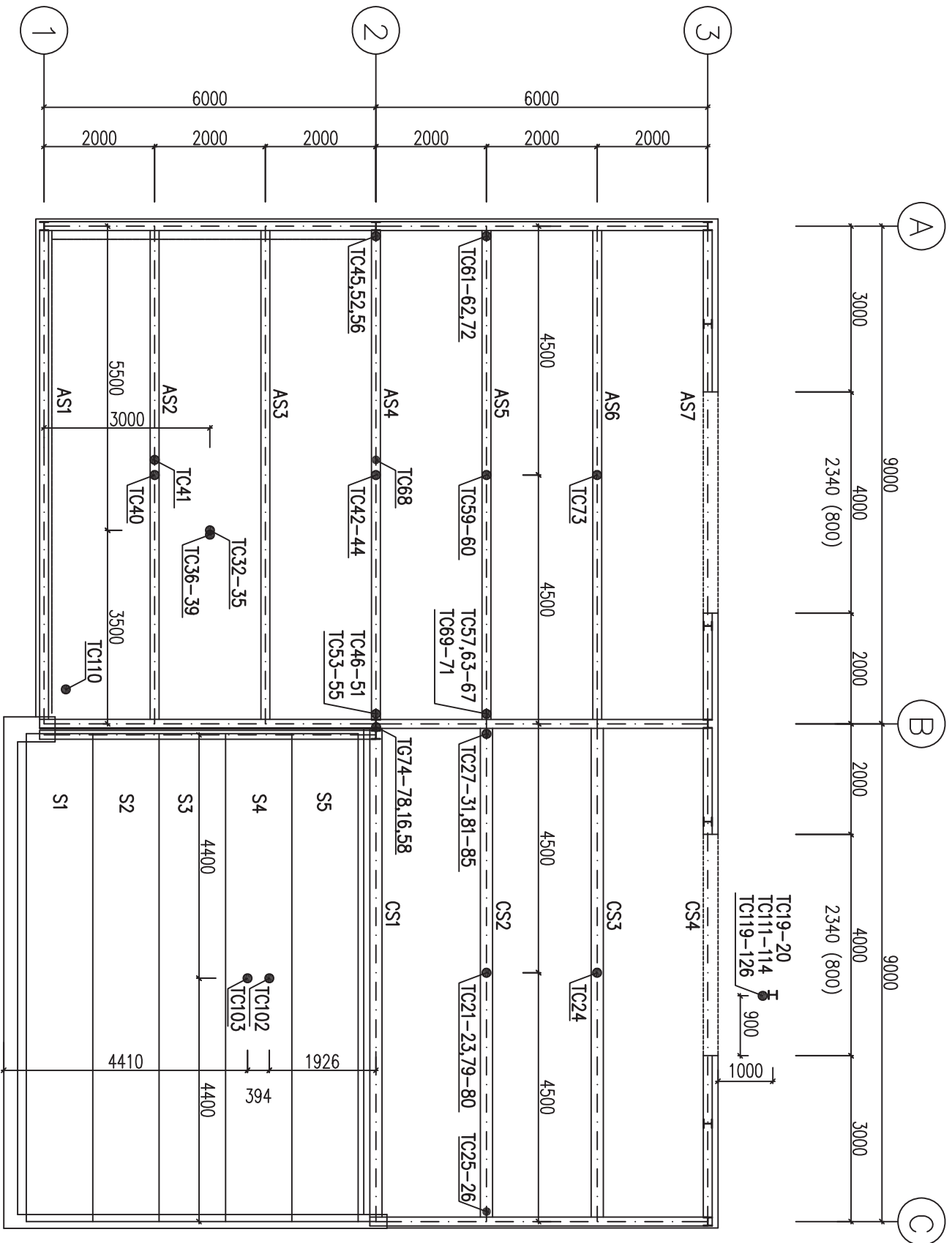
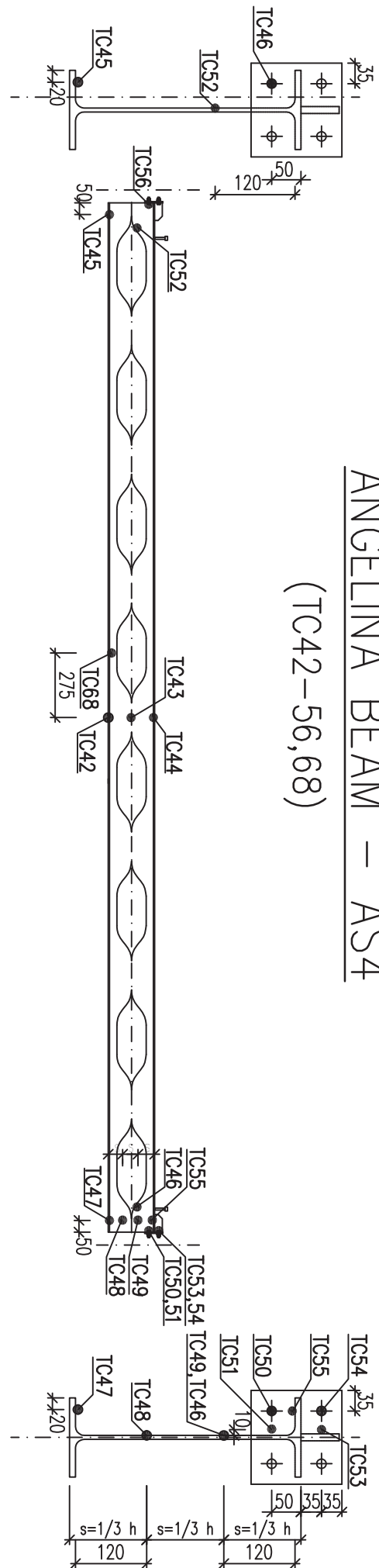


Fig. A.5 - Location of thermocouples for structural temperature

ANGELINA BEAM - AS4
(TC42-56,68)



ANGELINA BEAM - AS2
(TC40-41)

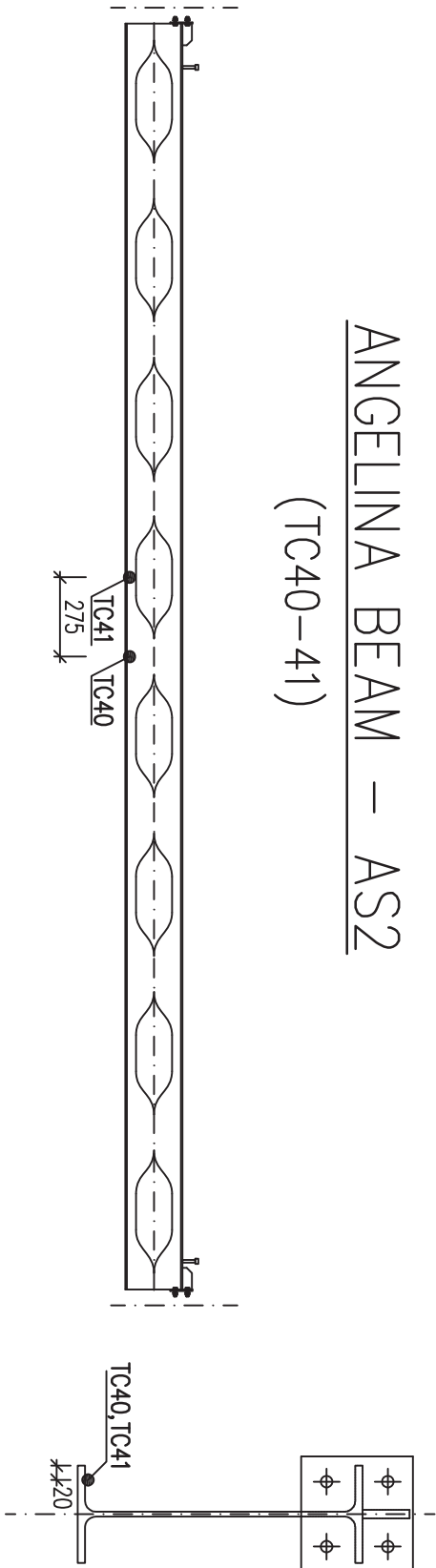
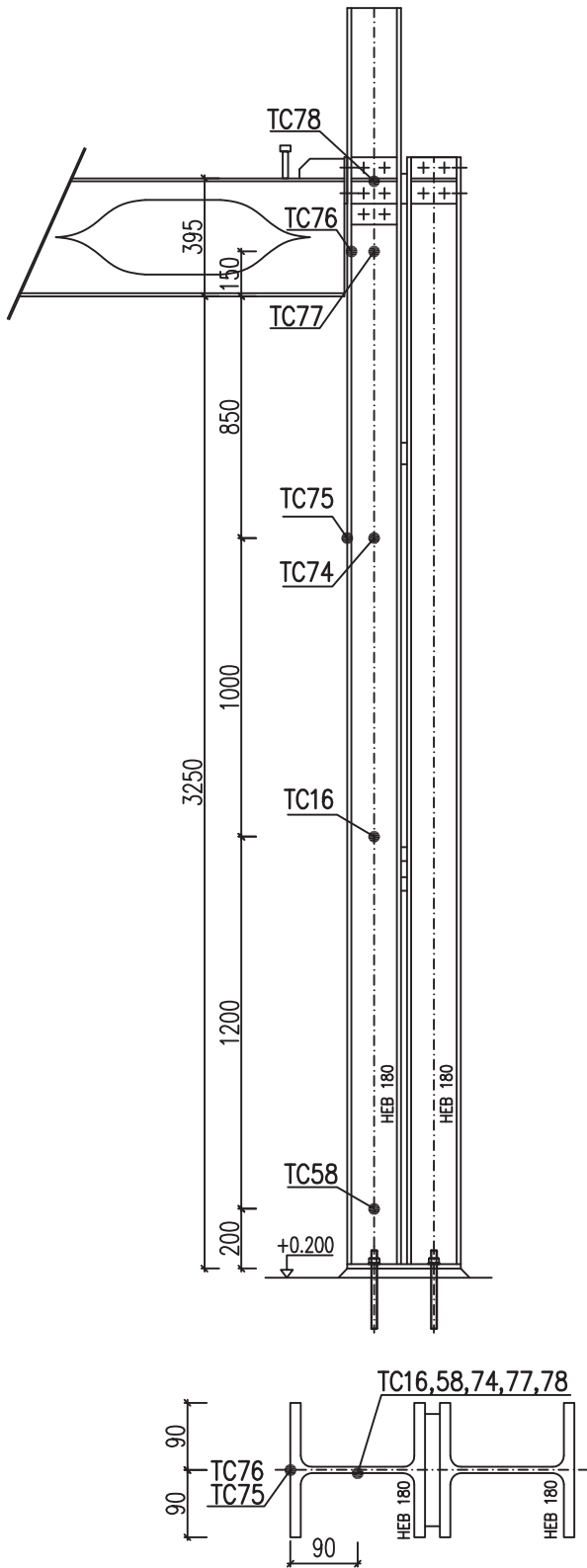
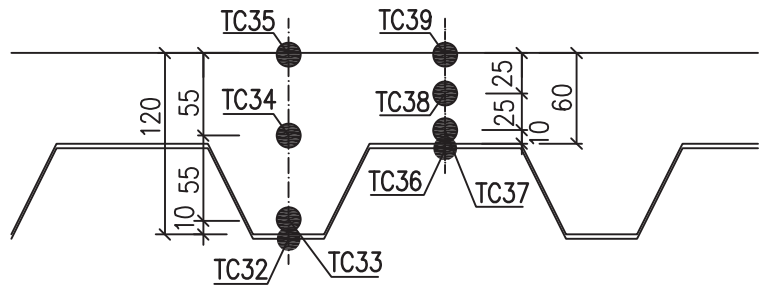


Fig. A.6 - Location of measurements on Angelina beams AS2 and AS4

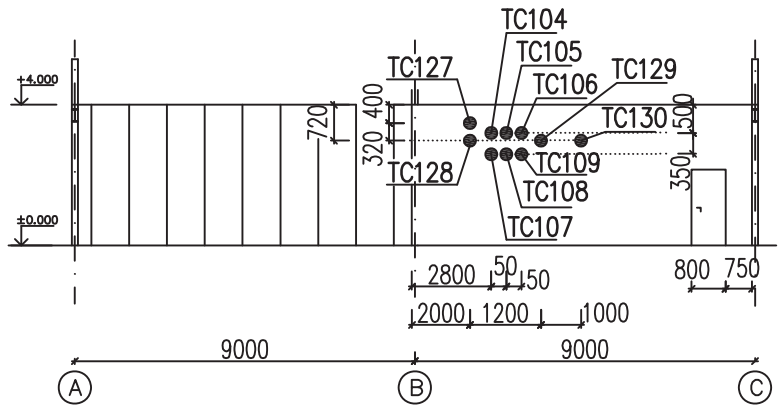
INTERNAL COLUMN
(TC 74-78,16,58)



COMPOSITE SLAB
(TC32-39)



CONCRETE WALL
(TC104-109, 127-130)



PLASTER WALL
(PL01-06)

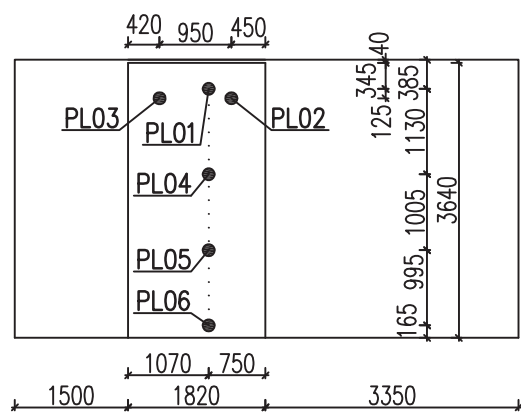


Fig. A.9 - Location of measurements on internal column, composite slab, concrete and plaster walls

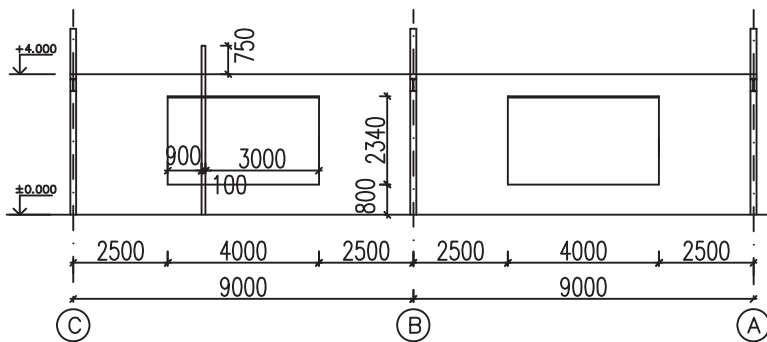
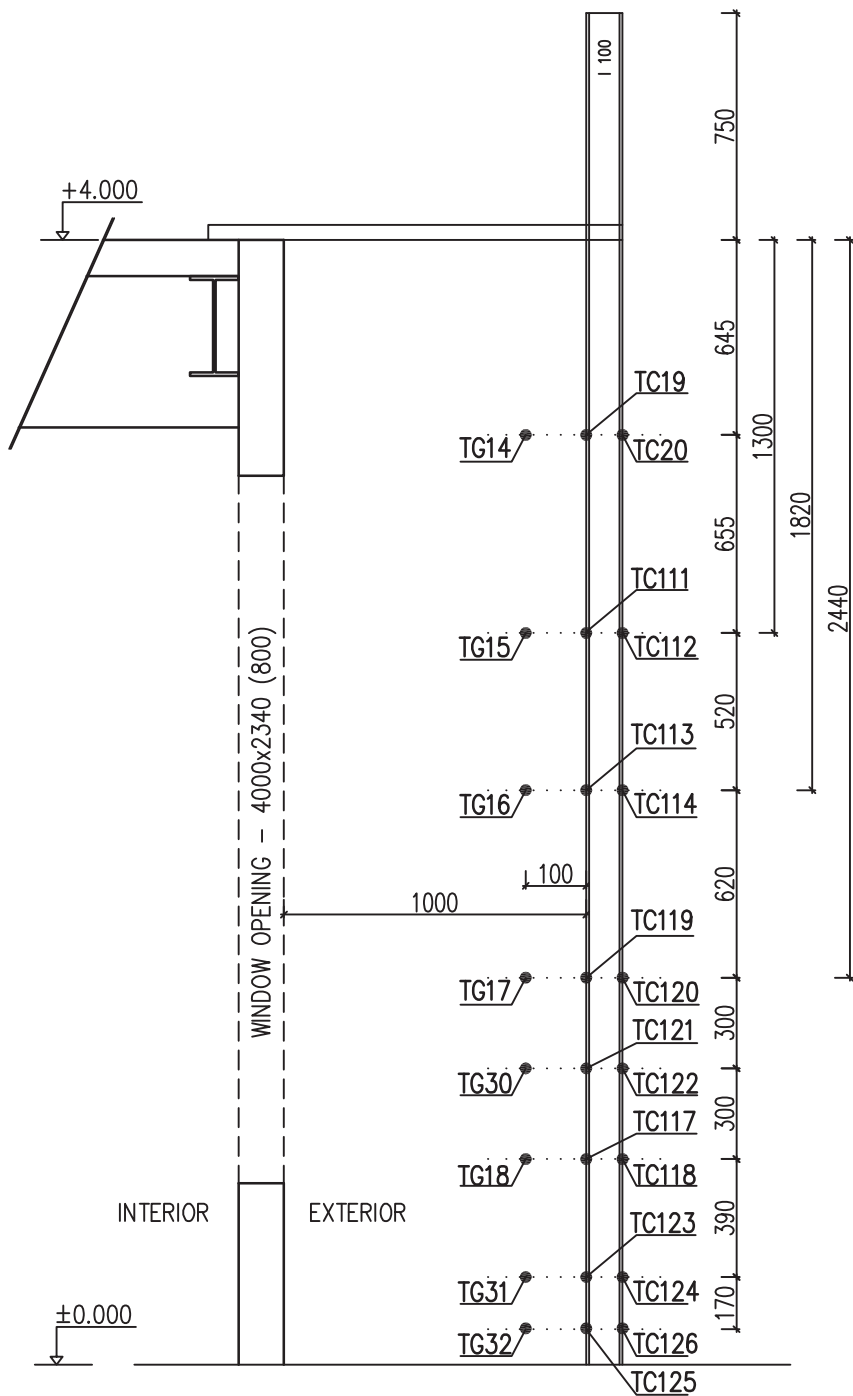


Fig. A.10 - Location of measurements on the external column

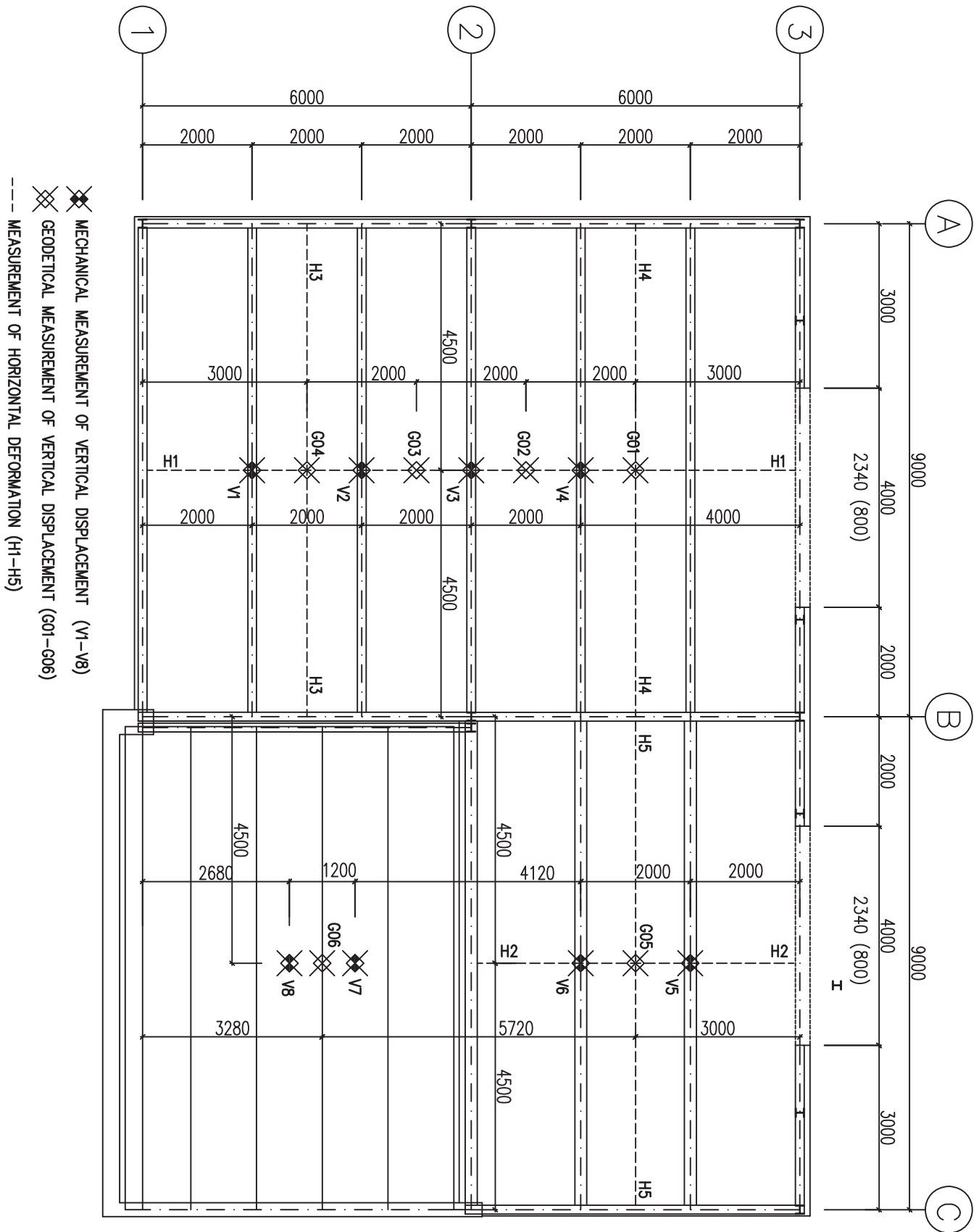


Fig. A.11 - Location of measurements for vertical and horizontal deflection

ANNEX B.
TABLES OF MEASURED VALUES



LIST OF TABLES

| | |
|---|-----|
| Tab. B.1 - Gas temperatures in fire compartment; TG01-07 | 132 |
| Tab. B.2 - Gas temperatures in fire compartment; TG08-13 | 132 |
| Tab. B.3 - Gas temperatures in fire compartment; TG20-26 | 133 |
| Tab. B.4 - Gas temperatures in fire compartment; TG27-30 | 133 |
| Tab. B.5 - Gas temperatures measured close to external column; TG14-18, TG30-32 | 134 |
| Tab. B.6 - Steel temperatures on external column; TC19-20, TC111-117 | 134 |
| Tab. B.7 - Steel temperatures on external column; TC118-126 | 135 |
| Tab. B.8 - Steel temperatures on internal column B2 | 135 |
| Tab. B.9 - Steel temperatures on beams with corrugated web CS2; TC27-31, TC81-85 | 136 |
| Tab. B.10 - Steel temperatures on beam with corrugated web CS2; TC21-23, 25-26, 79-80 | 137 |
| Tab. B.11 - Steel temperatures on beams AS2, AS6 and CS3 | 138 |
| Tab. B.12 - Steel temperatures on cellular Angelina beam AS4; TC42-45, 52, 56, 58 | 139 |
| Tab. B.13 - Steel temperatures on cellular Angelina beam AS4; TC46-51, TC53-55 | 140 |
| Tab. B.14 - Steel temperatures on cellular Angelina beam AS5; TC59-62, TC72 | 141 |
| Tab. B.15 - Steel temperatures on cellular Angelina beam AS5; TC57, 63-67, 69-71 | 142 |
| Tab. B.16 - Temperatures of the concrete slab | 143 |
| Tab. B.17 - Temperatures at two sandwich walls and at the hollow core panel | 144 |
| Tab. B.18 - Temperatures on concrete wall; TC104-109 | 145 |
| Tab. B.19 - Temperatures on concrete wall; TC127 | 146 |
| Tab. B.20 - Temperatures on concrete wall; TC128 | 146 |
| Tab. B.21 - Temperatures on plaster wall; PL02 | 147 |
| Tab. B.22 - Temperatures on plaster wall; PL03 | 148 |
| Tab. B.23 - Temperatures on plaster wall; PL05 | 149 |
| Tab. B.24 - Vertical deflections of the floor structure | 149 |
| Tab. B.25 - Horizontal deformations of the floor structure | 150 |
| Tab. B.26 - Temperatures and pressures in the concrete wall | 150 |
| Tab. B.27 - Flux density of the heat | 151 |

Tab. B.1 - Gas temperatures in fire compartment; TG01-07

| Time | TG01 | TG02 | TG03 | TG04 | TG05 | TG06 | TG07 |
|-------|-------|-------|-------|-------|-------|-------|-------|
| [min] | [°C] |
| 0 | 31.4 | 26.2 | 26.5 | 28.2 | 26.8 | 22.3 | 18.8 |
| 5 | 239.2 | 148.7 | 151.4 | 155.6 | 185.0 | 168.8 | 99.2 |
| 10 | 332.3 | 347.4 | 347.6 | 348.0 | 468.9 | 426.1 | 419.8 |
| 15 | 386.6 | 379.9 | 389.1 | 393.2 | 514.9 | 513.2 | 443.8 |
| 20 | 532.0 | 548.6 | 576.7 | 611.2 | 717.6 | 658.8 | 413.5 |
| 25 | 545.0 | 560.8 | 574.0 | 589.0 | 696.2 | 671.1 | 574.9 |
| 30 | 783.8 | 923.4 | 914.7 | 898.1 | 877.0 | 804.4 | 675.5 |
| 35 | 691.8 | 745.5 | 752.9 | 755.9 | 810.9 | 763.3 | 636.2 |
| 40 | 761.5 | 840.9 | 834.7 | 824.9 | 836.6 | 770.3 | 715.5 |
| 45 | 768.0 | 799.2 | 800.8 | 804.4 | 837.1 | 776.0 | 769.9 |
| 50 | 738.4 | 770.2 | 768.6 | 767.9 | 769.2 | 699.5 | 890.7 |
| 55 | 764.6 | 804.3 | 809.6 | 817.3 | 762.4 | 682.1 | 951.7 |
| 60 | 723.2 | 745.5 | 749.8 | 759.9 | 738.8 | 659.8 | 937.3 |
| 65 | 85.5 | 81.5 | 88.4 | 91.0 | 209.5 | 208.5 | 87.5 |
| 70 | 68.8 | 65.7 | 69.9 | 77.1 | 180.6 | 197.7 | 45.1 |
| 75 | 56.2 | 51.4 | 56.5 | 59.9 | 130.8 | 148.2 | 34.7 |
| 80 | 42.0 | 32.3 | 34.6 | 36.5 | 106.5 | 106.0 | 33.7 |
| 85 | 45.1 | 38.5 | 39.8 | 40.3 | 106.0 | 108.7 | 31.3 |

Tab. B.2 - Gas temperatures in fire compartment; TG08-13

| Time | TG08 | TG09 | TG10 | TG11 | TG12 | TG13 |
|-------|-------|-------|-------|-------|-------|-------|
| [min] | [°C] | [°C] | [°C] | [°C] | [°C] | [°C] |
| 0 | 20.3 | 20.1 | 19.6 | 20.9 | 22.0 | 21.1 |
| 5 | 82.7 | 94.5 | 91.1 | 99.4 | 170.2 | 136.6 |
| 10 | 316.9 | 377.0 | 349.9 | 342.8 | 382.0 | 273.3 |
| 15 | 497.1 | 534.2 | 512.8 | 516.2 | 500.7 | 451.3 |
| 20 | 546.2 | 625.6 | 628.2 | 600.2 | 616.8 | 572.5 |
| 25 | 742.4 | 756.2 | 781.8 | 780.8 | 660.7 | 611.0 |
| 30 | 798.4 | 827.8 | 777.6 | 749.5 | 749.1 | 699.3 |
| 35 | 819.4 | 851.7 | 845.2 | 832.8 | 709.5 | 692.7 |
| 40 | 851.8 | 859.7 | 830.9 | 809.4 | 715.3 | 644.6 |
| 45 | 942.5 | 922.2 | 840.5 | 819.4 | 727.3 | 695.6 |
| 50 | 947.4 | 901.7 | 782.0 | 751.6 | 681.6 | 664.3 |
| 55 | 923.0 | 889.6 | 795.9 | 769.8 | 665.9 | 637.8 |
| 60 | 931.0 | 887.7 | 782.8 | 754.8 | 640.6 | 588.1 |
| 65 | 65.3 | - | 52.6 | 316.2 | 146.8 | 77.9 |
| 70 | 41.0 | - | 32.9 | 370.8 | 140.4 | 72.3 |
| 75 | 33.1 | - | 25.5 | 308.0 | 91.0 | 50.4 |
| 80 | 27.9 | - | 28.8 | 159.6 | 71.9 | 47.9 |
| 85 | 27.8 | - | 24.9 | 21.4 | 83.7 | 42.5 |

Tab. B.3 - Gas temperatures in fire compartment; TG20-26

| Time | TG20 | TG21 | TG22 | TG23 | TG24 | TG25 | TG26 |
|-------------|-------------|-------------|-------------|-------------|-------------|-------------|-------------|
| [min] | [°C] |
| 0 | 14.1 | 14.5 | 15.0 | 13.1 | 14.3 | 12.7 | 12.7 |
| 5 | 26.9 | 27.8 | 27.4 | 23.3 | 30.1 | 27.5 | 26.7 |
| 10 | 190.2 | 193.8 | 189.3 | 146.7 | 193.0 | 167.2 | 161.7 |
| 15 | 396.1 | 386.7 | 369.4 | 290.5 | 434.4 | 383.2 | 378.2 |
| 20 | 550.5 | 543.3 | 486.6 | 404.0 | 401.7 | 427.4 | 427.6 |
| 25 | 676.8 | 670.5 | 593.0 | 503.8 | 520.8 | 528.7 | 527.7 |
| 30 | 765.6 | 739.5 | 688.8 | 537.2 | 555.5 | 581.9 | 592.4 |
| 35 | 857.1 | 831.8 | 782.7 | 612.5 | 667.8 | 691.7 | 697.9 |
| 40 | 840.1 | 839.8 | 817.5 | 718.0 | 675.4 | 692.5 | 690.9 |
| 45 | 805.9 | 806.5 | 788.3 | 701.2 | 740.8 | 763.2 | 769.2 |
| 50 | 814.5 | 817.0 | 802.9 | 724.8 | 794.4 | 850.6 | 869.6 |
| 55 | 783.2 | 783.4 | 770.2 | 665.9 | 898.8 | 930.4 | 927.8 |
| 60 | 761.4 | 769.2 | 756.8 | 660.9 | 941.0 | 967.3 | 959.9 |

Tab. B.4 - Gas temperatures in fire compartment; TG27-30

| Time | TG27 | TG28 | TG29 | TG30 |
|-------------|-------------|-------------|-------------|-------------|
| [min] | [°C] | [°C] | [°C] | [°C] |
| 0 | 14.1 | 14.0 | 11.8 | 12.8 |
| 5 | 28.1 | 25.5 | 20.2 | 16.6 |
| 10 | 158.9 | 194.4 | 64.0 | 24.9 |
| 15 | 377.4 | 331.7 | 65.2 | 46.2 |
| 20 | 476.0 | 487.6 | 279.1 | 75.7 |
| 25 | 576.5 | 567.2 | 257.3 | 128.3 |
| 30 | 644.4 | 649.6 | 318.8 | 141.7 |
| 35 | 749.6 | 783.1 | 528.6 | 227.9 |
| 40 | 725.4 | 631.3 | 233.4 | 192.2 |
| 45 | 838.7 | 510.4 | 201.3 | 166.8 |
| 50 | 948.3 | 675.1 | 494.8 | 188.9 |
| 55 | 941.2 | 456.6 | 277.4 | 143.0 |
| 60 | 945.8 | 488.7 | 188.1 | 122.5 |

Tab. B.5 - Gas temperatures measured close to external column; TG14-18, TG30-32

| Time | TG14 | TG15 | TG16 | TG17 | TG30 | TG18 | TG31 | TG32 |
|-------------|-------------|-------------|-------------|-------------|-------------|-------------|-------------|-------------|
| [min] | [°C] |
| 0 | 20.7 | 20.9 | 18.9 | 17.3 | 17.3 | 18.4 | 18.9 | 18.5 |
| 5 | 138.6 | 95.5 | 33.9 | 18.2 | 19.9 | 20.7 | 20.2 | 19.4 |
| 10 | 275.0 | 175.9 | 57.6 | 31.6 | 37.2 | 39.5 | 36.4 | 39.2 |
| 15 | 349.9 | 368.5 | 223.5 | 52.4 | 49.2 | 47.0 | 46.6 | 49.8 |
| 23 | 642.8 | 471.5 | 292.5 | 115.8 | 142.1 | 123.1 | 113.1 | 111.5 |
| 25 | 366.8 | 314.4 | 207.1 | 76.5 | 104.1 | 80.2 | 79.0 | 71.7 |
| 31 | 673.5 | 628.5 | 440.7 | 145.3 | 173.2 | 142.3 | 145.0 | 129.8 |
| 35 | 495.8 | 330.0 | 222.7 | 143.3 | 167.9 | 128.5 | 130.5 | 106.6 |
| 40 | 461.7 | 275.7 | 163.6 | 119.9 | 137.9 | 103.8 | 101.2 | 93.9 |
| 48 | 330.9 | 659.4 | 574.4 | 156.7 | 171.7 | 102.1 | 76.9 | 103.1 |
| 50 | 578.3 | 504.1 | 255.3 | 117.9 | 118.3 | 127.5 | 107.9 | 117.8 |
| 55 | 573.3 | 440.6 | 191.5 | 103.2 | 114.0 | 91.4 | 101.7 | 85.8 |
| 60 | 487.0 | 393.4 | 206.8 | 94.7 | 122.6 | 104.6 | 107.8 | 100.0 |
| 65 | 57.1 | 51.3 | 48.2 | 47.5 | 53.2 | 54.7 | 41.7 | 49.4 |
| 70 | 30.9 | 31.6 | 33.6 | 42.4 | 45.6 | 47.2 | 44.1 | 45.8 |
| 75 | 29.6 | 28.3 | 30.9 | 34.9 | 36.8 | 34.4 | 38.1 | 37.3 |
| 80 | 28.5 | 24.6 | 24.2 | 27.2 | 32.6 | 33.4 | 34.5 | 36.7 |

Tab. B.6 - Steel temperatures on external column; TC19-20, TC111-117

| Time | TC19 | TC20 | TC111 | TC112 | TC113 | TC114 | TC115 | TC116 | TC117 |
|-------------|-------------|-------------|--------------|--------------|--------------|--------------|--------------|--------------|--------------|
| [min] | [°C] | [°C] | [°C] | [°C] | [°C] | [°C] | [°C] | [°C] | [°C] |
| 0 | 25.9 | 25.2 | 26.5 | 25.6 | 18.5 | 18.5 | 16.6 | 16.4 | 16.8 |
| 5 | 41.9 | 44.8 | 35.9 | 32.4 | 24.8 | 22.6 | 21.4 | 18.8 | 19.0 |
| 10 | 134.5 | 124.4 | 113.7 | 95.2 | 72.9 | 53.9 | 55.2 | 38.9 | 45.9 |
| 15 | 235.4 | 226.0 | 222.7 | 190.0 | 149.5 | 108.0 | 106.5 | 76.5 | 87.6 |
| 20 | 274.8 | 239.6 | 268.3 | 222.3 | 205.3 | 147.3 | 171.7 | 116.6 | 137.9 |
| 25 | 369.5 | 315.3 | 353.3 | 288.9 | 304.5 | 224.7 | 287.5 | 201.5 | 256.5 |
| 32 | 433.0 | 423.3 | 451.5 | 380.4 | 391.1 | 300.1 | 383.2 | 282.8 | 341.3 |
| 35 | 407.4 | 358.3 | 408.2 | 348.4 | 382.2 | 305.6 | 388.5 | 303.2 | 335.9 |
| 40 | 374.2 | 322.5 | 372.2 | 314.5 | 369.5 | 294.7 | 387.7 | 298.6 | 334.0 |
| 45 | 382.2 | 339.1 | 376.2 | 317.1 | 364.9 | 291.8 | 383.2 | 293.7 | 335.0 |
| 49 | 380.6 | 382.1 | 483.5 | 439.0 | 417.1 | 343.2 | 359.0 | 282.7 | 306.9 |
| 55 | 365.7 | 331.2 | 355.3 | 304.5 | 326.6 | 265.9 | 327.0 | 250.8 | 283.0 |
| 60 | 365.0 | 329.0 | 338.9 | 288.8 | 310.9 | 253.6 | 313.7 | 243.4 | 284.6 |
| 65 | 221.1 | 193.0 | 222.1 | 197.4 | 219.8 | 182.6 | 220.5 | 183.1 | 214.7 |
| 70 | 140.1 | 126.5 | 158.0 | 143.0 | 163.4 | 140.3 | 166.2 | 142.6 | 159.0 |
| 75 | 95.9 | 87.7 | 118.6 | 107.4 | 126.4 | 107.4 | 129.1 | 111.3 | 121.4 |
| 80 | 67.4 | 61.6 | 90.6 | 82.1 | 98.2 | 84.1 | 101.4 | 86.2 | 97.8 |

Tab. B.7 - Steel temperatures on external column; TC118-126

| Time | TC118 | TC119 | TC120 | TC121 | TC122 | TC123 | TC124 | TC125 | TC126 |
|-------|-------|-------|-------|-------|-------|-------|-------|-------|-------|
| [min] | [°C] |
| 0 | 17.1 | 16.7 | 16.9 | 17.0 | 16.5 | 15.6 | 15.8 | 16.8 | 17.0 |
| 5 | 17.7 | 18.3 | 17.4 | 18.8 | 17.1 | 16.3 | 16.3 | 17.0 | 17.0 |
| 10 | 32.5 | 44.3 | 33.5 | 46.0 | 32.9 | 28.7 | 28.1 | 30.6 | 28.8 |
| 15 | 62.8 | 83.8 | 64.8 | 87.7 | 64.1 | 54.2 | 53.1 | 54.5 | 51.5 |
| 20 | 101.3 | 132.7 | 99.4 | 138.9 | 102.0 | 82.9 | 82.0 | 78.7 | 74.5 |
| 25 | 192.8 | 252.3 | 184.6 | 253.2 | 196.3 | 156.2 | 154.7 | 153.2 | 149.9 |
| 32 | 265.1 | 341.3 | 263.4 | 335.2 | 279.9 | 222.4 | 220.5 | 209.4 | 208.4 |
| 35 | 283.7 | 344.0 | 284.2 | 329.4 | 295.0 | 241.2 | 240.1 | 212.6 | 223.9 |
| 40 | 284.9 | 344.2 | 280.6 | 326.3 | 295.6 | 248.5 | 246.5 | 221.9 | 227.3 |
| 45 | 283.0 | 342.1 | 277.4 | 335.1 | 293.9 | 260.3 | 259.2 | 224.1 | 229.9 |
| 49 | 255.7 | 313.6 | 259.8 | 303.0 | 268.6 | 237.2 | 236.2 | 202.0 | 205.3 |
| 55 | 239.2 | 289.7 | 229.1 | 286.2 | 246.5 | 223.5 | 223.2 | 195.1 | 194.5 |
| 60 | 244.2 | 285.9 | 236.0 | 285.5 | 251.6 | 229.1 | 228.7 | 199.6 | 205.8 |
| 65 | 177.2 | 214.4 | 178.4 | 211.6 | 188.4 | 175.5 | 175.0 | 144.5 | 137.4 |
| 70 | 133.6 | 155.5 | 134.2 | 155.1 | 140.4 | 132.1 | 131.9 | 100.8 | 93.7 |
| 75 | 104.8 | 116.9 | 104.7 | 121.0 | 104.4 | 102.3 | 102.3 | 76.7 | 71.4 |
| 80 | 82.3 | 92.8 | 83.0 | 96.4 | 82.7 | 79.9 | 79.6 | 60.6 | 55.9 |

Tab. B.8 - Steel temperatures on internal column B2

| Time | TC16 | TC58 | TC74 | TC75 | TC76 | TC77 | TC78 |
|-------|------|------|-------|-------|-------|-------|-------|
| [min] | [°C] | [°C] | [°C] | [°C] | [°C] | [°C] | [°C] |
| 0 | 7.2 | 7.9 | 7.2 | 7.5 | 9.6 | 7.9 | 9.0 |
| 5 | 7.3 | 8.0 | 7.2 | 7.6 | 20.6 | 8.6 | 11.5 |
| 15 | 7.4 | 8.6 | 7.8 | 14.2 | 77.7 | 28.5 | 36.7 |
| 18 | 8.0 | 9.9 | 10.4 | 28.4 | 102.0 | 38.3 | 47.7 |
| 22 | 11.1 | 13.5 | 22.2 | 85.7 | 159.7 | 57.9 | 70.7 |
| 25 | 16.7 | 18.8 | 38.5 | 96.9 | 198.5 | 80.5 | 89.0 |
| 30 | 34.9 | 31.4 | 70.7 | 98.4 | 293.3 | 127.7 | 130.2 |
| 35 | 70.0 | 46.0 | 95.1 | 98.9 | 394.6 | 175.2 | 163.4 |
| 40 | 95.6 | 64.4 | 99.0 | 101.0 | 490.9 | 218.0 | 197.4 |
| 45 | 99.6 | 95.3 | 99.5 | 112.5 | 570.4 | 264.5 | 243.7 |
| 50 | 99.8 | 99.5 | 99.7 | 119.0 | 642.7 | 307.3 | 275.4 |
| 55 | 99.8 | 99.6 | 102.3 | 122.3 | 658.9 | 344.8 | 307.4 |
| 60 | 99.8 | 99.9 | 106.3 | 130.4 | 663.6 | 368.7 | 325.4 |

Tab. B.9 - Steel temperatures on beams with corrugated web CS2; TC27-31, TC81-85

| Time | TC 27 | TC 28 | TC 29 | TC 30 | TC 31 | TC 81 | TC 82 | TC 83 | TC 84 | TC 85 |
|-------|--------------|-------|-------|-------|-------|----------------------------------|-------|-------|-------|-------|
| | connection B | | | | | corrugated web near connection B | | | | |
| [min] | [°C] | [°C] | [°C] | [°C] | [°C] | [°C] | [°C] | [°C] | [°C] | [°C] |
| 0 | 10.8 | 8.3 | 8.4 | 7.7 | 7.9 | 12.7 | 11.9 | 11.2 | 11.5 | 12.8 |
| 5 | 21.2 | 16.1 | 14.1 | 8.0 | 8.2 | 40.8 | 31.5 | 36.6 | 38.1 | 42.4 |
| 10 | 100.5 | 47.9 | 37.9 | 11.8 | 11.1 | 203.9 | 149.9 | 157.5 | 165.2 | 217.5 |
| 15 | 237.2 | 84.5 | 68.9 | 22.2 | 19.9 | 370.0 | 303.9 | 286.7 | 288.3 | 385.4 |
| 20 | 354.3 | 118.2 | 99.6 | 37.2 | 33.8 | 447.4 | 403.6 | 364.0 | 357.0 | 460.7 |
| 25 | 566.8 | 191.5 | 155.7 | 59.0 | 53.5 | 658.0 | 622.6 | 555.7 | 562.0 | 672.9 |
| 30 | 679.8 | 245.0 | 203.9 | 96.3 | 98.4 | 705.8 | 694.1 | 616.1 | 622.6 | 725.7 |
| 35 | 777.7 | 307.4 | 263.6 | 111.0 | 101.9 | 770.0 | 770.4 | 694.2 | 694.5 | 789.9 |
| 40 | 823.8 | 354.5 | 311.9 | 135.4 | 114.9 | 798.8 | 806.1 | 734.1 | 739.4 | 814.8 |
| 45 | 822.0 | 387.8 | 347.4 | 160.6 | 136.2 | 804.5 | 812.5 | 743.6 | 748.2 | 816.2 |
| 50 | 823.5 | 417.8 | 375.9 | 184.1 | 154.9 | 802.6 | 812.7 | 748.6 | 753.5 | 815.0 |
| 55 | 792.7 | 424.3 | 388.3 | 203.3 | 171.1 | 745.2 | 758.3 | 707.6 | 712.8 | 758.8 |
| 60 | 777.1 | 428.5 | 394.3 | 218.4 | 184.1 | 733.4 | 745.1 | 695.3 | 702.0 | 749.5 |
| 65 | 670.4 | 403.8 | 395.6 | 227.6 | 190.2 | 499.5 | 542.8 | 531.4 | 532.0 | 505.0 |
| 70 | 525.0 | 365.3 | 362.8 | 232.9 | 199.6 | 371.8 | 416.8 | 416.4 | 425.8 | 363.8 |
| 75 | 426.7 | 330.3 | 329.9 | 233.3 | 205.7 | 306.6 | 339.1 | 349.0 | 364.0 | 295.5 |
| 80 | 359.0 | 300.8 | 300.8 | 232.0 | 206.1 | 267.0 | 292.7 | 305.0 | 324.0 | 256.6 |
| 85 | 309.1 | 276.6 | 275.8 | 230.4 | 203.4 | 234.9 | 253.6 | 268.9 | 292.7 | 224.4 |
| 90 | 271.2 | 257.4 | 257.5 | 225.3 | 199.3 | 209.3 | 225.6 | 239.6 | 265.9 | 198.6 |

Tab. B.10 - Steel temperatures on beams with corrugated web CS2; TC21-23, 25-26, 79-80

| Time | TC21 | TC22 | TC23 | TC79 | TC80 | TC26 | TC25 |
|-------|--------------------|-------|-------|-------|-------|--------------|-------|
| | the middle of beam | | | | | connection A | |
| [min] | [°C] | [°C] | [°C] | [°C] | [°C] | [°C] | [°C] |
| 0 | 12.7 | 16.3 | 12.0 | 14.9 | 14.4 | 10.1 | 11.0 |
| 5 | 32.5 | 80.2 | 34.5 | 60.4 | 66.4 | 19.0 | 21.3 |
| 10 | 157.3 | 321.0 | 134.2 | 247.5 | 252.2 | 48.9 | 83.1 |
| 15 | 334.4 | 464.7 | 246.4 | 405.6 | 381.3 | 75.5 | 169.6 |
| 20 | 496.7 | 567.2 | 360.6 | 527.0 | 494.3 | 123.1 | 294.4 |
| 25 | 658.2 | 651.0 | 471.3 | 636.0 | 590.9 | 182.4 | 504.0 |
| 30 | 719.4 | 732.7 | 555.9 | 724.6 | 684.6 | 260.5 | 655.3 |
| 35 | 744.1 | 723.7 | 602.2 | 719.5 | 693.1 | 291.9 | 698.6 |
| 40 | 773.2 | 760.0 | 645.8 | 754.9 | 735.4 | 360.6 | 780.2 |
| 45 | 781.6 | 763.0 | 666.3 | 761.7 | 743.8 | 392.6 | 793.6 |
| 50 | 767.7 | 734.8 | 663.6 | 739.3 | 725.4 | 400.0 | 760.5 |
| 55 | 746.5 | 713.7 | 654.2 | 717.5 | 708.4 | 406.9 | 739.0 |
| 60 | 728.7 | 698.4 | 642.7 | 702.3 | 695.0 | 409.5 | 719.4 |
| 65 | 614.4 | 422.7 | 549.2 | 465.4 | 480.5 | 384.4 | 624.4 |
| 70 | 498.7 | 335.2 | 473.7 | 381.3 | 398.0 | 352.6 | 518.3 |
| 75 | 413.7 | 271.9 | 408.4 | 314.1 | 334.3 | 322.6 | 434.2 |
| 80 | 356.4 | 234.5 | 360.5 | 268.7 | 294.0 | 296.8 | 376.7 |
| 85 | 312.6 | 210.9 | 324.6 | 245.3 | 265.3 | 274.8 | 330.2 |
| 90 | 282.0 | 187.8 | 296.6 | 217.2 | 240.4 | 260.6 | 298.4 |

Tab. B.11 - Steel temperatures on beams AS2, AS6 and CS3

| Time | TC 41 | TC 40 | TC 73 | TC 24 |
|-------|----------|-------|----------|----------|
| | Beam AS2 | | Beam AS6 | Beam CS3 |
| [min] | [°C] | [°C] | [°C] | [°C] |
| 0 | 11.6 | 10.7 | 12.9 | 13.3 |
| 5 | 21.2 | 21.9 | 21.5 | 28.9 |
| 18 | 350.8 | 347.0 | 350.5 | 370.8 |
| 20 | 365.9 | 361.5 | 413.8 | 438.9 |
| 21 | 377.0 | 373.2 | 435.5 | 483.0 |
| 29 | 507.9 | 498.7 | 660.9 | 660.3 |
| 32 | 535.6 | 526.4 | 697.8 | 715.2 |
| 34 | 608.6 | 597.1 | 747.2 | 715.1 |
| 36 | 649.4 | 637.3 | 785.9 | 723.9 |
| 38 | 657.6 | 644.2 | 778.8 | 735.0 |
| 41 | 665.2 | 652.2 | 782.6 | 733.2 |
| 44 | 700.0 | 686.1 | 785.2 | 726.8 |
| 48 | 733.5 | 720.3 | - | 720.1 |
| 52 | 838.2 | 809.6 | - | 702.9 |
| 55 | 940.4 | 911.6 | - | 689.7 |
| 57 | 946.5 | 930.4 | - | 681.4 |
| 61 | 969.4 | 963.1 | - | 662.2 |
| 90 | - | - | - | 268.1 |

Tab. B.12 - Steel temperatures on cellular Angelina beam AS4; TC42-45, 52, 56, 68

| Time | TC 45 | TC 52 | TC 56 | TC 68 | TC 42 | TC 43 | TC 44 |
|-------|--------------|-------|-------|--------------------|-------|-------|-------|
| | connection A | | | the middle of beam | | | |
| [min] | [°C] | [°C] | [°C] | [°C] | [°C] | [°C] | [°C] |
| 0 | 9.7 | 11.3 | 11.0 | 11.9 | 11.9 | 13.8 | 11.9 |
| 15 | 145.3 | 173.1 | 68.9 | 249.6 | 261.2 | 326.4 | 191.9 |
| 20 | 210.0 | 277.5 | 99.7 | 413.5 | 415.5 | 457.5 | 304.6 |
| 25 | 299.4 | 382.8 | 137.5 | 588.9 | 571.1 | 606.4 | 434.3 |
| 30 | 350.6 | 472.4 | 161.6 | 695.3 | 673.0 | 683.8 | 539.1 |
| 35 | 456.8 | 593.4 | 218.7 | 828.5 | 811.4 | 780.7 | 644.7 |
| 40 | 447.3 | 577.7 | 225.1 | 834.7 | 804.6 | 781.6 | 671.2 |
| 45 | 474.7 | 612.4 | 258.2 | 898.1 | 861.5 | 853.1 | 721.3 |
| 47 | 542.1 | 685.4 | 295.2 | 937.0 | 918.1 | 918.5 | 756.0 |
| 50 | 604.4 | 739.2 | 328.6 | 916.7 | 911.8 | 919.3 | 808.8 |
| 52 | 620.7 | 742.2 | 327.6 | 936.5 | 932.5 | 939.8 | 833.4 |
| 55 | 631.3 | 746.7 | 338.0 | 885.4 | 889.7 | 907.2 | 834.3 |
| 60 | 710.7 | 825.6 | 388.5 | - | 901.4 | 916.2 | 854.0 |
| 65 | 799.1 | 873.7 | 645.1 | - | - | - | - |
| 70 | 794.6 | 814.5 | 558.0 | - | - | - | - |
| 75 | 740.7 | 747.4 | 592.6 | - | - | - | - |
| 80 | 677.0 | 675.1 | 558.6 | - | - | - | - |
| 85 | 628.2 | 627.7 | 525.3 | - | - | - | - |
| 90 | 568.8 | 562.3 | 479.7 | - | - | - | - |

Tab. B.13 - Steel temperatures on cellular Angelina beam AS4; TC46-51, TC53-55

| Time | TC 46 | TC 47 | TC 48 | TC 49 | TC 50 | TC 51 | TC 53 | TC 54 | TC 55 |
|-------|--------------|-------|-------|-------|-------|-------|-------|-------|-------|
| | Connection B | | | | | | | | |
| [min] | [°C] | [°C] | [°C] | [°C] | [°C] | [°C] | [°C] | [°C] | [°C] |
| 0 | 11.5 | 10.0 | 10.9 | 10.4 | 9.8 | 10.2 | 9.6 | 9.6 | 10.4 |
| 15 | 195.6 | 134.1 | 193.4 | 163.3 | 96.2 | 79.3 | 26.1 | 23.6 | 99.1 |
| 20 | 281.4 | 211.7 | 283.5 | 239.3 | 142.6 | 115.2 | 32.8 | 38.2 | 152.2 |
| 25 | 450.5 | 360.2 | 434.4 | 384.4 | 252.2 | 157.8 | 77.9 | 73.5 | 237.9 |
| 30 | 568.3 | 476.0 | 536.2 | 486.1 | 276.2 | 205.9 | 87.4 | 93.9 | 303.3 |
| 35 | 682.1 | 585.1 | 622.7 | 581.3 | 345.1 | 304.6 | 87.3 | 100.4 | 395.5 |
| 40 | 728.0 | 658.3 | 670.4 | 633.1 | 395.6 | 364.0 | 95.7 | 101.2 | 466.8 |
| 45 | 808.3 | 715.5 | 726.1 | 693.7 | 446.2 | 422.6 | 119.6 | 114.1 | 523.3 |
| 47 | 817.6 | 727.4 | 735.8 | 702.7 | 463.3 | 440.1 | 132.7 | 129.7 | 538.1 |
| 50 | 858.9 | 748.3 | 772.9 | 734.5 | 479.2 | 467.3 | 148.0 | 142.8 | 557.8 |
| 52 | 854.0 | 758.7 | 785.8 | 750.4 | 493.8 | 482.5 | 157.7 | 135.5 | 570.4 |
| 55 | 818.9 | 751.4 | 769.0 | 738.4 | 500.6 | 490.3 | 167.3 | 136.6 | 574.4 |
| 60 | 805.4 | 749.9 | 762.6 | 731.8 | 520.0 | 504.8 | 195.5 | 156.0 | 587.8 |
| 65 | - | - | - | - | - | - | 193.1 | 152.8 | - |
| 70 | - | - | - | - | - | - | 186.8 | 152.7 | - |
| 75 | - | - | - | - | - | - | 173.3 | 146.7 | - |
| 80 | - | - | - | - | - | - | 157.1 | 140.1 | - |
| 85 | - | - | - | - | - | - | 140.7 | 132.2 | - |
| 90 | - | - | - | - | - | - | 125.0 | 122.3 | - |

Tab. B.14 - Steel temperatures on cellular Angelina beam AS5; TC59-62, TC72

| Time | TC 61 | TC 62 | TC 72 | TC 59 | TC 60 |
|-------|--------------|-------|-------|----------------|-------|
| | connection A | | | middle of beam | |
| [min] | [°C] | [°C] | [°C] | [°C] | [°C] |
| 0 | 9.9 | 9.7 | 10.4 | 12.4 | 12.1 |
| 20 | 251.2 | 108.1 | 292.1 | 456.7 | 457.2 |
| 25 | 359.0 | 148.0 | 391.4 | 597.3 | 626.9 |
| 30 | 485.5 | 201.1 | 492.6 | 678.9 | 723.7 |
| 35 | 678.1 | 296.7 | 667.8 | 805.8 | 854.0 |
| 40 | 617.0 | 284.2 | 625.4 | 794.5 | 845.6 |
| 43 | 601.4 | 289.3 | 617.8 | 803.9 | 848.2 |
| 45 | 635.6 | 328.9 | 660.7 | 833.4 | 861.7 |
| 48 | 738.1 | 391.5 | 771.8 | 878.2 | 880.8 |
| 50 | 760.1 | 403.8 | 809.4 | 866.7 | 862.3 |
| 52 | 784.3 | 445.2 | 819.6 | 891.5 | 883.9 |
| 55 | 760.5 | 442.3 | 790.8 | 865.1 | 846.9 |
| 60 | 789.9 | 476.2 | 848.5 | 879.2 | - |
| 63 | 788.2 | 746.7 | 880.2 | - | - |
| 70 | 772.2 | 703.5 | 759.4 | - | - |
| 75 | 725.4 | 647.3 | 687.2 | - | - |
| 80 | 676.1 | 594.7 | 625.3 | - | - |
| 85 | 575.9 | 530.0 | 552.5 | - | - |
| 90 | 510.1 | 484.5 | 493.7 | - | - |

Tab. B.15 - Steel temperatures on cellular Angelina beam AS5; TC57, 63-67, 69-71

| Time | TC 57 | TC 63 | TC 64 | TC 65 | TC 66 | TC 67 | TC 69 | TC 70 | TC 71 |
|-------|--------------|-------|-------|-------|-------|-------|-------|-------|-------|
| | connection B | | | | | | | | |
| [min] | [°C] | [°C] | [°C] | [°C] | [°C] | [°C] | [°C] | [°C] | [°C] |
| 0 | 10.9 | 11.3 | 11.0 | 10.2 | 8.4 | 8.1 | 7.4 | 7.3 | 8.2 |
| 20 | 375.6 | 314.3 | 336.9 | 302.2 | 107.8 | 95.1 | 44.3 | 37.9 | 107.8 |
| 25 | 554.5 | 475.3 | 491.7 | 456.9 | 163.3 | 148.5 | 69.4 | 59.3 | 170.2 |
| 30 | 643.9 | 579.0 | 594.6 | 559.2 | 221.4 | 200.9 | 100.0 | 86.1 | 232.8 |
| 35 | 736.0 | 679.0 | 697.1 | 663.0 | 294.8 | 265.6 | 124.7 | 101.3 | 313.5 |
| 40 | 769.3 | 713.8 | 738.2 | 706.5 | 336.4 | 308.0 | 147.9 | 107.6 | 360.2 |
| 43 | 783.5 | 719.5 | 759.2 | 725.4 | 351.4 | 330.3 | 153.6 | 116.6 | 378.3 |
| 45 | 791.6 | 727.1 | 771.5 | 733.8 | 366.6 | 343.7 | 162.4 | 121.7 | 392.8 |
| 48 | 804.8 | 737.7 | 787.4 | 747.7 | 382.9 | 362.1 | 184.4 | 134.8 | 411.8 |
| 50 | 807.6 | 740.8 | 791.9 | 751.6 | 389.2 | 371.4 | 198.1 | 143.4 | 422.0 |
| 52 | 803.0 | 742.6 | 795.1 | 755.5 | 397.0 | 381.0 | 210.3 | 153.4 | 433.7 |
| 55 | 776.0 | 731.2 | 774.7 | 736.9 | 396.2 | 385.0 | 225.8 | 166.8 | 438.6 |
| 60 | 768.2 | 728.7 | 767.9 | 728.8 | 407.1 | 394.7 | 246.5 | 190.7 | 451.8 |
| 63 | - | - | - | - | - | - | - | 172.2 | - |
| 70 | - | - | - | - | - | - | - | 156.2 | - |
| 75 | - | - | - | - | - | - | - | 133.8 | - |
| 80 | - | - | - | - | - | - | - | 119.9 | - |
| 85 | - | - | - | - | - | - | - | 122.1 | - |
| 90 | - | - | - | - | - | - | - | 96.3 | - |

Tab. B.16 - Temperatures of the concrete slab

| Time | TC 32 | TC 33 | TC 34 | TC 35 | TC 36 | TC 37 | TC 38 | TC 39 |
|-------|----------|-------|-------|-------|--------------|-------|-------|-------|
| | in a rib | | | | between ribs | | | |
| [min] | [°C] | [°C] | [°C] | [°C] | [°C] | [°C] | [°C] | [°C] |
| 0 | 8.5 | 7.6 | 7.9 | 10.9 | 9.6 | 8.4 | 8.1 | 10.8 |
| 6 | 21.9 | 10.7 | 8.1 | 11.2 | 26.3 | 9.1 | 8.3 | 11.1 |
| 15 | 111.4 | 60.0 | 12.9 | 12.0 | 120.2 | 22.8 | 11.9 | 12.3 |
| 20 | 149.8 | 95.6 | 22.5 | 14.4 | 115.2 | 51.8 | 19.4 | 15.1 |
| 26 | 410.0 | 100.2 | 45.1 | 20.2 | 372.7 | 97.8 | 36.2 | 24.1 |
| 27 | 382.3 | 100.3 | 47.6 | 21.2 | 358.2 | 98.0 | 39.0 | 25.8 |
| 34 | 577.3 | 100.0 | 63.2 | 35.2 | 529.3 | 99.9 | 24.5 | 42.0 |
| 38 | 582.8 | 100.0 | 72.8 | 49.1 | 529.8 | 99.1 | 25.6 | 51.2 |
| 41 | 646.2 | 116.4 | 95.0 | 61.3 | 587.8 | 100.4 | 35.4 | 60.1 |
| 45 | 753.2 | 139.6 | 101.6 | 69.6 | 685.8 | 100.4 | 29.4 | 80.9 |
| 52 | 895.0 | 186.8 | 100.3 | 84.7 | 797.2 | 44.5 | 46.8 | - |
| 54 | 866.6 | 216.1 | 93.0 | 84.2 | 781.6 | 28.2 | 22.6 | - |
| 56 | - | 227.4 | 84.2 | - | 789.7 | 51.6 | 51.5 | - |
| 60 | - | 46.4 | 43.2 | - | - | 32.4 | 34.9 | - |
| 66 | - | 37.8 | 37.5 | - | - | 39.4 | 84.1 | - |
| 70 | - | 30.9 | 31.4 | - | - | 32.7 | 69.6 | - |
| 80 | - | 18.6 | 19.1 | - | - | 21.4 | 54.9 | - |

Tab. B.17 - Temperatures at two sandwich walls and at the hollow core panel

| Time | TC102 | TC103 | TC03 | TC04 | TC05 | TC06 |
|-------|---------|-------|----------------|-------|-------|------|
| | Spiroll | | Sandwich walls | | | |
| [min] | [°C] | [°C] | [°C] | [°C] | [°C] | [°C] |
| 0 | 8.6 | 8.5 | 19.0 | 14.2 | 14.2 | 35.8 |
| 5 | 9.0 | 8.6 | 19.5 | 56.5 | 37.0 | 35.7 |
| 13 | 9.4 | 9.4 | 20.0 | 404.4 | 369.6 | 36.7 |
| 16 | 10.5 | 10.5 | 19.9 | 440.1 | 400.4 | 36.3 |
| 19 | 12.2 | 12.4 | 19.7 | 500.3 | 373.2 | 34.4 |
| 22 | 14.6 | 14.9 | 19.5 | 772.1 | 430.1 | 30.3 |
| 25 | 18.0 | 18.5 | 19.6 | 662.3 | 535.4 | 27.3 |
| 27 | 20.9 | 21.8 | 20.3 | 727.7 | 530.0 | 24.4 |
| 30 | 26.8 | 28.4 | 22.8 | 930.1 | 613.6 | 24.8 |
| 34 | 38.7 | 41.8 | 26.9 | 722.0 | 608.1 | 26.4 |
| 37 | 56.0 | 64.4 | 30.0 | 866.1 | 655.1 | 28.3 |
| 40 | 99.0 | 87.1 | 32.2 | 821.5 | 674.8 | 30.0 |
| 43 | 100.5 | 94.0 | 32.8 | 799.3 | 703.7 | 30.1 |
| 48 | 100.7 | 99.0 | 35.0 | 768.0 | 779.4 | 32.0 |
| 52 | 100.5 | 100.6 | 36.2 | 723.5 | 883.9 | 31.8 |
| 54 | 100.3 | 100.4 | 35.4 | 716.3 | 900.2 | 30.1 |
| 57 | 100.2 | 100.1 | 35.6 | 715.6 | 955.6 | 29.3 |
| 60 | 100.1 | 100.0 | 36.2 | 693.0 | 934.5 | 29.2 |

Tab. B.18 - Temperatures on concrete wall; TC104-109

| Time | TC104 | TC105 | TC106 | TC107 | TC108 | TC109 |
|-------------|--------------|--------------|--------------|--------------|--------------|--------------|
| [min] | [°C] | [°C] | [°C] | [°C] | [°C] | [°C] |
| 0 | 10.2 | 11.2 | 11.7 | 11.0 | 10.9 | 11.3 |
| 5 | 10.8 | 11.7 | 11.7 | 11.9 | 11.2 | 11.2 |
| 10 | 15.7 | 13.5 | 12.5 | 18.6 | 13.7 | 11.6 |
| 15 | 26.6 | 18.9 | 14.2 | 32.1 | 20.9 | 13.4 |
| 20 | 40.4 | 28.1 | 18.2 | 47.5 | 30.8 | 16.3 |
| 25 | 62.8 | 41.8 | 23.9 | 74.5 | 45.9 | 20.9 |
| 30 | 91.4 | 59.8 | 32.9 | 102.5 | 67.5 | 28.5 |
| 35 | 99.8 | 88.4 | 47.7 | 117.8 | 96.9 | 42.1 |
| 40 | 99.9 | 99.3 | 72.4 | 261.5 | 99.9 | 72.2 |
| 45 | 102.0 | 100.3 | 97.3 | 295.5 | 110.0 | 99.5 |
| 50 | 166.8 | 100.3 | 100.3 | 202.7 | 101.9 | 100.0 |
| 55 | 260.7 | 100.7 | 100.0 | 230.0 | 100.7 | 99.8 |
| 60 | 300.3 | 192.1 | 100.0 | 355.4 | 100.5 | 99.6 |
| 62 | 307.5 | 207.1 | 100.0 | 265.2 | 100.3 | 99.6 |
| 70 | 229.5 | 193.2 | 113.8 | 181.1 | 108.2 | 99.7 |
| 75 | 197.5 | 175.8 | 113.9 | 159.7 | 121.1 | 99.6 |
| 80 | 175.4 | 160.8 | 112.2 | 146.1 | 118.5 | 99.8 |
| 85 | 159.2 | 148.7 | 110.8 | 133.4 | 114.7 | 99.6 |
| 90 | 150.3 | 141.4 | 109.4 | 124.9 | 112.8 | 99.6 |

Tab. B.19 - Temperatures on concrete wall; TC127

| Time | TC127 | | | | | |
|-------|-------|-------|-------|-------|-------|--------|
| | 0 mm | 10 mm | 20 mm | 30 mm | 50 mm | 70 mm |
| [min] | [°C] | [°C] | [°C] | [°C] | [°C] | [°C] |
| 0 | 21.6 | 20.2 | 20.0 | 19.1 | 22.1 | 21.7 |
| 5 | 26.5 | 24.7 | 27.8 | 26.4 | 29.8 | 27.5 |
| 10 | 39.1 | 38.1 | 38.9 | 34.4 | 37.3 | 36.3 |
| 15 | 65.1 | 63.2 | 64.9 | 57.4 | 60.3 | 59.4 |
| 20 | 90.6 | 89.0 | 90.4 | 80.4 | 82.9 | 83.6 |
| 25 | 148.9 | 147.7 | 149.0 | 127.7 | 130.3 | 128.3 |
| 30 | 182.5 | 190.9 | 190.8 | 163.1 | 162.9 | 160.6 |
| 35 | 281.5 | 276.8 | 274.2 | 221.3 | 219.2 | 216.6 |
| 40 | 325.0 | 315.9 | 311.5 | 286.1 | 261.3 | 260.0 |
| 45 | 355.3 | 342.0 | 335.8 | 325.2 | 316.2 | 311.5 |
| 50 | 404.8 | 386.2 | 374.4 | 364.4 | 350.7 | 3400.7 |
| 55 | 460.0 | 449.9 | 440.2 | 431.5 | 415.0 | 403.8 |
| 60 | 469.0 | 462.5 | 455.3 | 448.9 | 433.9 | 422.8 |
| 65 | 445.5 | 440.6 | 437.1 | 432.2 | 418.1 | 408.0 |
| 70 | 265.9 | 261.9 | 257.7 | 253.8 | 243.4 | 234.8 |
| 75 | 204.0 | 201.0 | 197.8 | 195.0 | 186.8 | 179.8 |
| 80 | 167.2 | 164.8 | 162.4 | 160.0 | 153.3 | 147.5 |
| 85 | 138.2 | 136.3 | 134.4 | 132.7 | 127.2 | 121.9 |
| 90 | 121.3 | 119.6 | 117.9 | 116.4 | 111.6 | 106.7 |

Tab. B.20 - Temperatures on concrete wall; TC128

| Time | TC128 | | | | | |
|-------|-------|-------|-------|-------|-------|-------|
| | 0 mm | 10 mm | 20 mm | 30 mm | 50 mm | 70 mm |
| [min] | [°C] | [°C] | [°C] | [°C] | [°C] | [°C] |
| 0 | 13.1 | 13.3 | 13.8 | 18.3 | 16.7 | 14.2 |
| 5 | 12.2 | 12.7 | 13.2 | 16.6 | 16.3 | 14.0 |
| 10 | 13.0 | 13.4 | 13.4 | 16.4 | 16.6 | 14.0 |
| 15 | 10.9 | 11.2 | 11.4 | 14.1 | 15.1 | 12.4 |
| 20 | 12.6 | 13.2 | 14.1 | 17.4 | 22.7 | 16.9 |
| 25 | 15.1 | 16.4 | 19.2 | 23.0 | 35.6 | 24.8 |
| 30 | 20.9 | 22.5 | 27.1 | 33.8 | 57.6 | 36.4 |
| 35 | 27.5 | 34.1 | 43.4 | 88.4 | 139.4 | 62.2 |

Tab. B.21 - Temperatures on plaster wall; PL02

| Time [min] | PL02 | | | | | |
|---------------|-----------------|--------------|---------------|---------------|---------------|---------------|
| | - 10 mm [°C] | 0 mm [°C] | 10 mm [°C] | 20 mm [°C] | 40 mm [°C] | 60 mm [°C] |
| 0 | 21.6 | 20.6 | 20.9 | 20.6 | 18.7 | 18.2 |
| 5 | 48.3 | 40.3 | 25.8 | 25.6 | 19.4 | 18.8 |
| 10 | 161.0 | 128.6 | 54.9 | 47.6 | 20.8 | 19.0 |
| 15 | 274.2 | 228.4 | 118.6 | 72.4 | 24.3 | 19.2 |
| 20 | 303.5 | 261.5 | 143.5 | 81.4 | 34.9 | 21.3 |
| 25 | 584.8 | 520.5 | 241.9 | 142.4 | 47.4 | 25.7 |
| 30 | 533.5 | 482.0 | 289.3 | 139.0 | 60.6 | 25.1 |
| 35 | 584.4 | 545.8 | 364.1 | 152.4 | 43.9 | - |
| 40 | 583.3 | 543.7 | 363.4 | 152.7 | 43.8 | 1.6 |
| 45 | 628.3 | 594.9 | 424.6 | 168.0 | 40.4 | 0.9 |
| 50 | 598.9 | 569.8 | 434.4 | 163.0 | 37.2 | 4.5 |
| 55 | 603.3 | 570.6 | 433.7 | 164.1 | 37.9 | 10.2 |
| 60 | 638.6 | 604.3 | 468.6 | 174.7 | 36.1 | 12.3 |
| 65 | 668.4 | 617.0 | 492.3 | 180.3 | 34.1 | 11.1 |
| 70 | 284.4 | 298.6 | 326.0 | 102.1 | 62.3 | 39.3 |
| 75 | 223.3 | 241.9 | 263.2 | 86.8 | 71.2 | 47.7 |
| 80 | 185.9 | 202.3 | 222.2 | 77.1 | 76.1 | 52.4 |
| 85 | 156.0 | 171.2 | 193.1 | 69.5 | 78.1 | 54.6 |
| 90 | 135.8 | 151.1 | 172.9 | 64.2 | 79.1 | 56.4 |

Tab. B.22 - Temperatures on plaster wall; PL03

| Time [min] | PL03 | | | | | |
|---------------|-----------------|--------------|---------------|---------------|---------------|---------------|
| | - 10 mm [°C] | 0 mm [°C] | 10 mm [°C] | 20 mm [°C] | 40 mm [°C] | 60 mm [°C] |
| 0 | 19.2 | 18.7 | 21.2 | 21.4 | 21.0 | 19.5 |
| 5 | 39.0 | 28.9 | 23.6 | 21.1 | 20.7 | 20.4 |
| 10 | 129.7 | 85.5 | 49.2 | 30.7 | 21.3 | 20.9 |
| 15 | 251.8 | 187.2 | 111.3 | 63.8 | 26.6 | 22.5 |
| 20 | 294.4 | 238.7 | 145.1 | 89.9 | 37.3 | 24.8 |
| 25 | 582.4 | 498.2 | 263.1 | 134.8 | 51.2 | 31.8 |
| 30 | 537.2 | 472.6 | 304.2 | 168.1 | 67.7 | 37.5 |
| 35 | 635.3 | 591.0 | 405.3 | 220.5 | 84.3 | 46.9 |
| 40 | 643.2 | 592.1 | 420.3 | 251.2 | 97.9 | 57.3 |
| 45 | 704.4 | 657.0 | 486.5 | 308.7 | 112.0 | 69.5 |
| 50 | 694.0 | 652.8 | 508.0 | 345.4 | 121.8 | 80.0 |
| 55 | 683.6 | 644.0 | 508.2 | 360.3 | 129.4 | 88.8 |
| 60 | 718.9 | 678.1 | 543.3 | 394.8 | 139.2 | 95.9 |
| 65 | 731.4 | 690.6 | 561.5 | 418.4 | 148.6 | 100.7 |
| 70 | 388.8 | 415.0 | 400.4 | 343.2 | 143.2 | 98.0 |
| 75 | 315.3 | 345.9 | 336.5 | 293.8 | 138.3 | 96.6 |
| 80 | 272.1 | 298.5 | 291.9 | 259.0 | 133.4 | 94.8 |
| 85 | 237.1 | 263.3 | 259.3 | 232.8 | 127.8 | 91.9 |
| 90 | 214.2 | 238.1 | 234.4 | 212.3 | 122.9 | 89.5 |

Tab. B.23 - Temperatures on plaster wall; PL05

| Time [min] | PL05 | | | | | |
|---------------|-----------------|--------------|---------------|---------------|---------------|---------------|
| | - 10 mm [°C] | 0 mm [°C] | 10 mm [°C] | 20 mm [°C] | 40 mm [°C] | 60 mm [°C] |
| 0 | 20.2 | 19.8 | 20.3 | 19.8 | 18.9 | 18.6 |
| 5 | 28.7 | 23.6 | 21.6 | 20.1 | 19.0 | 18.8 |
| 10 | 120.0 | 68.8 | 38.2 | 24.1 | 19.0 | 18.6 |
| 15 | 219.3 | 145.4 | 88.7 | 48.7 | 22.3 | 19.3 |
| 20 | 257.8 | 183.4 | 116.8 | 78.3 | 32.7 | 21.7 |
| 25 | 492.4 | 345.7 | 163.0 | 100.4 | 50.9 | 26.2 |
| 30 | 457.8 | 374.2 | 232.6 | 122.8 | 92.3 | 45.8 |
| 35 | 590.3 | 513.7 | 340.1 | 155.9 | 101.2 | 78.0 |
| 40 | 612.9 | 527.1 | 353.8 | 180.2 | 104.3 | 92.9 |
| 45 | 650.2 | 571.2 | 413.1 | 225.2 | 106.4 | 101.8 |
| 50 | 647.1 | 590.2 | 449.5 | 267.2 | 107.7 | 103.8 |
| 55 | 640.7 | 588.1 | 450.2 | 284.3 | 108.0 | 102.3 |
| 60 | 796.6 | 697.0 | 514.3 | 329.1 | 111.6 | 103.3 |
| 65 | 708.4 | 684.0 | 542.4 | 364.9 | 112.8 | 95.9 |
| 70 | 505.6 | 526.3 | 458.2 | 340.6 | 114.6 | 96.2 |
| 75 | 400.3 | 438.8 | 406.6 | 318.9 | 116.9 | 100.0 |
| 80 | 341.4 | 385.3 | 365.3 | 291.9 | 115.5 | 95.8 |
| 85 | 268.1 | 304.0 | 297.6 | 252.7 | 112.2 | 91.6 |
| 90 | 230.8 | 265.5 | 262.4 | 228.3 | 112.3 | 90.7 |

Tab. B.24 - Vertical deflection of the floor structure

| Time [min] | V1 [mm] | V2 [mm] | V3 [mm] | V4 [mm] | V5 [mm] | V6 [mm] | V7 [mm] | V8 [mm] |
|---------------|------------|------------|------------|------------|------------|------------|------------|------------|
| 0 | 0.22 | 0.22 | -0.63 | -1.57 | 0.25 | -0.32 | 2.45 | 1.48 |
| 5 | -2.71 | -3.59 | -4.81 | -6.48 | -2.53 | -3.26 | 1.76 | 0.68 |
| 10 | -23.98 | -28.58 | -30.14 | -33.99 | -20.15 | -21.66 | -3.02 | -4.33 |
| 20 | -81.33 | -107.63 | -108.04 | -135.62 | -80.77 | -80.48 | -17.01 | -16.87 |
| 33 | -214.08 | -324.95 | -380.38 | -368.10 | -209.97 | -215.80 | -55.02 | -51.14 |
| 43 | -280.66 | -411.88 | -461.13 | -429.33 | -244.91 | -258.50 | -81.79 | -75.11 |
| 50 | -345.62 | -499.79 | -555.00 | -504.16 | -253.31 | -269.26 | -89.77 | -83.93 |
| 58 | -422.70 | -598.63 | -652.99 | -586.71 | -256.27 | -275.16 | -98.61 | -91.66 |
| 60 | -739.78 | -891.88 | -877.96 | -758.76 | -256.32 | -275.68 | -100.86 | -94.17 |
| 62 | 130.27 | 141.23 | 13.24 | -117.95 | -264.34 | -277.48 | - | - |
| 65 | 130.24 | 141.17 | 45.57 | -63.67 | -250.37 | -262.78 | - | - |

Tab. B.25 - Horizontal deformation of the floor structure

| Time | H1 | H2 | H3 | H4 | H5 |
|-------------|-----------|-----------|-----------|-----------|-----------|
| [min] | [mm] | [mm] | [mm] | [mm] | [mm] |
| 0 | 0.64 | 0.18 | 0.24 | 0.21 | 0.31 |
| 5 | 0.65 | 0.19 | 0.25 | 0.24 | 0.16 |
| 10 | 1.37 | 1.38 | 1.07 | 0.54 | -0.83 |
| 18 | 5.04 | 4.81 | 1.02 | -2.18 | -5.83 |
| 21 | 5.76 | 8.18 | 0.95 | -3.10 | -8.41 |
| 28 | 5.81 | 13.43 | 8.53 | 5.10 | -11.80 |
| 32 | 5.81 | 13.43 | 8.53 | 12.81 | -9.33 |
| 35 | 5.81 | 13.43 | 8.53 | 12.80 | -9.32 |

Tab. B.26 - Temperatures and pressures in the concrete wall

| Time | TC129 | | TC130 | |
|-------------|--------------|--------------|--------------|--------------|
| | 40 mm | 40 mm | 70 mm | 70 mm |
| [min] | [°C] | [hPa] | [°C] | [hPa] |
| 0 | 22.3 | 6.0 | 30.6 | 7.8 |
| 5 | 29.8 | 6.0 | 33.8 | 7.9 |
| 10 | 37.7 | 5.7 | 36.8 | 7.7 |
| 15 | 60.7 | 6.8 | 50.2 | 8.0 |
| 20 | 83.1 | 9.4 | 60.9 | 8.5 |
| 25 | 131.7 | 12.3 | 83.5 | 9.4 |
| 30 | 162.9 | 27.1 | 102.5 | 10.4 |
| 35 | 219.2 | 33.8 | 153.0 | 12.2 |
| 40 | 261.1 | 47.1 | 164.6 | 15.1 |
| 45 | 316.8 | 246.2 | 163.0 | 20.2 |
| 50 | 348.9 | 382.7 | 168.1 | 26.6 |
| 55 | 414.4 | 318.6 | 194.1 | 32.7 |
| 60 | 434.1 | 307.0 | 205.1 | 40.0 |
| 65 | 427.8 | 283.8 | 196.9 | 48.3 |
| 70 | 244.5 | 239.4 | 98.2 | 55.8 |
| 75 | 187.1 | 173.3 | 62.4 | 62.2 |
| 80 | 154.0 | 127.2 | 41.5 | 68.9 |
| 85 | 127.4 | 95.4 | 24.3 | 76.2 |
| 90 | 111.6 | 77.0 | 14.2 | 82.3 |
| 95 | 100.9 | 66.1 | - | 86.1 |
| 100 | 93.9 | 59.4 | - | 87.2 |
| 105 | 88.2 | 53.9 | - | 86.8 |
| 110 | 83.8 | 50.3 | - | 85.3 |
| 115 | 79.3 | 47.9 | - | 83.3 |
| 120 | 79.7 | 45.9 | - | 80.2 |

Tab. B.27 - Flux density of the heat

| Time | Q1 | Q2 | Q3 | Q4 |
|-------------|----------------------|----------------------|----------------------|----------------------|
| [min] | [kW/m ²] | [kW/m ²] | [kW/m ²] | [kW/m ²] |
| 0 | -0.07 | -0.16 | -0.17 | -0.10 |
| 5 | 0.08 | -0.01 | 0.45 | 0.48 |
| 10 | 4.84 | 1.97 | 5.83 | 8.97 |
| 15 | 7.23 | 7.78 | 16.36 | 28.43 |
| 20 | 9.06 | 6.37 | 24.52 | 18.47 |
| 25 | 15.60 | 10.55 | 30.60 | 25.20 |
| 30 | 21.30 | 13.03 | 32.05 | 25.70 |
| 35 | 35.26 | 23.21 | 65.76 | 43.67 |
| 40 | 26.90 | 19.13 | 55.56 | 41.46 |
| 45 | 28.42 | 7.47 | 73.98 | 70.50 |
| 50 | 30.91 | 4.51 | 92.17 | 95.04 |
| 55 | 37.25 | 6.00 | 98.90 | 112.74 |
| 60 | 51.09 | 6.17 | 109.08 | 112.74 |